Cyclic Bending Behavior of Hollow Structural Sections and their Application in Seismic Moment Frame Systems

by

Matthew Floyd Fadden

A dissertation submitted in partial fulfillment
of the requirements for the degree of
Doctor of Philosophy
(Civil Engineering)
in the University of Michigan
2013

Doctoral Committee:

Assistant Professor Jason P. McCormick, Chair
Professor Sherif El-Tawil
Professor Jwo Pan
Professor Gustavo Parra-Montesinos, University of Wisconsin

DEDICATION

This dissertation is dedicated to my parents Janyce, Philip, and Cathy for their unconditional love and support.

ACKNOWLEDGEMENTS

Completing my higher education over the last ten years was not done alone. I am extremely thankful for the people and organizations that have supported me throughout graduate school.

I would first like to thank my advisor, Jason McCormick. His support and guidance has contributed to my success and completion of graduate school and this doctoral research. He has taught me to think critically about engineering problems and has shaped me into a better researcher and communicator. Additionally, Prof. McCormick has set a very high standard for professionalism, respect, and integrity. As I start my career in academia, I will strive to maintain his continued respect.

I would also like to thank my committee members Prof. Gustavo Parra-Montesinos, Prof. Sherif El-Tawil, and Prof. Jwo Pan. Their insight and support in both the classroom and research has been constructive and enlightening. As well, I owe thanks to Prof. James Wight, Prof. Ann Jeffers, and Prof. Simon (Shi-Ho) Chao for their advice throughout my graduate studies. I also cannot forget Prof. Leslie Struble and Prof. Glaucio Paulino from the University of Illinois Urbana-Champaign for giving me the opportunity to do undergraduate research with them and inspiring me to continue on with research.

This research could not have been completed without the support of the National Science Foundation (Grant No. EEC-0926858) and the American Institute of Steel Construction. Material donations were also provided by Atlas Tube and Bull Moose Tube, and fabrication of the test specimens was provided by Douglas Steel. These contributions made the experimental studies possible.

Throughout my time at the University of Michigan I have been lucky enough to work with some of really wonderful students and technicians. I owe a great debt of gratitude to my officemate, Xiaohu Fan, for his advice and friendship. I could have not finished my laboratory work without the assistance of the knowledgeable and helpful technicians Bob Fischer, Bob Spence, and Jan Pantolin. Additionally, I would like to

thank numerous others including: Lynn Itani, Min-Yuan Cheng, Monthian Setkit, Jennifer Buison, Alexa Holmes, Olivia Marshall, Remy Lequesne, Mike Stultz, Mantia Athanasopoulou, Thai Dam, Ravi Ranade, En-Hua Yang, Mo Li, Qian (Maple) Zhang, Qianru Guo, Andy Zimmerman, Dan Wei, Elizabeth Stek, Pete Heeringa, and Terry McGovern.

Finally, I would like to thank my parents. Their love and support have been forever constant. They have taught me to work hard, find what makes me happy in life, and never settle until I reach my goals. I truly am lucky to have grown up with them.

TABLE OF CONTENTS

LIST OF TABLES

LIST OF FIGURES

LIST OF SYMBOLS

b_b	Length of the flat portion of the beam flange
b/t	Width-thickness ratio
b/h	Aspect ratio
d	Member depth
d_b	Beam depth
d_c	Column depth
$Deg_{0.04}$	Percent degradation of the maximum moment at 0.04 rad.
E	Modulus of elasticity
E_D	Hysteretic energy dissipation
E_{S0}	Elastic strain energy
e_y	Yield strain
e_u	Ultimate tensile strain
e_u/e_y	Ductility ratio
F_{EXX}	Weld metal strength
F_u/F_y	Ultimate-yield strength ratio
F_{BM}	Base metal shear strength ($0.6F_y$ for shear yielding and $0.6F_u$ for shear rupture)
F_f	Force transferred through the flange plates
F_u	Tensile Strength
F_w	Weld metal strength for HSS-to-HSS moment connection
F_y	Yield strength
$F_{y,exp}$	Experimentally measured yield strength
h_b	Length of the flat portion of the beam web
h/t	Depth-thickness ratio
K	Connection stiffness based on load-displacement hysteresis
K_{beam}	Beam stiffness based on beam moment-rotation hysteresis

K_{col}	Column stiffness based on column moment-rotation hysteresis
K_{cf}	Column face stiffness based on column face moment-rotation hysteresis
K_{pz}	Panel zone stiffness based on panel zone moment-rotation hysteresis
L/r	Member slenderness ratio
l_c	Column length
l_b	Beam length
L_{pl}	Diaphragm plate length
M	Moment
M_{cf}	Beam moment at the column face
M_{conn}	Connection moment
M_{max}	Maximum moment
M_p	Member plastic moment capacity
$M_{p,beam}$	Beam plastic moment capacity
$(M_p)_{exp}$	Plastic moment capacity using experimentally measured material properties
$(M_p)_{min}$	Plastic moment capacity using specified material properties
M_{uc}	Ultimate moment capacity
n	Shape parameter
P	Applioed load
P/P_y	Axial load ratio
P_y	Axial yield load
R	Flare-bevel groove weld throat
R_{ki}	Initial connection stiffness
R_y	Ratio of expected to specified yield strength
R_t	Ratio of expected to specified ultimate strength
S	Elastic section modulus
t	Member wall thickness
t_b	Beam wall thickness
t_c	Column wall thickness
t_b/t_c	Beam-column thickness ratio
t_{pl}	Diaphragm plate thickness

$t_{pl,block\ shear}$	Required plate thickness based on block shear limit state
$t_{pl,plate}$	Required plate thickness based on plate failure
$t_{pl,rupture}$	Required plate thickness based on tensile rupture limit state
$t_{pl,weld}$	Required plate thickness based on the weld capacity
t_w	Weld thickness
$t_{w,fb}$	Effective thickness of the flare bevel groove weld
$t_{w,fillet}$	Required thickness of fillet weld between the beam flange and the diaphragm plate
$t_{w,shear}$	Required thickness of fillet weld between the beam wend and column face
V_{cf}	Shear force at column face
V_c	Shear force in column
$V_{n,pz}$	Panel zone shear capacity
$V_{u,pz}$	Panel zone shear demand
V_g	Shear force due to gravity load
w_b	Beam width
w_{pl}	Diaphragm plate width at the column face
Z	Plastic section modulus
β	Beam width-to-column ratio
γ_1	Panel zone rotation angle at back of the connection
γ_2	Panel zone rotation angle at front of the connection
γ_{xy}	Shear strain
$\delta_{actuator}$	Actuator displacement
ε_{45}	45 degree angle strain component
ε_x	X-direction strain component
ε_y	Y-direction strain component
ε_E	Engineering strain
ε_T	True strain
θ	Rotation
$\theta_{0.8Mmax}$	Rotational capacity at $0.8M_{max}$
θ_{beam}	Beam rotation

$\theta_{beam,overall}$	Overall beam rotation
$\theta_{beam,rigid}$	Rigid beam rotation
$\theta_{beam,pl}$	Beam plastic rotation
$\theta_{beam,pl}^{CL}$	Beam plastic rotation about the column centerline
θ_{cf}	Column face rotation
$\theta_{cf,pl}$	Column face plastic rotation
$\theta_{cf,pl}^{CL}$	Column face plastic rotation about column centerline
θ_{col}	Column rotation
$\theta_{col,pl}$	Column plastic rotation
θ_{conn}	Connection rotation
$\theta_{conn,pl}$	Connection plastic rotation
θ_{pz}	Panel zone rotation
$\theta_{pz,pl}$	Plastic panel zone rotation
λ_p	Beam member compactness limit
ξ_{eq}	Equivalent viscous damping ratio
σ_E	Engineering stress
σ_T	True stress
σ_0	Yield stress
ϕ_{BM}	Base metal strength resistance factor (0.75)
ϕ_{pz}	Resistance factor for panel zone (0.9)
$\phi_{pz}R_{n,pz}$	Panel zone design strength
$\phi_{rupture}$	Resistance factor for plate rupture (0.75)
ϕ_w	Weld strength resistance factor (0.75)
$\phi_w R_{n,fb}$	Flare bevel groove weld design strength
$\phi_w R_{n,fillet}$	Fillet weld design strength
ϕ_{yield}	Resistance factor for plate yielding (0.9)

ABSTRACT

Hollow structural sections (HSS) make up a significant portion of the steel market, where the typical uses in building structures are as column members, bracing members, exposed structural steel, cladding supports, concrete filled tube sections, and truss members. Recent seismic steel research focused on improvements to wide-flange seismic moment resisting frame (SMRF) systems. HSS members provide a possible means of improving the performance of SMRF systems in low- to mid-rise structures based on their high strength-to-weight ratio, good compression and bending properties, and high torsional stiffness. However, an understanding of the behavior of HSS under cyclic bending loads is required along with detailing requirements of HSS-to-HSS moment connections to ensure proper ductility and strength is achieved.

An experimental and analytical program is undertaken to characterize the ability of HSS beam members to withstand large plastic rotations with minor degradation of the maximum moment capacity. Experimental testing of eleven full-scale HSS beam members is carried out. These experimental results are used to calibrate a finite element model for analysis of 133 different beam members. The models account for section geometry, material properties, and local buckling. Local buckling limits the ability of these members to form stable plastic hinges and the behavior is highly dependent on the width-thickness (*b/t*) and the depth-thickness ratio (*h/t*).

With an understanding of the limiting *b/t* and *h/t* ratios for HSS beam members, a connection design methodology is derived for both unreinforced and reinforced fully welded HSS-to-HSS moment connections. A finite element model parametric study is undertaken to better understand the effect of different parameters on the connection performance under cyclic loads typical of an earthquake. Experimental testing of two unreinforced HSS-to-HSS connections with unmatched and matched beam and column widths are also cyclically tested to failure. The hysteretic behavior shows that these connections are limited in their ability to isolate inelastic behavior in the beam member and panel zone region and suggest that unreinforced HSS-to-HSS moment connections cannot achieve a strong column-weak beam mechanism. Based on the finite element model and the experimental study results, recommendations are provided for the design of HSS-to-HSS seismic moment connections.

CHAPTER 1: INTRODUCTION

1.1 Problem Description

In seismically active areas, low to mid-rise moment frames provide lateral load resistance through development of bending moments and shear forces in the members and joints. This mechanism allows moment frames to behave in a ductile manner provided proper detailing of the connections. However, the 1994 Northridge and 1995 Hyogo-ken Nanbu (Kobe) Earthquakes showed that complete joint penetration welds between the beam flanges and the columns are not sufficient to develop the plastic moment strength of the beam member and can result in brittle fracture of the connection (Kurobane et al. 2001). Nearly $25 billion dollars of damage resulted from the Northridge Earthquake (U.S. DOT 1994), while over 240,000 buildings were damaged by the Hyogo-ken Nanbu Earthquake (AIJ 1998). In response to these findings the SAC Joint Venture was created leading to improvements in the design of steel moment frame systems and an understanding of the behavior and damage mechanisms associated with large cyclic loads (FEMA 2000). The need for a more predictable and reliable performance of structures under extreme loads also led to a focus on performance-based seismic design allowing owners and engineers to consider appropriate performance objectives and acceptable displacement or damage levels, for their buildings. For steel moment frame design, this included the development of specific ductility and detailing requirements for special (SMF) and intermediate (IMF) systems. Although this work has significantly improved the performance of steel moment frame systems, it has mainly focused on wide flange-to-wide flange moment connections leading to missed opportunities for further improvements through the use of other beneficial sections, such as square and rectangular hollow structural sections (HSS).

HSS are a cold formed structural member made from rolling steel sheets into circular, square, or rectangular cross sections (Figure 1.1). Typically HSS have been used as column members, truss elements, bracing members, and cladding supports because of their excellent compression, bending, and torsional properties. However, HSS have been underutilized in bending applications. In addition, HSS make up approximately 30% of the steel market in Europe and Japan where it is common practice to use HSS columns with wide flange beams in seismic moment frames systems. In the United States their use has been more limited, making up only 15% of the market, which has reduced their potential benefit in cyclic bending applications. Potential benefits of using HSS members in moment frame systems include reduced weight, possible reduction in lateral bracing requirements, applications to modular construction, use in steel-concrete composite systems, and implementation in architecturally exposed structural steel frames. The American Institute of Steel Construction (AISC) has recognized the benefits of HSS and now includes design specifications for HSS in Chapter K of the main body of the design specification (AISC 2010a) and has made program recommendations for the development of HSS seismic moment connections (Sabol 2006).

Because of their beneficial properties, research into the behavior of HSS members continues to grow. Studies have been carried out considering HSS as axially loaded members in braced frames and trusses (Tremblay et al. 2003) or as concrete filled tube (CTF) columns (Packer 2000, Hajjar 2000, Kurobane 2002). Several researchers have considered HSS beam behavior (Korol and Houdba 1972, Hasan and Hancock 1988, Wilkinson and Hancock 1998) and connection behavior under monotonic loads (Hancock et al. 2000). Further, the International Committee for Research and Technical Support for Hollow Section Structures (CIDECT) has created design guidelines based on this current research current research. This has led to uniplanar and multiplanar truss and bolted HSS connection design requirements and limitations for static loading conditions (CIDECT 2010). Structural shear and semi-rigid beam-column connections between HSS beam and column members and HSS column and wide-flange beam members have also been specified to ensure their performance under static loads. Several rigid connections suitable for seismic moment resisting frame systems have been studied and created for HSS column-to-wide flange beam connections utilizing internal and external diaphragm reinforcement plates (CIDECT 2005). However, ductile moment connections between

HSS beam and HSS column members have not been studied which has limited the ability to consider tube based moment frames in areas of high seismicity.

Only recently have researchers considered the use of HSS-to-HSS moment connections for seismic loading. The lack of application of these moment connections is partially due to the fact that connection configurations have not been developed (Kumar and Rao 2006). The only studies to consider HSS-to-HSS seismic moment connections are by Kumar and Rao (2006) and Rao and Kumar (2006) who considered the behavior of an innovative bolted moment connection with channels and web openings. This work suggests the feasibility of HSS-to-HSS moment frame connections, but the information needed for their widespread use is still lacking. *The goal of this project is to characterize the behavior of HSS beams and welded HSS-to-HSS moment connections both experimentally and analytically under large cyclic deformations to provide a basis for the design and utilization of HSS-to-HSS moment frame systems for low to mid-rise structures in regions of high seismicity.*

1.2 Project Objectives

This research achieves the goal of characterizing the behavior of HSS-to-HSS moment frame systems by addressing the lack of understanding of HSS bending behavior and the behavior of HSS-to-HSS moment connections under cyclic loads. In the process of characterizing this behavior, geometric and material properties are taken into consideration through a range of experimental and numerical studies. With an understanding of HSS and potential limiting factors for their use in seismic bending applications, HSS-to-HSS moment connection configurations are developed and studied experimentally to determine their efficiency and reliability to withstand earthquake loads. The findings provide direct recommendations for the design of HSS-to-HSS seismic connections for use in low-to-midrise moment frames. This is accomplished through three main tasks.

TASK 1: The behavior of eleven HSS beam members ranging in size from HSS 8x6x1/4 to HSS 12x6x1/4 are experimentally characterized under cyclic loads to:

- Understand the variation in material properties from locations around the cross section (flats, corners, and welds) of HSS and to analyze the effects of cold working on the tensile properties.
- Identify and understand limit states, associated with failure of HSS beam members in cyclic bending, such as local buckling and fracture.
- Ensure adequate plastic hinge behavior for strong column-weak beam requirements with *b/t* ranging from 8.46 to 31.3 and *h/t* ranging from 19.9 to 48.5.
- Evaluate the hysteretic moment rotation behavior, secant stiffness, and equivalent viscous damping of HSS beam specimens in bending.
- Determine limiting parameters for HSS beam members to form stable plastic hinges with limited local buckling behavior under earthquake type loading conditions.
- Characterize the yielding and plastic hinge length utilizing strain gage data.

TASK 2: Finite element methods are used to capture the local buckling and global hysteretic behavior of HSS members in cyclic bending in order to:

- Calibrate and validate a finite element model (FEM) for HSS in bending to the experimental data from TASK 1 so that the model accurately captures local and global behavior observed during the experiments.
- Utilize the FEM to study the behavior of 133 different HSS beam members ranging in size from HSS 6x2x3/16 to HSS 20x12x5/8.
- Identify more accurate limiting parameters for the use of HSS in cyclic bending applications based on rotation at maximum moment and moment degradation.
- Predict limit states and failure moments and their corresponding rotation levels based on member dimensions and material properties.

TASK 3: The behavior of welded HSS-to-HSS moment connections subjected to cyclic loads is characterized analytically and experimentally. Analytical parametric studies of unreinforced and reinforced connections are conducted and large-scale experimental tests of two unreinforced HSS-to-HSS connections are conducted under cyclic bending loads:

- Determine viable welded unreinforced and reinforced HSS-to-HSS moment connection detailing requirements based on previous research and the findings in Task 1 and 2 considering limit states that could affect HSS-to-HSS moment connection behavior.
- Study the behavior of unreinforced and reinforced HSS-to-HSS moment connections analytically to better understand the sensitivity of pertinent parameters such as depth, beam width-to-column width ratio (β), thickness ratio (t_b/t_c), and reinforcement dimensions on the cyclic connection behavior.
- Experimentally evaluate the behavior of unreinforced exterior moment connections considering the effect of the beam width-to-column width ratio with HSS 12x8x3/8 (β=0.80) and HSS 12x10x3/8 (β=1.0) beam members and a HSS 10x10x5/8 column.
- Develop design guidelines for the use of HSS-to-HSS moment connections in seismic moment frames.

1.3 Dissertation Outline

The content of the dissertation is organized into the following chapters:

Chapter 2: An introduction to hollow structural sections and their behavior under various loading conditions is presented. An overview of past studies on the axial and flexural behavior of HSS and HSS connections is also discussed.

Chapter 3: A study on the variation of material properties around the cross section of HSS members. The effect of HSS thickness and specimen location on the cross-section is carefully examined in terms of both strength and ductility.

Chapter 4: Eleven HSS beam members are examined experimentally under cyclic loading to high rotation levels. The plastic hinging, buckling, and hysteretic behavior are analyzed.

Chapter 5: A finite element model of HSS beam members utilizing experimental material properties, specified section geometries, and considering local buckling is calibrated to experimental results and used to compare 133 different HSS beam members under cyclic bending to further characterize their behavior.

Chapter 6: Design procedures and a finite element model for exterior unreinforced and reinforced HSS-to-HSS moment connections are developed to analyze the effect of pertinent parameters on the hysteretic behavior and performance of the connections under large cyclic loads.

Chapter 7: Two unreinforced HSS-to-HSS moment connections are tested experimentally under cyclic reversals to further understand the behavior of HSS-to-HSS moment connections for seismic applications. These tests provide information on the load path through the connection, allow for improved detailing requirements, and identify potential limit states.

Chapter 8: A summary and conclusions from the research are presented. Suggestions for future research in regards to seismic application of HSS are also made.

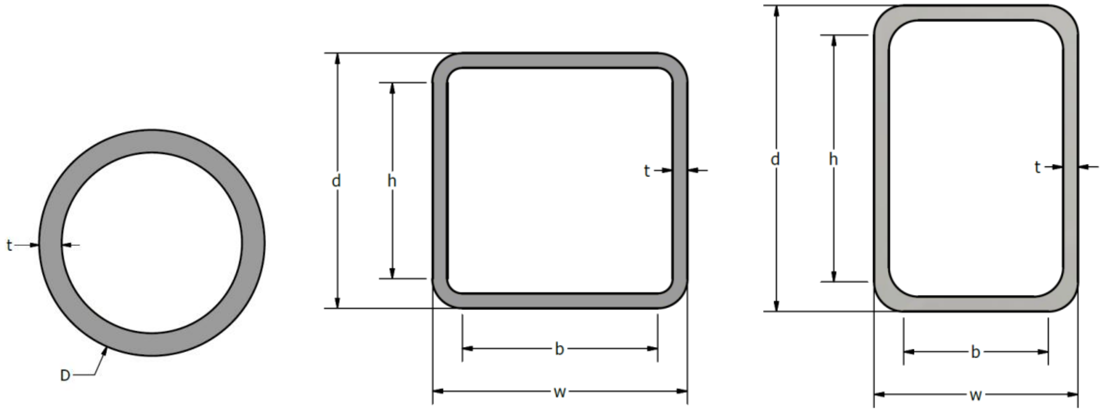

(a) (b) (c)

Figure 1.1 Cross section of (a) circular, (b) square, and (c) rectangular HSS members with geometric variables

CHAPTER 2: LITERATURE REVIEW

2.1 Background

Cold formed hollow structural sections (HSS) were first manufactured in 1952 in the United Kingdom. As a consequence, research on HSS spread especially to Europe, Japan, the United States, and Australia. In the United States the use of circular HSS for offshore structures became increasingly popular and gave rise to some of the design rules used for onshore structures. HSS research has been active in North America since the 1970's due to favorable market conditions for the offshore tubular structure industry. The growth of onshore HSS use continues to expand with the most active areas of research being fatigue in welded connections, fire resistance, seismic structural applications, column connections, bolted connections, composite members, and composite connections (Packer 2000). Figure 2.1 shows some of the uses for HSS members. In steel building construction HSS are commonly used as braces, cladding support, truss members, columns, beams, and scaffolding. Other uses for HSS include applications in the transportation and highway industry, agricultural equipment, mechanical members, and recreational structures (Zhao et al. 2005).

In the United States development of onshore tubular structures has moved slowly relative to the rest of the world. The American Institute of Steel Construction (AISC) published the Hollow Structural Sections Connections Manual in 1997 with specifications and commentary specifically focused on onshore HSS design and construction (AISC 1997). This specification, which was based on the American Welding Society D1.1 code (AWS 2010), covers material properties, load combinations, tension, compression, bending, shear, torsion, beam-column resistance, concentrated loads on hollow sections, fasteners and welds, directly welded truss connections, and fabrication requirements (Packer 2000). The HSS Connections Manual relies heavily on the AISC

LRFD Specification for Steel Buildings (1993) and includes many pre-designed connections (Packer 2000).

2.1.1 Design Guides and Specifications

The 3rd Edition of the Manual of Steel Construction LRFD (AISC 2001) and the LRFD Specification for Steel Hollow Structural Sections (2000) was updated from the 1997 specification for the first time and included in the main steel manual. This specification included the design of HSS-to-HSS planar T-, Y-, X-, and gap K-connections. However, multi-planar and overlapped connections were not included (Packer 2000). Revisions to the AISC specification (2005, 2010a) made the ability to design using HSS in the United States more readily accessible. Currently, the AISC Specification (2010a) Chapter K is the sole design specification for HSS connections in the United States. However, the current specification does not cover seismic or fatigue design. Topics, such as columns and bracing members, are covered in the AISC Seismic Specification (2010b), but further research is needed before HSS can be fully utilized for these applications.

In addition to the AISC Specification (AISC 2010a), the other major standards that address the use of HSS members include: British Standard BS 5950 Part1 (2000), Australian Standard AS 4100 (1998), Canadian Standard CSA-S16-01 (2001), Eurocode 3 Part 1.1 (2003), New Zealand Standard NZS 3404 (1997) and the Architectural Institute of Japan (AIJ) (1990). CIDECT has produced nine design guides that assist engineers in designing structures with tubular members and address some aspects that are not included in the AISC Specifications. Also, several books have been written discussing tubular structure design (Wardenier 1982, Marshall 1992, Hancock 1998, Packer and Henderson 1997, Eekhout 1996, Wardenier 2001, Hancock et al. 2001, Dutta 2002, Zhao et al. 2005). Recently, a new design guide has been published by AISC, Design Guide 24 - Hollow Structural Section Connections (Packer et al. 2010). This guide provides examples and information for the design of connections in many configurations including moment, shear, and axial truss connections. The design guide also discusses important details such as welding and bolting requirements for HSS members.

2.2 Axial Behavior of HSS

2.2.1 HSS Braces

HSS are very efficient in tension and compression and are often used as bracing members in braced frames (Tremblay 2002). Early experimental work on the development of HSS as bracing members for seismic applications was done at the University of Michigan (Gugerli 1982, Lee and Goel 1987, Liu 1987) and throughout the world (Foutch et al. 1987, Bertero et al. 1989, Fukuta et al. 1989, Walpole 1996). Experiments and observations after earthquakes showed that HSS braces are prone to fracture due to local buckling (Tremblay et al. 2003). Tremblay (2002) compiled results of more than 100 tests, of which many are HSS members, and found several useful engineering design guidelines. Fracture of HSS braces depends strongly on the slenderness ratio and width-thickness ratio (*b/t*) of the bracing member. More stringent width-thickness ratios are needed for slender members because of the high ductility demand on these sections. Several analytical models also have been created to predict the fatigue life of HSS members under cyclic loading (Lee and Goel 1987, Tang and Goel 1987, Hassan and Goel 1991, Ikeda and Mahin 1986, Huang 2009). Figure 2.2 shows a recent experiment that has been performed on X-bracing members (Tremblay et al. 2003). Other researchers have worked on understanding the limit states for slotted tubes (Yang and Mahin 2005), circular HSS braces (Elchalakani 2003), and bracing members under cyclic loads (Goggins et al. 2005, Tremblay et al. 2008).

Extensive modeling of HSS braces in braced frames has been performed. Early work focused on phenomenological models that are simple and computationally efficient. These models typically used truss elements that mimic the experimental response and are calibrated using experimental data (Uriz et al. 2008). Phenomenological studies include work by Ikeda and Mahin (1986) and Fukuta et al. (1989). Ikeda and Mahin (1986) considered the use of beam-column elements with inelastic hinges. Finite element models have also been considered for braces. Jin and El-Tawil (2003) used a special beam-column element with distributed inelasticity and a bounding plasticity model. Huang (2009) created a finite element model for a single HSS bracing member. This model used LS-DYNA and had no initial imperfection and was cyclically axially loaded. Global buckling was first seen in the model then local buckling triggered by round off errors. A damage model was incorporated that allows for fracture and the deterioration was predicted with some accuracy. Figure 2.3 shows the comparison of the experimental work and the finite element model. This model was then applied to a chevron bracing subassembly with HSS braces and correlated well with experimental data. Recognizing the complexity of these models, Chen et al. (2009) compared the model described by Huang (2009) to a fiber element modeled in OpenSees. This study found that the two different models can have very different results and can show different failure modes.

While axially loaded braces do not have the same boundary conditions as HSS beam members, many of the failure modes observed are important when considering the cyclic bending behavior of HSS. More specifically these members undergo large cyclic displacements and undergo local buckling and fracture. The local buckling and fracture limit states in braced frames provide insight into the effect of parameters that may control the behavior of HSS under large inelastic bending cycles.

2.2.2 HSS Columns

Early work by Dywer and Galambos (1965) studied the effects of beam-columns at fixed axial load ratios and increasing moments. Tests performed in Australia focused on both stub and long columns and then developed analytical models based on the finite strip method (Key et. al 1988, Key and Hancock 1993). More recent non-seismic research considered the axial load-moment interaction behavior of square and rectangular tube sections. These tests found that the current design standards are mostly conservative and the interaction is nearly linear for square HSS members (Hancock and Rasmussen 1998). Continued beam-column research has allowed for less conservative standards to be used (Sully and Hancock 1996, Sully and Hancock 1998). Dean et al. (2001) looked more closely at the effects of the aspect ratio (*h/b*) and slenderness parameters of the section finding that these parameters affect the amount of degradation of the load carrying capacity at large rotations.

Cyclic tests performed recently in Japan considered the seismic performance of HSS column members. Experimental results from columns under constant axial load were replicated with finite element analysis, but accuracy was limited to when the section began to buckle excessively (Nakashima and Liu 2005). Other tests considered the width-thickness ratio as well as the axial load ratio and found these factors have a large effect on the seismic resistance capacity of HSS columns (Kurata et al. 2005). An online hybrid simulation was able to model building behavior while the column bases were tested experimentally. These experiments showed the significance of varying axial load on the behavior of HSS at the column base (Wang et al. 2008).

While a considerable amount of seismic research has been performed on HSS bracing members under seismic loads, research also has focused on the use HSS column members. The bending behavior of column members provides an idea of the behavior of beam members including the effect of dimensional properties. It can be expected that the buckling behavior of beams would be less severe than HSS columns due to smaller axial loads.

2.2.3 Concrete Filled Tubes

Concrete filled tube (CFT) sections have been used throughout the world in seismic and non-seismic applications. CFTs are able to mitigate the effects of local buckling in the steel section and increase its stiffness. The use of CFT in moment frames may improve the seismic response of the connection and mitigate local buckling under cyclic loads.

As with HSS members, CFTs are very efficient in compression and have been used in many applications such as slender columns when combined with high strength concrete (Roeder 1998). CFTs are effective because the steel lies on the outside and resists flexure, axial tension, and compression. The concrete forms a core that resists axial compression and local buckling of the surrounding steel (Hajjar 2000). Researchers have considered the behavior of CFT members under several loading conditions including axial (Prion and Boehme 1994, Bergmann 1994, Furlong R.W. 1967), flexure (Lu and Kennedy 1994), combined axial and flexure (Tomii and Sakino 1979, Tsuda et al. 1996), and torsion (Lee et al. 1991), as well as their behavior under seismic loading conditions (Liu and Goel 1988, Kawano and Matsui 1997, Sakino and Tomii 1981, Sakino and Ishibashi 1985, Hajjar et al. 1998, Morino et al. 1993, Varma et al. 1998, Kawaguchi et al. 1998, Nishiyama 2004). In addition research has also considered the effects of creep and shrinkage, bond, and residual stresses on CFT members (Hajjar 2000).

Experimental testing of CFT members has found that the axial strength is affected by the width-to-thickness ratios, which also are shown to be factors in local buckling of unfilled HSS (Prion and Boehme 1994). Beam-column experiments found that parameters such as concrete strength, width-to-thickness ratio, length-to-depth ratio, and axial load ratio affect the strength of CFT beam-columns and can cause adverse effects on the ductility of the section (Hajjar and Gourley 1996). Studies concerning the cyclic behavior of CFT columns showed that concrete delays the local buckling and increases the number of cycles to failure (Liu and Goel 1988, Kawano and Matsui 1997). This behavior provided full hysteresis loops and considerable energy dissipation (Morino et al. 1993, Sakino and Tomii 1981, Kawaguchi et al. 1998). Recent work by Perea et al. (2010) considered the behavior of slender CFT beam-columns under biaxial bending while including the effects of large width-thickness ratios (Figure 2.4). These tests were able to determine the critical column load, the beam-column axial load-moment interaction diagram, and the strength and effective stiffness degradation for cyclic uniaxial and biaxial bending of CFT beam-columns using different biaxial loading protocols. The results confirmed the resilience of CFT members.

In addition CFTs have been shown to be very effective in connections. Concrete filled composite column connections provide increased bearing strength and prevent punching shear. The stiffness of the connection is increased along with the yield load (Packer 1995). A tension transfer mechanism needs to be added to the concrete to ensure that the steel still provides proper confinement (Packer and Henderson 1997).

Although CFTs are heavier than HSS members, CFT members provide a way to control local buckling and increase the stiffness of HSS members. If suitable behavior for seismic loading cannot be achieved with HSS alone, CFTs provide a possible alternative to unfilled HSS members. In addition the effect of increasing the width-thickness ratio in CFTs provides further insight into the behavior of HSS members.

2.3 Flexural Behavior of HSS

2.3.1 Experimental Research on the Flexural Behavior of HSS

Limited experimental research has been performed on the flexural behavior of HSS. As previously mentioned, most research considering the flexural behavior has focused on axially loaded beam-columns. This work has given important insight into the bending behavior of HSS beam members and presents a preliminary knowledge base. An understanding of the cyclic bending behavior of HSS beams is needed for moment frame systems to ensure strong column-weak beam design requirements and proper behavior can be met.

Early tests by Korol and Hudoba (1972) focused on the monotonic bending behavior of HSS through testing of fourteen rectangular and two round sections. This series of experiments found that residual stresses caused by fabrication lowered the initial yield moment below that of the stress free section. Korol and Hudoba (1972) also noted the importance of the width -thickness ratio in regards to the reduction of the moment capacity of a section during large rotations. Sections with lower width-thickness ratios showed local buckling and degradation of moments at larger curvature values. Korol and Hudoba (1972) recommended an inelastic rotation capacity (R) of four times the rotation corresponding to M_p (R=4) for moment redistribution to be achieved in plastic design. A slenderness limit of $b/t \leq 150/\sqrt{\sigma_0}$ (ksi) was also recommended. Where σ_0 is the yield strength.

In the late 1980's, an Australian group tested nineteen specimens of ten different HSS sizes under monotonic bending to find the plastic hinge rotation capacities with different flange width-thickness ratios (Figure 2.5). Recommendations were made to increase the acceptable width-thickness limits for 50 ksi (350 MPa) sections from 21 recommended by Korol and Hudoba (1972) to 25 to achieve an R=4. It is important to note that this study considered the importance of the aspect ratio of the section and its effect on buckling in the webs (Hasan and Hancock 1988). Later studies considered the bending behavior of an HSS member due to bearing of a chord member. In addition, pure bending tests were conducted as a control. The pure bending tests considered several square and rectangular sections and found that these sections performed above the expected strength determined analytically using the material data strength from both the coupon specimens and the required nominal strength. Like previous research, this set of experiments suggested the importance of the loading conditions and the effects that it has on the behavior of the HSS beam member. A mechanism model also was developed using the plate theory strength of the member to estimate the design parameters for the loading conditions (Zhao and Hancock 1991, Zhao and Hancock 1992, Hancock and Zhao 1992).

Wilkinson and Hancock (1998) performed 44 monotonic bending tests with three different loading schemes to consider the effect of the web slenderness or depth-thickness (h/t) ratio on the behavior of HSS members. The results suggested that sections are more likely to yield in the flange at low aspect ratios (less than 2), while at high aspect ratios buckling will likely occur in the web of the HSS. Figure 2.6 shows the expected behavior for different classes of HSS defined by their compactness. These experiments found that the current web slenderness limits specified by AISC LRFD, AS 4100, and Eurocode 3 are non-conservative and the interaction between flange and web slenderness must be interrelated. Figure 2.7 shows isorotation curves for the expected rotation capacity given a web and flange slenderness. A bilinear interaction formula for the flange and web slenderness relationship was developed during this study. A recommendation was made for updated b/t and h/t limits that led to a change in the compactness limit in the AISC Specification (2005) from $\lambda_p = 3.76\sqrt{E/F_y}$ (h/t=94.4 for F_y=46 ksi) to $\lambda_p = 2.42\sqrt{E/F_y}$ (h/t=60.8 for F_y=46 ksi) to allow beams to reach a target rotation capacity of R=3. These tests were critical in evaluating the behavior of HSS beam members, but do not account for the behavior associated with large cyclic loads due to earthquakes.

The number of tests on the cyclic response of HSS members for seismic applications is even more limited. Guerrero et al. (2007) performed biaxial bending tests on three different HSS under monotonic load and four specimens under cyclic loads. It was found that a lumped damage mechanics models is suitable for accurately representing the force-displacement hysteresis. Studies have also considered the seismic response more closely. Four different cantilevered HSS beam members were cycled according to the loading protocol specified by the AISC Seismic Design Manual (2006) with b/t ratios ranging from 18.5 to 25.6 and h/t ratios ranging from 18 to 35.5. The hysteretic curves were compared to monotonic tests. The cross sectional shape parameters, such as *b/t* and *h/t*, were found to play an important role in the load capacity degradation. In addition the plastic hinge was typically seen at 1.2 times the flange width from the base of the connection (Brescia et al. 2009).

Other studies focused exclusively on the buckling behavior of HSS members. Corona and Vaze (1996) ran experiments and noted the rippling behavior in the sections that initiated buckling. The amount of rippling on the compression flange increased as the depth-thickness ratio grew. Tubes with high *h/t* showed very strong ripples while tubes with lower *h/t* showed less pronounced deformations. Failure occurred when a kink formed in the compression flange for all specimens. Another experimental study considered the lateral-torsional buckling of HSS members and found that the predicted lateral-torsional buckling load was less than that specified according to AISC LFRD (1993). Based on these experiments recommendations were made for the design of HSS beam sections (Zhao et al. 1995). Currently, there is no code requirement for adequate bracing against lateral torsional buckling of HSS beam members in the AISC Specification (2010a).

Because of the popularity of HSS columns, particularly in Japan and Europe, the most extensive flexural testing of HSS has focused on beam-columns. Early monotonic tests performed by Dwyer and Galambos (1965) considered the behavior of tubular beam-columns focusing on the relationship between the axial load and moment. More recent tests considered the behavior under cyclic loading conditions. Nakishima and Liu (2005) compared slenderness ratio, axial load ratio, and hysteretic behavior to gain an understanding of the plastic hinge behavior of HSS members. Figure 2.8 shows the effect of the axial load ratio ((a) 0, (b) 0.3, (c) 0.6) that led to increased degradation. These results were used to create a finite element model of the HSS behavior under cyclic loads. Similar tests found that the web and flange slenderness ratios were important parameters for the cyclic inelastic behavior of these sections. This study allowed for the development of models that considered the importance of the degradation behavior at the column base (Kurata et al. 2005). In addition, the plastic hinge region of HSS column bases was considered using hybrid testing to simulate the behavior of a building during an earthquake. Frame components that could be modeled accurately were addressed analytically while the complicated nature of the plastic hinge region was evaluated experimentally. These results reiterated previous work and found that the axial load ratio and width-thickness ratio are important in understanding the ability to reach the plastic moment strength and the degradation of the section with continued cycling (Wang et al. 2008).

2.3.2 Analytical Studies of the Behavior of HSS

To supplement the experimental research on HSS beam members, models have been developed to predict the behavior and understand different failure modes of HSS beam members. Analytical modeling has been used to study HSS in flexure, during buckling, and as braces and columns using both phenomenological models and physical (or mechanics based) models. While some research has focused on modeling the overall beam behavior, others have tried to study strictly the buckling behavior to better understand the inelastic response of HSS members.

Sohal and Chen (1988) considered the local buckling behavior of round HSS. They developed a kinematic model that can be used to consider the cyclic behavior. This model allowed for the prediction of the load-deflection relationship of the section based on several assumptions such as, the critical strain, shape of the buckle, propagation of the buckle, and stress in the HSS. The findings showed that closed formed expressions could be used to define the cyclic response. Febres et al. (2003) used a local buckling model that lumps the local buckling at the plastic hinge region for round HSS. A counter-buckling concept was introduced with the idea that local buckling in one direction impedes local buckling in the other directions. The amount of buckling was related to section properties. The model compared reasonably well to small-scale frame test results.

Other studies focused on square and rectangular HSS. Hancock et al. (1990) used the finite strip method and developed analytical models for nonlinear behavior of members with local, distortional, and overall buckling. This model provided accurate results for members under inelastic displacements. However, additional theory is needed when considering cold-formed members because of the substantial yielding that can occur before local buckling. In this model the coefficient method for beam-column bending and nonlinear local buckling analysis were combined to account for axial-moment interaction. Key and Hancock (1993) considered the behavior of columns and again used the finite strip method for stub and pinned-end columns. This analysis accounted for imperfections, change in yield stress, and the stress-strain behavior. The results suggested that the addition of residual stresses became increasingly important to the behavior of the column.

Nakashima and Liu (2005) used a finite element model to study sections cycled to complete failure. The model used thick shell elements for the HSS member. It was able to obtain a buckled shape that was close to the buckled shape found experimentally. The model was reasonably accurate for the case of no axial load and small rotations. At larger rotations the accuracy decreased, but still predicted the general behavior. For sections with axial load, the prediction was less accurate. The finite element model broke down when the buckles start bending over on one another leading to contact between buckled surfaces.

Kurata et al. (2005) applied a phenomenological model to frame behavior. This study again found that the axial load and the slenderness ratios were important concerning column behavior. This model accounted for the negative hysteretic slope caused by degradation and related it to the total plastic deformation. More recent work used the same model, but considered data from an online hybrid test (Wang et al. 2008). One shortcoming of this model was that only a constant axial load ratio could be input.

Few studies have used analytical models to understand the behavior of HSS beam members. Wilkinson and Hancock (2002) modeled the bending behavior of HSS beam members based on the test setup used for flexural tests (Figure 2.9) (Wilkinson and Hancock 1998). The model attempted to predict the behavior of sections that would be suitable for plastic design using two different material properties from coupon tests taken from the corners and flats of the HSS member. The FEM used four node double curved shell elements and initial imperfections, such as bow out of the webs and flanges, measured directly from the experimental specimens. The results were affected by the amount of imperfection and type. Several different imperfection schemes were tested including constant distortion across the web and flange, sinusoidal distortion across the web and flanges, and sinusoidal distortion across the web and flange with a linearly varying term. The linearly varying term caused the distortions near the compression flange of the member to be larger. Ultimately, this model found that a bow out that is experimentally measured is not great enough to influence the FEM results under monotonic loading.

These past studies show that modeling HSS members under cyclic loading is feasible. Both the phenomenological and finite element models present an efficient way to better understand the behavior of HSS beam members. When properly calibrated, these models provide a useful tool in understanding the behavior of many HSS members when experimental testing is limited.

2.4 Connections to HSS Members

2.4.1 Truss Connections

HSS have been used extensively for truss connections. Often these connections are not designed to carry moment, but the effects of the connection angle, bearing area, loading conditions, and failure modes can provide insight helpful in considering HSS-to-HSS moment connections.

Current design specifications consider four different planar truss connections, X-, T-, Y-, and K-connections. Packer et al. (1992) gives recommendations for K-connections of square and rectangular HSS. Research has shown that the ratio of the brace width-to-chord width is extremely important (Davies et al. 1984, Koskimaki and Niemi 1990). As this ratio approaches 1.0, the failure mode changes abruptly because the webs of the chord stiffen the connection. Other researchers have considered T-connections and X-connections, which are considered permutations of K-connections that can come under combined axial loads and bending moments. The findings indicated that the pre-stress caused by an initial moment in the chord can control the connection strength and ductility (Liu et al. 1998). Ono et al. (1991, 1993, 1994), Owen et al. (1996) and Davies et al. (2001) have studied bird-beak connections where the brace and chord members are rotated 45 degrees about the longitudinal axis. The rotation of the member can greatly increase the stiffness and strength of the connections.

A major concern for unreinforced HSS-to-HSS connections is the effectiveness of the weld. AISC Design Guide 21 (Miller 2006) and Design Guide 24 (Packer et al. 2010) provide advice on welding HSS members. Two design methods are developed: (1) the weld can be proportioned to develop the yield strength of the connected member at all locations around that member or (2) the weld can be proportioned for the branch forces provided there is confidence in these expected values (Packer and Sun 2011). Past research considering HSS truss systems showed that for many connections the whole length of the fillet weld should not be considered effective (Frater and Packer 1992a, Frater and Packer 1992b). Weld effectiveness criteria were developed leading to a detailed design methodology for of welds in HSS T- and X- connections. These criteria were included in the AISC specification chapter K (AISC 2010a). The chord and branch member geometry are included in the formulation of the effective weld length. These more sophisticated design methodologies help reduce weld size, increasing weld design economy (Packer and Sun 2011).

The use of multi-planar welded truss connections has also received some consideration. The CIDECT Design Guide (Wardenier et al. 1991) uses the planar connections strength and multiplies it by a correction factor to give the multi-planar connection strength (Kurobane 2002). Liu and Wardenier (1998, 2001) considered KK-joints, while Kurobane and Ogawa (1993) studied how connections behaved in truss failures. This research concluded that under static loads the trusses behaved as predicted, whereas under cyclic loads cracks propagated at the connection and caused local material deterioration, then premature failure due to load redistributions after buckling.

2.4.2 HSS Column-to-Wide Flange (WF) Beam Connections

Considerable research has been performed on HSS column-to-wide flange beam connections. These studies provide a better understanding of possible connection methods and failure modes of HSS-to-HSS moment connections.

Early studies considered five different simple shear connections and made recommendations for their uses. This work noted that an increase in the wall slenderness of the column increased the flexibility of the section and reduced its capacity, but no limit was set as critical (White and Fang 1966). Sherman (1995) considered many experiments on HSS to wide flange connections with a variety of different shear connectors: double angles, shear tabs, through-plates, narrow tees, wide tees, unstiffened seats, single angles, and web end plates. For all these connections except for the web end plate and seated connections, the connection element was welded to the HSS column and the beam was bolted to the connection element. These tests found the controlling failure to be punching shear failure of the column face. To mitigate this, compactness limits were determined. If the HSS column face width-thickness ratio is less than 35.6 for 350 MPa stee,l then distortion may be seen in the column and the use of through plates is required. Other problems may occur if the tab is too long, resulting in out of plane twisting and fracture (Packer and Henderson 1997). Dawe and Mehendale (1995) considered tee (WT) connections (Figure 2.10) and found that the strength of the connection was limited by bolt failure, the column width-to-tee width ratio, and the column thickness-to-tee flange thickness ratio.

For seismic moment connection design, connections need to resist flexure from dynamic earthquake loads. A strong column-weak beam design philosophy is applied to moment frames that require a majority of the inelastic behavior to occur in the beam member. This prevents failure of the column and soft story collapse. For compliance with strong column-weak beam design requirements, the HSS column must be sufficiently stiffened and able to transfer loads such that yielding or local buckling does not occur on the column face and cause an undesirable failure mode.

While the use of HSS box columns in the United States is limited, over 90% of steel buildings in Japan use box columns because of their ability to resist biaxial loads (Kurobane 2002). Since connections must behave in a rigid manner, unstiffened HSS columns currently are not acceptable (Packer and Henderson 1997). In Japan a number of studies responded to this requirement by including internal and external connection diaphragms (Kamba and Tabuchi 1994) or by increasing the wall thickness (Kamba et al. 1994, Tanaka et al. 1996).

Other design possibilities include continuous beams where the column is split and the beam sits on the column endplates. Stiffeners are added and the ends of the columns are bolted to the flanges to transfer moment. Continuity of the beam has also been achieved using through plates that interrupt the column. The flanges of the beam are bolted to the plate and the web of the beam is bolted to a shear tab or double angle depending on loading conditions. Kurobane et al. (2001) proposed a new connection detail where the beam end is welded to a U-shaped joint attached to the plate diaphragm. Shear tabs are also employed. In all cases the top flange was welded while the bottom flange was either bolted or welded. These sections showed better performance and ductility rather than the formation of brittle cracks.

Strap angles attempt to provide continuity by connecting flanges of one end of the beam to the other using angles (Figure 2.11). Early tests showed that as long as the beam and column were the same size, the full moment could be transfered although displacements needed to be monitored (Picard and Giroux 1976). Later tests showed that if the beam is narrower than the column, special attention must be paid to the layout geometry. In addition, a tab might need to be welded between the column face and the beam (Giroux and Picard 1977).

External flange diaphragms fit around the HSS column and sandwich the wide flange beam. Beams are then connected using simple shear connections at the inflection points. The design of this connection has been included in the AIJ specification and recommendations since 1980 (Kurobane 2002). Figure 2.12 is a recently proposed connection detail (Kurobane 2002) that considers the use of a bolted and welded configuration.

Another design philosophy is to reinforce the column face. Dawe and Grondin (1990) and Dawe and Guravich (1993) developed an experimental program with connections that have a reinforcing column plate and flange stiffeners. Four failure modes were found: rupture of the beam tension flange, punching shear failure, web crippling of the side walls, and punching shear at the doubler plate. Others suggested the use of angles wrapping the column. Local wall thickening is possible and is done by heating the specimen and then compressing axially. The use of high strength blind bolts can make these connections easy to install (Packer and Henderson 1997). Mourad et al. (1995) concluded that extended end plate connections with blind bolts were able to be used with caution because of significant stiffness degradations. A design of the connection that is 30% stronger than the beams is recommended to ensure the connection remains elastic.

Ting et al. (1990) created finite element models of connections with different details to stiffen the flange with triangular stiffeners, angle stiffeners, and T stiffeners.

The analysis found that T-stiffeners are the most efficient at transferring load, redistributing stress, and maximizing stiffness. The analysis also found that for effective connections the stiffeners needed to be as wide as the column face. Shanmugam et al. (1991) carried out experimental tests on two of the analyzed connections and compared them to internal continuity plates (Figure 2.13). The test found that T-stiffeners performed better than continuity plates and angles. Ductility ranged from 5.1 to 8.0 percent rotation which was deemed sufficient. Failure modes were found to be buckling of the column web, buckling of the beam flange, and fracture at the stiffener or beam flange. To ensure strong column-weak beam design, the column web may need to be thickened to prevent local buckling.

2.4.3 HSS-to-HSS Frame Connections

The previous section showed that many connections between HSS columns and wide flange beams are feasible and efficient based on extensive research; although, few studies have considered connections between multiple HSS members for moment frame systems. Further, HSS-to-HSS connection research is needed to consider many of the same issues seen in truss and HSS-to-wide flange connection design, including the effect of the *b/t* and *h/t* ratios, the beam width-column width ratio, loading conditions, welding, bolting, and the use of stiffeners.

2.4.3.1 Welded HSS-to-HSS Connections

Early studies of the behavior of HSS-to-HSS connections were performed on Viernedeel truss connections that resist bending in the branch members much like moment frame systems. Research by Jubb and Redwood (1966) showed that sections of equal width could achieve full moment transfer. Korol et al. (1977) considered the behavior of 29 different connections of unequal width. This research program found that such sections cannot transfer the full moment without some reinforcement by considering five different connection types including an unreinforced design (Figure 2.14). For the unreinforced connection the capacity was independent of the weld type. The limiting factors were the column flange slenderness and the beam width-column width ratio. Connection (b) showed improved performance compared to the the unreinforced connection (a). The chord flange stiffener (c), haunch (d), and truncated pyramid (e) connections all showed adequate performance. At high beam to column width ratios the chord flange stiffener performed well. For the haunch connection, it was found that the larger the haunch, the higher the stiffness. The truncated pyramid remained rigid, but lacked application due to the nature of its complicated fabrication and welding.

Finite element analyses were also performed as part of this study (Korol and Mirza 1982). 73 combinations of different beam and chord sizes were analyzed for moment transfer, while 50 combination of different beam and chord sizes were analyzed for puching shear capcity. The results showed that unreinforced joints genereally were too flexible to be considered rigid moment connections. Increasing the width of the brace from 40% to 80% of the chord width increased the moment capacity 60% and the punching shear capacity 160%. If the chord was too thin, punching shear could still occur and the use of a haunch could greatly increase the performance of the connection.

2.4.3.2 Bolted HSS-to-HSS Connections

Few studies have focused on bolted HSS-to-HSS connections. These connections often use details that include tees, angles and plates. Typically a tee is welded to the end of the HSS beam to create a shear tab while the HSS column has either angles or another tee to complete the bolted connection (Packer and Henderson 1997). Another possible connection is a moment end plate connection (Figure 2.15) as proposed by Wheeler et al. (1998). A plate wider than the column is welded to the column flange and an endplate is welded to the beam section. A yield line analysis is used to determine the design criteria. Bolt failure is recommended as the limit state for design efficiency. The finite element model that is used for the connections considers bolt tensioning and heat distortions from the welds. The behavior of the connection is controlled by the stiffness of the endplate connection that is determined by the thickness of the end plate and bolt placement (Wheeler et al. 2000).

Other types of bolted connections include the use of special blind bolts and through bolts. For blind bolts, an endplate can be welded to the beam section and the blind bolts pass through the column flange. The blind bolts are special proprietary bolts that expand and create compression between the two bolting surfaces as it is tightened (Figure 2.16).

Several testing schemes have been considered to impart forces on the bolts including shear, tension, and bending (combined shear and tension). This testing shows that blind bolted connections are sufficient for simple shear connections. While semi-rigid moment connections are possible, the clamping force between the HSS column face and the beam endplate may not be sufficient (Yoemans 1998). Another more recent research program considered the use of blind bolts for moment resisting connections (Tizani and Ridley-Ellis 2003). An improved blind bolt has been introduced and showed improved behavior. In addition, filling the connection region with concrete increases the performance. Although the blind-bolts provided sufficient stiffness for moment connections, their tensile strength is lower than typically needed for a moment type connection. The use of through bolts also is possible in a connection, but research has found that they only provided adequate shear resistance (Linder 1993). Due to limited research, there only have been limited applications of these bolted HSS-to-HSS connections in practice.

2.4.3.3 Cast HSS-to-HSS Connections

Cast connections have been used for many mechanical applications, but their use in structural applications has been growing. Grube and Landskroner (2001) introduced a new connection for tubular structures that provided an efficient rigid connection. The cast connection consisted of male and female components. A bolt was added to control slip. The connectors could sustain load into the strain hardening range where the cast joint showed considerable deformations.

2.4.3.4 HSS-to-HSS Connections under Cyclic Loading

While certain HSS to wide flange connections have been found to be suitable for seismic moment frame systems, minimal research has considered the inelastic cyclic performance of HSS-to-HSS connections for seismic applications. Kumar and Rao (2006) and Rao and Kumar (2006) have proposed a connection detail for earthquake regions. Channel sections sandwich the HSS beam at the top and bottom flanges and are welded to the column. Those members transfer load through tension and compression, but do also experience shear lag as a result of unconnected elements. Web openings are used so the beam section can be bolted to the channel connectors in the field (Figure

2.17). Web stiffeners can be added to the column to improve performance. Overall the sections showed adequate performance with increasing load carrying capacity until the net section began to yield and rupture.

Two analytical tools are used to model the moment-rotation characteristics of the HSS-to-HSS moment connection (Kumar and Rao 2006, Rao and Kumar 2006). A finite element model is first considered. After a phenomenological model that relates rotation to moment, previously developed by Kishi and Chen (1990) is used. The formulation for this relationship is shown in Equation 2.1.

$$M = \frac{R_{ki} \times \theta}{\left(1+\left(\frac{\theta}{\theta_0}\right)^n\right)^{1/n}} \text{ and } \theta_0 = \frac{M_{uc}}{R_{ki}} \qquad \text{Equation 2.1}$$

where M is the moment, θ is the rotation, R_{ki} is the initial stiffness, M_{uc} is the ultimate moment capacity, and n is the shape parameter. This model has been used in a parametric study that studied the connection behavior. The study has found that the initial stiffness is primarily controlled by the depth of the connection and to a lesser extent by the width-thickness ratio of the column web panel zones. The ultimate moment capacity of the connection increases with an increase in depth of the channel connector and is limited to the capacity of the beam net section. Also, rotational ductility increases with an increase in depth of the connection causing the ultimate rotation to occur at a smaller rotation.

More research is needed prior to widespread use of HSS-to-HSS moment connections for seismic applications. Many of the limit states that control the behavior of various connections have been identified, but each connection presents its own nuances. In addition it is important to ensure that connections are efficient, constructible, and feasible.

(a) (b) (c)

Figure 2.1 Different uses of HSS (a) Munich Airport – Munich, Germany (b) Roller Coaster – Munich, Germany (c) Library and Civic Centre of San Jorge – Pamplona, Spain (www.cidect.com)

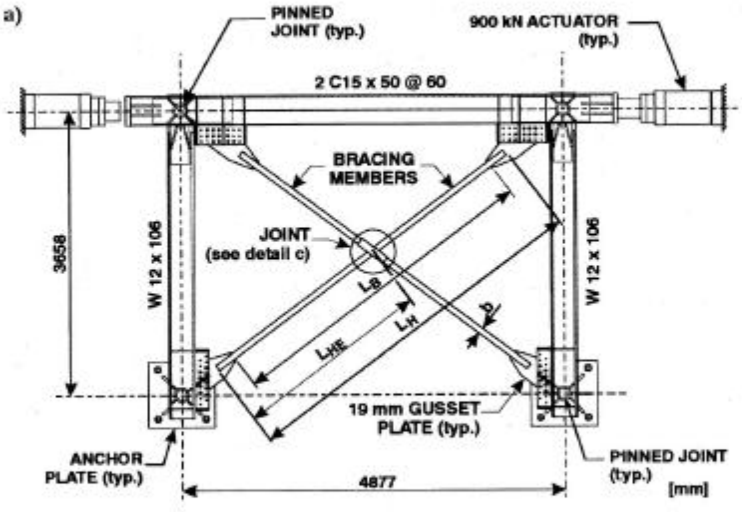

Figure 2.2 HSS X-bracing test setup (Tremblay et al. 2003)

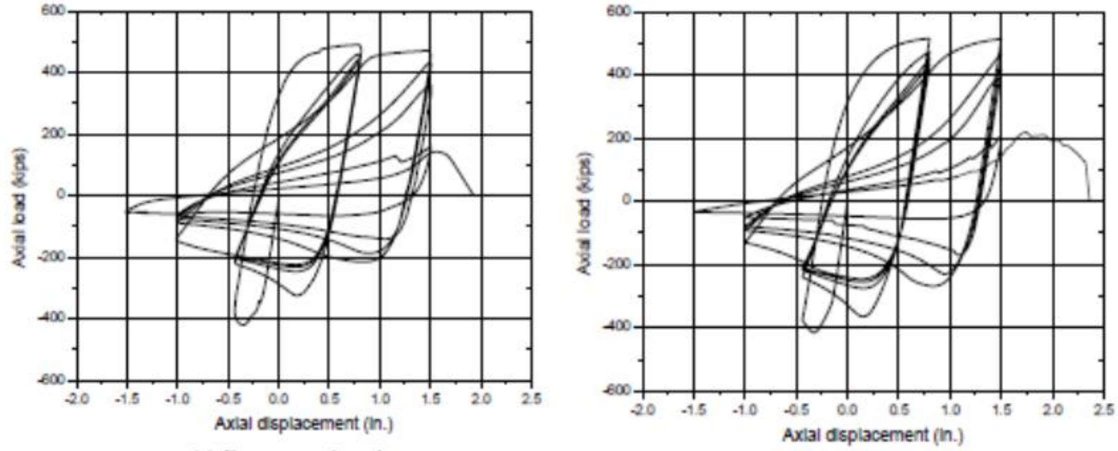

(a) Experimental result

(b) Numerical result

Figure 2.3 Hysteresis for an HSS brace using (a) experimental data and (b) LS-DYNA model (Huang 2009)

Figure 2.4 Biaxial testing of CFT beam-columns (Perea et al. 2010)

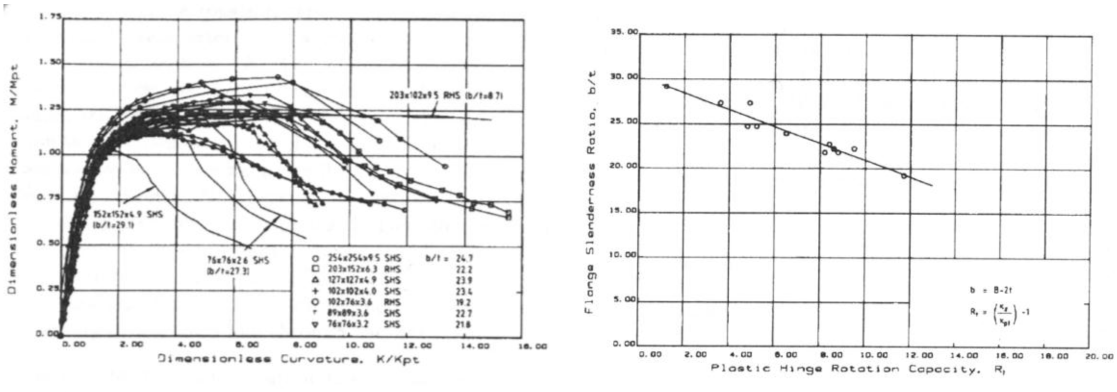

(a) (b)

Figure 2.5 HSS beam moment-curvature and plastic hinge rotation capacity
(a) normalized moment-curvature plots for HSS beam tests and (b) plastic hinge rotation capacity versus flange slenderness results (Hasan and Hancock 1988)

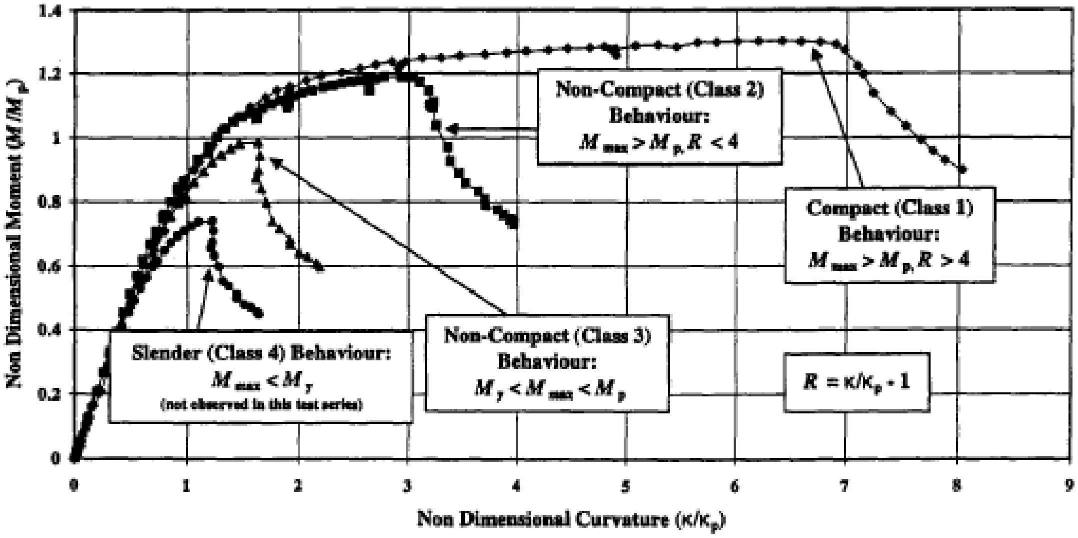

Figure 2.6 Compactness of HSS in flexure (Wilkinson and Hancock 1998)

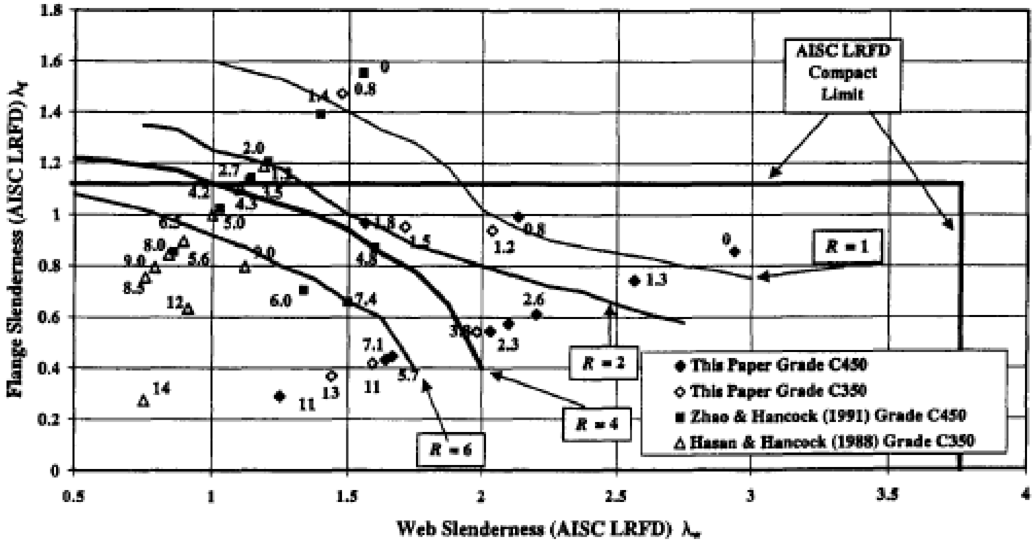

Figure 2.7 Isorotation curves comparing flange and web slenderness for HSS members in bending (Wilkinson and Hancock 1998)

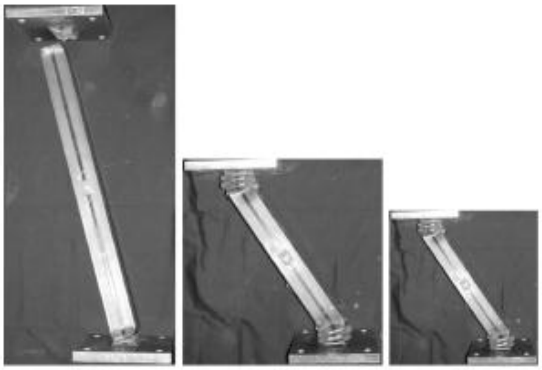

Figure 2.8 Effect of axial load ratio on column failure (a) P/P_y =0, (b) P/P_y =0.3, and (c) P/P_y =0.6 (Nakashima and Liu 2005)

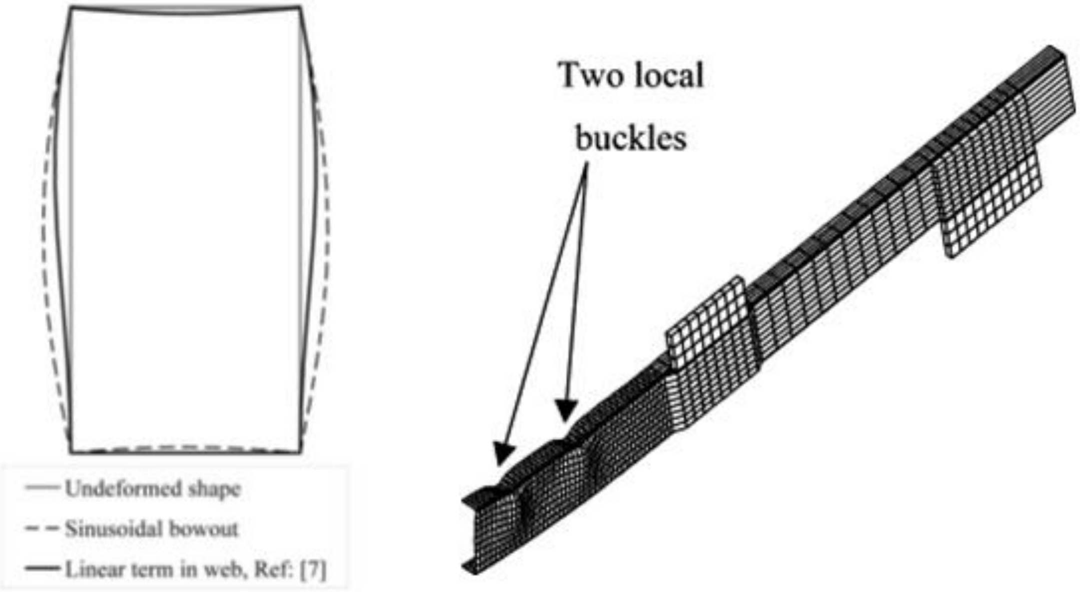

Figure 2.9 HSS FEM including distortions (Wilkinson and Hancock 2002)

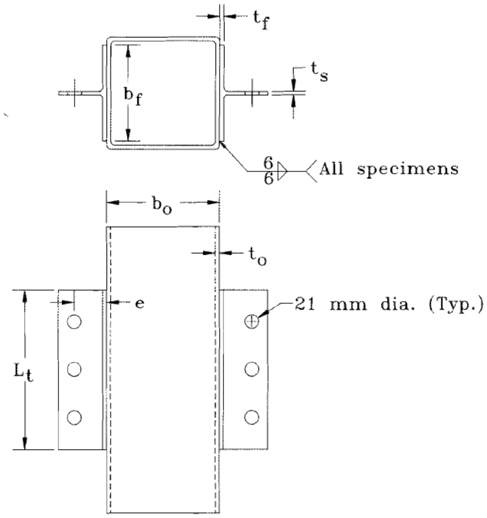

Figure 2.10 Tee HSS-to-wide flange shear connection (Dawe and Mehendale 1995)

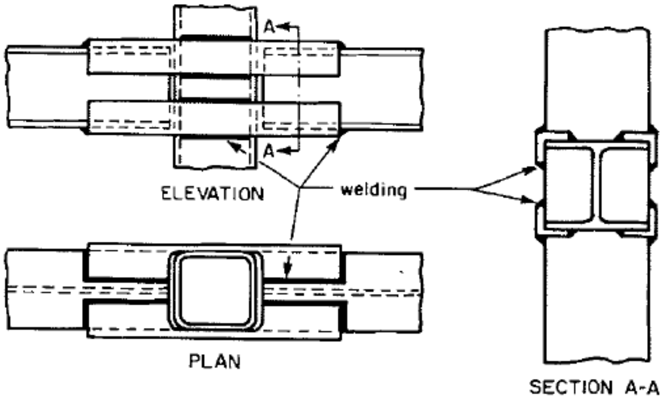

Figure 2.11 Moment connection with strap angles (Picard and Giroux 1976)

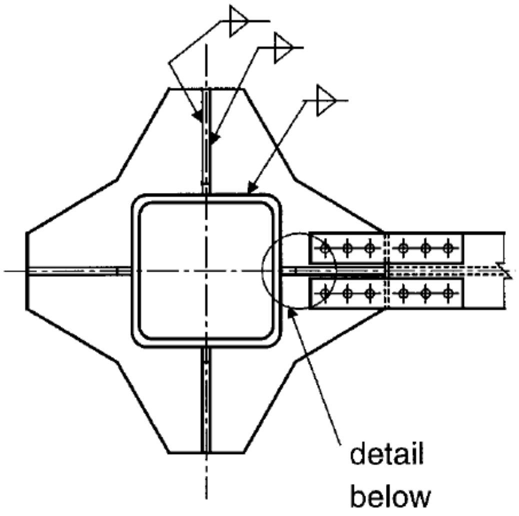

Figure 2.12 Connection detail with external diaphragms (Kurobane 2002)

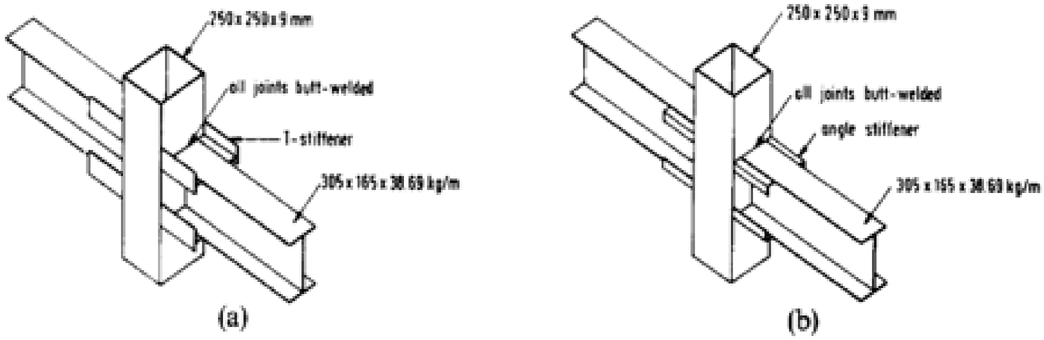

Figure 2.13 Moment connection with (a) external T stiffeners and (b) angle stiffeners (Shanmugam et al. 1991)

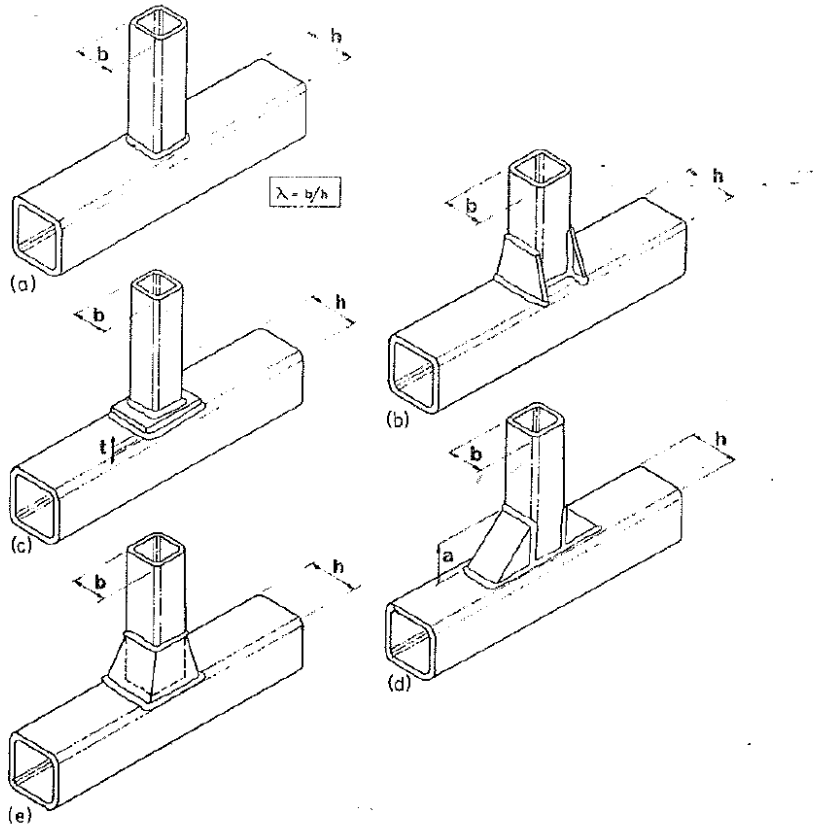

Figure 2.14 Vierendeel truss connections (a) unreinforced, (b) branch flange reinforcing plates, (c) chord flange stiffener, (d) haunch, (e) truncated pyramid (Korol et al. 1977)

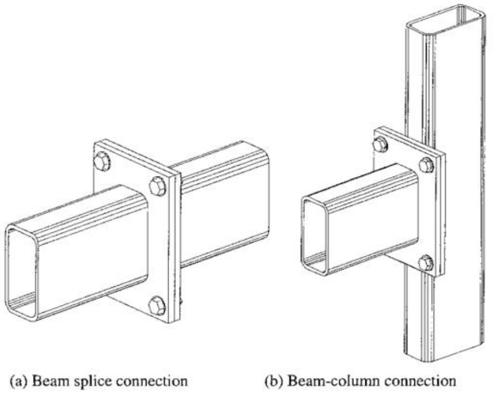

Figure 2.15 HSS moment end plate connection (Wheeler et al. 2000)

Figure 2.16 Blind bolted connection using Lindapter Hollo Bolt (www.lindapter.com)

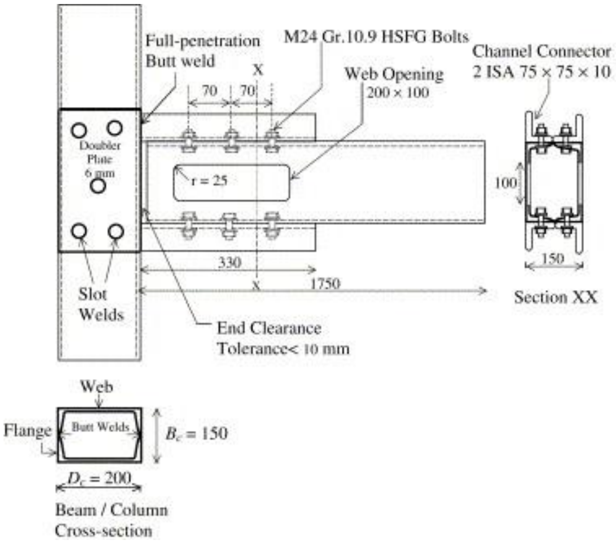

Figure 2.17 HSS-to-HSS bolted moment connection (Kumar and Rao 2006)

CHAPTER 3: HSS MATERIAL PROPERTIES

3.1 Introduction

HSS material properties vary across their cross-section due to how they are fabricated. Typical HSS in the United States are fabricated by rolling steel plates and welding the seam together using electric resistance welding. The rolled tube is then passed through shaping rollers to make the square or rectangular HSS shape. The variability of material properties stems from the buildup of residual stresses as a result of: (1) uneven cooling of the plate stock used to make HSS after hot rolling, (2) cold-forming of the plate stock to its tubular shape and, (3) welding the seam to create the closed HSS member (Weng and Pekoz 1988). The residual stresses are highest at the corners where HSS members experience significant plastic strains that can lead to micro-cracking and fatigue crack initiation (Henila et al. 2008). An understanding of how the residual stresses affect the behavior of HSS members under varying loads and fatigue cycles is important. However, during cyclic loading, relaxation of the residual stresses can be achieved as a result of the complex interaction of the stress amplitude, number of loading cycles, temperature, state of initial residual stress, and mechanical properties of the steel (Lu et al. 1988).

This study focuses on the effect of residual stress and cold working on the material properties of HSS members across the cross-section. Tensile coupon specimens are taken from the perimeter of the HSS members, tested, and analyzed with respect to the size of the corner radius and location along the cross section where the specimen was taken. The findings from these tensile coupon tests allow for a better understanding of the fabrication effects on the corner material and material within the heat affected zone of the weld seam. These data can then be used to more accurately model HSS members and better identify locations that may be susceptible to fracture under large cyclic bending loads.

3.2 Experimental Program

To understand the effects of cold-working on the HSS material properties, tensile coupon specimens are taken from the corners, flats, and seam welds of the eleven different HSS members. The HSS members range in size from HSS 8x4x1/4 to HSS 12x6x1/4 and include sections with thicknesses of 0.25 in. and 0.375 in. The HSS members were manufactured by Atlas Tube and originated from Canada and the United States. All of the members used AISC recommended ASTM A500 Gr. B steel with a nominal yield strength of 46 ksi and a nominal ultimate tensile capacity of 58 ksi (AISC 2011, ASTM 2010). The sections were formed using a process where flat strip steel is formed into a round steel tube. The strip edges are welded at the seam using electric resistance welding (ERW) without any additional filler metal. The round section then passes through a set of sizing and shaping rollers that cold form the HSS to the required square or rectangular shape.

At least ten tensile coupon specimens are obtained from each cross section of the HSS members. ASTM A370 (2012) protocols are followed to carry out the tensile coupon tests. However, limitations due to the HSS geometry, particularly at the corners and welds, does not allow for strict adherence to the standards. A plasma cutter is used to first cut larger specimens from the cross-section at specified locations. These cut out pieces are then machined to meet the sub-sized specimen requirements of ASTM A370 (Figure 3.1). The gage length of each specimen is approximately 2 in. long and the width is 0.25 in. The cross section location of each specimen is shown in Figure 3.2. Coupon specimens are each given a label corresponding to their location. Specimens taken from the flats are designated f1-f8, from the corner are designated c1-c3, and from the weld are designated w. Once machined, the specimens are then tested in an MTS Universal Testing Machine with a 22 kip capacity in accordance with ASTM A370 (2012) utilizing a 1 in. gage length extensometer to measure strains. The test machine is run in displacement control at a loading rate of 0.01 in/min. The extensometer is removed upon the occurrence of necking so as to prevent damage to the device.

3.3 Experimental Results

The load is converted to stress using the average cross-sectional area of 3 sections along the gage length measured using a digital caliper. The stress-strain curves for each specimen are shown in Figure 3.3. Additionally, Table 3.1 provides a summary of important properties obtained for each specimen, including the tensile yield and ultimate strength, tensile yield and ultimate strain, ultimate tensile strength-to-yield strength ratio, ultimate strain-to-yield strain ratio, and Young's modulus. The yield strength (F_y) is calculated using the 0.2% offset yield method because the steel is cold-formed and there is no defined yield plateau. The ultimate tensile strength (F_u) is the maximum stress achieved throughout testing. The yield (e_y) and ultimate tensile (e_u) strain corresponded to the strain when the yield strength and the ultimate strength is reached, respectively.

3.3.1 HSS Strength

Table 3.2 summarizes statistical information for the corners, flats, and welds. Specimens taken from the flats have an average yield strength of 59.4 ksi with a 7.25 ksi standard deviation and an average ultimate tensile strength of 71.1 ksi with a 5.39 ksi standard deviation. The yield strength ranges from 47.5 ksi for the HSS 10x6x1/4 (f8) to 79.8 ksi for the HSS 8x4x3/8 (f7). The ultimate tensile strength ranges from 63.4 ksi for the HSS 8x4x1/4 (f2) to 87.7 ksi for the HSS 8x4x3/8 (f7). The corners have higher average yield and ultimate tensile strengths of 73.8 ksi with a 5.96 ksi standard deviation and 82.4 ksi with a 6.55 ksi standard deviation, respectively. The yield strength ranges from 65.5 ksi for the HSS 8x4x1/4 (c1) to 83.0 ksi for the HSS 8x6x3/8 (c1). The ultimate tensile strength ranges from 72.3 ksi for the HSS 8x8x3/8 (c2) to 92.6 ksi for the HSS 8x6x3/8 (c1). The increased yield and ultimate tensile strength values in the corners are due to the large plastic deformation at these locations during HSS fabrication. The welds have the highest average yield strength of 81.6 ksi with a 7.10 ksi standard deviation and an average ultimate strength of 89.5 ksi with a 4.24 ksi standard deviation. The yield strength ranges from 72.7 ksi for the HSS 10x6x1/4 to 93.0 ksi for the HSS 8x4x3/8. The ultimate tensile strength ranges from 84.4 ksi for the HSS 8x4x1/4 to 95.9 ksi for the HSS 8x6x3/8. These high yield and ultimate tensile strength values are due to the effects of heat input during the electric resistance welding (ERW) process resulting in a heat affected zone.

To ensure sufficient strength after yielding for plastic design, Eurocode 3 (EC3 2003) requires the strength ratio (F_u/F_y) be greater than 1.20. This is important in seismic design to ensure sufficient spread of plasticity. For the eleven sections considered, only specimens from the flats meet this strength ratio requirement. However, only 50% of coupon specimens taken from the flats meet this requirement with the strength ratio ranging between 1.04 and 1.35 and an average strength ratio of 1.20. Due to the effects of cold working the strength ratio in the corners is much lower ranging between 1.08 and 1.15 with an average of 1.12. Similarly, the effects of the electric resistance welding process reduce the strength ratio to an average of 1.10 with a range between 1.00 and 1.18. The cold working caused an increase in yield strength with only a small increase in ultimate strength leading to low strength ratios.

3.3.2 HSS Ductility

The yield strain (e_y) is consistent between all specimens and all locations and ranges between 0.0039 to 0.0061 measured using the 0.2% offset method. The average yield strain for the corner specimen is 0.0046 with a standard deviation of 0.0002. For the weld specimen, the average is 0.0049 with a standard deviation of 0.0005. For the flat specimens the average yield strain is 0.0042 with a standard deviation of 0.0003. The consistency of the yield strain is partially due to the constant elastic modulus (E) for steel.

ASTM A500/A500M-10a (2010) also notes the importance of ductility for HSS material. For ASTM A500 Gr. B steel, the percent elongation in 2 in. should be greater than or equal to 23% at fracture. Since this study used a 1 in. gage length extensometer, a conversion is made to convert the elongation in terms of 1 in. For a 1 in. gage length, the elongation in 2 in. should be 11.5% (0.115); however, for this study the extensometer was removed from the specimen after the ultimate tensile strength is reached but before fracture occurs. For the flats, many tensile specimens meet the ASTM requirements for elongation at fracture even at the ultimate capacity. The average strain corresponding to the ultimate tensile strength is 0.129 with a 0.039 standard deviation. Twenty-one out of 80 specimens taken from the flats have elongation values below 11.5% at the ultimate tensile strength. Many of these specimens come from the HSS 8x4x3/8, HSS 8x6x1/4, HSS 8x6x3/8, HSS 8x8x1/4, and HSS 10x4x1/4. Of all the specimens taken from the flats, the HSS 10x6x1/4 (f8) has the highest strain at the ultimate strength of 0.185, while the HSS 8x4x3/8 (f4) has the lowest strain at the ultimate strength of 0.034. On average both the corners and welds have much lower strains at their ultimate tensile strength due to the effects of cold working and heating. These values are 0.023 with a 0.007 standard deviation and 0.044 with a 0.013 standard deviation, respectively.

Another measurement of material ductility is the ductility ratio, e_u/e_y. Eurocode 3 (EC3 2003) requires a ductility ratio of 20. Most specimens from the flats meet this requirement with and average e_u/e_y of 31.1 and standard deviation of 9.94. The ductility ratio for the flats ranges from 7.56 to 47.0. Eleven specimens have e_u/e_y less than 20, with many of these coupons coming from the HSS 8x4x3/8, HSS 8x6x3/8, and HSS 10x4x1/4. Again, specimens from the corners and welds show much lower ductility with e_u/e_y for the corners ranging from 3.69 to 7.46 and for the welds ranging from 1.30 to 12.2. On average the ductility ratio for the corners is 5.23 with a standard deviation of 1.06, while the average ductility ratio for the welds is 9.22 with a standard deviation of 3.14. Overall these members, with exception of the HSS 8x4x3/8, should show adequate ductility due to the fact that a large percentage of each HSS cross-section consists of the flat region.

3.4 Discussion

The material properties measured from coupon specimens taken from different locations along the cross section show varying values when taken from the flats, corner, and weld seam. The effects from the ERW process and cold forming of the HSS members are well known. However, the extent that these fabrication processes affect the material properties is not well understood for large HSS members. The following discussion quantifies the effect of the HSS fabrication process on the material properties.

3.4.1 Distance from Weld

The weld seam where the two edges of the plate are joined to form the HSS member is found in the flat region along the flange or web of the member. The effect of heat from welding has been shown to increase both the yield and ultimate strength of steel in the area adjacent to the weld. The size of the heat affected zone needs to be well understood to ensure that a single material property for the flat region containing the weld is a reasonable assumption in modeling the cyclic bending behavior of HSS members.

Figure 3.4 (a) and (b) compare the yield and ultimate tensile strength from tensile coupons to the distance from the weld in ten of the HSS members. Both the yield and ultimate tensile strength of the weld material are on average higher than the yield and ultimate tensile strength of the material taken from locations further from the weld on the same side of the specimen. At a distance of 1 in. from the weld, the yield and ultimate tensile strength has decreased considerably for most specimens. The yield strength has decreased by 17.4% from that measured with the weld material for the HSS 8x6x1/4 specimen at 1.13 in. from the weld while a larger decrease of 35.1% is observed for the HSS 8x8x3/8 specimen at 0.94 in. from the weld. The ultimate tensile strength decreases by 10.0% from that measured with the weld material for the HSS 8x8x1/4 at 1.0 in. from the weld and as much as 26.1% at 0.94 in. from the weld for the HSS 8x8x3/8. Material further than 1 in. from the weld shows little change in the yield and ultimate tensile strength compared to the specimens taken only 1 in. from the weld seam. The percent decrease in yield strength at 2 in. or more ranges from 21.9% for the HSS 10x8x1/4 at 3.31 in. from the weld to 34.4% for the HSS 8x8x3/8 at 2.19 in. from the weld. Similarly, the ultimate tensile strength decreases 11.2% for the HSS 8x8x1/4 at 3.0 in. from the weld to 24.9% for the HSS 8x8x3/8 at 2.19 in from the weld. Based on this analysis the heat affected zone of the HSS members is small and it is appropriate to use the material properties for the HSS flats in modeling.

Considering the effect of the seam weld on ductility, Figure 3.4 (c) compares the change in ductility ratio as the distance from the weld increases. The ductility ratio for material in the heat affected zone has been shown to be very low due to heat input during the ERW process. For nearly all specimens, moving away from the weld significantly increases the ductility ratio. Only the HSS 8x4x3/8 shows little or no change in the ductility ratio as the distance from the weld increases. However, this specimen also produced the highest yield strengths over the whole cross-section suggesting a possible abnormality in the manufacturing process. For the weld material the ductility ratio is between 1.3 for the HSS 8x8x1/4 and 12.2 for the HSS 10x8x1/4. Meanwhile, material approximately 1 in. from the weld seam showed a considerable increase in the ductility ratio from 7.6 for the HSS 8x4x3/8 specimen at 1.13 in. to 45.9 at 1.13 in. for the HSS 8x4x1/4. Like the yield and ultimate tensile strength, the ductility ratio stabilizes for material further away from the weld seam. The range of ductility ratios for material further than 1in from the weld is very similar to specimens at 1 in. from the weld ranging from 10.5 at 2.38 in. for the HSS 8x4x3/8 to 40.6 at 4.94 in. for the HSS 12x6x1/4.

Based on this study, it is clear that the heat affected zone is confined to within 1 in. of the weld seam and the influence of the weld region on the material properties is confined to that area. Therefore, the weld will have only a small effect in terms of the overall behavior, but due to the lower ductility in the weld region care should be taken to ensure premature fracture does not occur as a result of the presence of the weld. It may be best to orient the members such that the weld seam experiences the least amount of local strain.

3.4.2 Distance from Corner

Cold working during the fabrication of HSS members increases the yield and ultimate strength and reduces the ductility of the section. The corners undergo the largest amount cold working and the extent of the effect of this is quantified to ensure that the change in material properties does not have a detrimental impact on the overall behavior and to allow the different material properties to be more accurately captured in numerical studies.

On average the yield and ultimate tensile strength of materials taken from the corners is 73.8 ksi and 82.4 ksi, respectively, while the yield and ultimate tensile strength for material obtained from the flats is 59.4 ksi and 71.1 ksi, respectively. The distance from the corner over which the cold working has an influence will be determined by considering material obtained from the HSS 12x6x1/4 member. For this study the distance from the corners is normalized to a percentage of the width or height of the member depending on where the material is obtained. The yield strength for this member ranges from 71.4 ksi to 72.3 ksi for specimens taken from the corners. Moving to a normalized distance of 0.24, the yield strength decreases to 58.0 ksi for specimen f5 (Figure 3.5 (a)). Specimens further from the corners have a similar yield strength to that measured a normalized distance of 0.24 from the corner. At a normalized distance of 0.5, in the middle of the HSS member, the yield strength ranges between 53.9 ksi and 61.0 ksi. Similarly, when considering the ultimate strength values of the HSS 12x6x1/4 material, F_u obtained for the corners specimens ranges between 80.8 ksi and 82.8 ksi. Figure 3.5 (b) shows that the ultimate strength for material away from the corner is much lower with values between 68.4 ksi and 71.5 ksi at all normalized distances between 0.24 and 0.5 from the corners. A similar trend is seen for the ductility ratio with respect to the normalized distance from the corners of the HSS 12x6x1/4 member (Figure 3.5 (c)). The ductility ratio for the corner material is low with values of 5.40 and 5.47, while at a normalized distance greater than 0.24, the ductility ratio is much higher with an average value of 33.6.

Overall, the effect of the cold working in the corners of the tested specimens is concentrated to the corners and does not affect more than 25% of the normalized length from each corner. This shows that the section properties should in large part be determined by the material taken from the flats of the specimens. However, like the weld region, the lack of ductility in the corners of the specimen is a concern for the initiation of micro-cracking and tearing.

3.4.3 Corner Radius

The amount of cold working in the corners is variable due to the HSS fabrication process and the thickness of the walls. With a decrease in the thickness of the HSS members, the radius of the corner decreases leading to higher amounts of cold working. This process can have an important consequence on the ductility of an HSS member and the extent of material property changes in the corners due to cold working. Based on previous experimental tests, HSS beam and column members tend to have the lowest fatigue resistance in the corners where tearing often initiates. This tearing can lead to premature degradation of the capacity of HSS members in cyclic bending applications.

The effect of the corner radius on the yield and ultimate capacity is plotted in Figure 3.6 (a) and (b). There is little correlation between the corner radius and the yield and ultimate strength of the specimens. The average yield strengths for the 0.25 in. and 0.375 in. thick sections are 73.1 ksi and 75.6 ksi, respectively, while the average ultimate strengths are 81.7 ksi and 84.2 ksi, respectively. The results suggest that the thickness of the specimen has only a minor effect on the yield and ultimate strength of the material in the corner of the specimen.

When considering ductility ratio (e_u/e_y) of the corners, a minor trend is recognizable. As the corner radius increases, the ductility ratio also increases (Figure 3.6 (c)). The smaller the corner radius results in higher amounts of cold working, lowering the ductility ratio. At a radius of 0.486 in. for the 0.25 in. thick members, the ductility ratio is on average 4.77, while at a radius of 0.698 in. for the 0.375 in. thick members the ductility ratio is on average 5.80. Thus, as the HSS member thickness and corner radius become smaller the reduction in ductility of the material becomes a concern especially for fatigue and seismic loads.

3.4.4 Comparison to Specified Properties

All of the experimentally tested sections use ASTM A500 Gr. B (2010) steel with a minimum yield strength of 46 ksi and tensile strength of 58 ksi. Based on the experimental data, it is reasonable to utilize the material properties taken from the flats to calculate section properties. From Table 3.2, the average yield strength for the flats is 59.4 ksi with a standard deviation of 7.25 ksi, while the average tensile strength for the flats is 71.1 ksi with a standard deviation of 5.39 ksi. The average yield strength is 13.4 ksi higher than the specified minimum and the average tensile strength is 13.1 ksi higher than the specified minimum.

In seismic design of structures it is important to have an accurate knowledge of the material properties to ensure desirable and ductile failure modes as a result of capacity design procedures. The AISC Seismic Provisions (2010b) Table A3.1 specifies R_y and R_t values. R_y and R_t are the ratios of the expected yield and ultimate tensile strengths to the specified minimum yield and ultimate tensile strengths, 1.4 and 1.3, respectively. Analysis of the data from this study suggests slightly lower R_y and R_t values. Utilizing the average yield strength, R_y is 1.29, while utilizing the average ultimate tensile strength, R_t is 1.23.

3.5 Conclusions

An extensive study of the material properties of 11 different HSS members is carried out utilizing 114 coupon specimens. Stress and strain are measured for each specimen under monotonic tensile loads to failure to characterize the behavior in terms of a number of properties including yield/ultimate strength and yield/ultimate strain. Additionally, the effects of cold working and electrical resistance welding are considered.

1. In terms of cross section location, it is found that the effects of the heat affected zone near the weld seam and cold working in the corners is localized. The effects do not spread into a significant portion of the flats of the HSS. However, care should be taken to monitor the welds and corners as failure of sections under various loads will likely initiate in these regions due to the less ductile nature of the material.
2. The amount of cold working does not affect the material strength as much as it affects the ductility of the corner material. The reduction in ductility in the corners only had a minor correlation to the material thickness and radius. Finally, the yield and ultimate strengths obtained from this testing suggest slightly lower R_y and R_t ratios than specified in the seismic provisions (2010b).

Table 3.1 HSS material properties

Specimen		F_y (ksi)	e_y (10^-3)	F_u (ksi)	e_u (10^-3)	e_u/e_y	F_u/F_y	E (ksi)	Notes
8x4x1/4	c1	65.5	4.31	72.5	19.2	4.45	1.11	28300	clip gage measurement started late
	c2	65.5	4.38	73.1	16.2	3.69	1.12	27700	
	w	71.5	4.6	84.4	49.8	10.8	1.1	29400	
	f1	53.8	4.17	63.7	166	39.9	1.18	24900	
	f2	53.1	4.15	63.4	177	42.6	1.19	24700	
	f3	54.3	4.08	64.5	178	43.6	1.19	26100	
	f4	53.3	3.94	63.5	181	45.9	1.19	27300	
	f5	45.9	4.95	75	170	34.4	1.63	15600	crushed before test was run
	f6	55.1	3.99	65	170	42.6	1.18	27800	
	f7	55.7	3.96	64.3	150	37.9	1.15	28100	
	c_{avg}	65.5	4.35	72.8	17.7	4.07	1.11	28000	
	f_{avg}	54.2	4.05	64	170	42.1	1.18	26500	f5 not included in average
8x4x3/8	c1	78.2	4.6	86.7	27.5	5.98	1.11	30200	clip gage missed fracture area
	c2	82.6	4.69	91.3	35	7.46	1.11	30600	
	w	93	5.13	95.9	42.4	8.26	1.03	29700	
	f1	71.3	4.27	78.3	56.6	13.3	1.1	31300	
	f2	72.6	4.38	79	53.9	12.3	1.09	30200	
	f3	72.1	4.43	81.1	68	15.3	1.12	29600	
	f4	76.2	4.55	79.4	34.4	7.56	1.04	29900	
	f5	72.1	4.36	78.2	45.9	10.5	1.09	30400	
	f6	78.6	4.6	87.7	46.7	10.2	1.12	30500	
	f7	79.8	4.67	87.4	43.5	9.32	1.1	29900	clip gage missed fracture area
	c_{avg}	80.4	4.64	89	31.2	6.72	1.11	30400	
	f_{avg}	73.8	4.43	80.6	50.9	11.5	1.09	30300	

Table 3.1 (cont.) HSS material properties

Specimen		F_y (ksi)	e_y (10^-3)	F_u (ksi)	e_u (10^-3)	e_u/e_y	F_u/F_y	E (ksi)	Notes
8x6x1/4	c1	69.8	4.6	75.5	29.6	6.4	1.08	26800	
	c2	73.7	4.57	81	19.4	4.24	1.1	28700	
	w	76.2	4.64	86.9	52.7	11.4	1.14	28600	
	f1	53.7	4.06	67.7	154	38	1.26	26000	
	f2	53	3.94	67.8	168	42.7	1.28	27500	
	f3	51	4.08	66.9	156	38.2	1.3	24800	
	f4	62.9	4.15	72.3	83.5	20.1	1.15	29200	
	f5	58.9	3.96	70.3	98.4	24.8	1.19	29900	
	f6	52.1	3.96	67.3	153	38.6	1.29	26400	clip gage missed fracture area
	f7	54	4.03	68.5	143	35.5	1.27	26600	
	f8	53	4.22	68.3	159	37.8	1.29	24100	
	c_{avg}	71.8	4.58	78.3	15.7	3.42	1.09	27700	
	f_{avg}	54.9	4.05	68.6	139	34.5	1.25	26800	
8x6x3/8	c1	83	4.71	92.6	30.6	6.5	1.12	31500	
	c2	74.5	4.71	85.9	24.5	5.2	1.15	27800	
	c3	76.3	5.06	84.5	21.2	4.19	1.11	28900	
	w	88.9	5.09	95.9	42	8.24	1.08	28900	
	f1	70.4	4.43	76.9	66.3	15	1.09	31400	
	f2	61.5	4.36	75	120	27.6	1.13	28900	
	f3	66.5	4.41	74.9	112	25.4	1.13	27000	
	f4	53.9	4.34	71.9	136	31.4	1.21	25900	
	f5	60.6	4.2	72.4	141	33.5	1.19	28100	
	f6	62.3	4.27	72.7	138	32.4	1.17	27600	
	c_{avg}	77.9	4.83	87.7	25.4	5.29	1.13	29400	
	f_{avg}	64.3	4.33	73.9	119	27.5	1.15	28200	

Table 3.1 (cont.) HSS material properties

Specimen		F_y (ksi)	e_y (10^-3)	F_u (ksi)	e_u (10^-3)	e_u/e_y	F_u/F_y	E (ksi)	Notes
8x8x1/4	c1	80.6	4.92	89.5	18.8	3.81	1.11	26800	
	c2	82.4	4.95	90.6	13.8	3.94	1.1	28000	
	c3	81.2	5.32	88.8	21.7	4.08	1.09	25600	
	w	87.9	6.07	88	7.92	1.3	1	21400	
	f1	69.1	5.16	79.1	117	22.7	1.14	30800	
	f2	66.6	4.53	79.2	141	31.1	1.19	27300	
	f3	63.1	4.43	78.2	138	31.2	1.24	26700	
	f4	63	4.48	75.5	141	31.5	1.2	26400	
	f5	61.4	4.24	76.7	139	32.7	1.25	26800	
	f6	72.3	4.67	76.2	110	23.6	1.05	25200	
	c_{avg}	81.4	5.06	89.6	20	3.94	1.1	26800	
	f_{avg}	65.9	4.58	77.5	131	28.8	1.18	27200	
8x8x3/8	c1	68.5	4.38	76.3	20.6	4.69	1.11	28800	
	c2	66.4	4.31	72.3	28.4	6.57	1.09	28700	
	w	87.1	4.92	90.6	32.5	6.59	1.04	29700	clip gage missed fracture area
	f1	57.7	4.1	67.9	132	32	1.18	27500	
	f2	57.9	4.13	67.9	127	30.7	1.17	27200	
	f3	57.6	4.03	67.2	142	35.3	1.17	28300	
	f4	56.5	4.1	67	156	38	1.18	26700	
	f5	57.2	4.08	68	148	36.3	1.19	27300	
	f6	56.4	4.1	61.4	157	38.3	1.18	26900	
	f7	57.3	4.08	67.3	140	34.4	1.17	27600	
	f8	55.6	4.01	66.7	147	36.6	1.2	27600	
	c_{avg}	67.4	4.35	74.3	24.5	5.63	1.1	28700	
	f_{avg}	57	4.08	67.3	144	35.2	1.18	27400	

Table 3.1 (cont.) HSS material properties

Specimen		F_y (ksi)	e_y (10^-3)	F_u (ksi)	e_u (10^-3)	e_u/e_y	F_u/F_y	E (ksi)	Notes
10x4x1/4	c1	68.3	4.57	76.7	21.8	4.76	1.12	26600	
	c2	78.4	4.6	88.1	27.2	5.92	1.12	30200	
	w	86.8	4.88	94.8	48.4	9.92	1.09	30100	
	f1	62.3	4.06	73.8	84.9	20.9	1.19	30400	
	f2	64	4.1	73.8	93.1	22.7	1.15	30500	
	f3	63.8	4.15	74.2	95.4	23	1.16	29900	
	f4	71.5	4.43	79.8	64.8	14.6	1.12	29500	
	f5	66.9	4.24	77.3	87	20.5	1.16	30000	
	f6	61.5	4.38	76.9	61.3	14	1.16	27800	
	f7	67.9	4.92	77.3	61	12.4	1.14	23200	
	c_{avg}	73.3	4.58	82.4	24.5	5.34	1.12	28400	
	f_{avg}	65.8	4.23	76	81.1	19.3	1.15	29700	
10x6x1/4	c1	68.3	4.34	77.6	20.5	4.73	1.14	29300	
	c2	65.5	4.5	73.8	28.4	6.31	1.13	26200	
	w	72.7	4.36	85.9	53	12.2	1.18	30900	
	f1	49.7	3.87	63.9	179	46.2	1.29	26500	
	f2	51	4.5	65.6	178	33.8	1.29	20400	
	f3	49.9	4.06	64.9	178	43.8	1.3	24200	
	f4	54.9	3.85	67.9	124	32.3	1.24	29800	
	f5	54.5	3.87	66.3	120	31.1	1.22	29100	
	f6	49.2	3.85	65.3	165	42.8	1.33	26500	
	f7	49.2	4.06	65	177	43.7	1.32	24000	
	f8	47.5	3.94	64.3	185	47	1.35	24600	
	c_{avg}	66.9	4.42	75.7	24.5	5.52	1.13	27700	
	f_{avg}	50.7	4	65.4	163	40.8	1.29	25600	

Table 3.1 (cont.) HSS material properties

Specimen		F_y (ksi)	e_y (10^-3)	F_u (ksi)	e_u (10^-3)	e_u/e_y	F_u/F_y	E (ksi)	Notes
10x8x1/4	c1	77.5	4.62	81.5	22.5	4.88	1.12	29700	clip gage missed fracture area
	c2	76.7	4.62	86.3	21.6	4.67	1.13	29400	
	w	74.9	4.43	88.6	53.7	12.1	1.18	30700	
	f1	58.4	4.29	71.3	95	22.1	1.22	25600	
	f2	58.5	3.94	70.5	141	35.7	1.21	30200	
	f3	58.4	4.03	71.4	109	27	1.22	28800	
	f4	56.5	3.89	71.2	130	33.3	1.26	29900	
	f5	58.5	4.43	73.6	105	23.7	1.26	24100	
	f6	57.3	3.92	72.1	129	33	1.26	30000	
	f7	55.8	4.08	71.3	133	32.6	1.28	27000	
	f8	53.1	3.89	71.2	154	39.7	1.34	28400	
	c_{avg}	77.1	4.62	81.4	22	4.77	1.12	29500	
	f_{avg}	57.1	4.06	71.6	125	30.9	1.25	28000	
12x4x1/4	c1	77	4.64	87	31.4	6.76	1.13	29100	
	c2	68.4	4.55	77.8	24.5	5.38	1.14	26800	
	w	75.8	4.55	87	48.7	10.7	1.15	29700	
	f1	55.9	4.64	67.3	173	37.3	1.2	26200	
	f2	55.5	4.24	67	162	38.1	1.21	24800	
	f3	56.6	4.2	68.4	145	34.5	1.21	25700	
	f4	57.6	4.06	69.4	143	35.3	1.2	28100	
	f5	54.3	4.06	67.2	165	40.6	1.24	26400	
	f6	53.5	4.27	69.3	160	37.4	1.29	23500	
	f7	52.3	4.17	68	163	39	1.3	24100	
	c_{avg}	72.7	4.6	82.4	27.9	6.07	1.13	27900	
	f_{avg}	55.6	4.24	68.1	158	37.2	1.23	25800	

Table 3.1 (cont.) HSS material properties

Specimen		F_y (ksi)	e_y (10^-3)	F_u (ksi)	e_u (10^-3)	e_u/e_y	F_u/F_y	E (ksi)	Notes
12x6x1/4	c1	72.3	4.48	82.8	24.2	5.4	1.15	28900	
	c2	71.4	4.46	80.8	24.4	5.47	1.13	29100	
	w	78.4	4.74	85.9	46.9	9.91	1.1	28800	
	f1	61	4.01	71.5	102	25.5	1.17	30200	
	f2	61.5	4.15	70.9	141	34.1	1.15	28600	
	f3	59	3.99	70.6	124	31.2	1.2	29800	
	f4	56.7	3.89	70.2	141	36.2	1.24	29800	
	f5	58	3.94	69.8	140	35.7	1.2	29600	
	f6	54.3	3.87	69.4	130	33.7	1.28	29300	
	f7	54.6	4.2	68.4	147	35.1	1.25	24800	
	f8	53.9	4.08	68.9	152	37.2	1.28	25900	
	c_{avg}	71.8	4.47	81.8	24.3	5.43	1.14	29000	
	f_{avg}	57.4	4.02	70	135	33.6	1.22	28500	

Table 3.2 Material properties statistics

Location		F_y (ksi)	e_y (10^-3)	F_u (ksi)	e_u (10^-3)	e_u/e_y	F_u/F_y	E (ksi)
Corners (c1-c3)	mean	73.8	4.62	82.4	23.4	5.23	1.12	28500
	median	74.1	4.6	83.6	23.4	5.04	1.12	28700
	std. dev.	5.96	0.24	6.55	6.51	1.06	0.02	1480
	max.	83	5.32	92.6	35	7.46	1.15	31500
	min.	65.5	4.31	72.3	1.83	3.69	1.08	25600
Flats (f1-f8)	mean	59.4	4.19	71.1	129	31.1	1.2	27500
	median	57.6	4.1	70.2	140	33.5	1.2	27500
	std. dev.	7.25	0.25	5.39	38.6	9.94	0.07	2280
	max.	79.8	5.16	87.7	185	47	1.35	31400
	min.	47.5	3.85	63.4	34.4	7.56	1.04	20400
Welds (w)	mean	81.6	4.86	89.5	43.5	9.22	1.1	28900
	median	78.4	4.74	88	48.4	9.92	1.1	29700
	std. dev.	7.1	0.48	4.24	13.3	3.14	0.06	2600
	max.	93	6.07	95.9	53.7	12.2	1.18	30900
	min.	72.7	4.36	84.4	7.92	1.3	1	21400

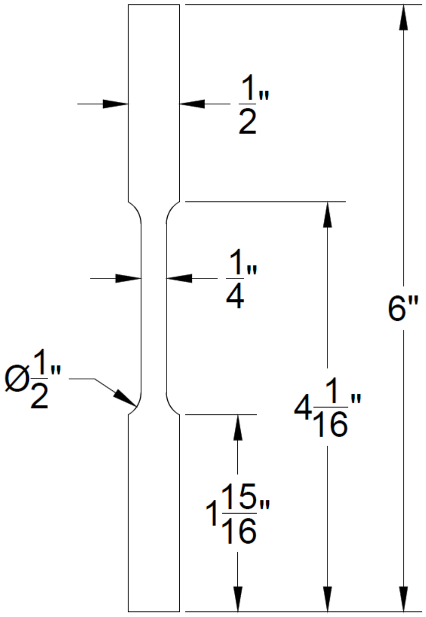

Figure 3.1 Typical HSS sub-size coupon specimen

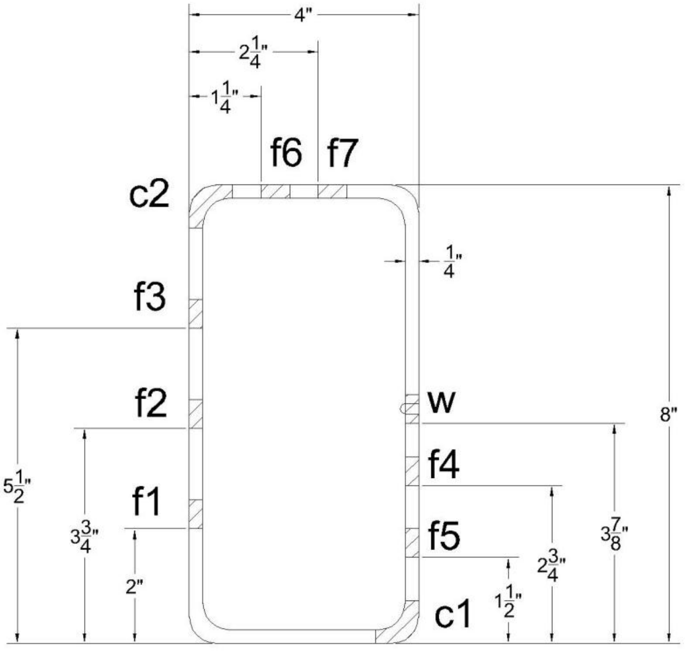

(a)

Figure 3.2 Tensile specimen locations for (a) HSS 8x4x1/4

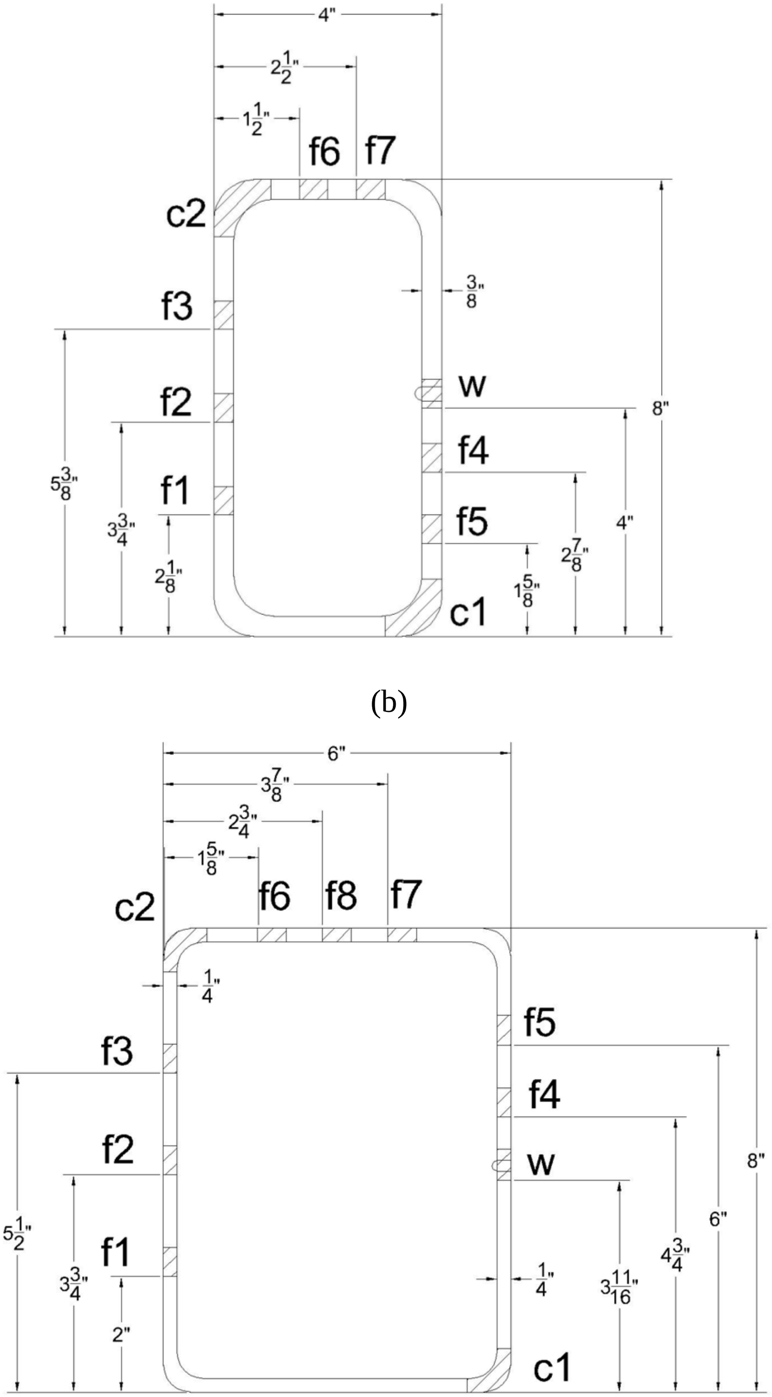

(b)

(c)

Figure 3.2 (cont.) Tensile specimen locations for (b) HSS 8x4x3/8 and (c) HSS 8x6x1/4

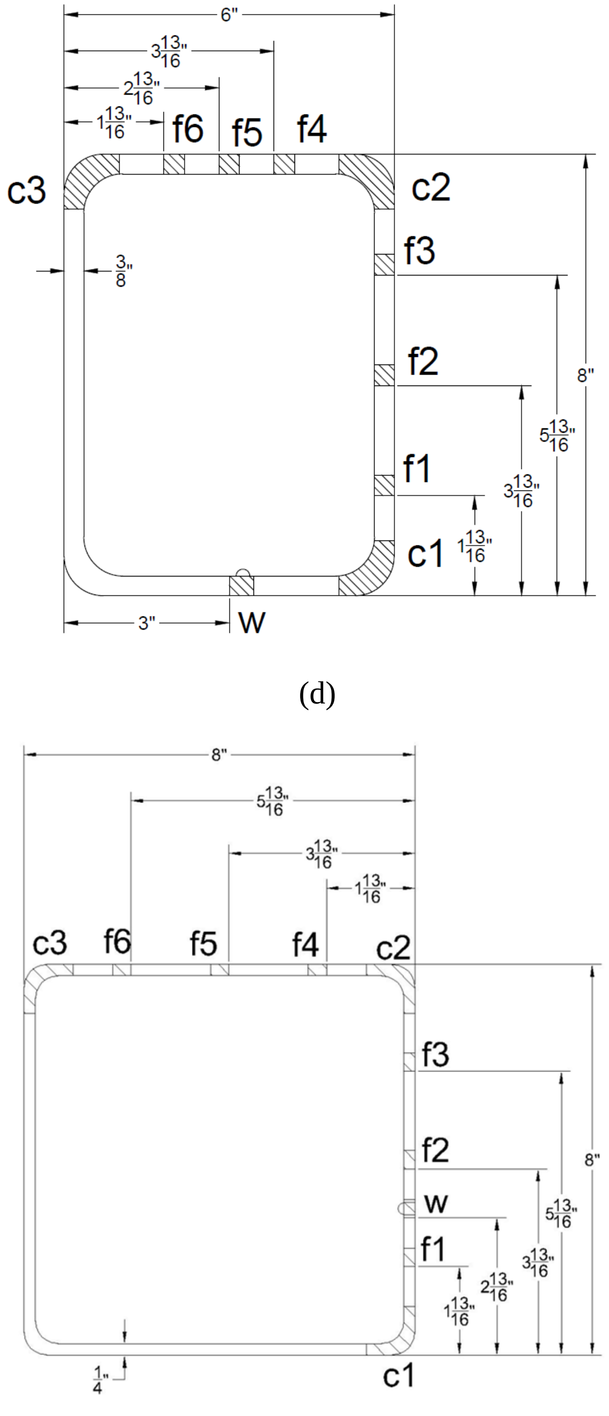

(d)

(e)

Figure 3.2 (cont.) Tensile specimen locations for (d) HSS 8x6x3/8 and (e) HSS 8x8x1/4

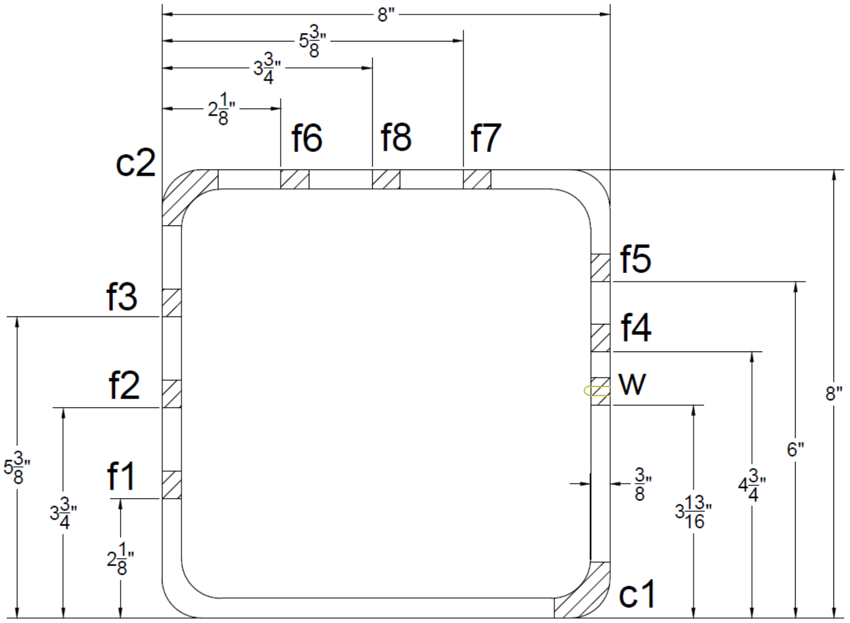

(f)

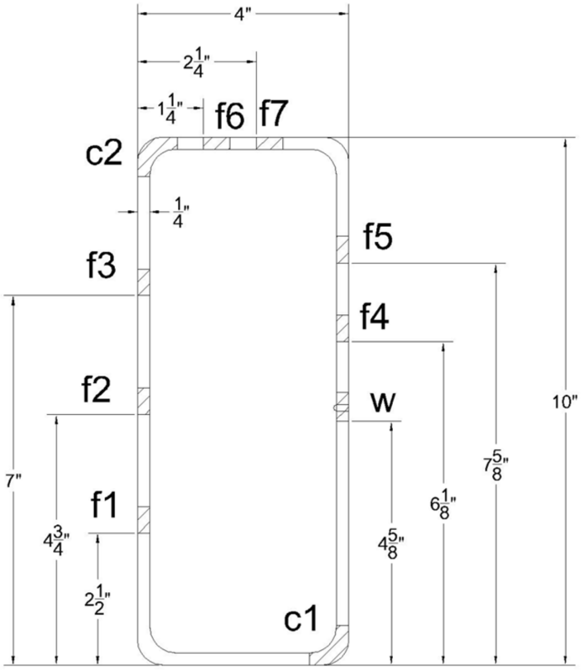

(g)

Figure 3.2 (cont.) Tensile specimen locations for (f) HSS 8x8x3/8 and (g) HSS 10x4x1/4

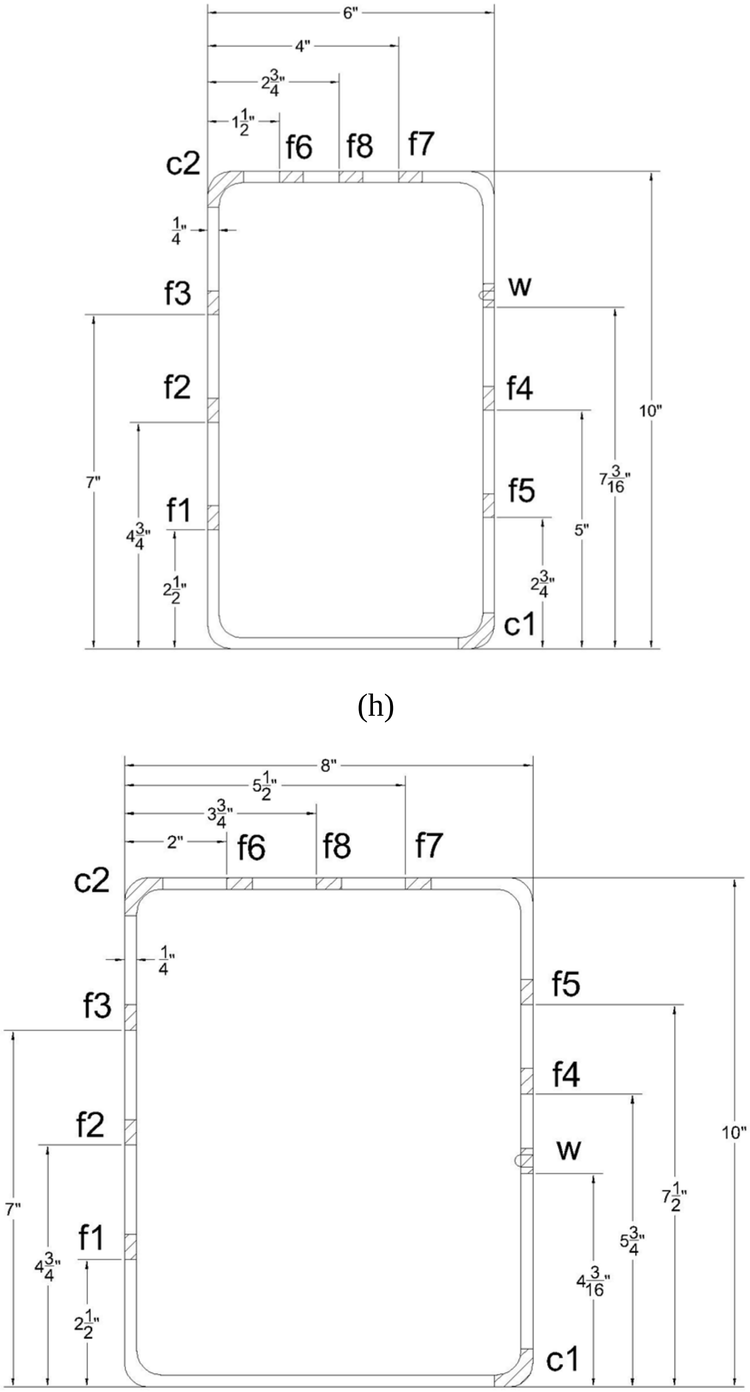

(h)

(i)

Figure 3.2 (cont.) Tensile specimen locations for and (h) HSS 10x6x1/4 and (i) HSS 10x8x1/4

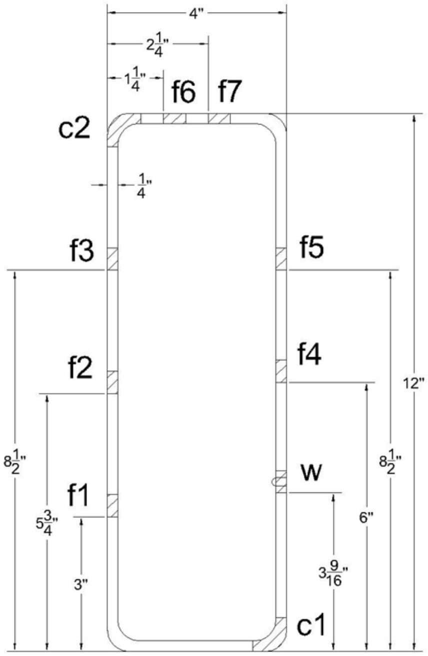

(j)

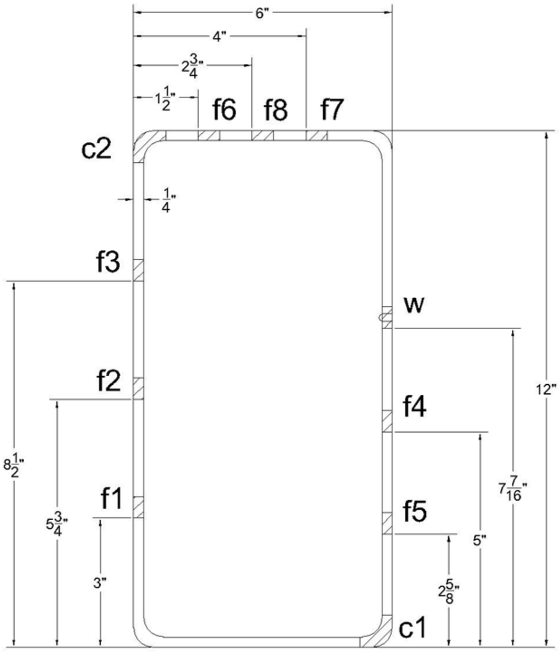

(k)

Figure 3.2 (cont.) Tensile specimen locations for (j) HSS 12x4x1/4 and (k) HSS 12x6x1/4

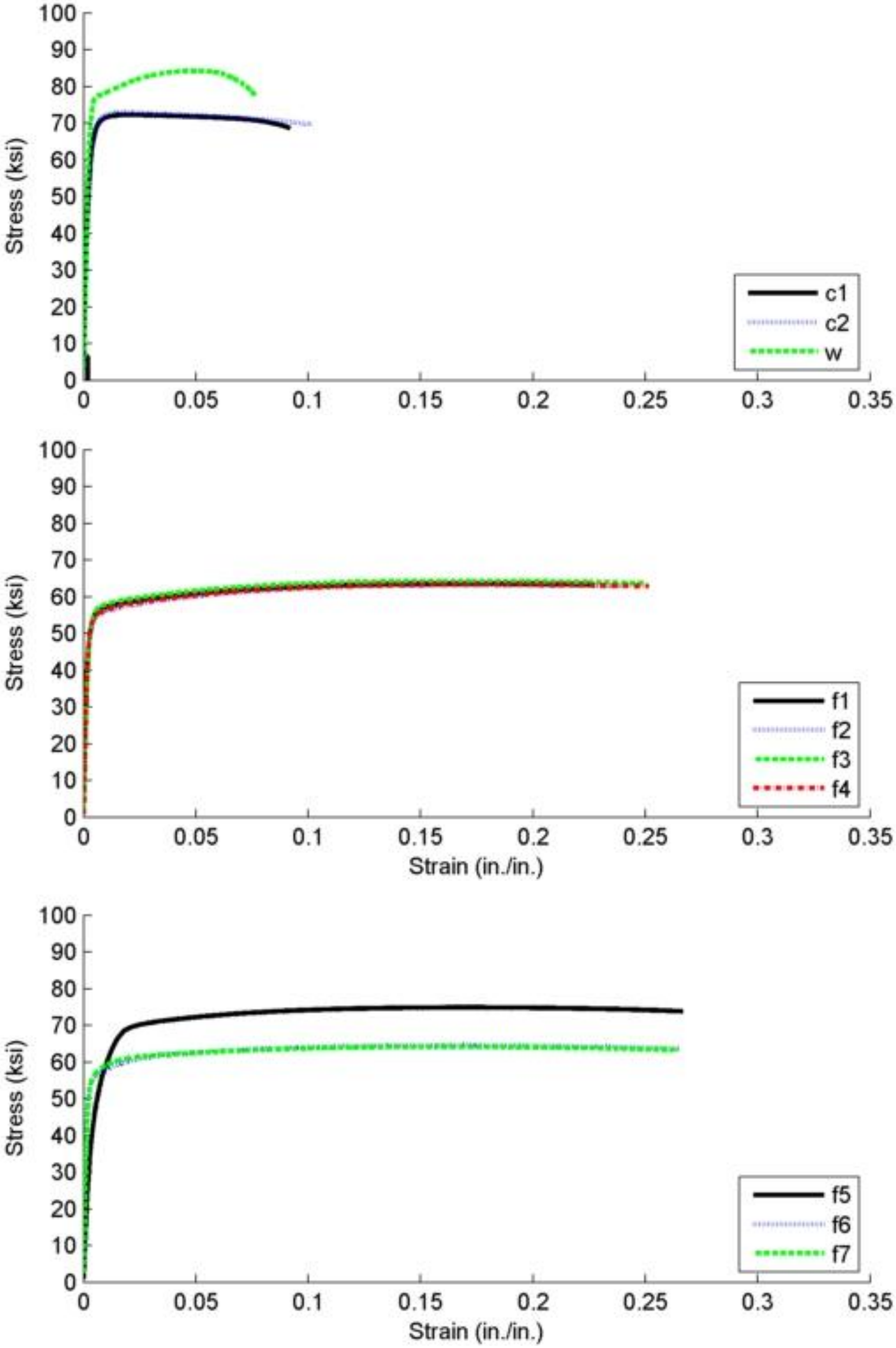

Figure 3.3 (a) HSS 8x4x1/4 stress-strain

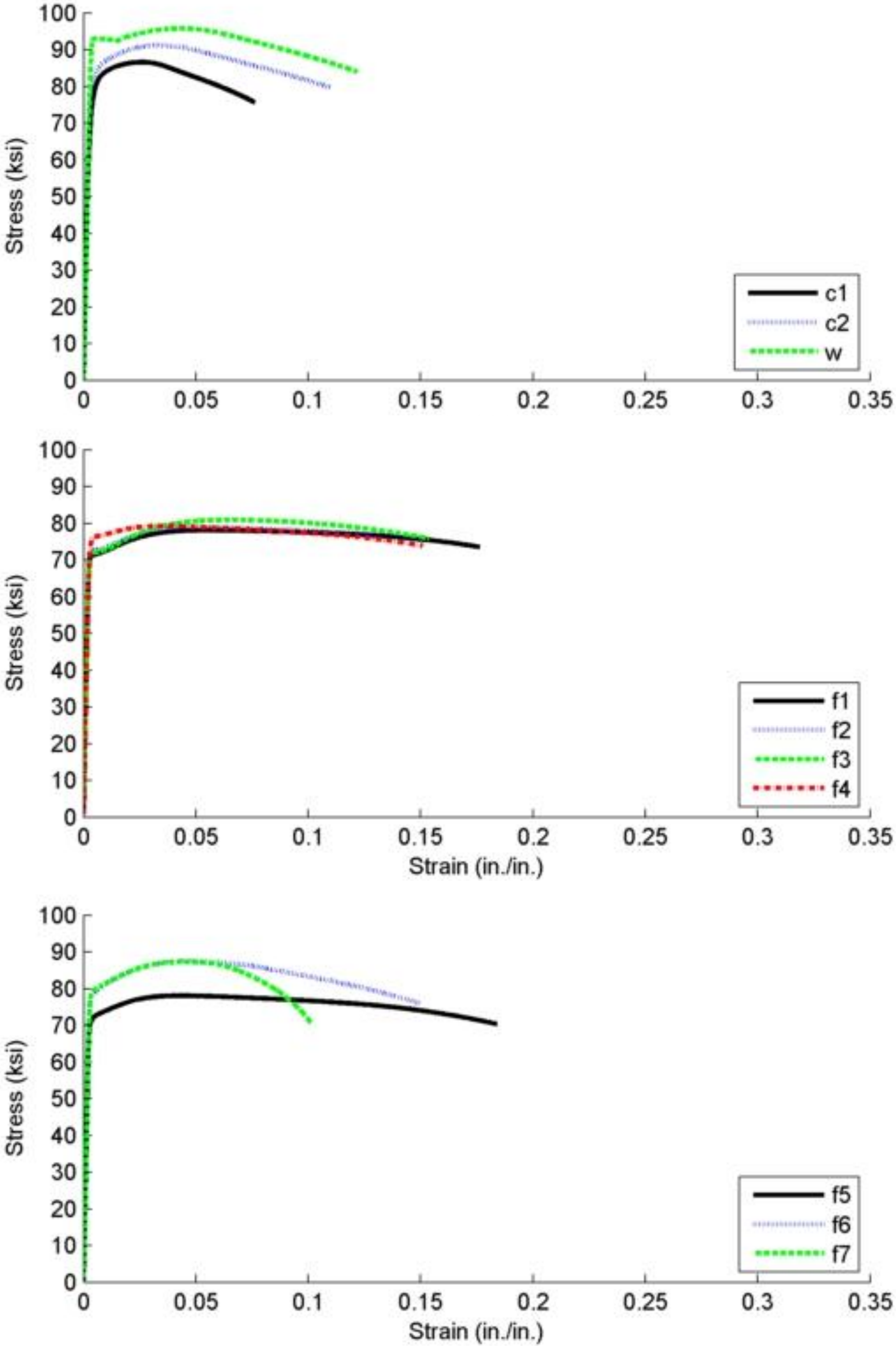

Figure 3.3 (b) HSS 8x4x3/8 stress-strain

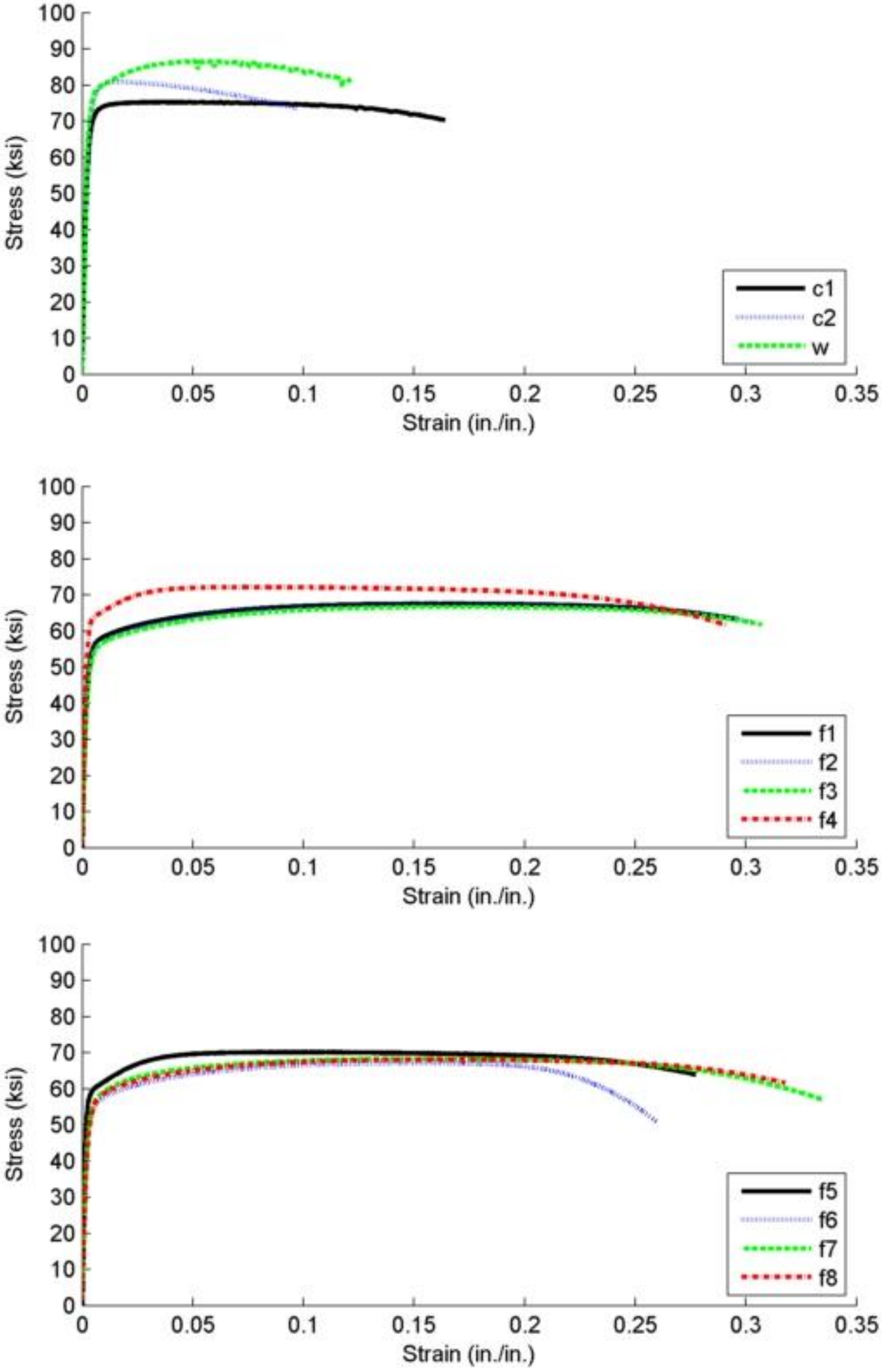

Figure 3.3 (c) HSS 8x6x1/4 stress-strain

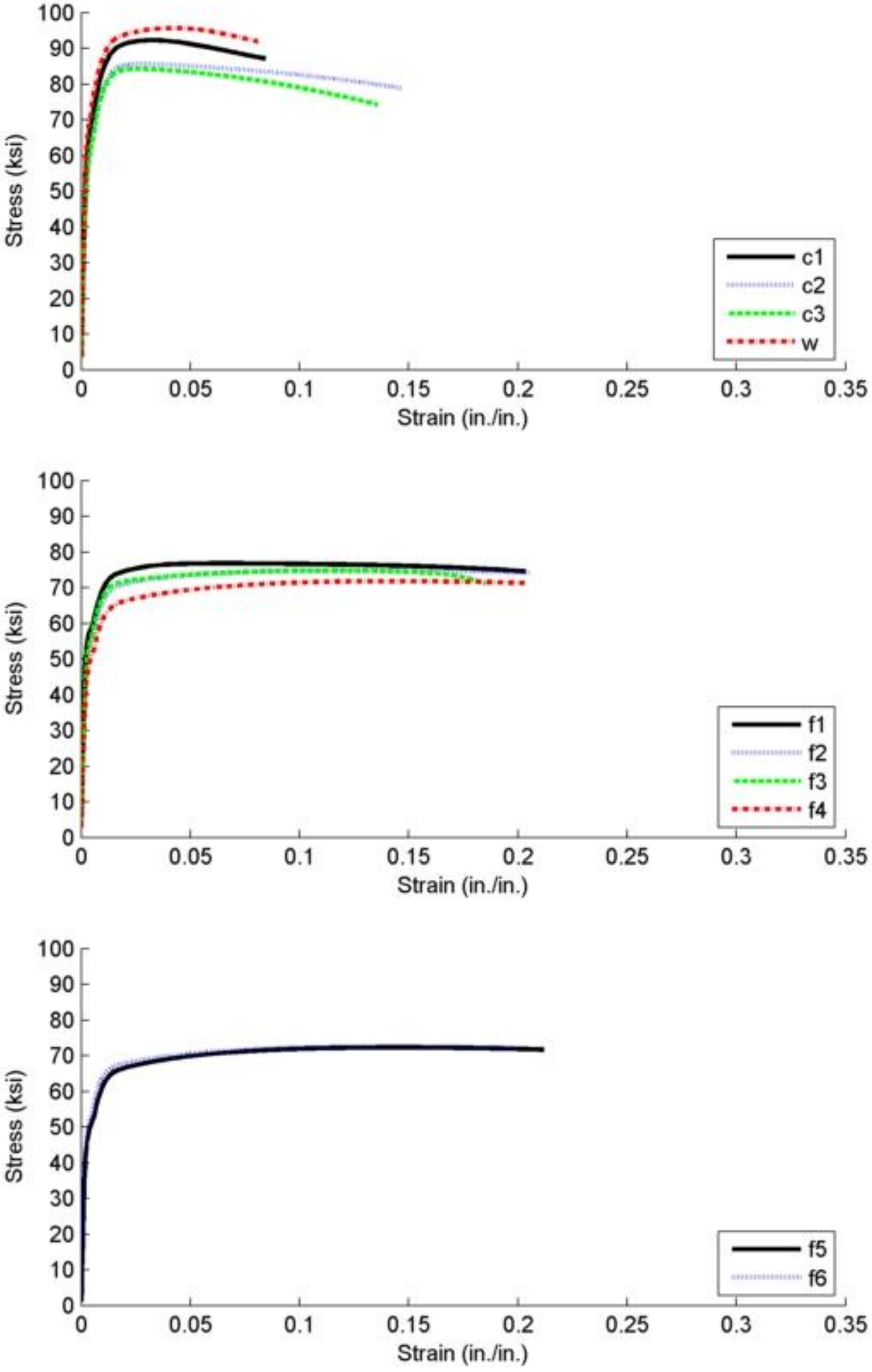

Figure 3.3 (d) HSS 8x6x3/8 stress-strain

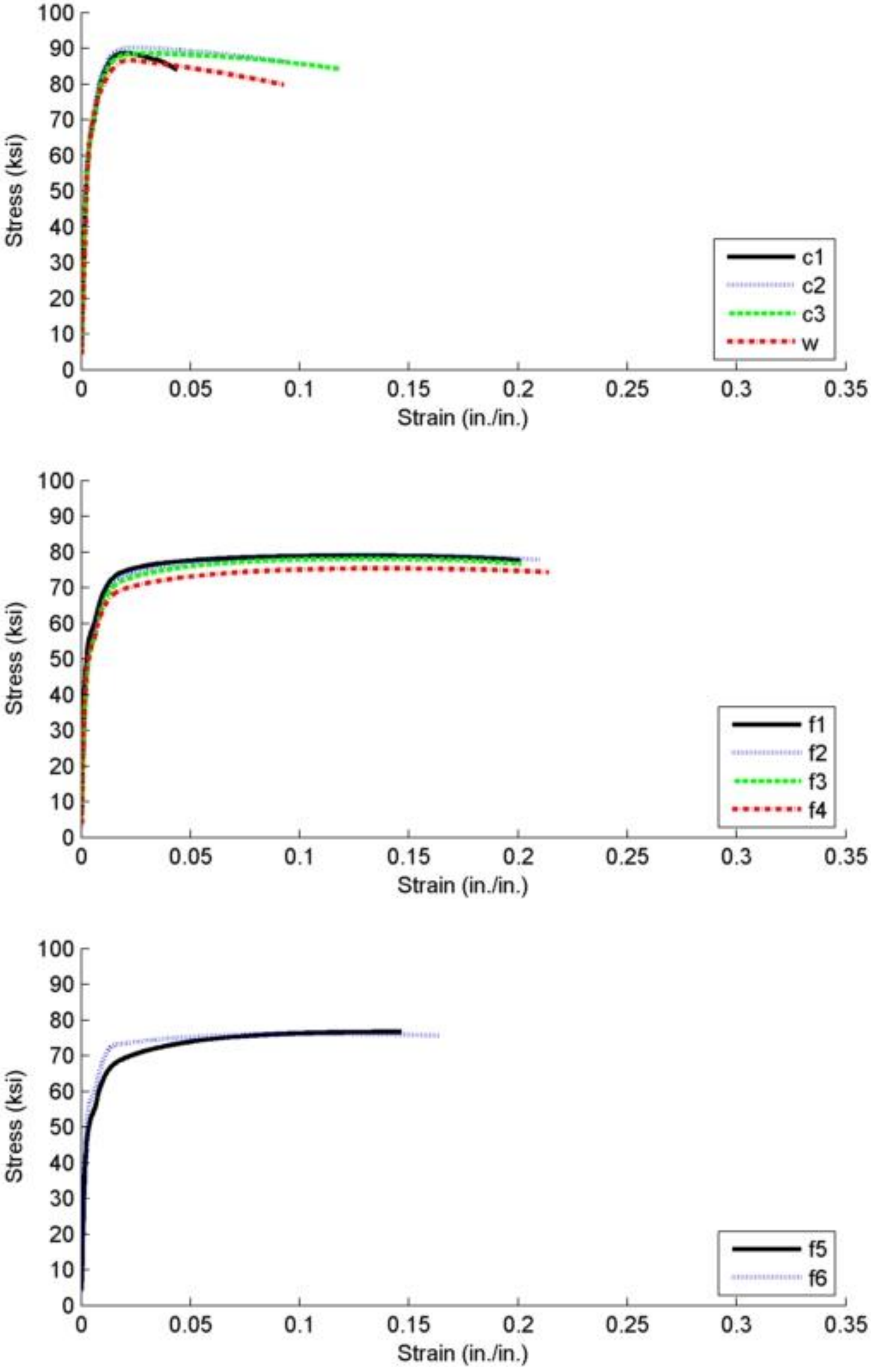

Figure 3.3 (e) HSS 8x8x1/4 stress-strain

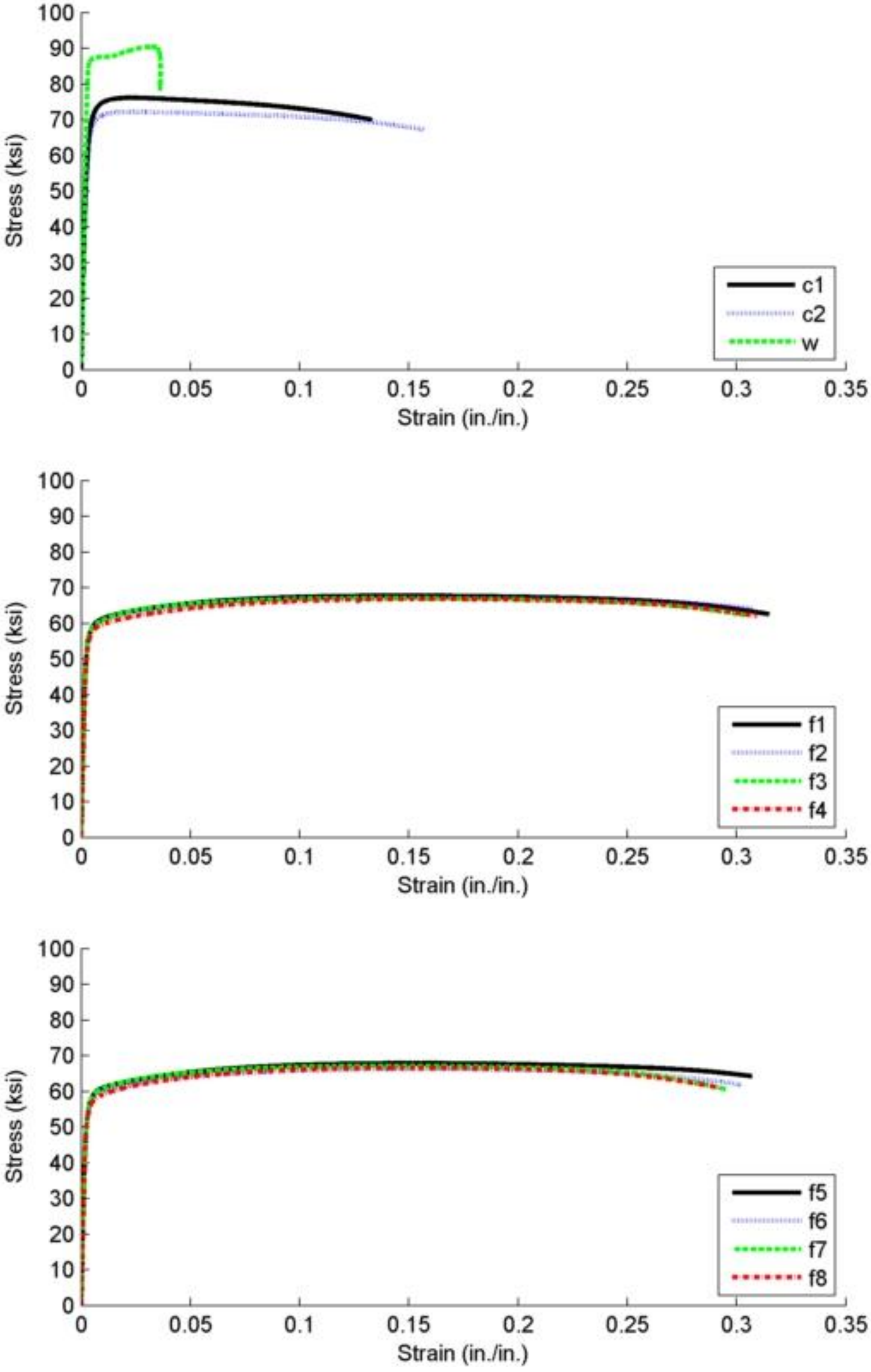

Figure 3.3 (f) HSS 8x8x3/8 stress-strain

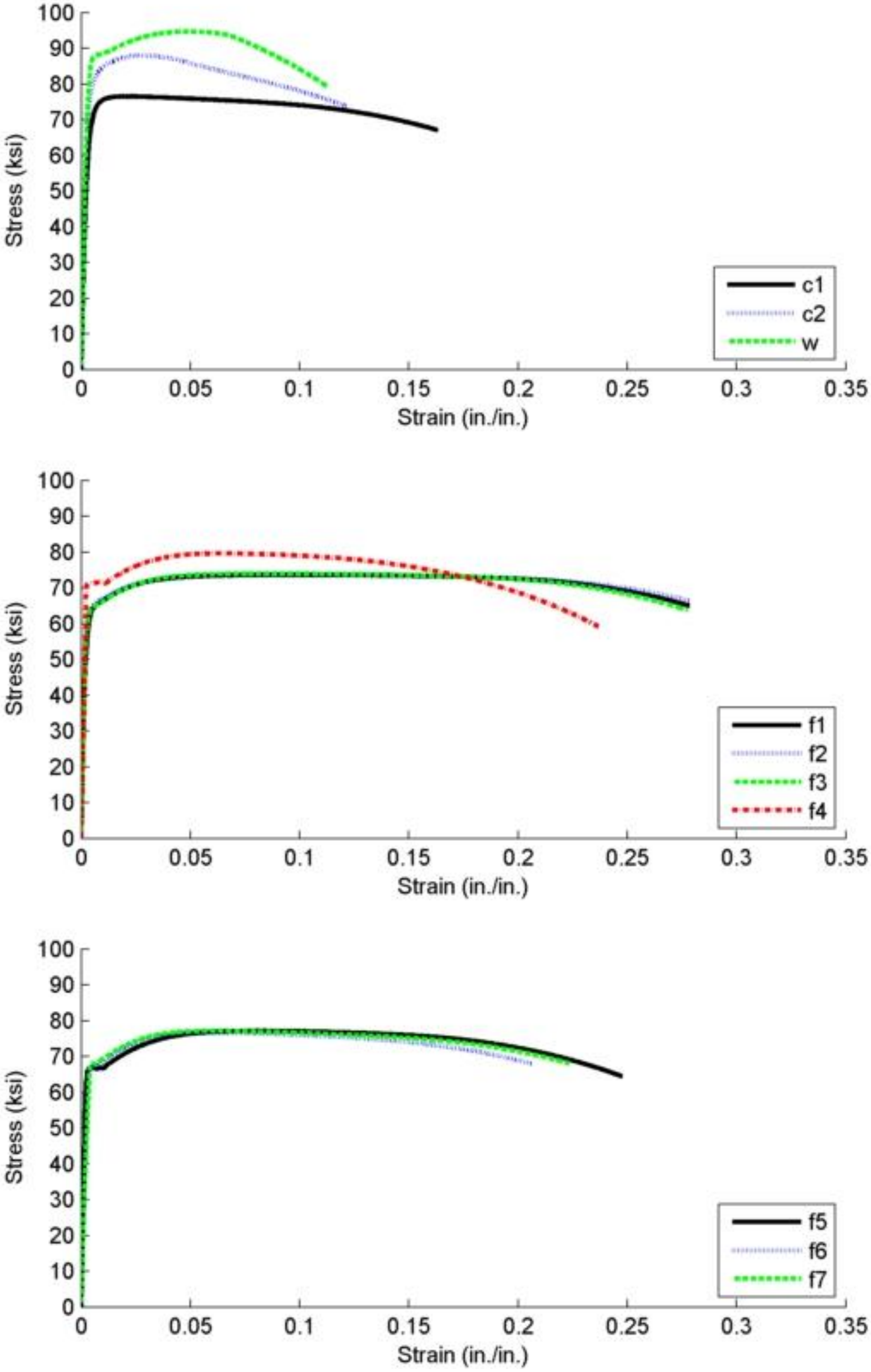

Figure 3.3 (g) HSS 10x4x1/4 stress-strain

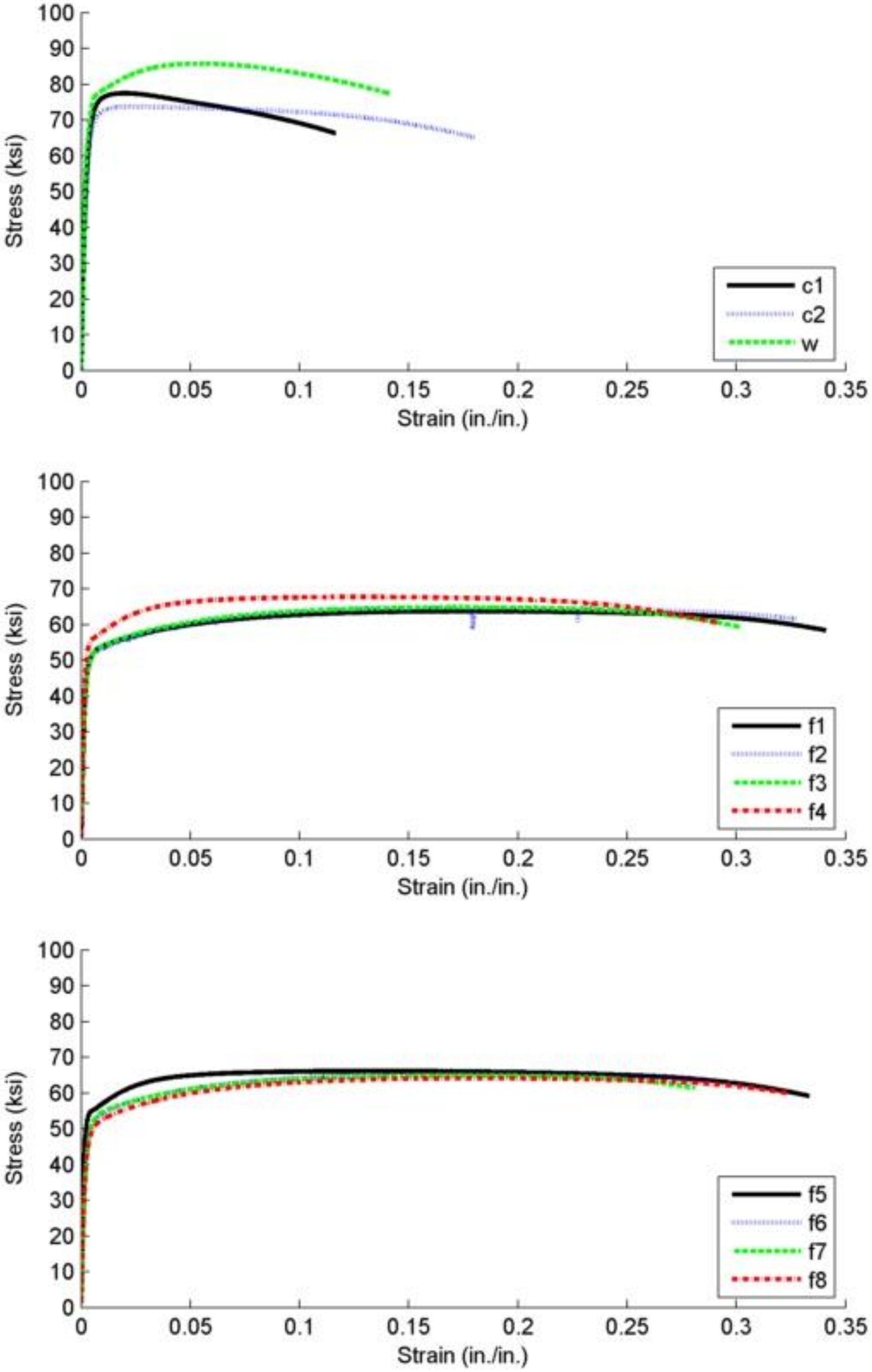

Figure 3.3(h) HSS 10x6x1/4 stress-strain

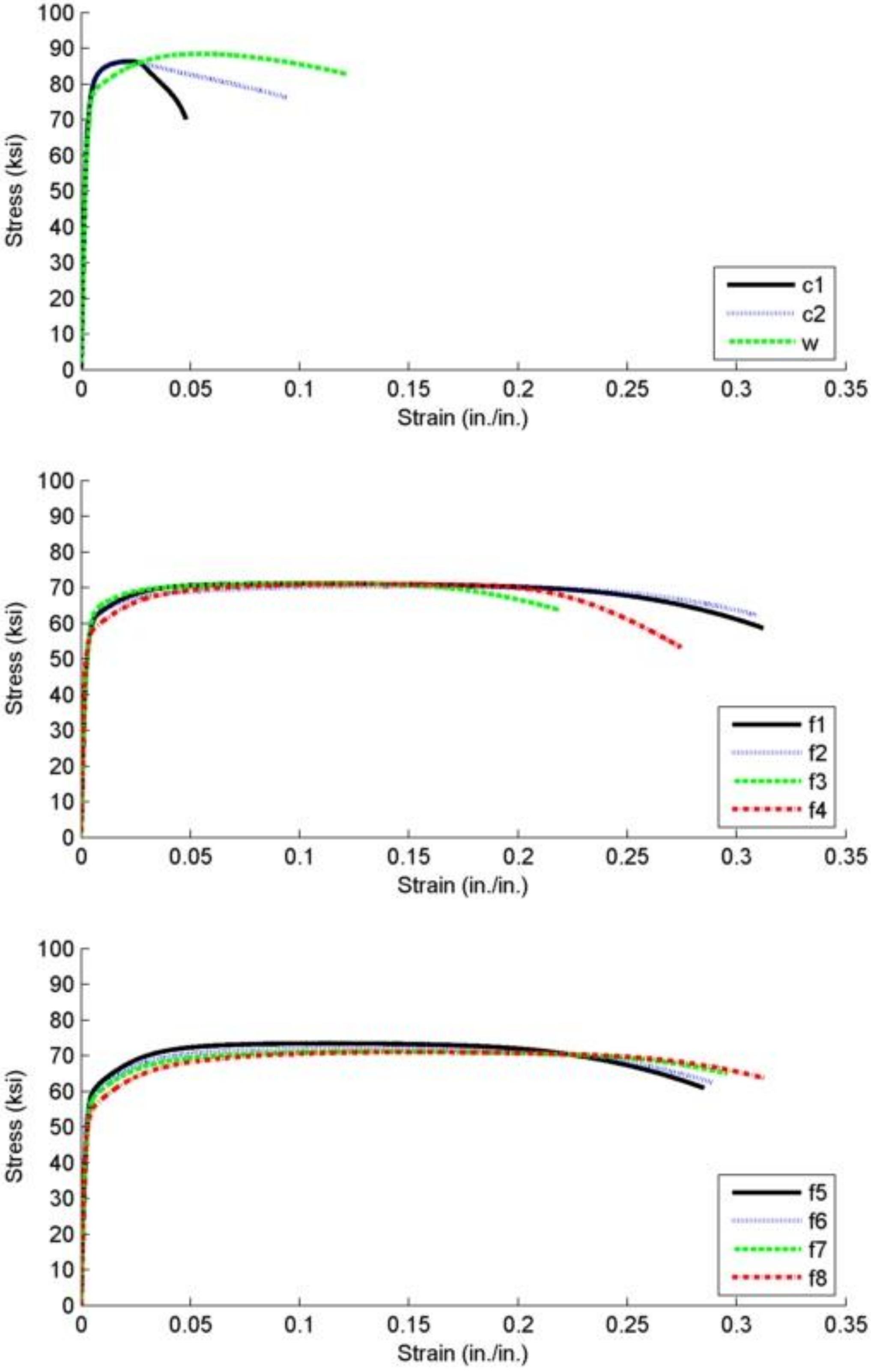

Figure 3.3 (i) HSS 10x8x1/4 stress-strain

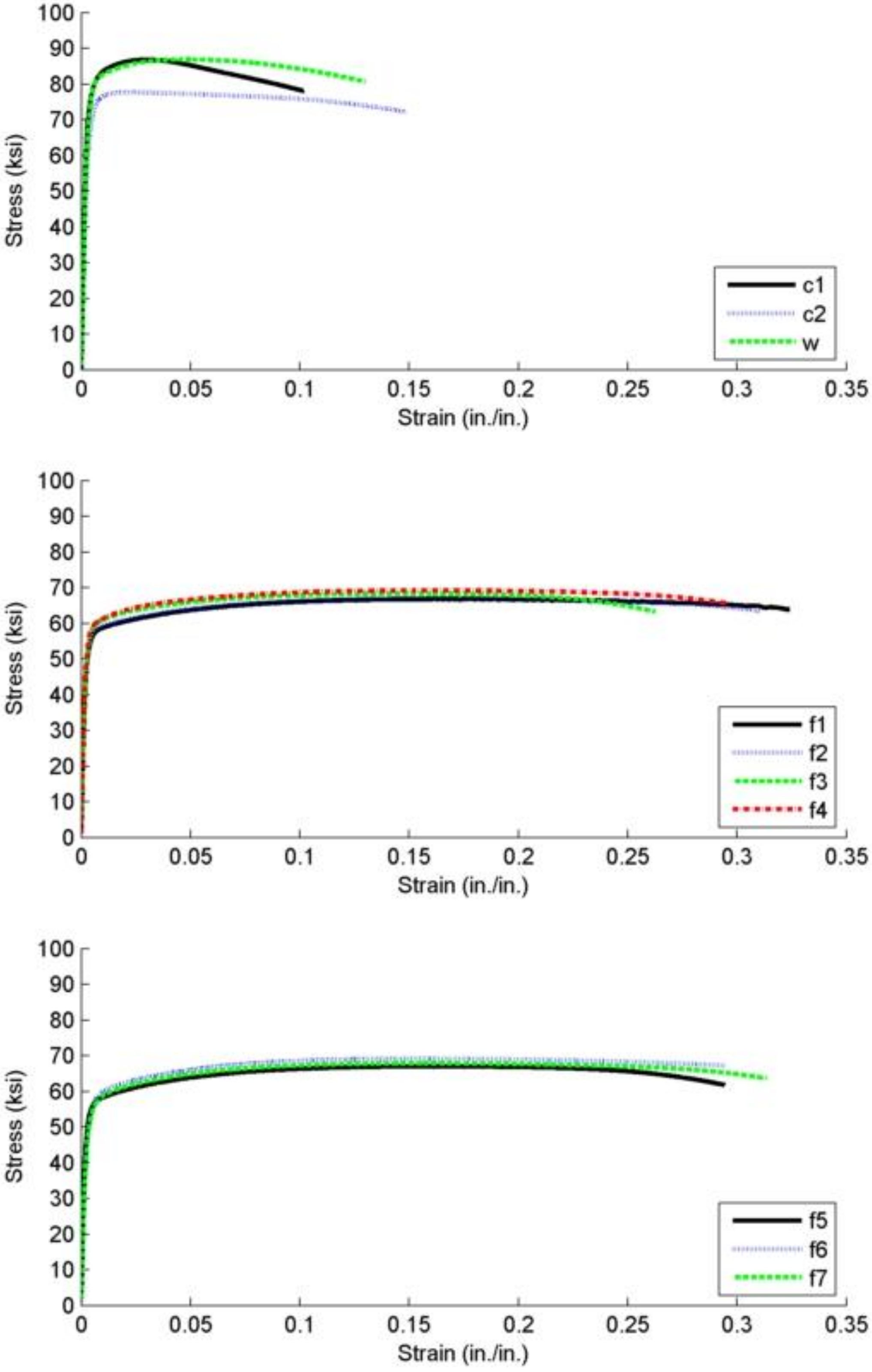

Figure 3.3 (j) HSS 12x4x1/4 stress-strain

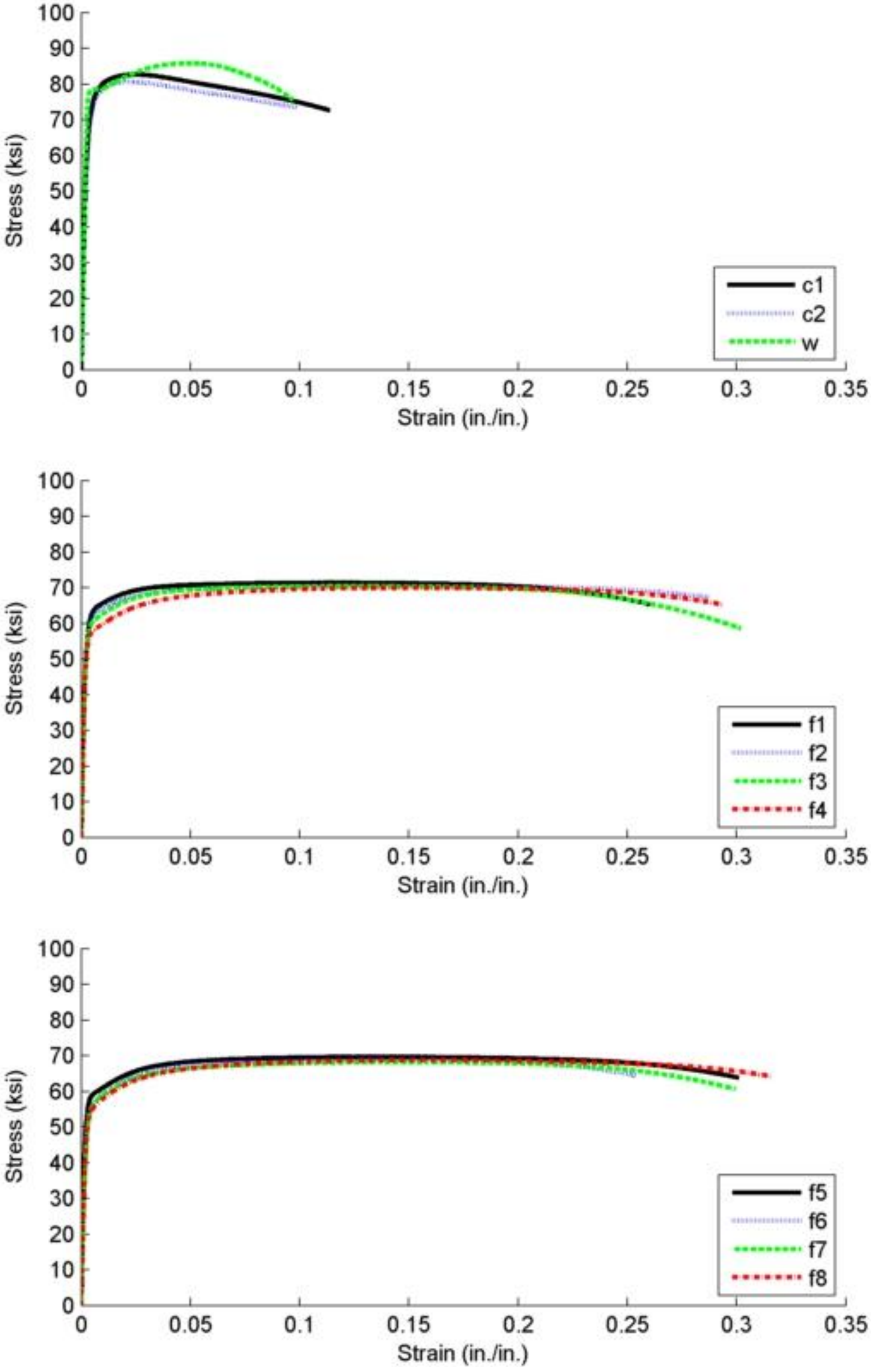

Figure 3.3 (k) HSS 12x6x1/4 stress-strain

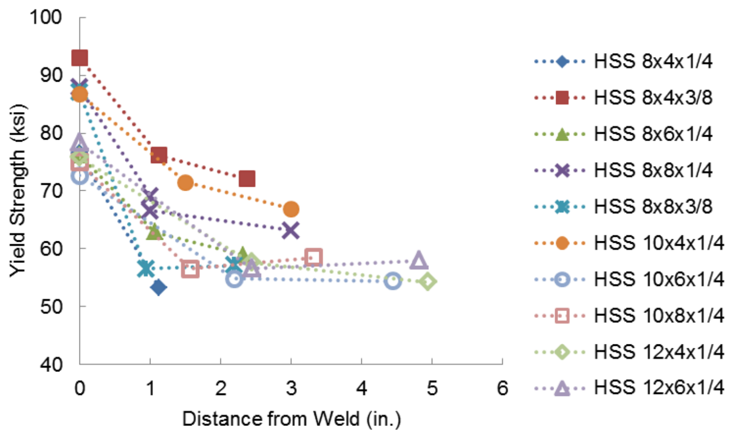

(a)

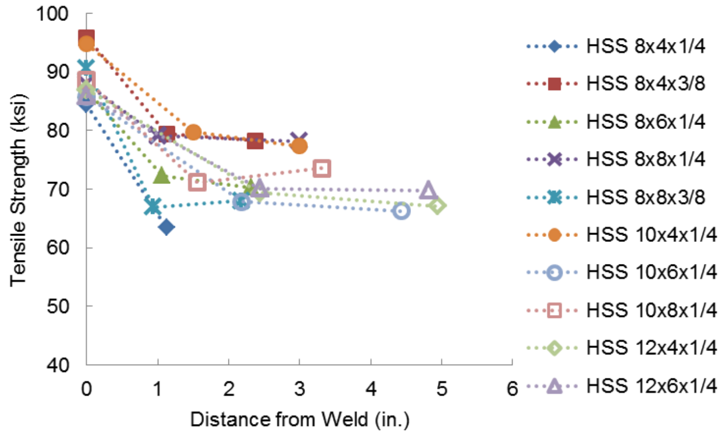

(b)

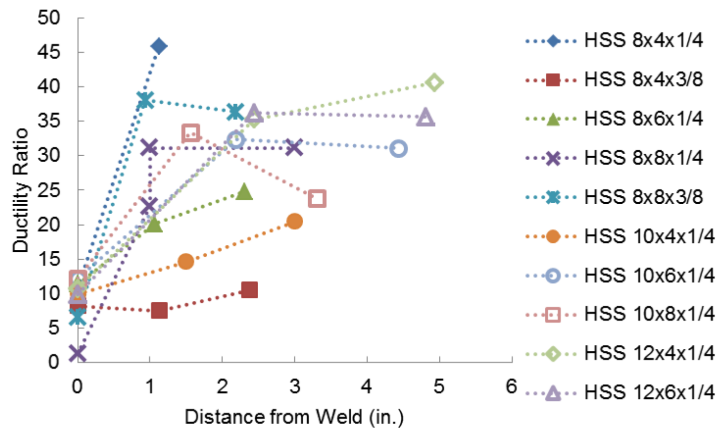

(c)

Figure 3.4 Effect of distance from the weld on (a) yield strength (F_y), (b) tensile strength (F_u), and (c) ductility ratio (e_u/e_y)

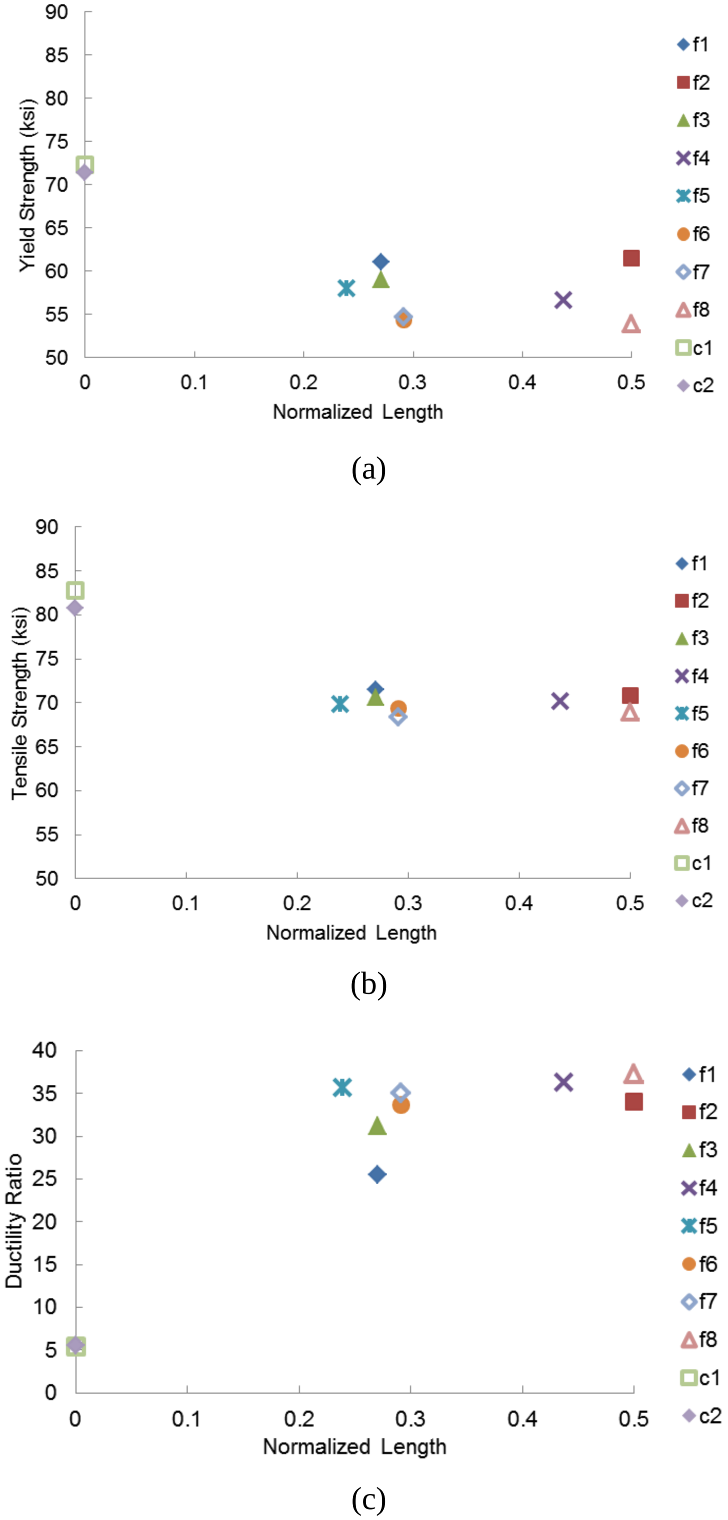

Figure 3.5 Effect of normalized distance from HSS corner on the (a) yield strength (F_y), (b) tensile strength (F_u), and (c) ductility ratio (e_u/e_y) for the HSS 12x6x1/4

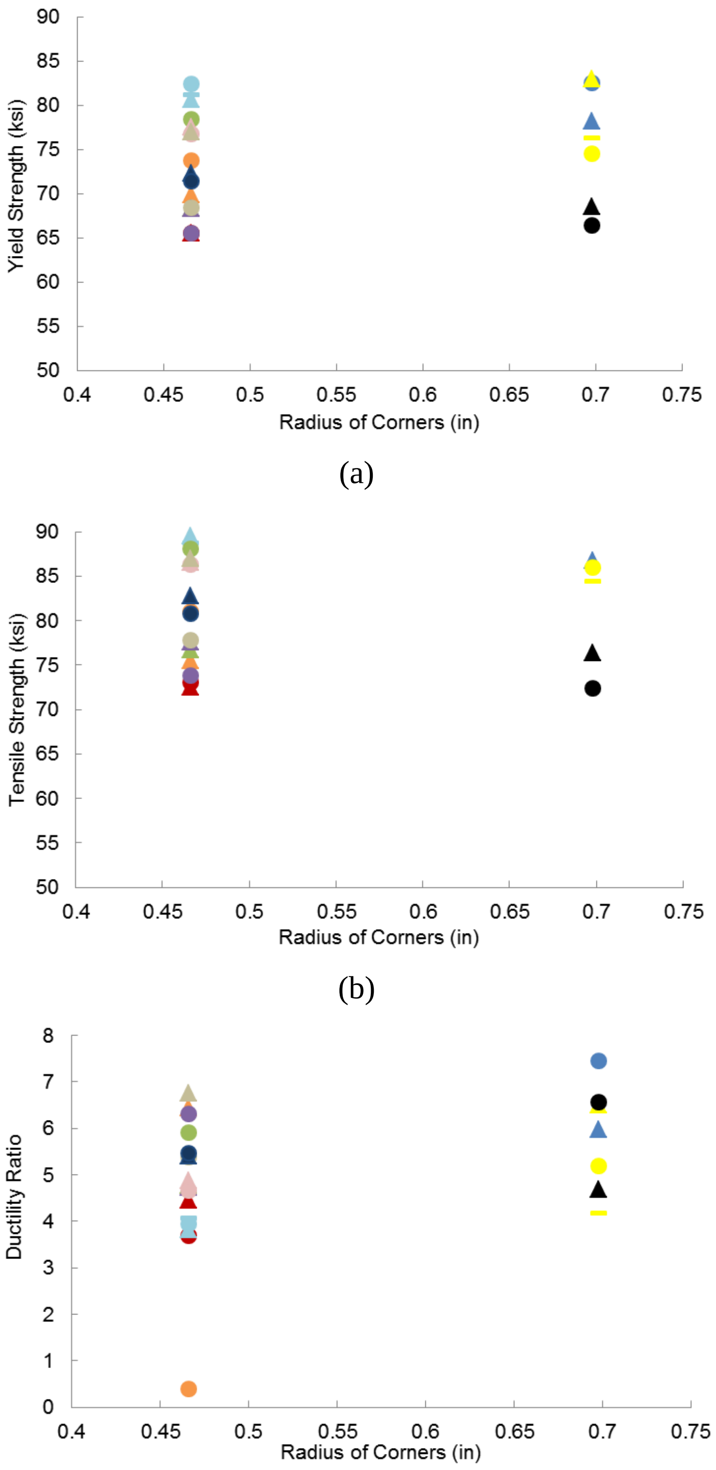

(a)

(b)

(c)

Figure 3.6 Effect of the HSS corner radius on (a) yield strength (F_y), (b) tensile strength (F_u), and (c) ductility ratio (e_u/e_y)

CHAPTER 4: HSS BEAM EXPERIMENTAL BEHAVIOR

4.1 Introduction

Hollow structural section (HSS) members have many desirable properties, such as favorable bending, compression and torsional resistance, which have initiated interest for their use in seismic moment resisting frames (SMRF). This interest can be seen in the use of HSS for a variety of other structural applications including column members (hollow or concrete filled), bracing elements, truss elements, exposed structural steel, and cladding supports. Most research has focused on axially loaded truss connections and connections between HSS or concrete filled tube (CFT) columns and wide flange beams, rather than HSS-to-HSS moment connections in cyclic bending (Hajjar 2000, Packer 2000, Nishiyama and Morino 2004).

To be able to use HSS beam members in low-to-midrise seismic moment frame systems, it is necessary to determine whether HSS beam members can form stable plastic hinges under cyclic bending and identify limiting parameters resulting in local buckling prior to yielding. Several seismic design specifications, such as the American Institute of Steel Construction’s (AISC) Seismic Design Specification (AISC 2010b), require moment frames to be capable of achieving specified interstory drift levels without significant loss of capacity implying inherent ductility in the connections and members. The seismic specifications require that moment connections in intermediate moment frame (IMF) systems and special moment frame (SMF) systems maintain at least 80% of their moment capacity under interstory drifts of 2% and 4%, respectively (AISC 2010b). Previous studies have considered the behavior of HSS members under monotonically increasing loads and noted the importance of the width-thickness (*b/t*), depth-thickness (*h/t*), and aspect ratio (*h/b*) (Korol and Houdba 1972, Hasan and Hancock 1988, Wilkinson and Hancock 1998). In order to effectively use HSS as bending members for seismic applications, an understanding of their behavior under cyclic loading conditions must be obtained.

This chapter presents the findings of an experimental study on the bending behavior of nine rectangular and two square HSS beam members under large cyclic displacements to better define limits associated with their use in seismic applications. This experimental program is designed to specifically study the effects of continued cycling at increasing rotation levels with respect to the moment capacity, occurrence of local buckling, secant stiffness, energy dissipation, and spread of yielding along the length of HSS beam members. The width-thickness (*b/t*) and depth-thickness (*h/t*) ratios are related to the degradation of the moment capacity and the rotation capacity of the HSS members under bending to provide better guidance for their use in earthquake resistant building systems.

4.2 Experimental Program

4.2.1 Hollow Structural Section Specimens

In order to evaluate the behavior of square and rectangular HSS under pure bending, eleven different standard U.S. cold-formed sections were chosen for the experimental study with varying depths, widths, and thicknesses. The depth of the sections ranged from 8 in. to 12 in., while the considered widths were 4 in. to 8 in. The wall thicknesses of the HSS were either 1/4 in. or 3/8 in. The wall thickness values were limited to 3/8 in. in consideration of practical issues associated with welding thicker sections. The eleven HSS that were tested are listed in Table 4.1 along with their associated properties. Figure 4.1 provides a comparison of the *b/t* and *h/t* for each section. These values ranged from 8.46 to 31.3 for *b/t* and 19.9 to 48.5 for *h/t*. HSS within these *b/t* and *h/t* limits were specifically chosen because they typify past square and rectangular tubular sections used in bending applications or tested in bending under monotonic loading. Figure 4.1 also shows the width-thickness and depth-thickness limits associated with HSS used in ordinary moment frame systems (OMF), where the HSS member is in bending, and special concentrically braced frame systems (SCBF), where the HSS member experiences axial loads, P-δ induced bending moments, and subsequent postbuckling bending moments. The eleven tested HSS members provided a good distribution of specimens above and below these limits.

4.2.2 HSS Material Properties

Prior to the detailed study of HSS material properties presented in Chapter 3, a preliminary study was conducted. The results of this study are utilized throughout Chapter 4 and are reported below. A more detailed discussion of the material properties of HSS can be found in Chapter 3.

All of the tested sections were manufactured with A500 Gr. B steel that had a specified minimum tensile yield strength, F_y, of 46 ksi and a specified minimum ultimate tensile strength, F_u, of 58 ksi. However, tension tests of coupon specimens taken from the flats (i.e. walls) of the HSS provided higher yield strength and ultimate tensile strength values (Table 4.2). The measured yield strengths ranged between 55.0 ksi and 65.8 ksi and the ultimate strength values ranged between 66.3 ksi and 76.7 ksi. For the bending study, coupon specimens were also taken from the corners of the HSS 8x6x3/8 and HSS 8x8x1/4 specimens and showed further effects of cold working with yield strength values of 74.5 ksi and 80.6 ksi, respectively, and ultimate strength values of 85.9 ksi and 83.8 ksi, respectively. The yield strength measured from the flats suggested an overstrength factor, R_y, of 1.31 which was slightly lower than the 1.4 value specified by the AISC Seismic Provisions (AISC 2010b).

Table 4.1 lists the minimum plastic moment capacity, $(M_p)_{min}$, of each section based on the minimum code specified yield strength of 46 ksi. The experimental plastic moment capacity, $(M_p)_{exp}$, of each section was calculated based on the measured yield strength from the coupon specimens taken from the wall of each respective HSS specimen as provided in Table 4.2. The minimum plastic moment strength of the tested sections were between 612 k-in. and 1431 k-in., while the experimental plastic moment strengths were between 875 k-in. and 1908 k-in.

4.3 Test Setup and Loading Protocol

The experimental test setup used to study the cyclic bending behavior of the HSS is shown in Figure 4.2. The HSS beam member was cantilevered vertically within the test frame which provided the input displacement to the top of the member through a pin (Figure 4.3). The pin passed through a slotted hole at the top of the HSS so as to prevent the application of axial load as the beam displaced and buckled (Figure 4.4 (a)). A bearing plate was also added to the end of the member around the slotted hole to prevent local deformation during loading. Although past studies of the bending behavior of HSS under monotonic loading typically used a four-point bending configuration (Korol and Hudoba 1972, Hasan and Hancock 1988, Zhao and Hancock 1991, Wilkinson and Hancock 1998), the use of a cantilevered HSS member allowed for a better evaluation of the hysteretic behavior and formation of the plastic hinge at the beam end as would be expected for a beam member in a seismic moment frame. The fixed end of the HSS was sandwiched between two large angles to provide a reusable connection and stiffener plates were added to ensure that the inelastic deformation occurred outside of the connection region. This connection was not a practical connection for a moment frame system, but provided a means of evaluating the bending behavior of the HSS members (Figure 4.4 (b)).

The specimen was instrumented to allow for the characterization of the deformation behavior within the plastic hinge region while also providing an overall understanding of the inelastic bending behavior under cyclic loading. The applied loads were measured using the 110 kip load cell attached to the actuator used to apply lateral displacements. Displacement measurements were obtained using an infrared optical tracking system. A grid of optical markers was also placed on the web of the HSS member, which allowed for further study of the deformation behavior within the plastic hinge region. Strain gages were applied to each of the flanges at 3 in., 9 in., 18 in., and 36 in. from the fixed connection to study the progression of yielding along the length with continued cycling (Figure 4.5). Figure 4.6 details the locations of the potentiometers where SP was used as a secondary measurement of beam tip displacement, PT0 to PT2 measured beam plastic hinge rotation, and BS measured test setup slip.

The loading protocol consisted of increasing end displacements and provided a means of evaluating the moment-rotation behavior of HSS under large cyclic deformations. Figure 4.7 shows a plot of the loading protocol that was applied in displacement control at a quasi-static loading rate. This protocol was chosen because current seismic design requirements stipulate that the majority of the connection deformation must occur in the beam member (AISC 2010b). The rotation of each section was calculated as the horizontal displacement divided by the clear span length of the beam, 60.5 in., which allowed for rotations up to 0.08 rad. given the constraints of the test setup.

4.4 Summary of Experimental Testing

For each of the eleven HSS members, the moment-rotation hysteresis was calculated allowing for the evaluation of the cyclic bending behavior. These findings are summarized in Table 4.3. During testing, it was observed that each section underwent some degree of rigid rotation at the connection. This resulted in no specimen reaching the full 0.08 rad. rotation level. To address this, the optical tracking markers on the beam at the fixed connection were used to measure the rigid body rotation of the specimen. The rigid body rotation was subtracted from the overall measured rotation leaving the actual rotation due to the deformation of the HSS members (Figure 4.8). Although no specimen reached the maximum desired rotation of 0.08 rad., several members still underwent rotations of 0.07 rad. and all specimens reached a maximum rotation of at least 0.05 rad. A summary of the behavior of each test specimen is given in the following sections.

4.4.1 HSS 8x4x1/4 Hysteretic Behavior

The HSS 8x4x1/4 member had moderate b/t and h/t ratios (b/t=14.2, h/t=31.3) and showed relatively stable hysteretic behavior throughout the loading protocol (Figure 4.8 (a)). The minimum plastic moment capacity was 612 k-in., whereas the expected plastic moment capacity using the measured yield strength from the coupon specimens was 875 k-in. During the cyclic bending test, the HSS 8x4x1/4 reached a maximum moment of 772 k-in at the 0.027 rad. cycle (Figure 4.9(a)). This was higher than the minimum plastic moment capacity ($M_{max}/(M_p)_{min}$=1.26), but lower than expected moment capacity based on the tested yield strength ($M_{max}/(M_p)_{exp}$=0.90) (Figure 4.9(b)).

The load carrying capacity of the member began to degrade at the 0.04 rad. cycle and considerable degradation began at 0.05 rad. During the last cycle, the specimen decreased to a moment capacity of 471 k-in. at 0.069 rad. This corresponded to a 38.9%

decrease in the maximum moment capacity at the final cycle. This degradation stemmed from a moderate amount of buckling in the flange and web and the initiation of tearing at the corners of member where cold working effects are the most significant (Figure 4.9(c)).

4.4.2 HSS 8x4x3/8 Hysteretic Behavior

With fairly low *b/t* and *h/t* ratios (*b/t*=8.46, *h/t*=19.9), the HSS 8x4x3/8 showed very stable hysteretic behavior throughout the loading protocol (Figure 4.8 (b)). Based on the specified material properties, the minimum plastic moment capacity was 865 k-in., while the expected plastic moment capacity based on the measured yield strength was 1172 k-in. The HSS 8x4x3/8 reached a maximum moment capacity of 1481 k-in at the 0.029 rad. cycle (Figure 4.10(a)). This was higher than both the specified minimum and expected plastic moment by a considerable margin with $M_{max}/(M_p)_{min}$ equal to 1.71 and $M_{max}/(M_p)_{exp}$ equal to 1.28 (Figure 4.10(b)).

The HSS 8x4x3/8 underwent considerable rigid rotation and as a result reached a maximum rotation level of only 0.06 rad. Only negligible degradation of the moment capacity was observed during cycling. During the final cycle, the HSS 8x4x3/8 reached a maximum moment of 1414 k-in. at 0.06 rad. meaning only a small degradation of the maximum moment capacity of 4.0% was observed. Figure 4.10(c) shows the plastic hinge region at the end of cycling with only minor bulging in the flanges and no tearing at the corners that further confirms the reason for stable hysteretic behavior.

4.4.3 HSS 8x6x1/4 Hysteretic Behavior

The HSS 8x6x1/4 had a high *b/t* ratio and moderate *h/t* ratio (*b/t*=22.8, *h/t*=31.3) leading to a considerable amount of degradation of the moment capacity throughout the loading protocol (Figure 4.8 (c)). The minimum plastic moment capacity based on specified material properties was 777 k-in., whereas the expected plastic moment capacity was 936 k-in., but the HSS 8x6x1/4 reached a maximum moment of 1007 k-in 0.030 rad. (Figure 4.11(a)). The experimental result was higher than the specified minimum and expected capacities with an $M_{max}/(M_p)_{min}$ of 1.30 and an $M_{max}/(M_p)_{exp}$ of 1.09 (Figure 4.11(b)).

The load carrying capacity of the member began to degrade after the 0.03 rad. cycles and considerable degradation in the moment capacity began during the 0.04 rad. cycles. During the last cycle, the moment capacity of the specimen decreased to 517 k-in. at 0.066 rad. This decrease corresponded to a 48.5% degradation in the maximum moment capacity at the end of the test. The large amount of degradation was a result of considerable flange and web buckling and small cracks forming in the HSS corners that initiated during the final cycle (Figure 4.11(c)).

4.4.4 HSS 8x6x3/8 Hysteretic Behavior

Having low *b/t* and *h/t* ratios (*b/t*=14.2, *h/t*=19.9), the HSS 8x6x3/8 showed very stable hysteretic behavior throughout the loading protocol. As a result of the occurrence of rigid body rotation, the rotation experienced by the member was limited to 0.056 rad. (Figure 4.8 (d)). Utilizing the specified material properties the minimum plastic moment capacity was 1109 k-in., while the expected moment capacity based on the section yield strength was 1460 k-in. This section reached a maximum moment capacity of 1796 k-in at 0.035 rad. (Figure 4.12 (a)). In comparison with the minimum and expected plastic moment, the experimental findings were higher by a considerable margin with an $M_{max}/(M_p)_{min}$ of 1.62 and an $M_{max}/(M_p)_{exp}$ of 1.25 (Figure 4.12 (b)).

The cyclic bending study of the HSS 8x6x3/8 resulted in minimal amounts of degradation. During the final cycle, the maximum moment reached was 1619 k-in. at 0.054 rad., which corresponds to a degradation of the maximum moment capacity of 9.8% at the last cycle. Figure 4.12 (c) further confirms the reason for this behavior as only minor bulging in the flanges was observed with considerable whitewash flaking indicating extensive yielding in the HSS member.

4.4.5 HSS 8x8x1/4 Hysteretic Behavior

The HSS 8x8x1/4, a square beam member with high *b/t* and *h/t* ratios (*b/t*=31.3, *h/t*=31.3), showed considerable degradation of the moment capacity during cycling. The minimum plastic moment capacity based on specified material properties was 943 k-in. and based on the tested yield strength the expected plastic moment capacity was 1258 k-in. However, the HSS 8x8x1/4 reached a maximum moment of 1245 k-in at 0.022 rad.

(Figure 4.13(a)). This resulted in a moment capacity that is higher than the specified minimum plastic moment capacity with an $M_{max}/(M_p)_{min}$ of 1.32 and one that is approximately equal to the expected plastic moment capacity with an $M_{max}/(M_p)_{exp}$ equal to 0.99 (Figure 4.13(b)).

The load caring capacity of the member began to degrade after the 0.03 rad. cycle. During the last cycle, the moment capacity of the specimen decreased to 602 k-in. at 0.068 rad. This degradation corresponds to a 51.6% degradation of the maximum moment capacity at the final cycle. The large amount of flange and web buckling and small cracks forming in the HSS corners that initiated during the final cycle led to the observed degradation of the hysteretic moment capacity (Figure 4.13(c)).

4.4.6 HSS 8x8x3/8 Hysteretic Behavior

The square HSS 8x8x3/8 had moderate *b/t* and *h/t* ratios (*b/t*=19.9, *h/t*=19.9) and showed relatively stable hysteretic behavior throughout the loading protocol. As a result of the rigid body rotation, the member only reached a maximum rotation of 0.051 rad. (Figure 4.8 (f))The expected plastic moment capacity based on specified material properties was 1352 k-in. and based on the tested yield strength was 1813 k-in. This section reached a maximum moment of 1988 k-in. at 0.03 rad. (Figure 4.14 (a)). The normalized capacity was greater than unity considering the specified yield strength ($M_{max}/(M_p)_{min}$=1.47) and the tested yield strength ($M_{max}/(M_p)_{exp}$=1.11) (Figure 4.14 (b)).

The load carrying capacity of the member began to degrade only slightly at the 0.04 rad. cycle due to slight buckling in the beam flanges. During the last cycle, at 0.048 rad., a decrease in maximum moment to1728 k-in. was observed. This degradation relates to a 13.0% decrease in the maximum moment capacity at the final cycle. Considering the deformation of the plastic hinge region after testing, increased rotations would likely have led to further degradation of the moment capacity with since an outward buckle had begun to develop in the beam flanges (Figure 4.14 (c)).

4.4.7 HSS 10x4x1/4 Hysteretic Behavior

Having a low *b/t* and high *h/t* ratio (*b/t*=14.2, *h/t*=39.9), the HSS 10x4x1/4 showed a considerable amount of degradation throughout the loading protocol (Figure 4.8 (g)).

This section reached a maximum moment capacity of 1370 k-in. at 0.031 rad. (Figure 4.15 (a)). However, the minimum specified plastic moment was only 874 k-in., while the expected moment capacity based on the material yield strength was 1196 k-in. As a result, the section reached a higher moment capacity under cyclic bending than both the specified minimum and expected capacities by a considerable margin with an $M_{max}/(M_p)_{min}$ of 1.57 and an $M_{max}/(M_p)_{exp}$ of 1.19 (Figure 4.15 (b)).

Testing showed large deterioration of the behavior of the HSS 10x4x1/4 as the result of local buckling especially in the webs, which eventually led to fracture in the corners (Figure 4.15 (c)). During the final cycle, the maximum moment reached was 552.5 k-in. at 0.070 rad. This value corresponds to a degradation of the maximum moment capacity of 62.9% at the last cycle.

4.4.8 HSS 10x6x1/4 Hysteretic Behavior

The HSS 10x6x1/4 had high *b/t* and *h/t* ratios (*b/t*=22.8, *h/t*=39.9) and showed large amounts of degradation throughout the loading protocol with continued cycling. The minimum plastic moment capacity was 1086 k-in. and based on the yield strength of the coupon specimens increased to 1299 k-in. This section reached a maximum moment of 1343 k-in. at the 0.023 rad. cycle (Figure 4.16 (a)). The normalized moment capacity was greater than unity with a $M_{max}/(M_p)_{min}$ of 1.24, and equal to 1.05 for $M_{max}/(M_p)_{exp}$ (Figure 4.16 (b)).

The HSS 10x6x1/4 showed significant degradation of the moment capacity due to flange buckling, large amounts of web buckling, and fracture at the beam corners (Figure 4.16 (c)). The load carrying capacity began to degrade after reaching the maximum moment and became more significant after the 0.03 rad. cycles. During the last cycle, the moment capacity decreased to 531 k-in. at 0.070 rad. This degradation relates to a 60.5% decrease in the maximum moment capacity at the final cycle.

4.4.9 HSS 10x8x1/4 Hysteretic Behavior

As a result of high *b/t* and *h/t* ratios (*b/t*=31.3, *h/t*=39.9), the HSS 10x8x1/4 underwent a large decrease in the maximum moment capacity throughout the loading protocol, reaching a maximum moment capacity of 1595 k-in at 0.018 rad. (Figure 4.17

(a)). The minimum plastic moment was calculated as 1293 k-in., while the expected moment capacity based on the actual section yield strength was 1658 k-in. The resulting $M_{max}/(M_p)_{min}$ was 1.23 and the resulting $M_{max}/(M_p)_{exp}$ was equal to 0.96 (Figure 4.17 (b)) suggesting that local buckling initiated prior to the formation of the full plastic hinge.

Experimental testing of the HSS 10x8x1/4 showed considerable and sudden degradation of the moment capacity. During the final cycle, the maximum moment reached was 677.4 k-in. at 0.068 rad. This results in a degradation of the maximum moment capacity of 67.6% at the last cycle. Figure 4.17 (c) suggested the reason for this behavior was large amounts of buckling in the web and flanges. Fracture in the corners added to the continued degradation of the moment capacity during later cycles.

4.4.10 HSS 12x4x1/4 Hysteretic Behavior

The HSS 12x4x1/4 had a moderate b/t ratio and the highest h/t ratio of all sections tested (b/t=14.2, h/t=48.5) and showed large amounts of degradation throughout the loading protocol. The HSS 12x4x1/4 member reached a maximum moment of 1509 k-in at 0.028 rad. (Figure 4.18 (a)). The calculated minimum plastic moment capacity was 1178 k-in. and based on the tested yield strength from the coupon specimens of the flats was 1454 k-in. Thus, the normalized capacity is greater than unity for the minimum yield strength with a $M_{max}/(M_p)_{min}$ of 1.28 and for the tested yield strength with a $M_{max}/(M_p)_{exp}$ of 1.06 (Figure 4.18(b)).

The HSS 12x4x1/4 showed significant degradation of the moment capacity due to large amounts of web buckling, flange buckling, and fracture in the beam corners (Figure 4.18 (c)). The load carrying capacity decreased significantly after reaching the maximum moment. During the last cycle, the moment capacity decreased to 635.4 k-in. at 0.067 rad. This degradation resulted in a 57.4% overall drop in the maximum moment capacity.

4.4.11 HSS 12x6x1/4 Hysteretic Behavior

The high b/t and h/t ratios (b/t=22.8, h/t=48.5) of the HSS 12x6x1/4 resulted in considerable degradation of the hysteretic behavior throughout the loading protocol (Figure 4.8 (k)). The minimum plastic moment capacity was calculated as 1431 k-in., while the expected value based on the actual yield strength was 1908 k-in. The beam member reached a maximum moment of 1884 k-in. during cycling that occurred at 0.018 rad. (Figure 4.19 (a)). This resulted in a moment capacity that was higher than the minimum with $M_{max}/(M_p)_{min}$ equal to 1.32 and an $M_{max}/(M_p)_{exp}$ equal to 0.99 (Figure 4.19 (b)).

During the last cycle, the moment capacity decreased to 570.3 k-in. at 0.068 rad. This corresponded to a 69.7% decrease in the maximum moment capacity at the final cycle. The large amount of degradation was a result of considerable flange and web buckling and the formation of large fractures at the corners of the HSS member (Figure 4.19 (c)).

4.5 Experimental Hysteretic Behavior

The normalized moment-rotation hysteresis of the HSS 8x6x3/8 (Figure 4.12), HSS 10x4x1/4 (Figure 4.15), and HSS 12x6x1/4 (Figure 4.19) are compared because they represent HSS members with increasing *b/t* and *h/t* ratios. The moment was normalized by the experimental plastic moment calculated using the experimental yield strength values. Overall, each section displayed full hysteretic loops indicating significant inelastic behavior and excellent energy dissipation capacity. At higher rotations, the hysteresis plots showed a decrease in moment capacity both with increasing rotation and during consecutive cycles to the same rotation level. Of all sections tested, the HSS 8x8x3/8 had the largest moment capacity, 1988 k-in., while the HSS 8x4x1/4 had the lowest moment capacity, 772 k-in. Additionally, the rotation at which the maximum moments were measured spanned between 0.017 rad. for the HSS 10x8x1/4 and 0.035 rad. for the HSS 8x6x3/8. In general, sections with thicknesses of 3/8 in. tended to show higher normalized maximum moments and higher rotations at maximum moment than the 1/4 in. thick specimens.

For the three mentioned sections the change in shape of the hysteresis plots due to varying amounts of localized buckling and degradation was considered. The HSS 8x6x3/8 had a full hysteresis curve (Figure 4.12 (b)) with only a minor decrease in moment capacity at large rotation levels and reached a maximum moment of 1796 k-in. at 0.035 rad. The section only lost 9.8% of its maximum moment at 0.054 rad., which corresponded to the smallest amount of moment degradation out of the three specimens.

Visual inspection was consistent with the hysteretic behavior, where only minor bulging in the flanges and full development of the plastic hinge region was visible. The maximum rotation reached with the HSS 8x6x3/8 specimen was lower than the others (Figure 4.12) due to a larger amount of rigid body rotation (Figure 4.8 (d)) and limitations associated with the test setup.

Figure 4.15 (b) shows the hysteresis curve for the HSS 10x4x1/4 specimen. This section experienced only a minor decrease in moment capacity up to rotations of approximately 0.04 rad. and attained a maximum moment of 1370 k-in. at 0.031 rad. Upon reacing the final cycle at 0.070 rad., the HSS 10x4x1/4 lost 60% of its maximum moment strength. A moderate amount of buckling in the flanges and web was seen at large rotations and fracture initiated at the corners of the cross-section and propagated through the flanges (Figure 4.15 (c)). This resulted in the observed decrease in hysteretic area during later cycles.

Considering the HSS 12x6x1/4 (Figure 4.19), the effect of significant local buckling on the hysteretic behavior was evident. The section reached a maximum moment of 1884 k-in. at 0.021 rad. and quickly degraded in moment capacity losing 68% of its maximum moment capacity at its final cycle to 0.072 rad. This corresponded to the highest amount of degradation seen for all tested sections. The HSS 12x6x1/4 member had a large decrease in moment strength due to early local buckling in the web and flanges with moderate amounts of tearing at the corners during the final test cycles (Figure 4.19 (c)). The moment-rotation results suggested that the amount of degradation could be partially attributed to the thickness of the walls as thicker walled specimens showed less moment degradation with cycling. The values of the width-thickness, *b/t*, and depth-thickness, *h/t*, ratios also correlated with the amount of buckling. Of the three HSS examined, HSS 8x6x3/8 (*b/t*=14.2, *h/t*=19.9), HSS 10x4x1/4 (*b/t*=14.2, *h/t*=39.9), and HSS 12x6x1/4 (*b/t*=22.8, *h/t*=48.5), it was clear that higher *b/t* and *h/t* ratios led to increased amounts of moment degradation.

Normalized moment-rotation backbone curves were created to further compare the hysteretic behavior of all tested sections. The normalized moment was plotted against the maximum rotation of each cycle (Figure 4.20). All sections showed good symmetry with respect to positive and negative loading indicating stable behavior in both directions.

Sections which were 3/8 in. thick experienced a smaller decreases in moment strength during later cycles. It was also observed that the 1/4 in. thick specimens with the same depth had similar moment capacities during their final cycles. This can partially be attributed to local buckling controlling the behavior at large rotation levels. Additionally as depth increased, the decrease in the moment capacity increased with continued cycling. All 8 in. deep sections showed smaller amounts of degradation than either the 10 in. or 12 in. deep sections. With respect to the widths of the sections, the HSS 10x4x1/4 maintained its maximum moment capacity for several cycles, while the HSS 10x6x1/4 maintained its moment capacity for only one cycle prior to decreasing with subsequent cycles. Furthermore, the HSS 10x8x1/4 reached its maximum moment and during the following cycle the section began losing moment capacity.

The backbone curves (Figure 4.20) showed that not all sections reach maximum moments greater than the experimental plastic moment capacity. Further comparison of the maximum moments and plastic moment capacity is provided in Table 4.3 which includes the $M_{max}/(M_p)_{min}$ ratio and the $M_{max}/(M_p)_{exp}$ ratio, where M_{max} is the overall maximum moment measured during testing, $(M_p)_{min}$ is the theoretical plastic moment capacity, and $(M_p)_{exp}$ is the experimental plastic moment capacity. The average value of $M_{max}/(M_p)_{min}$ for all tested HSS was 1.39. This increased moment capacity compared to the minimum plastic moment capacity stemmed from the fact that the measured yield strength of the coupon specimen taken from the wall of an HSS was greater than the specified minimum, cold working at the corners of HSS members increased the local yield strength, and strain hardening was ignored in calculating the minimum plastic moment capacity. Considering the actual yield strength of the coupons taken from the flats of the HSS, the $M_{max}/(M_p)_{exp}$ ratio was found to be lower than the $M_{max}/(M_p)_{min}$ ratio for each specimen. The $M_{max}/(M_p)_{exp}$ ratios ranged between 0.90 and 1.28 suggesting that buckling occurred prior to yielding in sections with values less than unity.

In general, the experimental hysteretic behavior showed that HSS members have the ability to develop full hysteretic. The ability to maintain the maximum moment at large rotations was shown to be dependent on the member thickness, the width and depth, and the width-thickness and depth-thickness ratios. It also was clear that the degradation of the moment capacity must be considered for seismic applications.

4.6 Cycling Effects

In order to consider HSS members for cyclic bending applications, such as seismic moment frame systems, these members must be able to form stable plastic hinges with consistent moment capacity and adequate ductility under repeated cycling. The general hysteretic behavior obtained from the eleven tested HSS combined with past studies by Wilkinson and Hancock (1998, 2002) suggests that the width-thickness, *b/t*, and depth-thickness, *h/t*, ratios are key parameters in determining which sections will provide adequate plastic hinging behavior under cyclic bending. Current design specifications (AISC 2010a) provide *b/t* and *h/t* limits for axial compression and flexure of non-seismic members. Axial and compression flange *b/t* and *h/t* limits also have been established for seismic applications of HSS, focusing mainly on braced frame systems (AISC 2010b). These values were developed based on the importance of preventing local buckling in HSS bracing members under cyclic axial loads (Liu and Goel 1988, Sherman 1995). A better understanding in regards to the effect of the *b/t* and *h/t* ratios on the cyclic bending behavior of HSS members is needed, particularly in regards to possible decreases in moment capacity, rotation capacity, secant stiffness, and energy dissipation with continued cycling to identify limiting parameters associated with the use of HSS in cyclic bending applications.

4.6.1 Moment Capacity Degradation Behavior

The hysteretic behavior of the eleven tested sections along with the backbone curves for all of the specimens (Figure 4.20) clearly showed that the moment capacity decreased significantly with continued cycling in some of the HSS members. This decrease could be attributed to the onset of buckling, which was more prevalent in sections with higher *b/t* and *h/t* ratios. All three of the 3/8 in. thick HSS demonstrated very stable behavior with only minimal decrease in their measured moment at the maximum cycle rotation with continually larger rotation levels. Considering the backbone curve results of the three 3/8 in. thick specimens, the HSS 8x8x3/8 specimen underwent the largest decrease in moment capacity. The measured moment at the peak of the 0.030 rad. cycle was 1988 k-in. and the moment at the peak of the 0.048 rad. cycle was 1729 k-in., which corresponded to an overall decrease in moment of only 13%. These thicker specimens all had *h/t* ratios equal to 19.9 and *b/t* ratios less than or equal to 19.9.

By comparison, the specimens with 10 in. and 12 in. depths whose *h/t* ratios were 39.9 and 48.5, respectively, demonstrated the largest decrease in moment measured at maximum rotation during cycling to higher rotation levels. The HSS 10x8x1/4 specimen’s largest moment, 1593 k-in., occurred during the 0.018 rad. cycle and decreased by 58% to 678 k-in. by the 0.068 rad. cycle. An even larger decrease was seen for the HSS 12x6x1/4 specimen over the same cycles as was discussed previously. Although the larger percent decrease in moment capacity compared to the 3/8 in. specimens was partially a result of reaching larger rotation levels, there also was a clear trend with respect to the *b/t* and *h/t* ratios where larger values led to earlier and more prevalent buckling behavior and a greater loss in bending strength.

Along with cycling to increased rotation levels, continued cycling at a single rotation level also resulted in a reduction of the bending strength after yielding had initiated. A larger percent decrease in the moment between the first and second cycle was seen for specimens with larger *b/t* and *h/t* ratios. This percent decrease in moment due to cycling at a given rotation level remained below 5% throughout the full loading for all of the 3/8 in. thick specimens, while for the HSS 10x8x1/4 specimen it ranged between 10% and 15% and for the HSS 12x6x1/4 specimen decreases as much as 19% were observed.

The effects of *b/t* and *h/t* can also be quantified by considering the degradation of the moment capacity between the overall maximum moment achieved by a specimen and the moment measured at the peak of the 0.04 rad. cycle. The 0.04 rad. cycle was chosen because current seismic design requirements for special moment resisting frame (SMF) systems necessitate that connections maintain a specified percentage of their maximum strength out to 0.04 rad. to ensure proper ductility under seismic loads (AISC 2010b). For such a connection, the majority of the deformation behavior occurs in the beam member, but in general the rotation of the beam would actually be less than 0.04 rad. as a result of panel zone and columns deformations and accounting for the depth of the column making the use of 0.04 rad. a conservative estimate.

Past studies suggested that *b/t* and *h/t* were not necessarily independent of each other (Wilkinson and Hancock 1998). To better consider the interaction between the width-thickness and depth-thickness ratios with respect to the degradation of the moment capacity, a multiple linear regression analysis was performed. Figure 4.21 provides contour lines representing the percent (in decimal form) decrease in moment from the overall measured maximum to the moment measured at the peak of the 0.04 rad. cycle with respect to both *h/t* and *b/t*. The HSS 8x4x3/8 specimen was included in the regression analysis, but was omitted from the plot because the degradation of the moment capacity at 0.04 rad. was below 5%.

The contour plots suggest that the moment degradation increases more rapidly with an increase in *b/t* as compared to an increase in *h/t* because the flanges contribute the most to the moment capacity. However, the nature of the 20%, 25%, and 30% moment degradation contour lines did suggest a clear interaction between the *b/t* and *h/t* parameters. At lower *h/t* and *b/t* values, the degradation decreased below 10% and the contour lines no longer remained linear, suggesting that the interdependence between *b/t* and *h/t* was less significant. The almost vertical portion of the 5% and 10% contours further suggest that when an HSS had a low *b/t* ratio, the *h/t* ratio could be any value less than 30 without causing a shift in the moment degradation. Thus, sections with low *h/t* ratios were more dependent on the flange behavior during bending. In general, Figure 4.21 provides a means of estimating the expected moment degradation with respect to the *b/t* and *h/t* ratios. The 20% degradation contour line provides a good limit for determining if an HSS will exhibit stable plastic hinging under cyclic bending loads.

4.6.2 Rotation Capacity

While knowledge of the degradation of the maximum moment based on the *b/t* and *h/t* ratios is useful for understanding change in moment capacity at have rotations, the rotation level that can be achieved during cycling while still maintaining a specified percentage of the maximum moment provides a good estimate of the stability of the plastic hinge and the ductility of the section under cyclic bending. AISC seismic specifications require that moment connections for special moment frames maintain 80% of their maximum moment at 0.04 rad. where the majority of the inelastic behavior occurs in the beam member through the formation of a plastic hinge (AISC 2010b). For this reason, it is important to establish how the *b/t* and *h/t* ratios affect the rotation capacity of an HSS member in cyclic bending. Figure 4.22 and Figure 4.23 provide contour plots of the rotation capacity of an HSS beam member obtained through multiple linear regression analysis to account for the interaction between the *b/t* and *h/t* ratios. The rotation capacity for the contour plot in Figure 4.22 corresponds to the current AISC requirement for a special moment frame connection and is taken as the maximum rotation cycle in which 80% of the maximum moment was achieved. For Figure 4.23, a stricter definition of the rotation capacity is used to establish *b/t* and *h/t* requirements that further ensure stable plastic hinging behavior. In this case, the rotation capacity is defined as the maximum rotation cycle at which 90% of the maximum moment was achieved.

The contour lines in Figure 4.22 suggest that all eleven specimens were able to maintain 80% of their maximum moment strength when cycled to between 0.03 and 0.035 rad. Four of the members maintained 80% of their maximum moment even when cycled past 0.05 rad., which was consistent with their very stable hysteretic behavior out to large rotation levels. Three of these four members, HSS 8x4x3/8, HSS 8x6x3/8, and HSS 8x8x3/8 that have *b/t* ratios of 8.46, 14.2, and 19.9 and *h/t* ratios of 19.9, never demonstrated degradation in moment capacity below 80% of their maximum value. The smaller *b/t* and *h/t* ratios clearly led to more stable behavior under cyclic loading. The linear nature of the contour plots for all rotation levels further suggest that the *b/t* and *h/t* ratios had equal influence on the rotation capacity. However, the rotation capacity was more tolerant of an increase in depth-thickness than width-thickness, suggesting that buckling of the flange had more influence on the behavior than buckling of the web. A linear equation (Equation 4.1) was established for the cyclically tested HSS beams to determine which specimens will have adequate plastic hinge stability for use in cyclic seismic bending applications. The formulation provides the maximum usable *h/t* value given *b/t* to ensure that the moment strength remains 80% of its maximum overall measured moment at a rotation level of 0.04 rad.

$$\frac{h}{t} < 66 - 1.37 * \frac{b}{t} \text{ for } 14 \leq \frac{\mathrm{b}}{\mathrm{t}} \leq 26 \qquad \text{Equation 4.1}$$

The *b/t* ratio is limited to between 14 and 26 to fit within the extent of the experimental data. These ratios should lead to adequate ductility in the beam member during cyclic inelastic loading.

Under the more stringent definition for rotation capacity, Figure 4.23, all eleven specimens achieved 90% of their maximum moment capacity only up to cycling between 0.025 and 0.03 rad. However, the HSS 8x4x3/8 (*b/t* = 8.46, *h/t* = 19.9) and the HSS 8x6x3/8 (*b/t* = 14.2, *h/t* = 19.9) did reach their maximum drift levels, 0.06 and 0.056 rad., while maintaining a bending strength greater than 90% of their maximum moment capacity. The contour plots in Figure 4.23 did not show the same linear behavior between *b/t* and *h/t* as was seen for the less stringent definition of rotation capacity. This required a piecewise function (Equation 4.2 and Equation 4.3) to be established to determine the maximum usable *h/t* ratio given a *b/t* ratio, that ensured 90% of the maximum moment capacity remained at beam rotation levels of 0.04 rad.

$$\frac{h}{t} < 55 - 1.05 * \frac{b}{t} \text{ for } 14 \leq \frac{\mathrm{b}}{\mathrm{t}} \leq 22 \qquad \text{Equation 4.2}$$

$$\frac{h}{t} < 67.1 - 1.6 * \frac{b}{t} \text{ for } 22 \leq \frac{\mathrm{b}}{\mathrm{t}} \leq 26 \qquad \text{Equation 4.3}$$

The piecewise function suggests that for *b/t* ratios less than 22, the influence of increasing *h/t* on the rotation capacity was less than when *b/t* was greater than 22. Also, smaller *h/t* ratios were required for a given *b/t* ratio in order to meet the more stringent rotation capacity than were observed in Figure 4.22. In general, both sets of contour plots provide guidelines for the selection of HSS for seismic bending applications and suggest that stable plastic hinging can be obtained provided members have appropriate *b/t* and *h/t* ratios.

4.6.3 Secant Stiffness

Change in secant stiffness with continued cycling was also influenced by the width-thickness and depth-thickness ratios. The secant stiffness was calculated for a given cycle as the load at maximum displacement divided by the maximum displacement. Figure 4.24 provides a comparison of the secant stiffness of the HSS 8x6x3/8, HSS 10x4x1/4, and

HSS 12x6x1/4 specimens measured during the first positive cycle at each rotation level following initial yielding. These specimens represented low, mid-range, and high *b/t* and *h/t* ratios with respect to all specimens tested. Of the three sections plotted, the HSS 12x6x1/4 displayed the largest secant stiffness of 35.4 k/in. at 0.008 rad., while the HSS 10x4x1/4 showed the lowest overall maximum secant stiffness of 20.4 k/in. at 0.009 rad. Although not shown, the HSS 8x4x1/4 had the smallest maximum secant stiffness of 12.9 k/in. at 0.009 rad.

All three of the specimens plotted experienced a decrease in secant stiffness at larger rotation cycles. The largest of these decreases was the HSS 12x6x1/4 specimen whose secant stiffness dropped by 33 k/in. at the 0.072 rad. rotation cycle from its maximum value. Both the HSS 8x6x3/8 and HSS 10x4x1/4 showed relatively stable secant stiffness degradation with the HSS 8x6x3/8 losing 15.8 k/in. at the 0.054 rad. cycle from its maximum secant stiffness and the HSS 10x4x1/4 losing 16.3 k/in. from its maximum stiffness by the 0.058 rad. cycle. This could be attributed to the low initial secant stiffness of the HSS 10x4x1/4 and the stable moment rotation behavior of the HSS 8x6x3/8. Of the eleven tested sections, the HSS 8x4x3/8 had the lowest amount of degradation due to its low *b/t* and *h/t* ratios and the HSS 10x8x1/4 had the largest decrease in secant stiffness attributed to high *b/t* and *h/t* ratios. In general, it was observed that HSS with higher *b/t* ratios tended to show more secant stiffness degradation with continued cycling. This indicated that secant stiffness was more dependent on flange buckling. As is demonstrated in Figure 4.24, all specimens tended to converge on the same secant stiffness value at the end of cycling no matter what their maximum secant stiffness reached, except for the 3/8 in. thick specimens which tended to have slightly larger secant stiffness values at the end of cycling.

4.6.4 Energy Dissipation

Equivalent viscous damping provides a measure of the energy dissipation capacity. Consideration of the equivalent viscous damping was important to further understanding the stability of the hysteretic behavior and the ability to dissipate energy through significant inelastic deformation in the plastic hinge region. Figure 4.25 provides plots of the equivalent viscous damping for the HSS 8x6x3/8, HSS 10x4x1/4 and HSS 12x6x1/4 specimens with respect to maximum cycle rotation. Cycling of the HSS 8x6x3/8 resulted in the lowest maximum value for equivalent viscous damping of 36% at 0.053 rad. Throughout its loading history, the equivalent viscous damping for this section remained below that of the HSS 10x4x1/4 and HSS 12x6x1/4. Both the HSS 10x4x1/4 and HSS 12x6x1/4 reached similar maximum values of 47% and 45% equivalent viscous damping, respectively. A degradation of the equivalent viscous damping was also observed for the HSS 12x6x1/4 specimen as a result of the onset of local buckling in the flange and web during later cycles.

Considering all of the tested specimens, the HSS 8x4x1/4 displayed the highest equivalent viscous damping, 50%, while the HSS 8x4x3/8 displayed the lowest equivalent viscous damping, 33%. Meanwhile, only the HSS 10x8x1/4, HSS 12x4x1/4, and HSS 12x6x1/4 saw degradation in equivalent viscous damping at later cycles. These results indicated that sections with higher *b/t* and *h/t* provided large amounts of damping at low rotations levels, but lose their ability to dissipate energy at large rotations. From the data it can be concluded that thicker sections with small *b/t* and *h/t* ratios tended to have lower equivalent viscous damping, but were more stable at large rotations.

4.6.5 Plastic Hinge Development

Characterization of the strain distribution along the flanges allowed for an understanding of the propagation of yielding along the length of the member. Strains were measured at distances of 3 in., 9 in., 18 in., and 36 in. from the rigid connection. The strains were considered for the HSS 8x6x3/8, HSS 10x4x1/4, and HSS 12x6x1/4 where the yield strains are 0.0021, 0.0023, and 0.0021, respectively, calculated based on the yield strength for each section (Table 4.2). The strains were compared for the at beam rotations of 0.012 rad., 0.035 rad., and 0.055 rad., which represent small, medium, and large rotation levels (Figure 4.26).

At the 0.012 rad. rotation level, the HSS 12x6x1/4 specimen developed the largest strain values. Compression and tension flange yielding occurred out to 9 in. from the fixed end, while the HSS 10x4x1/4 and HSS 8x6x3/8 remained elastic at this rotation level. For the 0.035 rad. rotation cycles, yielding in the flanges had extended to at least 18 in. from the fixed connection in all 3 of the HSS specimens. At the 0.055 rad. rotation level, the effect of the *b/t* and *h/t* ratios on the section became evident. The HSS 8x6x3/8 specimen had larger strains 9 in. from the fixed end than measured during the 0.035 rad. cycle, but the same level of strain at a distance of 18 in. Meanwhile, the strains at 9 in. and 18 in. from the fixed end of the HSS 10x4x1/4 and HSS 12x6x1/4 decreased compared to those measured during the previous cycles. This behavior was associated with the onset of local buckling in the section less than 9 in. from the fixed end where most of the subsequent inelastic deformation was concentrated. The strain analysis indicated that sections with large *h/t* and *b/t* ratios may have trouble developing stable plastic hinges due to the onset of local buckling at larger rotation levels resulting in a concentration of the inelastic behavior close to the fixed connection.

4.7 Conclusions

The objective of this portion of the study was to characterize the cyclic bending behavior of HSS to better define limits for their use in seismic building applications. Currently, limiting parameters for the use of HSS in seismic applications are based on tests conducted under monotonic bending, cyclic bending under large axial loads, or under cyclic axial loads. Eleven standard U.S. HSS members of the same length with width-thickness and depth-thickness ratios varying from 8.46 to 31.3 and 19.9 to 48.5, respectively, were tested experimentally under large inelastic bending cycles to analyze the resulting hysteretic behavior. Cycling effects associated with the degradation of the moment capacity, rotation capacity, secant stiffness, and energy dissipation were observed out to large rotation levels. Strain measurements in the flange also provided insight into the formation of the plastic hinge with increasing rotation. The key conclusions associated with this work are summarized below:

1. All tested HSS specimens produced stable hysteretic behavior during early cycling with moment capacities at least 1.23 times greater than the predicted theoretical plastic moment capacity and 0.90 times the predicted experimental plastic moment capacity. However, large *b/t* and *h/t* ratios led to a decrease in hysteretic area and loss of moment capacity with continued cycling to rotation levels above 0.02 rad.

2. Moderate to large *b/t* and *h/t* ratios led to the onset of local buckling in the plastic hinge region. Continued deformation after buckling also led to fatigue induced fracture at the corner of the HSS members that propagated across the face of the flange with increased cycling.
3. The three 3/8 in. thick specimens clearly showed the most stable behavior with very little degradation in their moment capacity. The maximum decrease in moment capacity was less than 15%.
4. Contour plots for predicting the degradation of the moment capacity between maximum moment and the moment measured at the peak of the 0.04 rad. rotation cycle provided a good estimate of limiting width-thickness and depth-thickness ratios and take into account the observed interaction between these two parameters.
5. Larger width-thickness ratios led to a more significant decrease in the moment capacity and rotation capacity due to the importance of the flange in resisting cyclic bending loads. The results suggest that *b/t* ratios below 25 and *h/t* ratios below 40 are necessary to maintain 90% of the maximum moment at rotations of 0.04 rad.
6. All specimens converged to a similar secant stiffness value of approximately 2.3 k/in. at their maximum rotation levels. However, the 3/8 in. thick specimens, on average, converged to a slightly higher value, 8.2 kip/in.
7. The full-scale cyclic bending tests demonstrated that HSS are viable for use in cyclic bending applications. Stable plastic hinging behavior can be obtained provided that the width-thickness and depth-thickness ratios are adequately chosen to limit local buckling at small rotation levels.

Table 4.1 Experimental HSS specimens

Section (in. x in. x in.)	Wall thickness, *t* (in.)	Area, *A* ($in.^2$)	Width-thickness ratio (*b*/*t*)	Depth-thickness ratio (*h*/*t*)	Plastic section modulus, *Z* ($in.^3$)	Minimum plastic moment capacity, $(M_p)_{min}$ (k-in.)	Expected plastic moment capacity, $(M_p)_{exp}$ (k-in.)
HSS 8x4x1/4	0.233	5.24	14.2	31.3	13.3	611.8	875.2
HSS 8x4x3/8	0.349	7.58	8.46	19.9	18.8	864.8	1172
HSS 8x6x1/4	0.233	6.17	22.8	31.3	16.9	777.4	936.3
HSS 8x6x3/8	0.349	8.97	14.2	19.9	24.1	1109	1460
HSS 8x8x1/4	0.233	7.10	31.3	31.3	20.5	943.0	1258
HSS 8x8x3/8	0.349	10.4	19.9	19.9	29.4	1352	1813
HSS 10x4x1/4	0.233	6.17	14.2	39.9	19.0	874.0	1196
HSS 10x6x1/4	0.233	7.10	22.8	39.9	23.6	1086	1299
HSS 10x8x1/4	0.233	8.03	31.3	39.9	28.1	1293	1658
HSS 12x4x1/4	0.233	7.10	14.2	48.5	25.6	1178	1454
HSS 12x6x1/4	0.233	8.03	22.8	48.5	31.1	1431	1908

Table 4.2 HSS beam specimen material properties

Specimen (in. x in. x in.)	F_y (ksi)	F_u (ksi)
HSS 8x4x1/4	65.81	71.01
HSS 8x4x3/8	62.36	70.7
HSS 8x6x1/4	55.38	68.11
HSS 8x6x3/8	60.59	72.38
HSS 8x8x1/4	61.39	76.74
HSS 8x8x3/8	61.67	69.89
HSS 10x4x1/4	62.95	73.24
HSS 10x6x1/4	55.05	66.32
HSS 10x8x1/4	58.98	71.87
HSS 12x4x1/4	56.75	68.08
HSS 12x6x1/4	61.34	71.23

Table 4.3 Properties of tested HSS beam members

HSS Specimen (in. x in. x in.)	Maximum rotation (rad.)	Maximum moment (k-in.)	$\frac{M_{max}}{(M_P)_{min}}$ -	$\frac{M_{max}}{(M_P)_{exp}}$ -
HSS 8x4x1/4	0.071	772	1.26	0.90
HSS 8x4x3/8	0.060	1481	1.71	1.28
HSS 8x6x1/4	0.066	1007	1.3	1.09
HSS 8x6x3/8	0.056	1796	1.62	1.25
HSS 8x8x1/4	0.069	1245	1.32	0.99
HSS 8x8x3/8	0.051	1988	1.47	1.11
HSS 10x4x1/4	0.072	1370	1.57	1.19
HSS 10x6x1/4	0.071	1343	1.24	1.05
HSS 10x8x1/4	0.068	1593	1.23	0.96
HSS 12x4x1/4	0.076	1509	1.28	1.06
HSS 12x6x1/4	0.072	2884	1.32	0.99

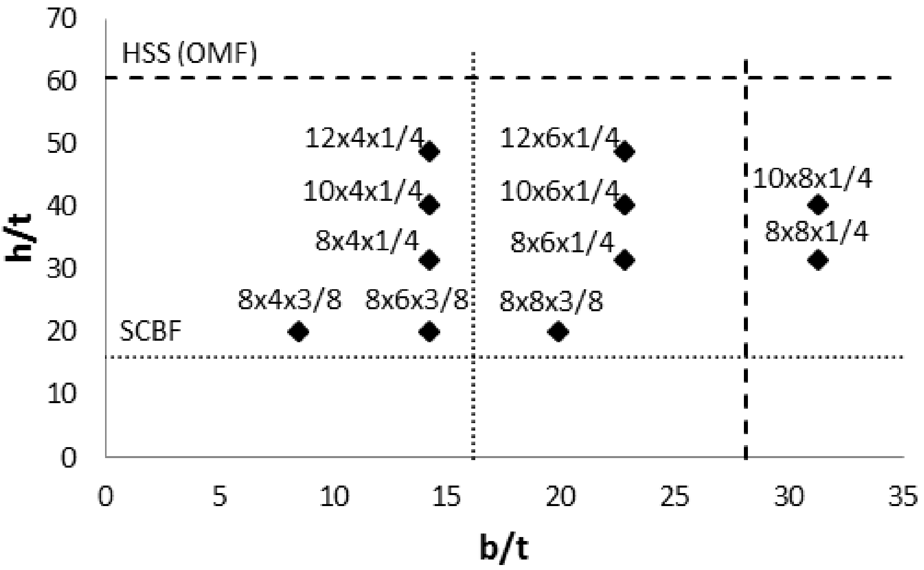

Figure 4.1 Distribution of experimental specimens with respect to *b/t* and *h/t* ratios

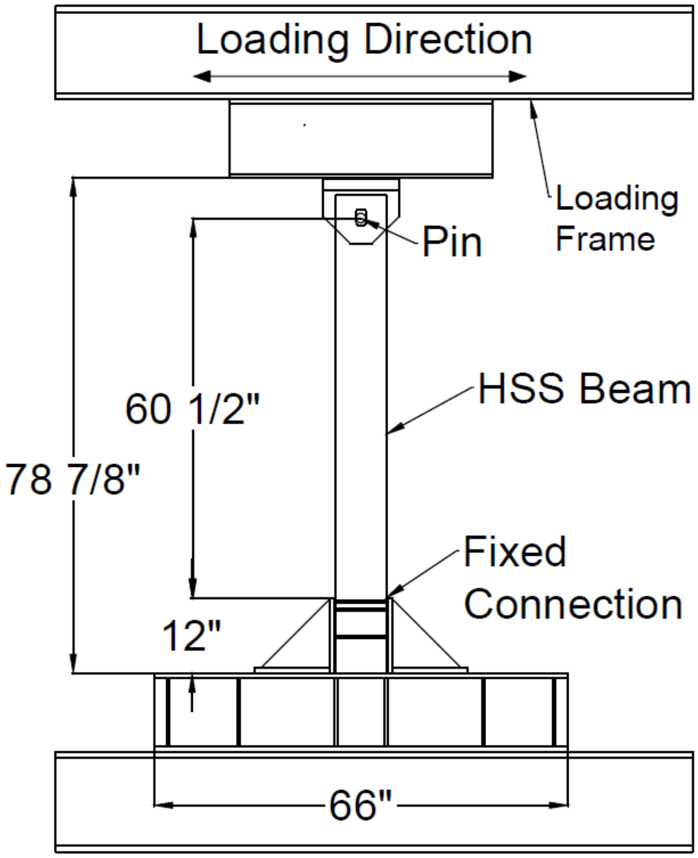

Figure 4.2 HSS beam test setup diagram

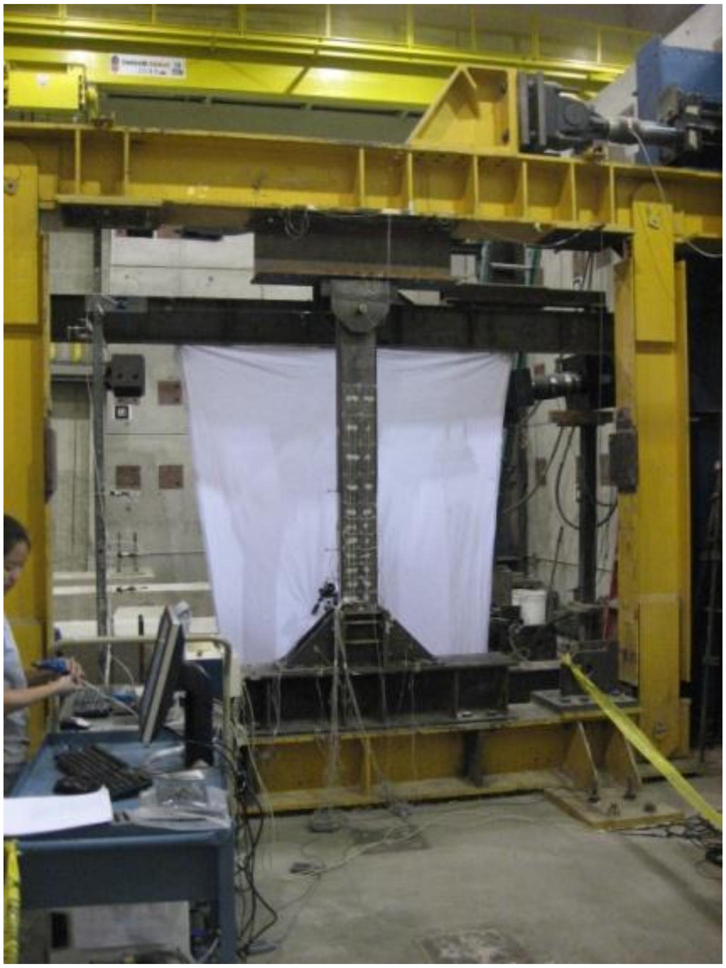

Figure 4.3 Photograph of HSS beam test setup

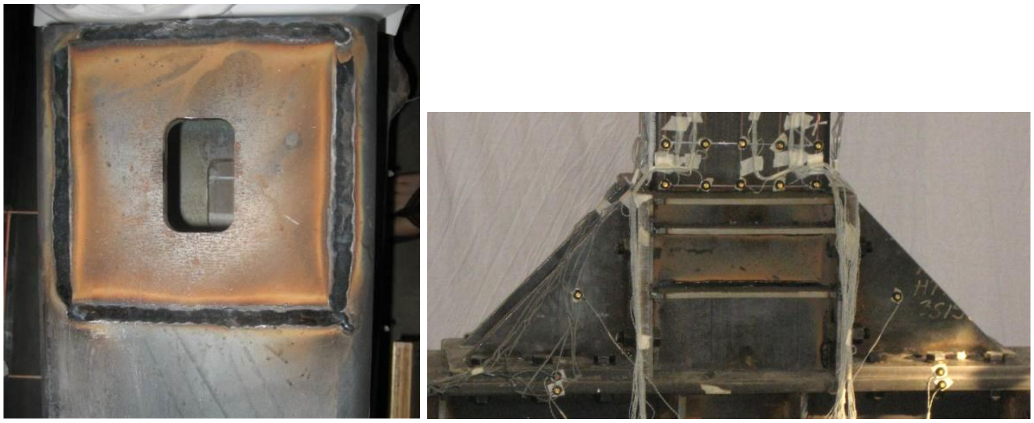

(a) (b)

Figure 4.4 Photograph of (a) slotted pinhole and (b) reusable rigid connections

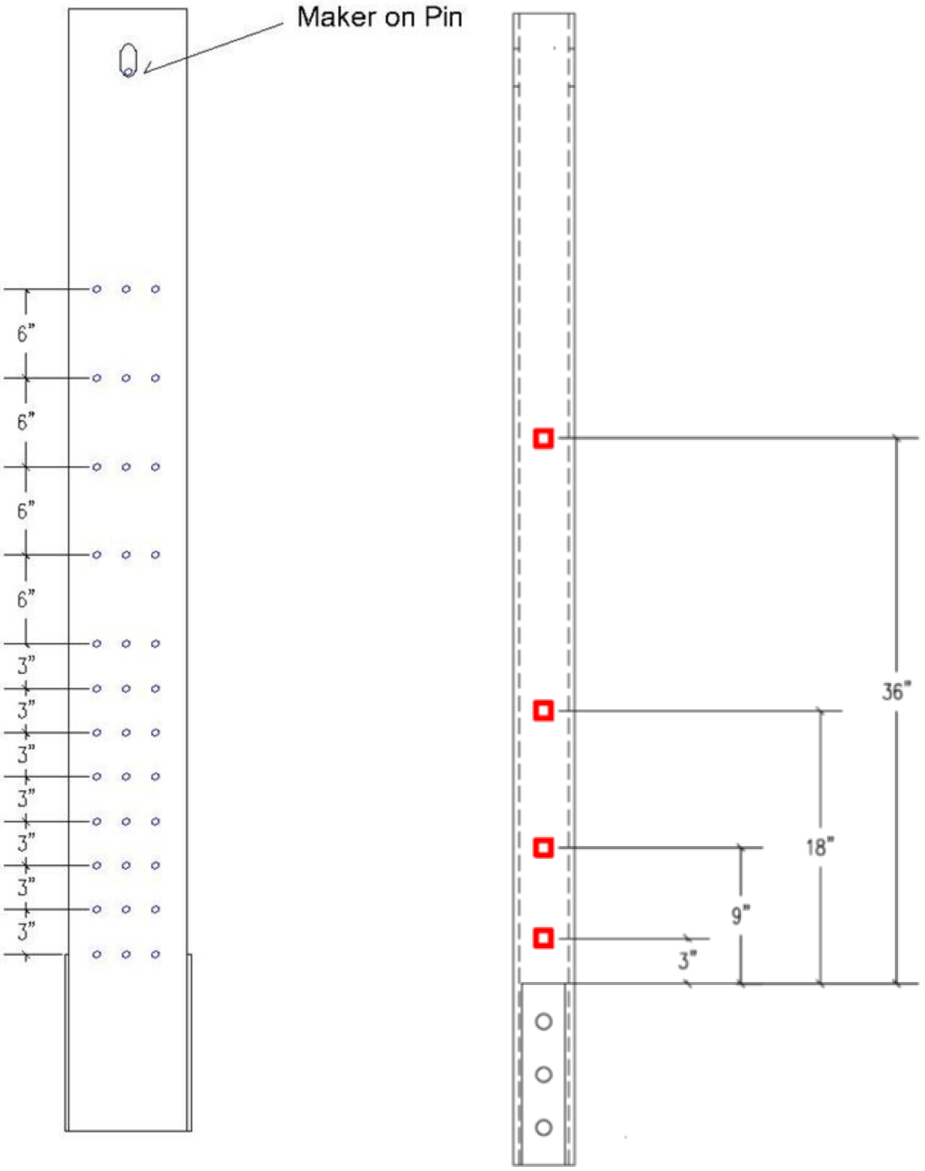

Optotrak

Strain Gages

Figure 4.5 Typical Optotrak marker and strain gage locations on HSS beam specimen

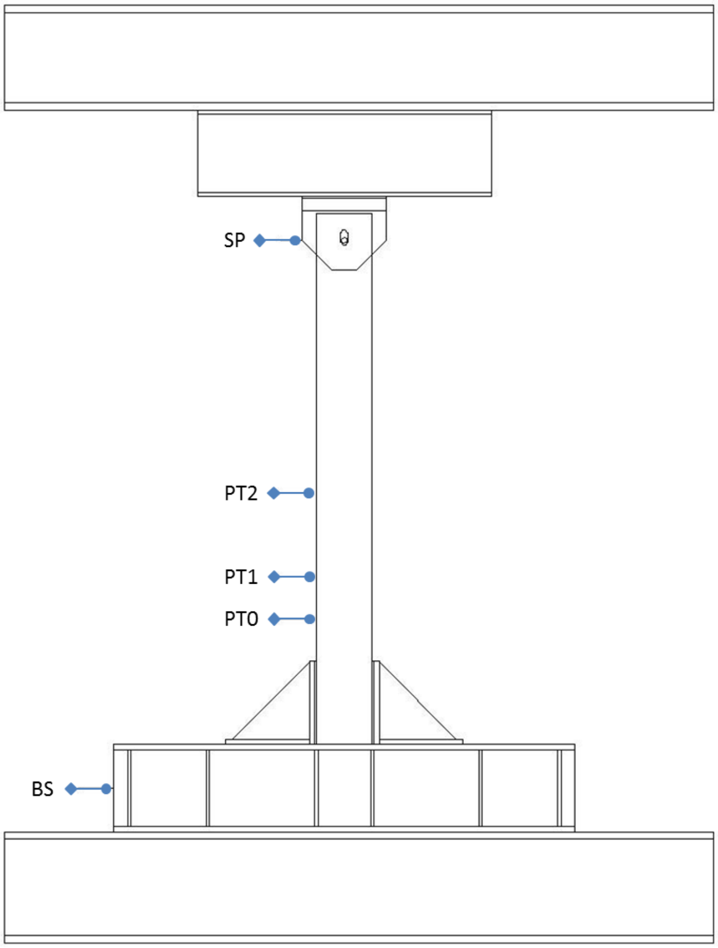

Figure 4.6 HSS beam test setup potentiometer locations

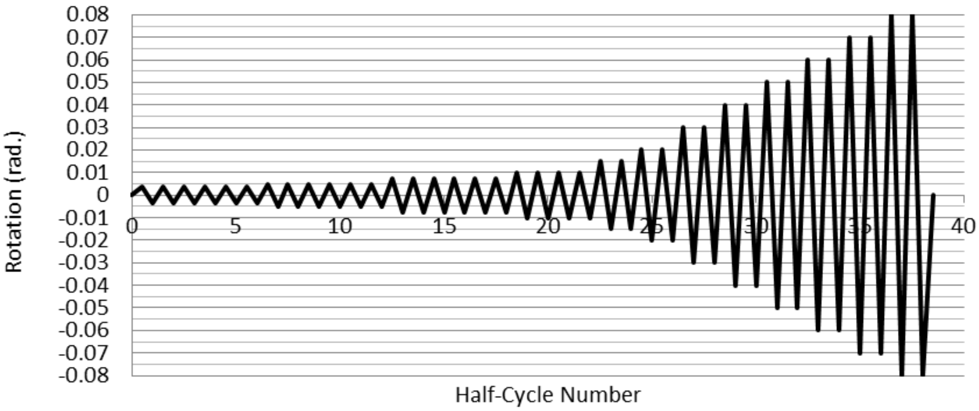

Figure 4.7 Experimental loading protocol

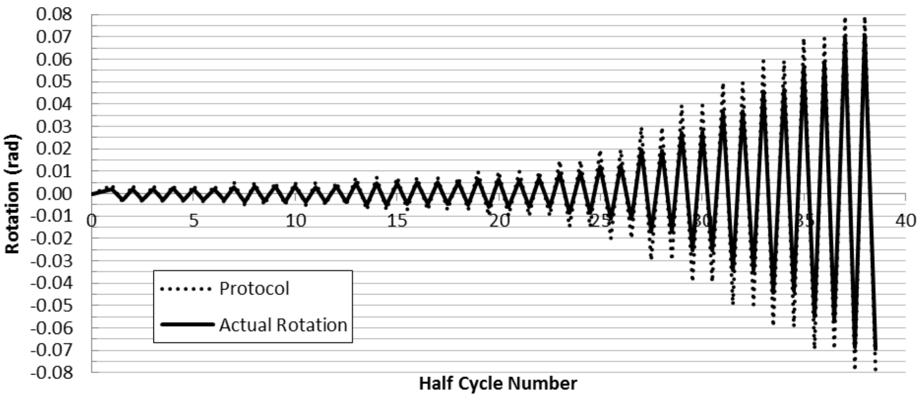

(a) HSS 8x4x1/4

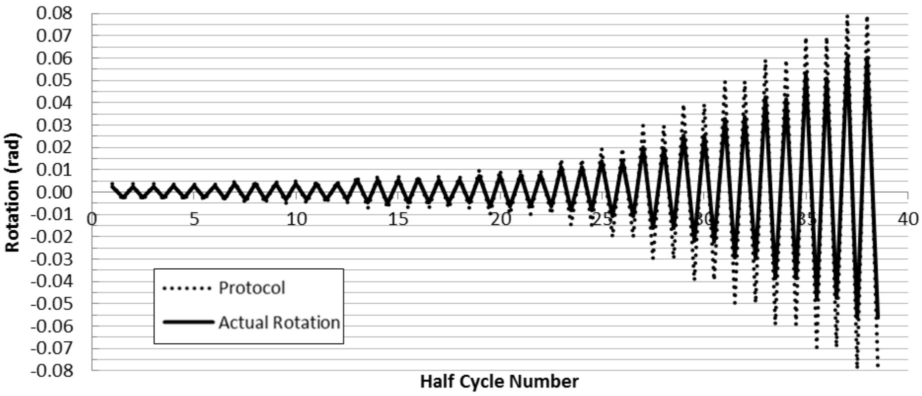

(b) HSS 8x4x3/8

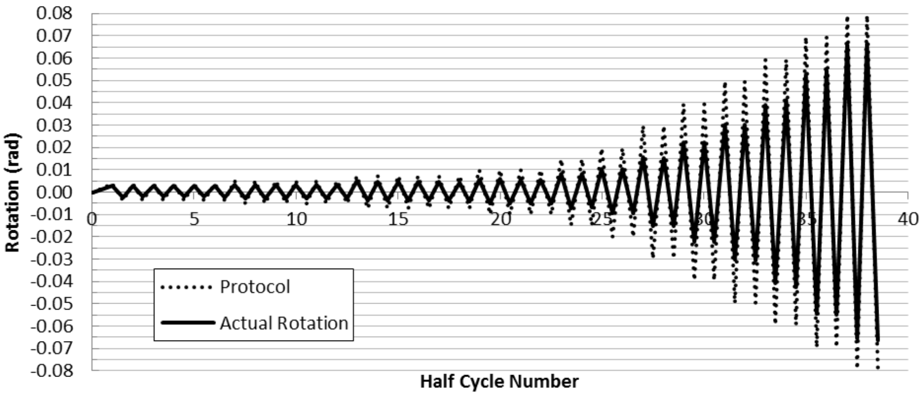

(c) HSS 8x6x1/4

Figure 4.8 Loading protocol with the actual achieved rotation level for the (a) HSS 8x4x1/4, (b) HSS 8x4x3/8, (c) HSS 8x6x1/4, (d) HSS 8x6x3/8, (e) HSS 8x8x1/4, (f) HSS 8x8x3/8, (g) HSS 10x4x1/4, (h) HSS 10x6x1/4, (i) HSS 10x8x1/4, (j) HSS 12x4x1/4, (k) HSS 12x6x1/4

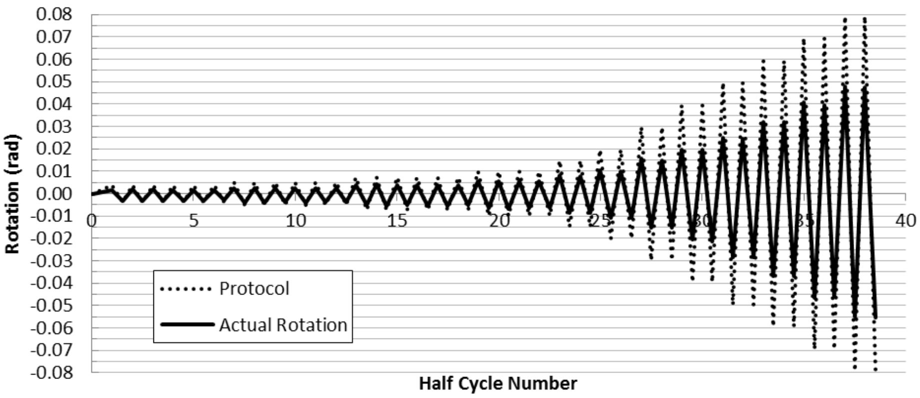

(d) HSS 8x6x3/8

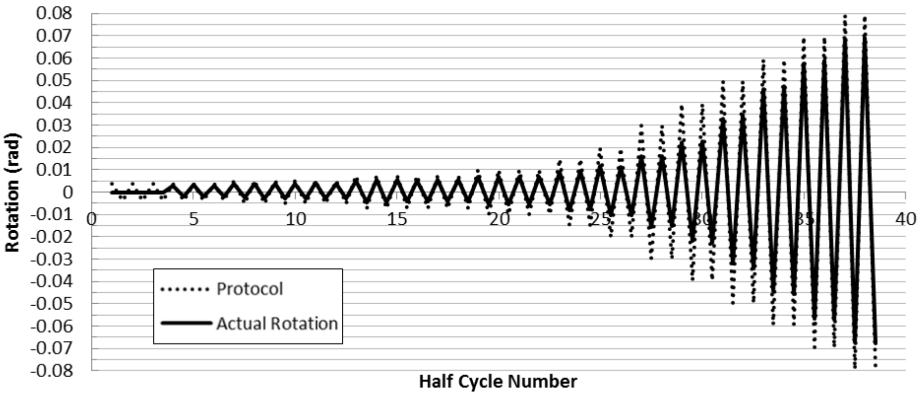

(e) HSS 8x8x1/4

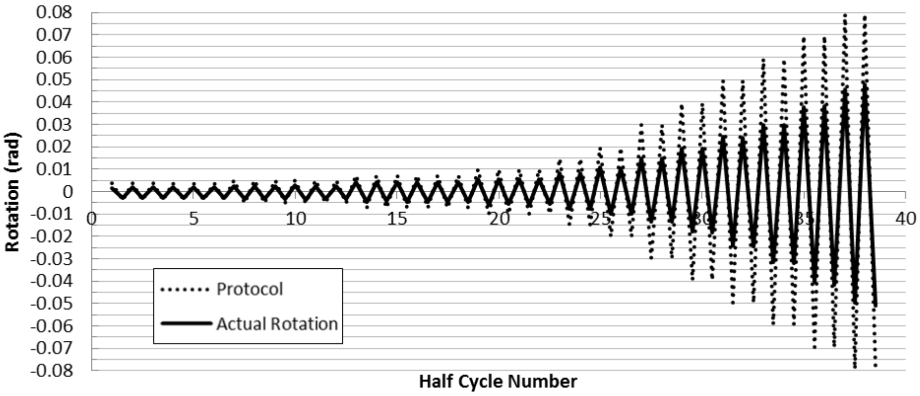

(f) HSS 8x8x3/8

Figure 4.8 (cont.) Loading protocol with the actual achieved rotation level for the (a) HSS 8x4x1/4, (b) HSS 8x4x3/8, (c) HSS 8x6x1/4, (d) HSS 8x6x3/8, (e) HSS 8x8x1/4, (f) HSS 8x8x3/8, (g) HSS 10x4x1/4, (h) HSS 10x6x1/4, (i) HSS 10x8x1/4, (j) HSS 12x4x1/4, (k) HSS 12x6x1/4

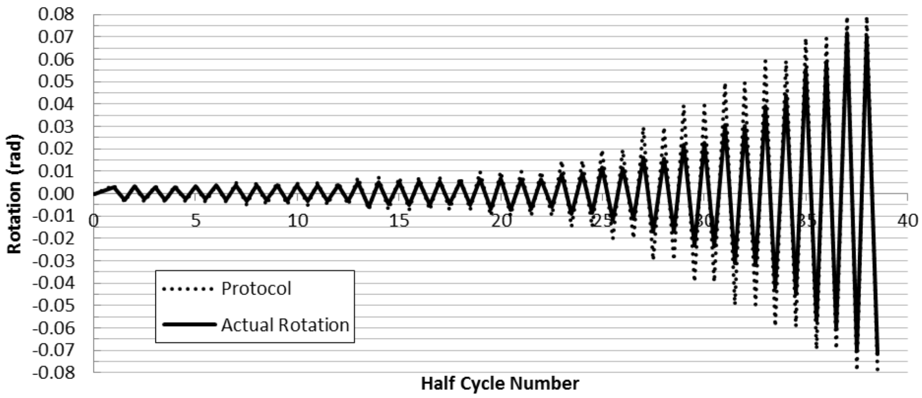

(g) HSS 10x4x1/4

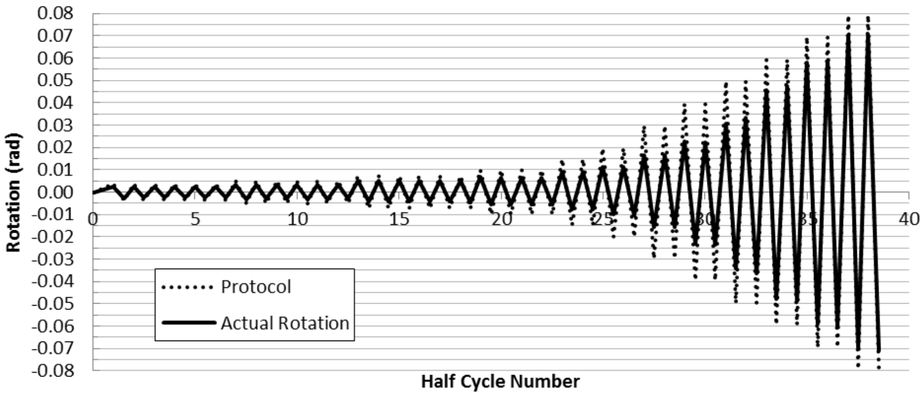

(h) HSS 10x6x1/4

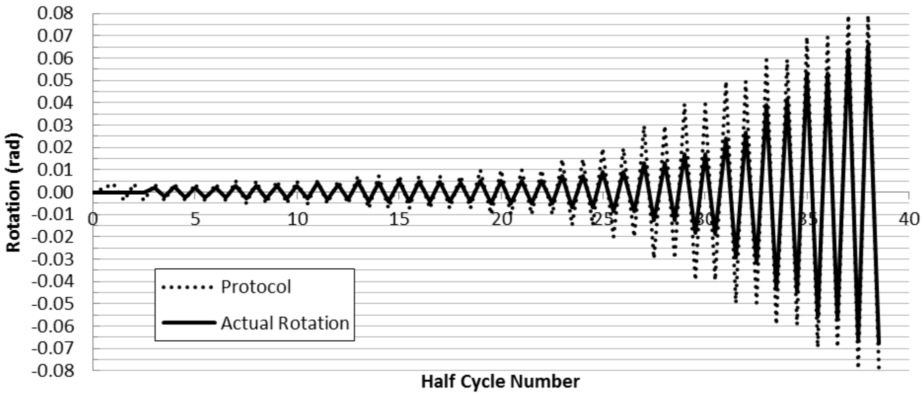

(i) HSS 10x8x1/4

Figure 4.8 (cont.) Loading protocol with the actual achieved rotation level for the (a) HSS 8x4x1/4, (b) HSS 8x4x3/8, (c) HSS 8x6x1/4, (d) HSS 8x6x3/8, (e) HSS 8x8x1/4, (f) HSS 8x8x3/8, (g) HSS 10x4x1/4, (h) HSS 10x6x1/4, (i) HSS 10x8x1/4, (j) HSS 12x4x1/4, (k) HSS 12x6x1/4

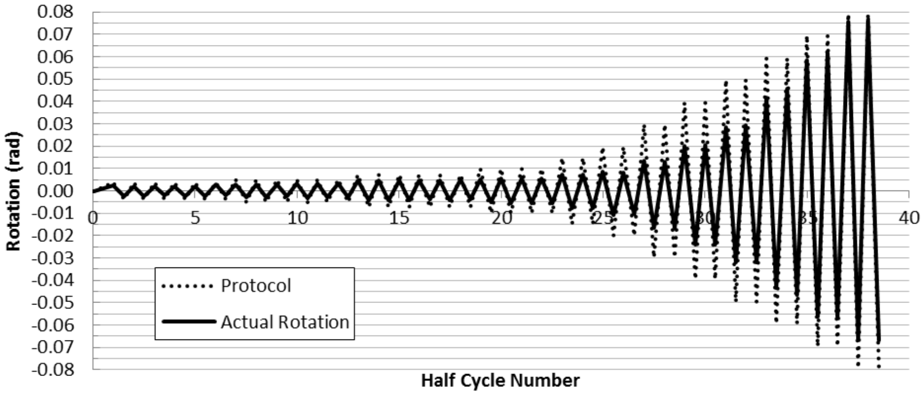

(j) HSS 12x4x1/4

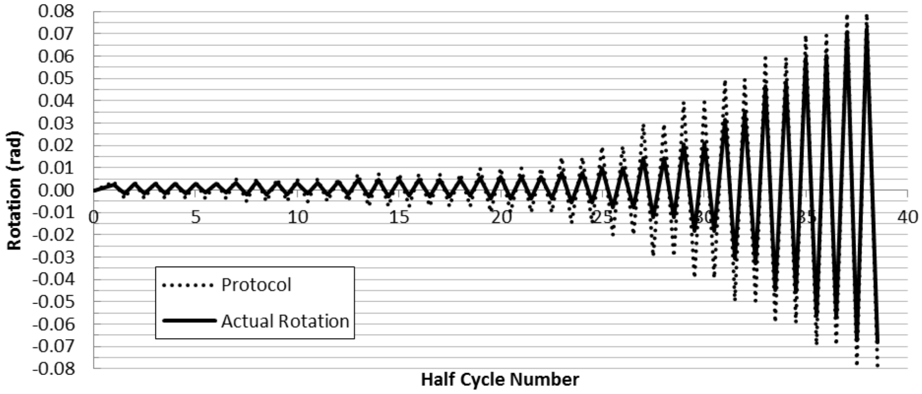

(k) HSS 12x6x1/4

Figure 4.8 (cont.) Loading protocol with the actual achieved rotation level for the (a) HSS 8x4x1/4, (b) HSS 8x4x3/8, (c) HSS 8x6x1/4, (d) HSS 8x6x3/8, (e) HSS 8x8x1/4, (f) HSS 8x8x3/8, (g) HSS 10x4x1/4, (h) HSS 10x6x1/4, (i) HSS 10x8x1/4, (j) HSS 12x4x1/4, (k) HSS 12x6x1/4

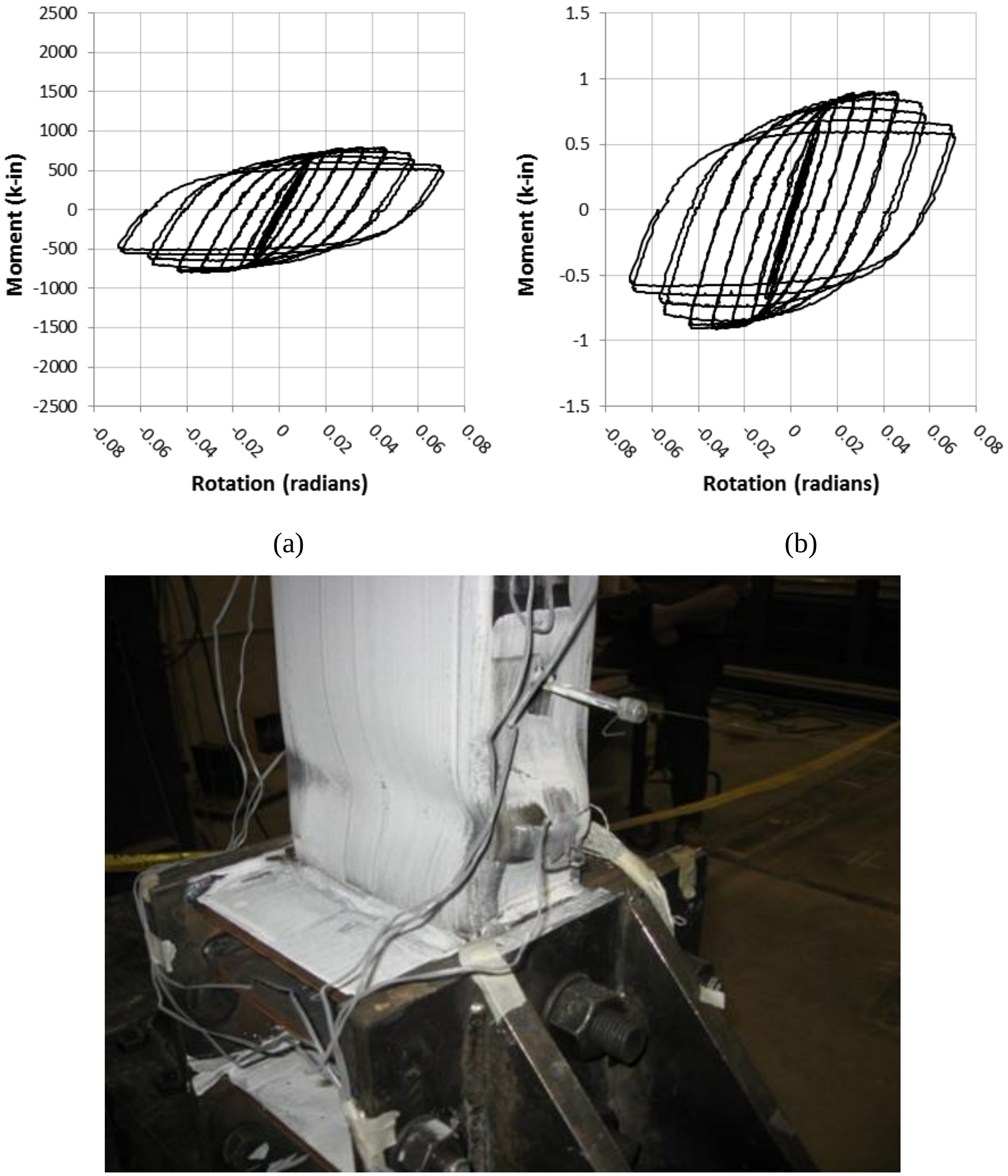

(a) (b)

(c)

Figure 4.9 Plots of the (a) moment-rotation and (b) normalized moment-rotation behavior and a photograph of the (c) plastic hinge region at the completion of testing for the HSS 8x4x1/4.

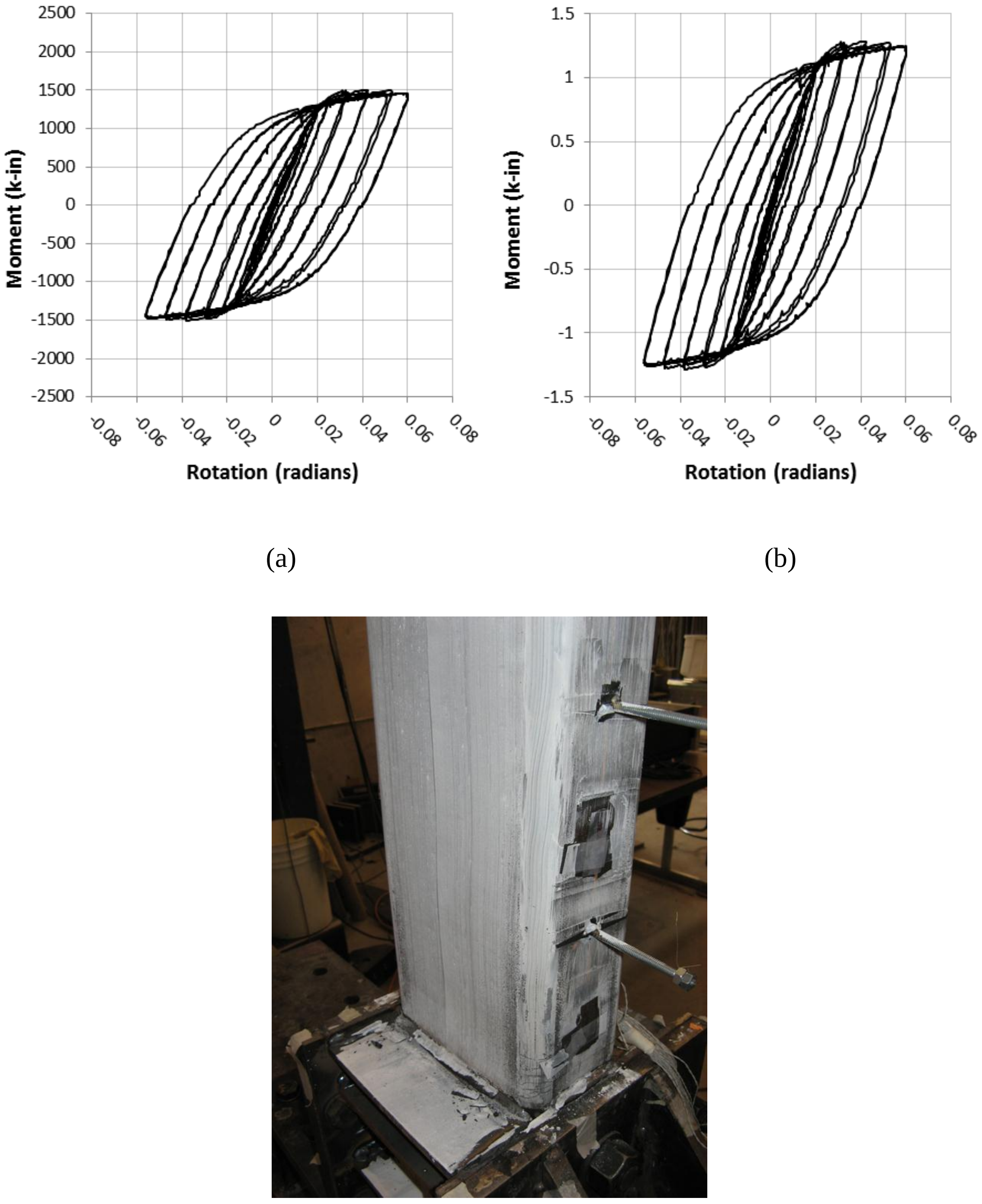

(a)

(b)

(c)

Figure 4.10 Plots of the (a) moment-rotation and (b) normalized moment-rotation behavior and a photograph of the (c) plastic hinge region at the completion of testing for the HSS 8x4x3/8.

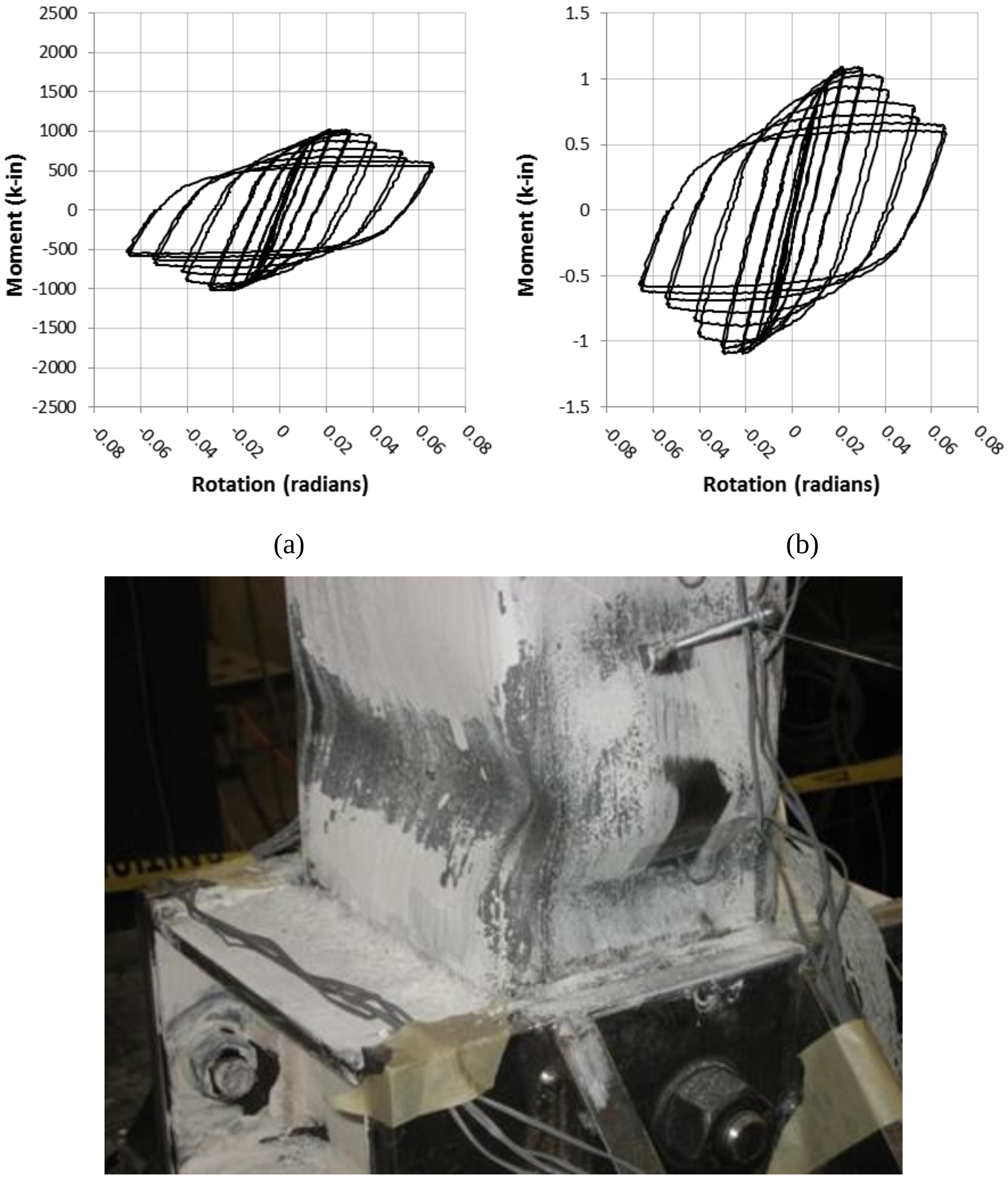

(a)

(b)

(c)

Figure 4.11 Plots of the (a) moment-rotation and (b) normalized moment-rotation behavior and a photograph of the (c) plastic hinge region at the completion of testing for the HSS 8x6x1/4.

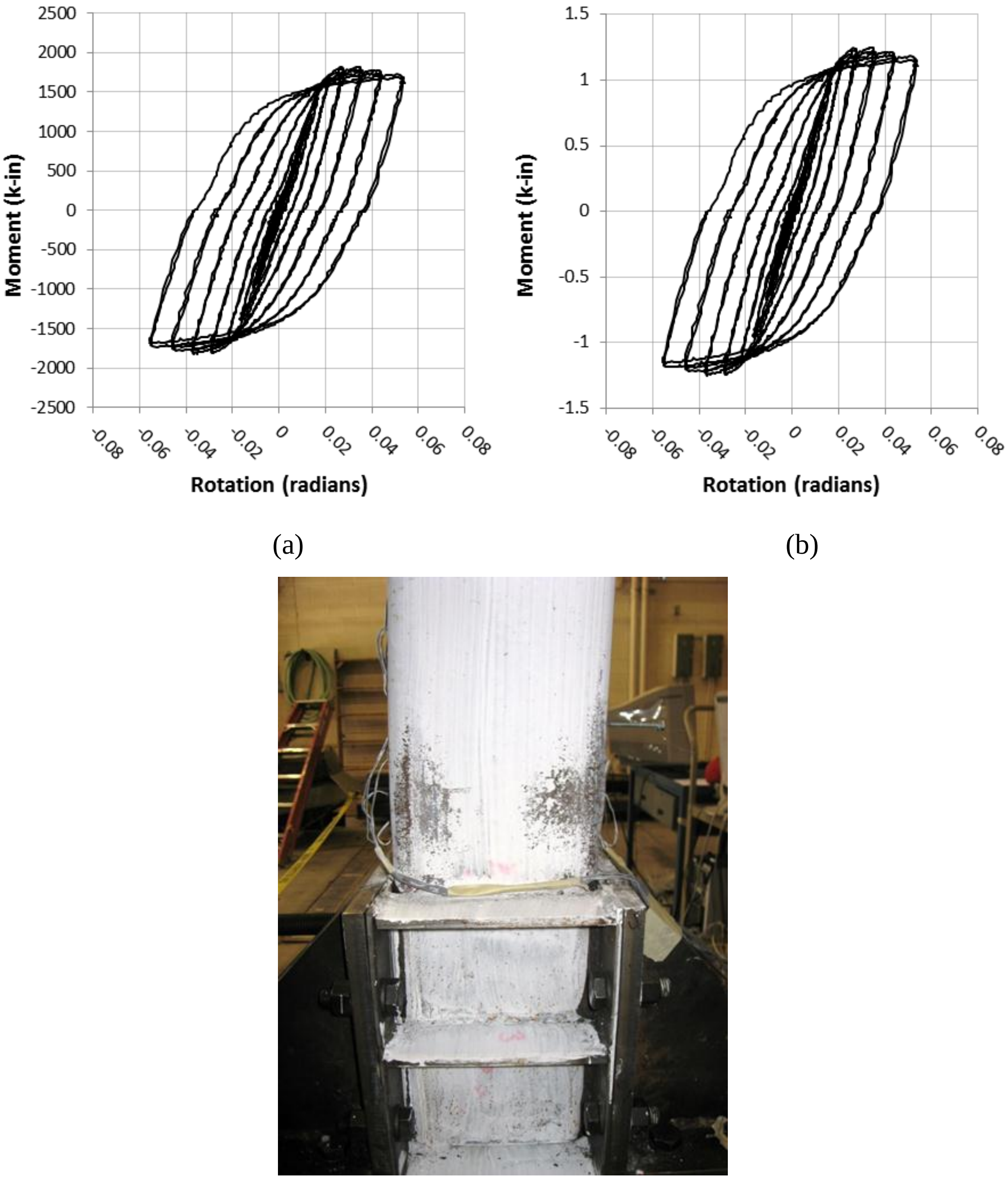

(a)

(b)

(c)

Figure 4.12 Plots of the (a) moment-rotation and (b) normalized moment-rotation behavior and a photograph of the (c) plastic hinge region at the completion of testing for the HSS 8x6x3/8.

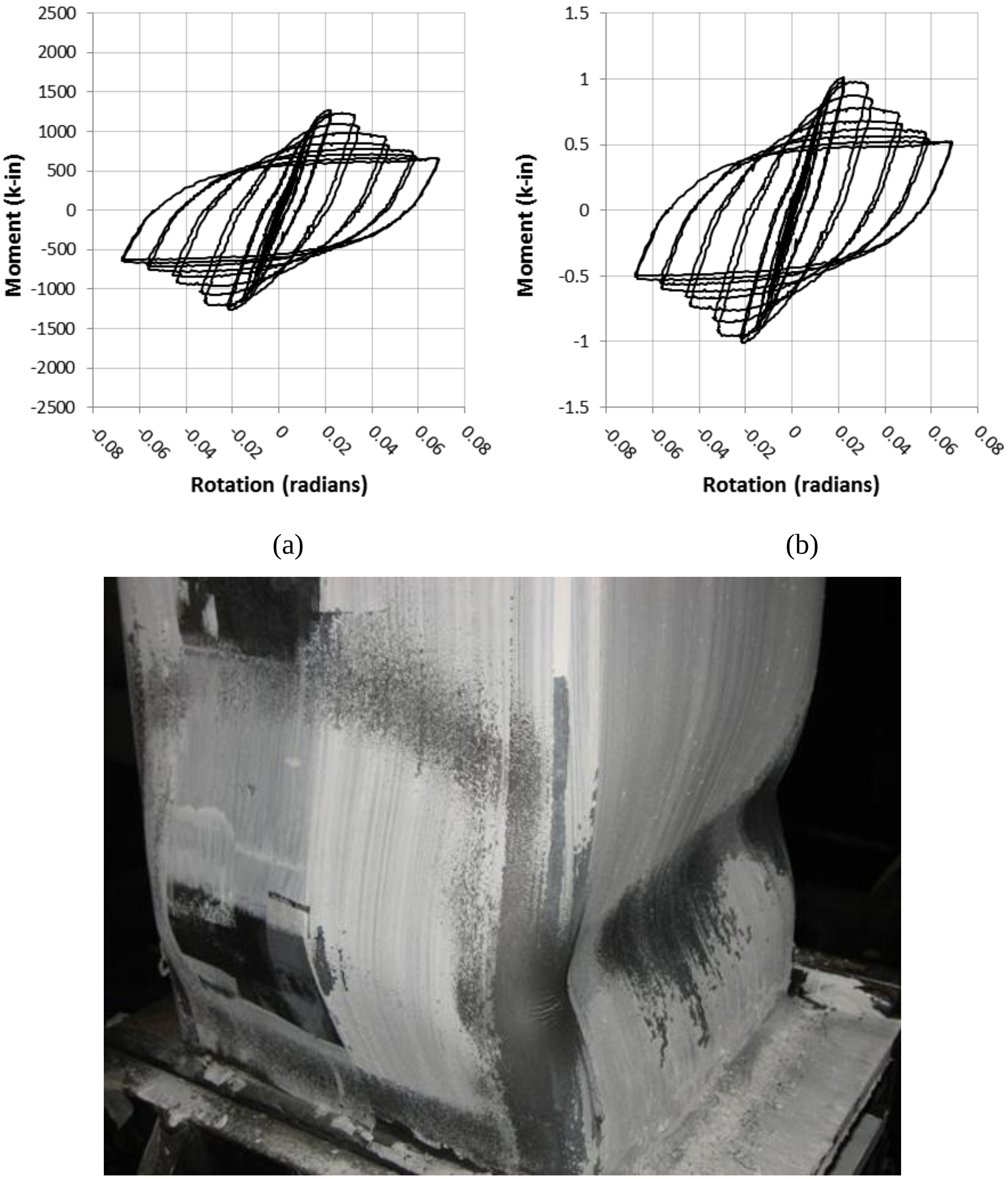

(a)

(b)

(c)

Figure 4.13 Plots of the (a) moment-rotation and (b) normalized moment-rotation behavior and a photograph of the (c) plastic hinge region at the completion of testing for the HSS 8x8x1/4.

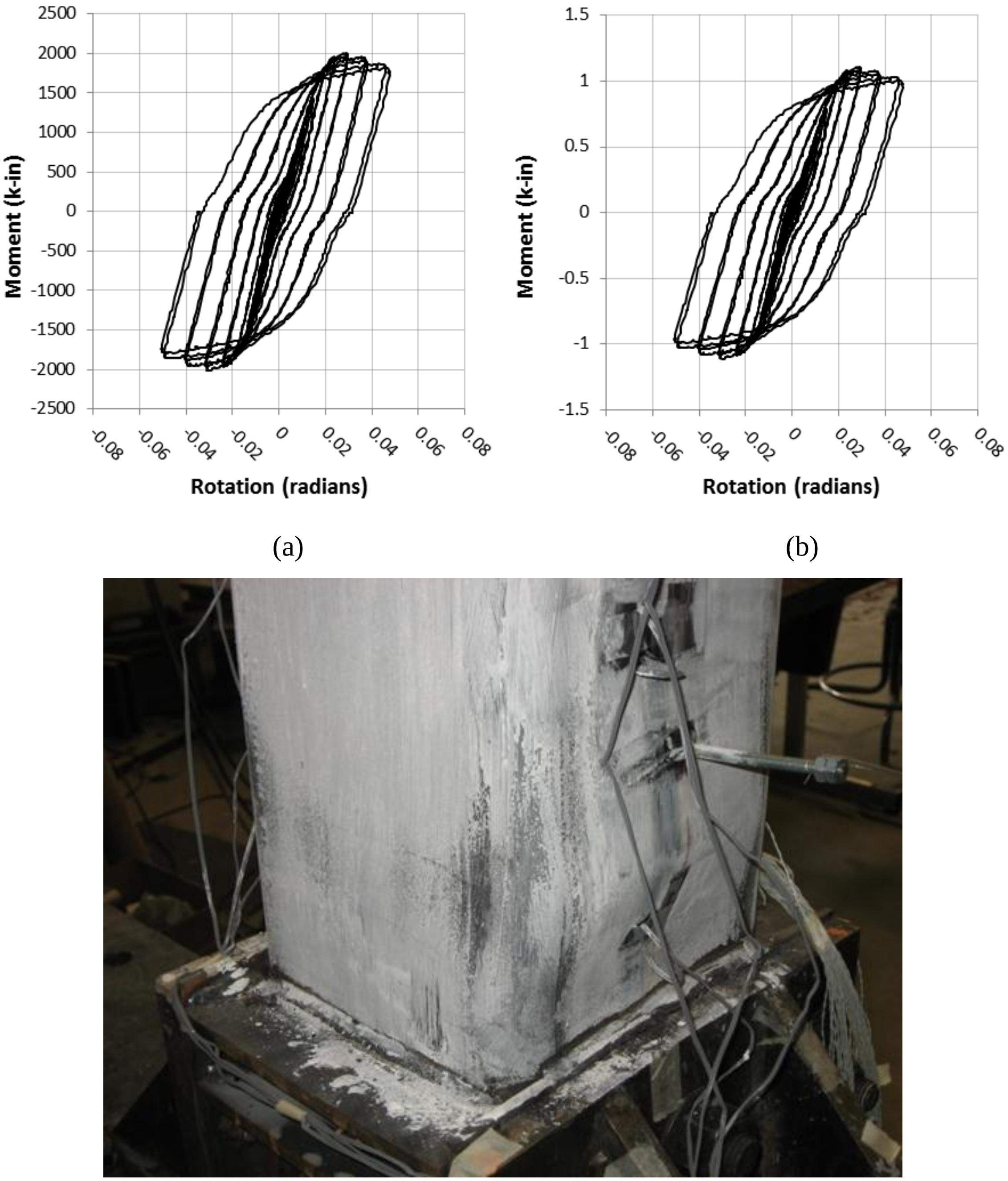

(a) (b)

(c)

Figure 4.14 Plots of the (a) moment-rotation and (b) normalized moment-rotation behavior and a photograph of the (c) plastic hinge region at the completion of testing for the HSS 8x8x3/8.

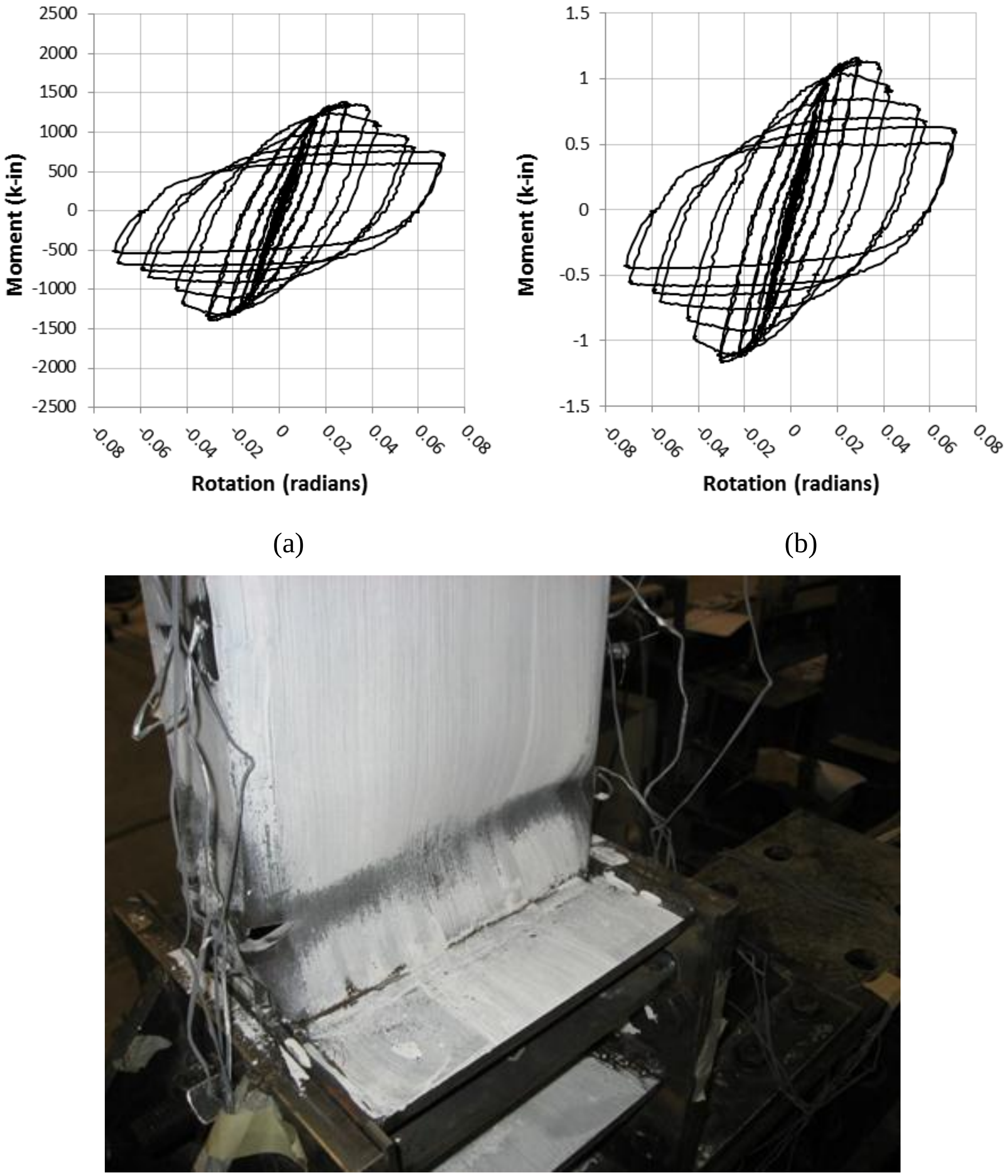

(a) (b)

(c)

Figure 4.15 Plots of the (a) moment-rotation and (b) normalized moment-rotation behavior and a photograph of the (c) plastic hinge region at the completion of testing for the HSS 10x4x1/4.

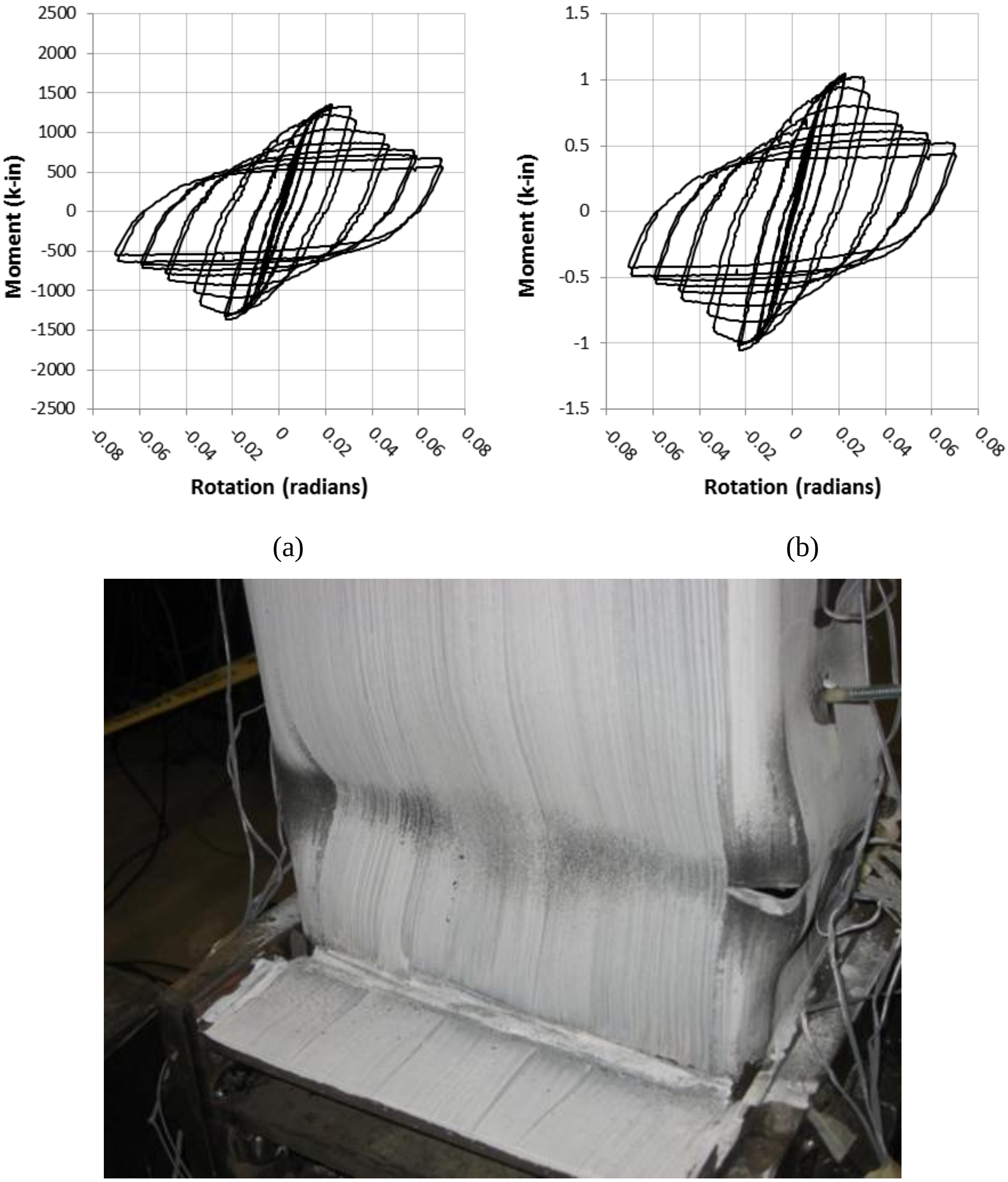

(a) (b)

(c)

Figure 4.16 Plots of the (a) moment-rotation and (b) normalized moment-rotation behavior and a photograph of the (c) plastic hinge region at the completion of testing for the HSS 10x6x1/4.

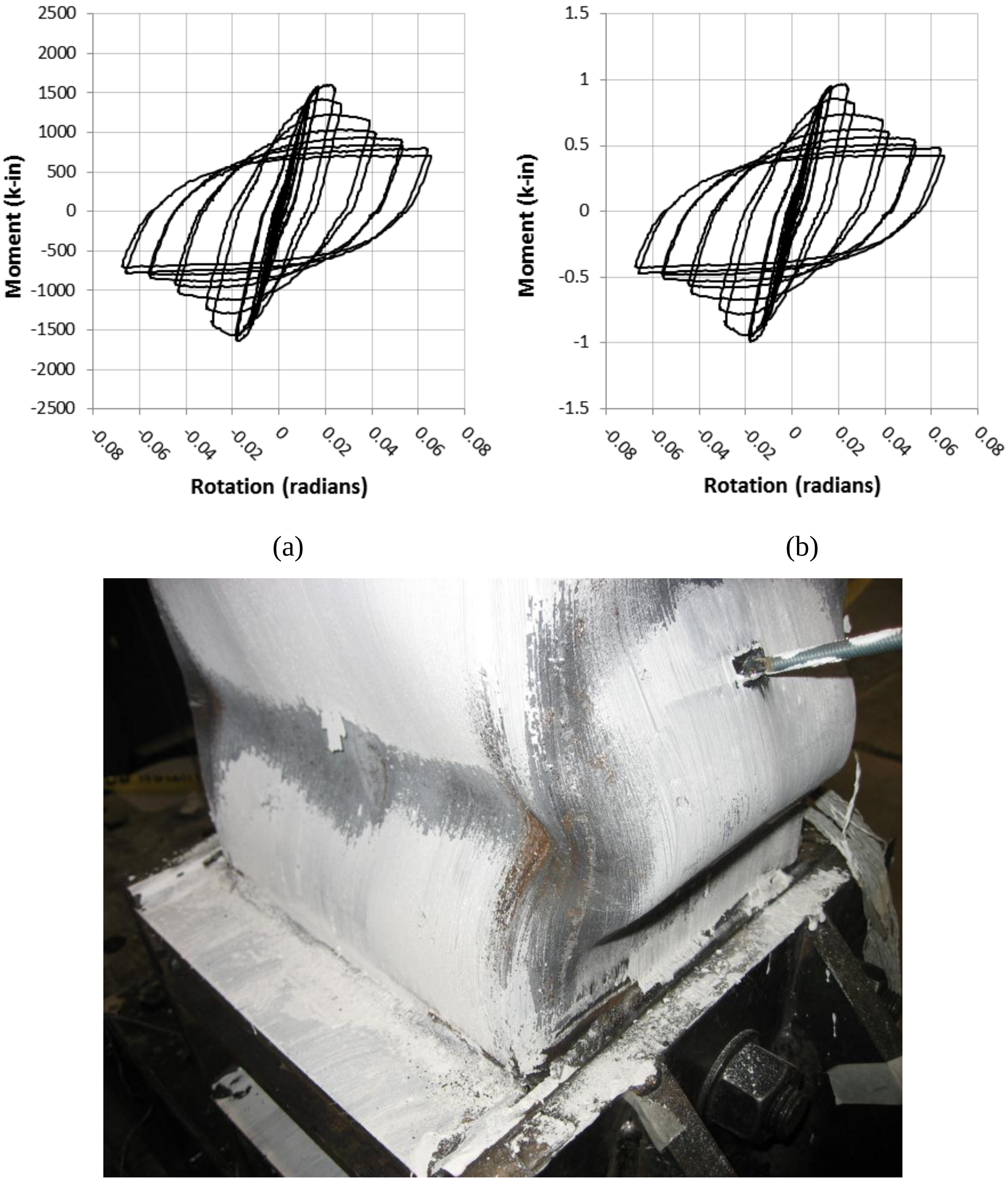

(a) (b)

(c)

Figure 4.17 Plots of the (a) moment-rotation and (b) normalized moment-rotation behavior and a photograph of the (c) plastic hinge region at the completion of testing for the HSS 10x8x1/4.

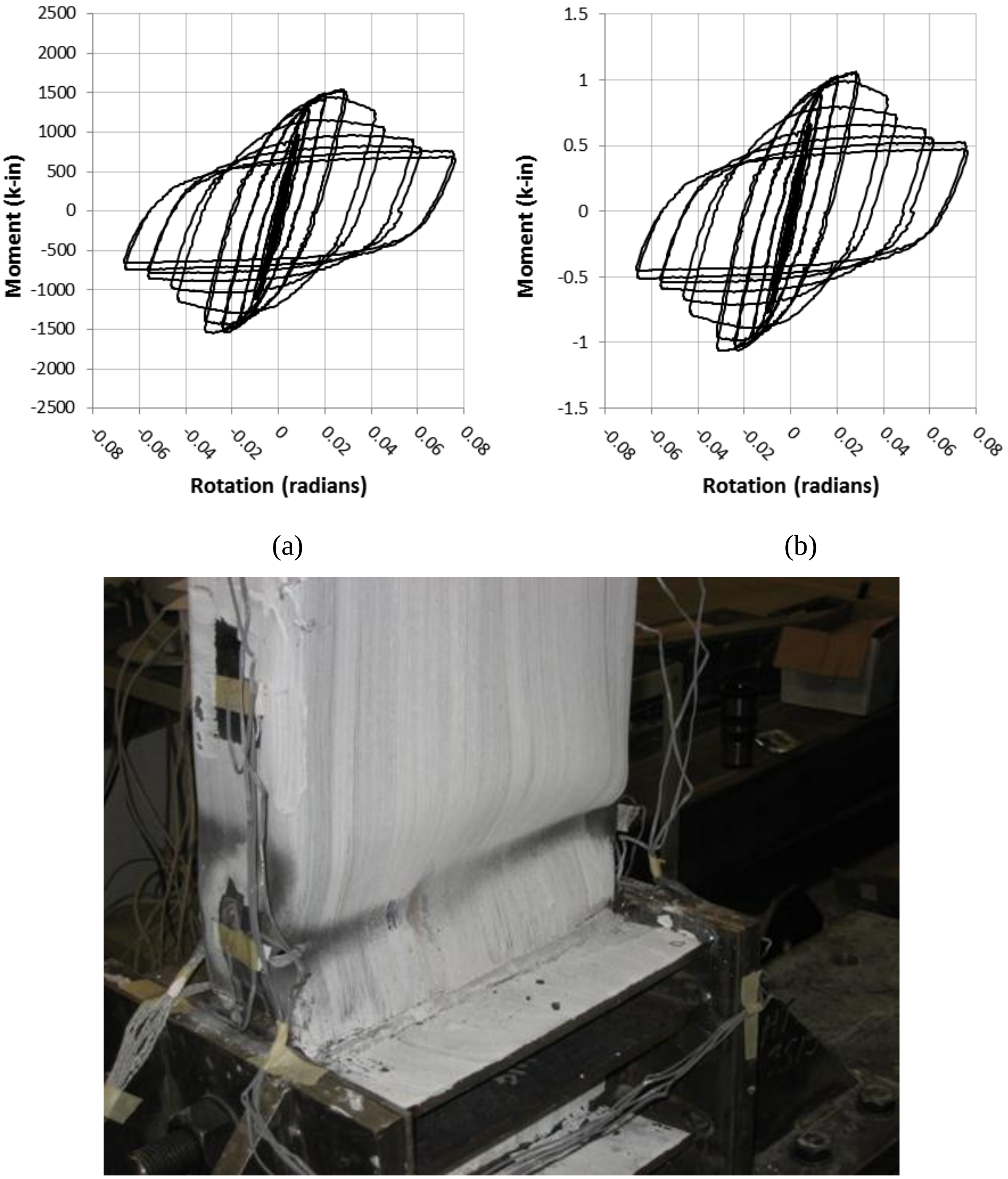

(a) (b)

(c)

Figure 4.18 Plots of the (a) moment-rotation and (b) normalized moment-rotation behavior and a photograph of the (c) plastic hinge region at the completion of testing for the HSS 12x4x1/4.

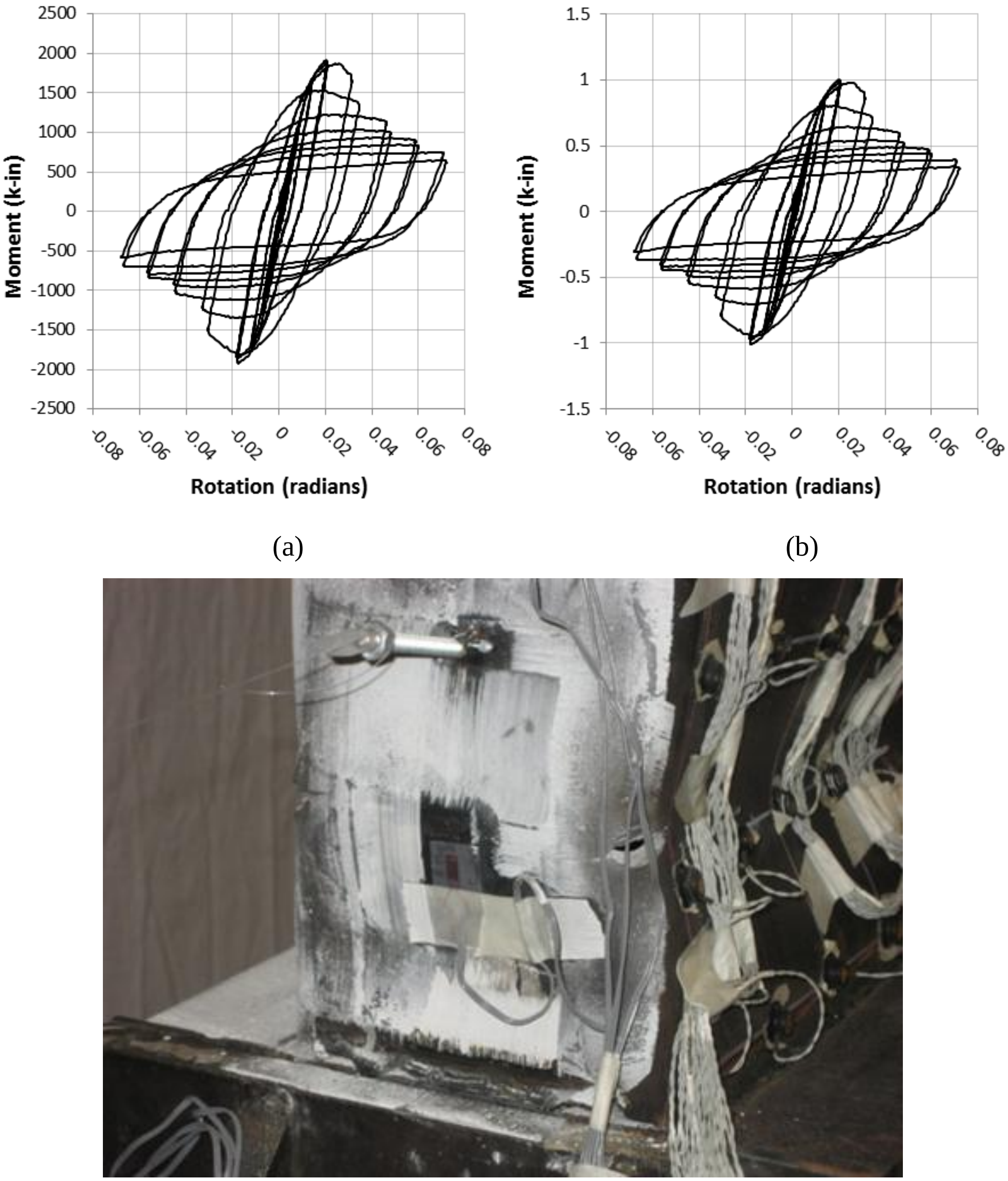

(a)

(b)

(c)

Figure 4.19 Plots of the (a) moment-rotation and (b) normalized moment-rotation behavior and a photograph of the (c) plastic hinge region at the completion of testing for the HSS 12x6x1/4.

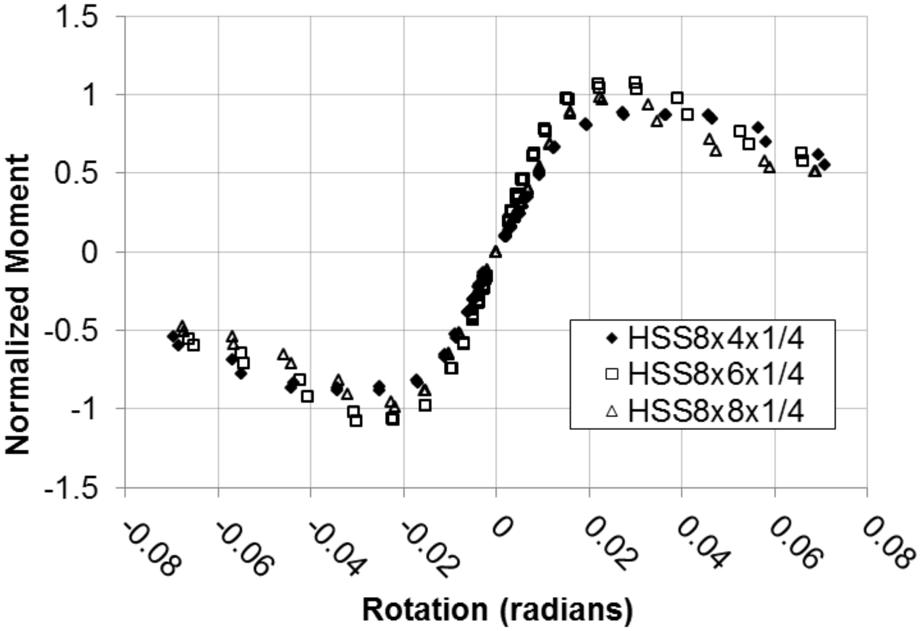

(a)

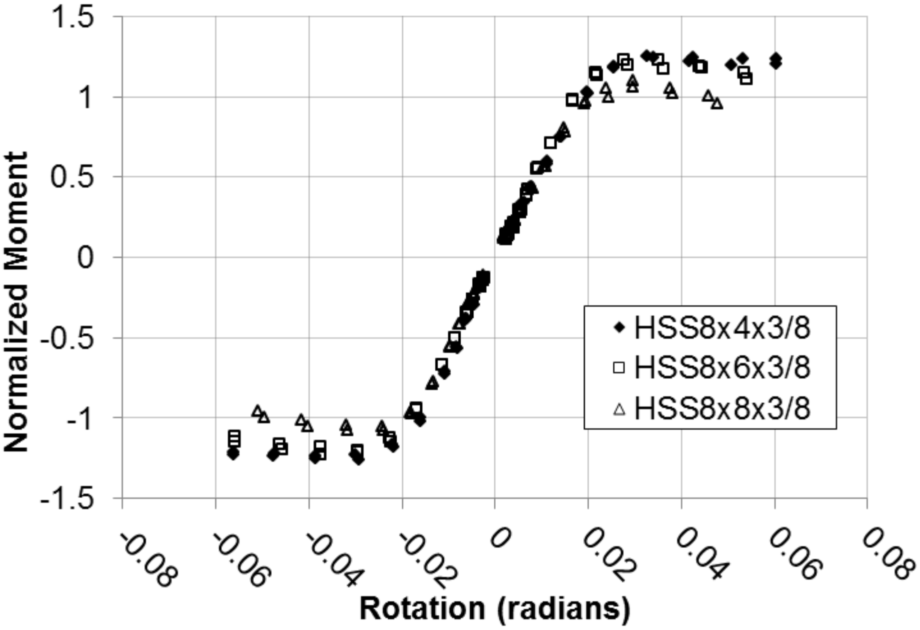

(b)

Figure 4.20 Normalized moment versus rotation backbone curves for all eleven HSS members

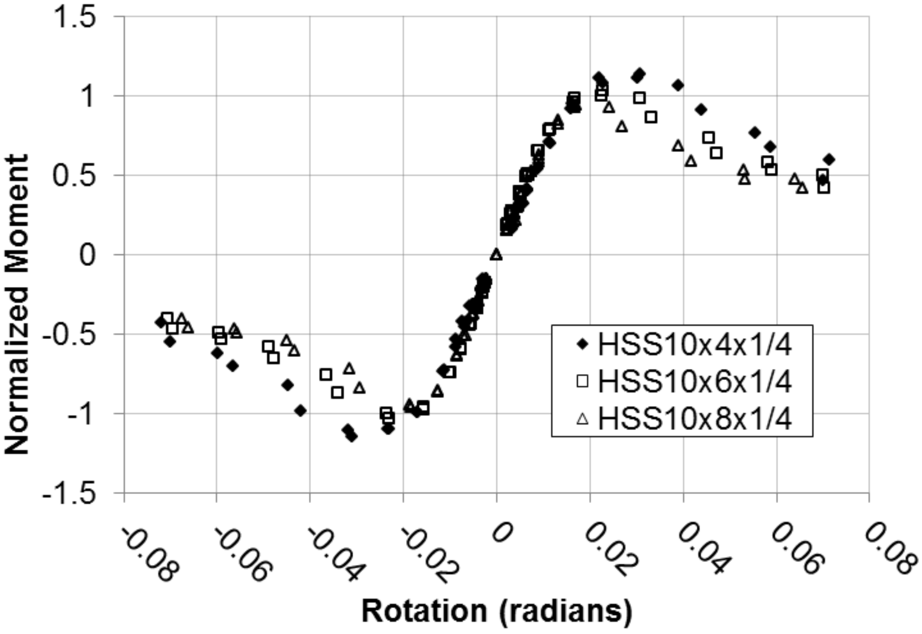

(c)

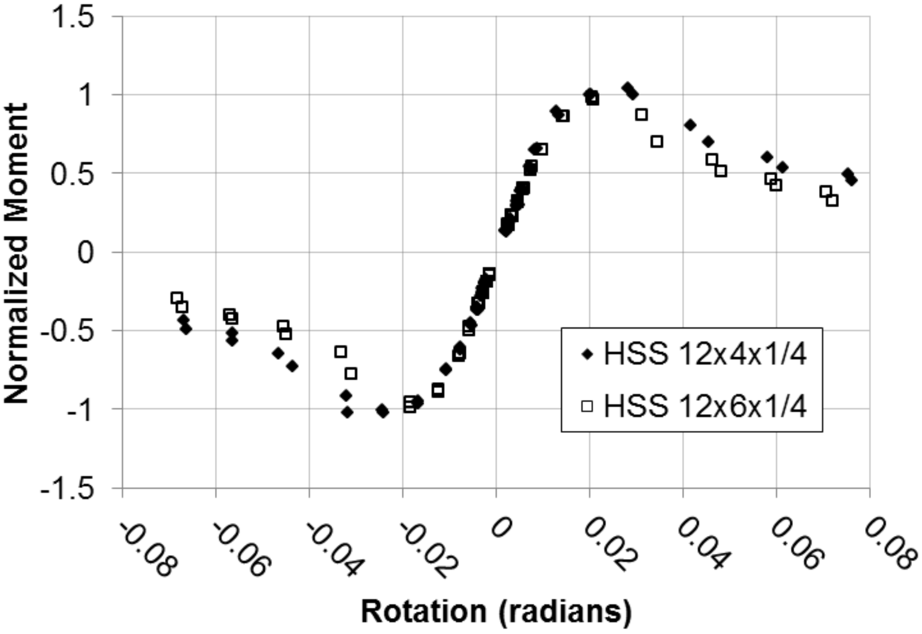

(d)

Figure 4.20 (cont.) Normalized moment versus rotation backbone curves for all eleven HSS members

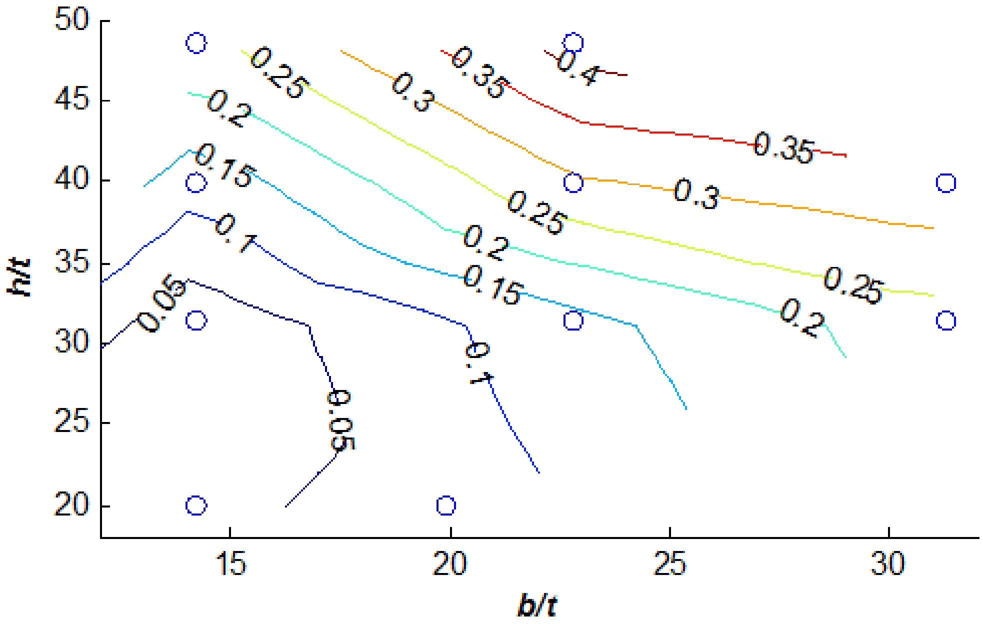

Figure 4.21 Degradation of moment capacity at 0.04 rad. with respect to width-thickness and depth-thickness ratios

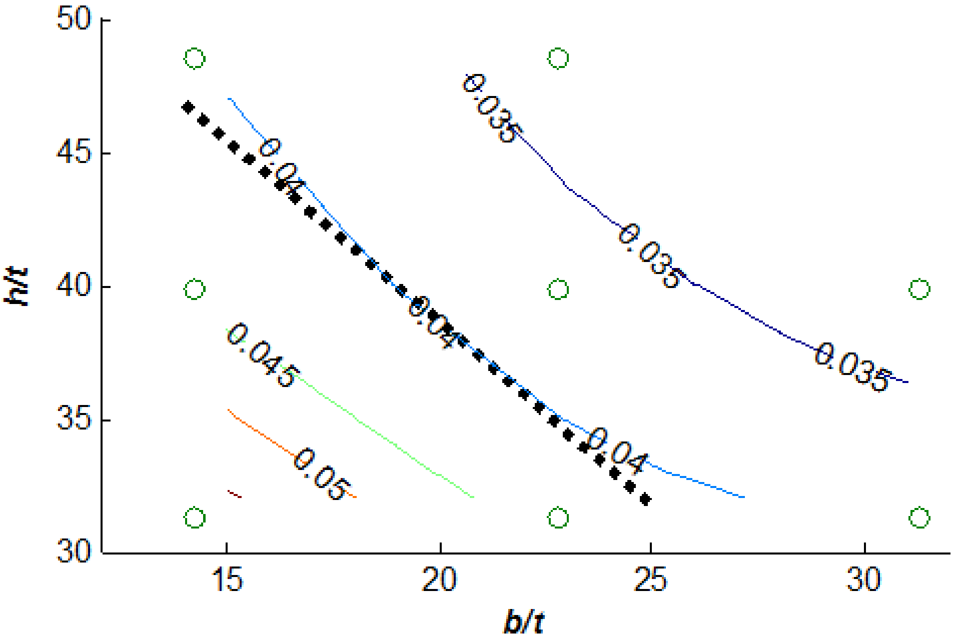

Figure 4.22 Rotational capacity at $0.8M_{max}$ with respect to width-thickness and depth-thickness ratios

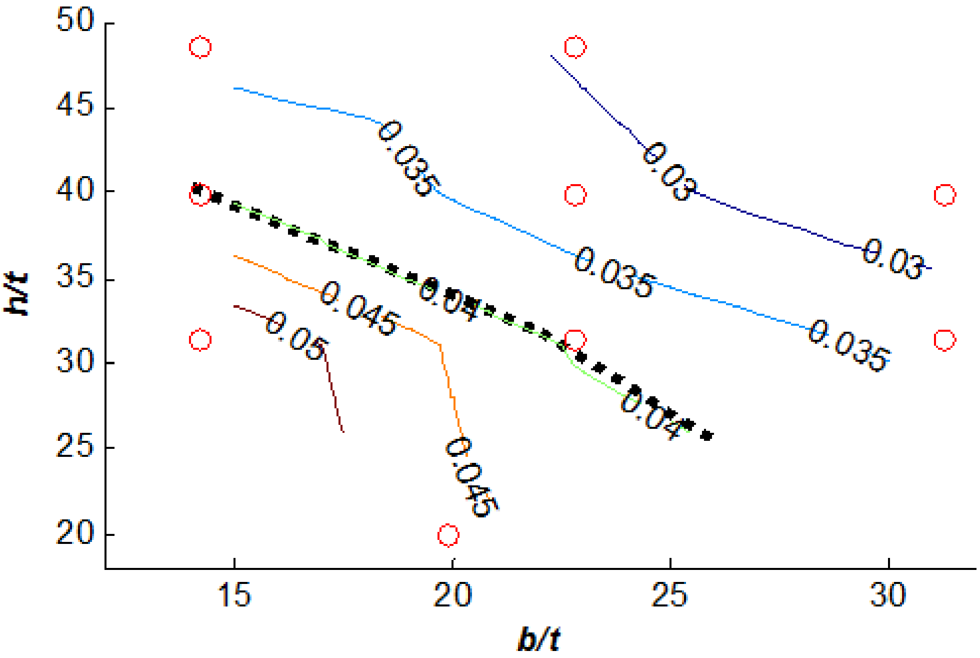

Figure 4.23 Rotational capacity at 0.9M_{max} with respect to the width-thickness and depth-thickness ratios

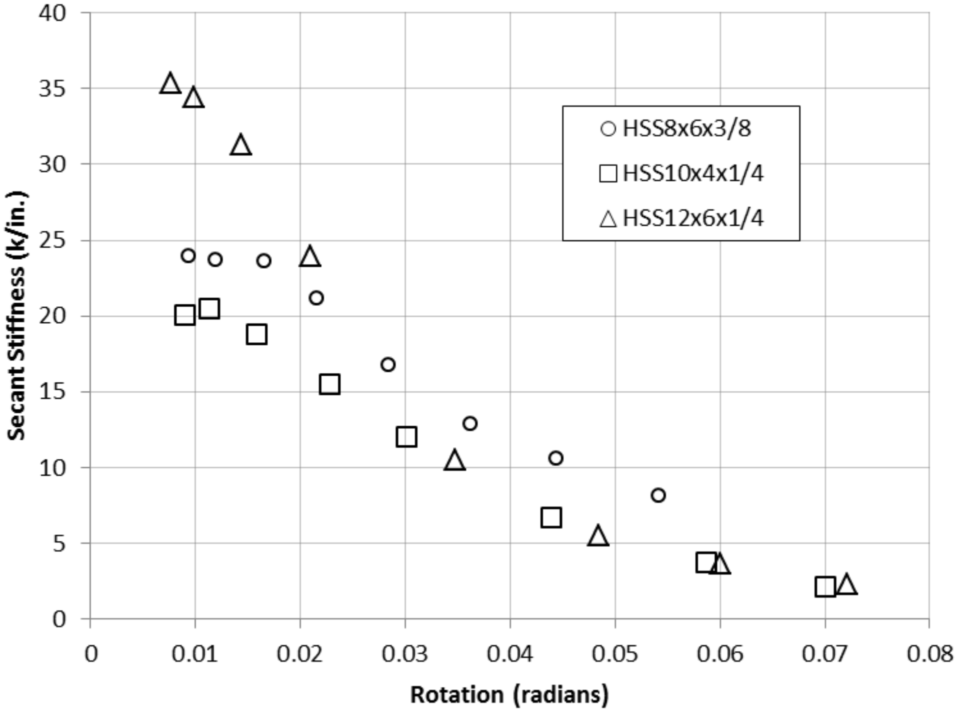

Figure 4.24 Secant stiffness versus rotation for selected members

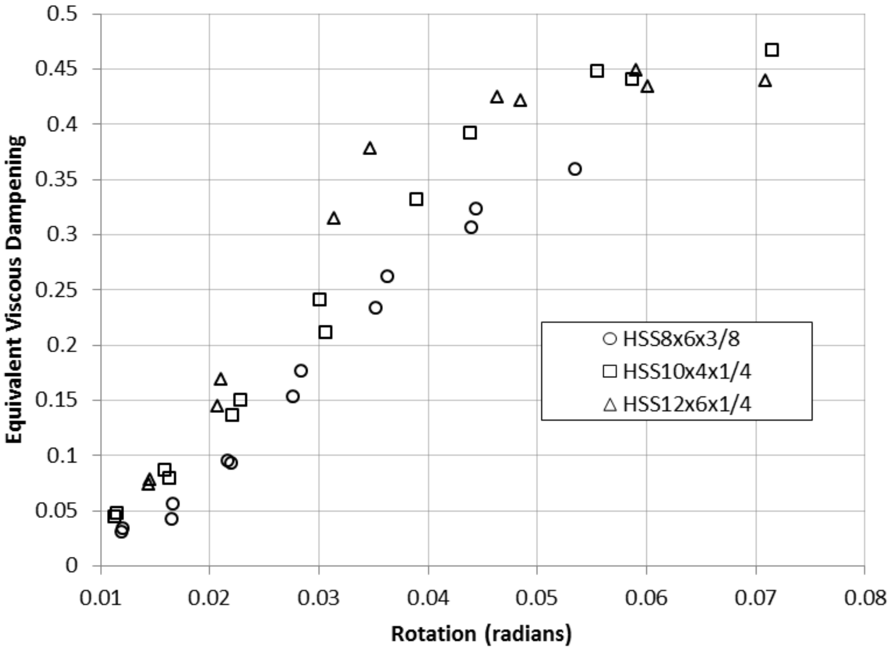

Figure 4.25 Equivalent viscous damping versus rotation for selected specimens

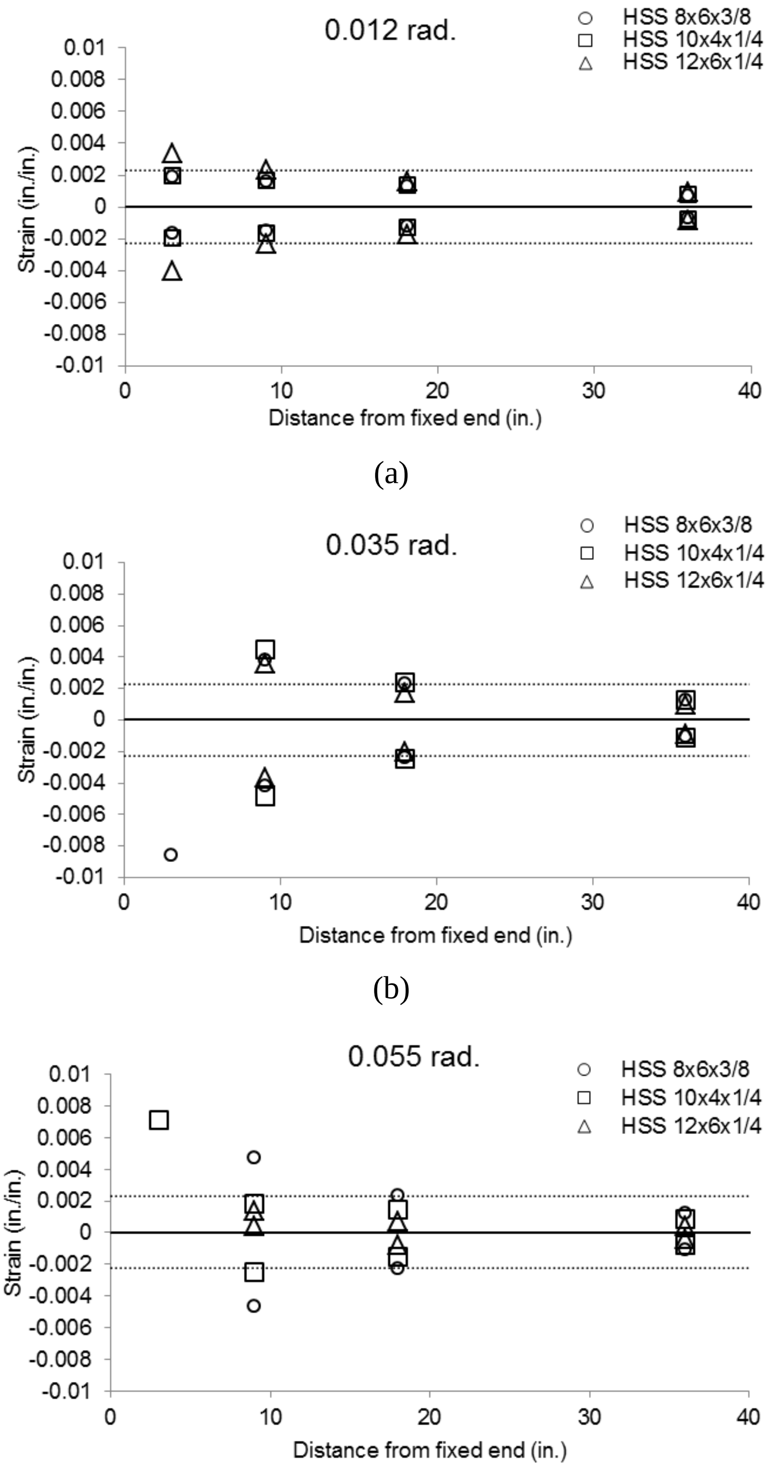

(a)

(b)

(c)

Figure 4.26 Strain along the beam flange at the (a) 0.012 rad., (b) 0.035 rad., (c) 0.055 rad. cycles for selected members

CHAPTER 5: FINITE ELEMENT MODELING OF HSS BEAM MEMBERS

5.1 Introduction

The more prevalent use of HSS in seismic flexural applications for building structures has been limited partially due to a lack of understanding of their behavior under large cyclic bending loads and possible lack of ductility and stable behavior over a number of cycles. Further applications in low and mid-rise seismic frames, such as both beam and column members, can provide significant benefits in terms of reduced seismic weight, decreased lateral bracing, applications in modular construction, and unique retrofit techniques. However, desire to have inelastic behavior focused in the beam member suggests an understanding of the cyclic bending behavior of HSS and an accurate means of modeling this behavior is necessary prior to the possible increased adoption of HSS for seismic flexural applications.

Until recently, most research on the flexural behavior of HSS focused on beam-column members. Dywer and Galambos (1965) tested three different beam-column members to failure, noting the importance of the slenderness ratio (L/r) and the axial load ratio (P/P_y). An experimental program by Nakashima and Liu (2005) considered the effect of the slenderness ratio and axial load ratio on the hysteretic behavior to gain an understanding of the cyclic plastic hinging of HSS columns in seismic applications. Wang et al. (2008) used hybrid testing to better understand the plastic hinge behavior of an HSS column base under varying axial load levels. Other studies considered the behavior of axially loaded truss-type connections and connections between HSS columns and wide flange beams for both hollow and concrete filled tube (CFT) sections (Hajjar 2000, Packer 2000, Kurobane 2002, Nishiyama and Morino 2004).

With regards to HSS beam member bending behavior, a number of experimental studies considered a variety of monotonic loading conditions. These tests showed the importance of the width-thickness (b/t), depth-thickness (h/t), and aspect ratio (b/h)

(Korol and Houdba 1972, Hasan and Hancock 1988, Zhao and Hancock 1992, Wilkinson and Hancock 1998). More recent large-scale experimental testing of HSS beam members considered flexural behavior under cyclic bending loads (Brescia et al. 2009). These experimental cyclic results reiterate the importance of *b/t* and *h/t* observed during monotonic testing and provide a further understanding of the expected cyclic local buckling behavior. However, experimental testing is still limited to a small subset of available HSS members and continued study of their cyclic behavior is needed.

Analytical models also have been developed to predict the behavior and understand the different failure modes associated with HSS members in structures. Sohal and Chen (1988) considered the local buckling behavior of round HSS columns and developed a kinematic model that can be utilized to predict the cyclic behavior based on several assumptions including the critical strain, shape and propagation of the buckle, and stress in the HSS member. Key et al. (1988) developed a theoretical plastic mechanism model to predict the post-peak load-deflection behavior of HSS columns. This yield line model based on the buckled shape is composed of three components: plate folding, corner yielding, and folding corner restraint mechanisms. However, the applicability of these models under cyclic bending loads is unknown.

Other numerical studies have successfully utilized finite element models (FEM) to capture the behavior of HSS columns and beam-columns. Nakashima and Liu (2005) used FEM to study cyclically loaded HSS columns under different axial load ratios to failure. This study captured the local buckling behavior and noted the importance of the magnitude of the axial load and its effect on the hysteretic behavior. Goto et al. (1998) modeled large HSS columns using a three-surface cyclic metal plasticity model that can provide very accurate results when calibrated to experimental data. Kurata et al. (2005) developed a phenomenological model that considers the effect of the axial load ratio and slenderness ratio on the hysteretic behavior, accounting for the negative hysteretic slope caused by degradation. Other models of HSS beam-column members consider their use as CFT under cyclic loads. One recently developed model utilizes fiber elements that have constitutive relationships for both the concrete and steel and accounts for confinement of the concrete core and cyclic local buckling of the steel tube (Denavit et al. 2010). Also, it has been shown that finite element models can be used to consider the ductility and failure mode of wide-flange (W-shape) beam members with local and global instabilities leading to a robust method for predicting the ductility of a beam member based on cross-section geometry, unbraced length, yield strength, yield ratio, and strain hardening behavior (Earls 2000). Models of square and rectangular HSS beam sections are more limited and focus mainly on sections under monotonic bending loads (Wilkinson and Hancock 2002). This model utilized imperfections of the section geometry to produce buckling and load-displacement results similar to those observed during experimental testing. The results from this model reiterate the importance of the *b/t* and *h/t* ratios on the local buckling behavior, but it has not been proven that such an approach is applicable for members under larger cyclic loads.

In order to further explore the behavior of HSS members under cyclic bending, a comprehensive finite element study is undertaken. This study adds to the experimental data on the bending behavior of HSS members under large cyclic loads and provides a means of defining limiting parameters for their use in seismic bending applications. The finite element model is calibrated to experimental data to ensure that both global and local behavior is accurately captured. With this model, a large parametric study of 133 different HSS sizes is conducted providing important information on the degradation of the moment, rotational capacity, and stiffness with cycling.

5.2 Experimental Bending Study Review

5.2.1 Experimental Specimens

The previously conducted experimental program considered the cyclic hysteretic behavior of eleven full-scale square and rectangular HSS cantilever beams under large cyclic bending loads (Chapter 4). The specimens were all stock U.S. cold formed members with ASTM A500 Gr. B steel. These tests considered the ability of HSS beam members to develop stable plastic hinge behavior, ductility, and energy dissipation necessary for use as beam members in seismic moment frames. Table 4.1 provides the relevant geometric properties for the tested sections.

5.2.2 Material Properties

As discussed in Chapter 3, the variability of material behavior across the HSS cross section was studied by taking coupon specimens from locations around the perimeter of the eleven members considered in the bending study. The FEM study utilized the behavior of the HSS 8x6x3/8 material properties for modeling (Figure 3.2 (d) and Figure 3.3 (d)) where detail of these material properties can be found in Table 3.1. A more detailed discussion of the material properties of HSS can be found in Chapter 3.

5.3 HSS Finite Element Model

5.3.1 Configuration and Details

Finite element models were generated in Abaqus FEA (Version 6.8-1) (DSS 2008) to further study the cyclic bending behavior of HSS and expand upon the limited available experimental data. The geometry of each section, including the width, depth, and thickness, was taken as that reported in the AISC Manual of Steel Construction (AISC 2011) for the studied HSS sizes. The corner radius was modeled as twice the thickness of the section. Boundary conditions simulating a fixed-end cantilever beam similar to the experimental bending tests (Chapter 4) were applied with one end completely fixed and the opposite end allowed to displace according to the same loading protocol used for the experimental bending tests up to 0.08 rad. (Figure 4.7).

Material properties from the tensile coupon tests of the HSS 8x6x3/8 were input and applied to the flats and corners of the HSS models. A combined isotropic-kinematic hardening law with no strain rate effects also was applied to more accurately capture the cyclic inelastic hysteretic behavior. Since the material test results showed little variation across the flats and corner specimens, only material properties from the corner (c3) and flat (f5) of the HSS 8x6x3/8 were used because they typify the average material properties of all tested sections (Figure 3.3 (d)). The weld (w) material properties were ignored in each section because of the relatively small area that they represented. The model material properties from the HSS 8x6x3/8 were applied with F_y of 59.6 ksi and F_u of 71.9 ksi for the flats and F_y of 76.3 ksi and F_u of 84.4 ksi for the corners. True stress-strain curves were input in Abaqus FEA by applying transformation up to the ultimate tensile strength using Equation 5.1 and Equation 5.2. By applying the different properties for the corners and flats, the cold-working effects were better simulated in considering the cyclic bending behavior of HSS (Figure 5.1).

$$\varepsilon_T = \ln(1 + \varepsilon_E) \qquad \text{Equation 5.1}$$

$$\sigma_T = \sigma_E(1 + \varepsilon_E) \qquad \text{Equation 5.2}$$

where ε_T is the true strain, ε_E is the engineering strain, σ_T is the true stress and σ_E is the engineering stress.

As shown in Figure 5.2, the FEM mesh was divided into three sections for improved efficiency: a fixed end region that spans from the fixed end to 12 in. out from the fixed end, a 1 in. transition region, and a displaced end region that included the remainder of the beam. The entire beam was modeled using shell elements. Element mesh size was optimized through a convergence study to ensure both the accuracy and efficiency of the model. The fixed end region and displaced end region were modeled using rectangular elements of approximately 0.50 in. square and 2 in. square, respectively. S4R elements were used that are 4-node double curved thin or thick shell elements that use reduced integration, hourglass control, and consider finite member strains. The transition region utilized S3 elements that are 3-node general-purpose shell elements that also consider finite membrane strains.

5.3.2 Initial Geometric Imperfections

The model for HSS flexural members needed to accurately capture both the global and local buckling behavior. To accurately model the local buckling and hysteretic behavior observed during experimental testing, geometric imperfections were applied in the plastic hinge region. The geometric imperfections created a continuous problem by removing the buckling bifurcation. These perturbations or imperfections to the geometry were based on the primary mode shapes obtained from an eigenvalue buckling analysis of the section and were a superposition of two different eigenmodes, one for each loading direction. In general this approach achieved a buckled shape similar to that observed during the experimental cyclic bending tests (Figure 5.3). The magnitude of the geometric imperfection was calibrated to the HSS that were tested experimentally to allow for further study of other HSS sizes. The eigenvalue buckling analysis provided the shape of the perturbation with a maximum nodal value of unity. This value was scaled to produce capacities and local buckling behavior that correlated to the experimental findings, while maintaining a reasonable level of imperfection near the tolerance for HSS members.

The calibration of the finite element model aimed to minimize the error between the overall maximum moment measured experimentally and that obtained from the finite element analysis. Models of the eleven previously tested experimental sections were run with no imperfection and maximum imperfections of 0.05 in., 0.10 in., and 0.20 in. to determine which value provided the most accurate correlation. Figure 5.4 provides the percent error between the overall maximum moment measured during the experimental tests and that obtained from the finite element analyses with respect to imperfection magnitude. The loading protocols used for the finite element analyses were derived from the actual rotations obtained during experimental testing to provide an accurate comparison.

With zero imperfection, the finite element model results over predicted the maximum moment for seven of the eleven specimens. The model of the HSS 8x4x1/4 provided the largest overprediction of M_{max} by 17.0% compared to the experimental results with no perturbation of the mesh geometry or zero imperfection magnitude. The HSS 8x8x1/4 and HSS 8x8x3/8 had very little difference between the experimental and numerical results for the overall maximum moment. The model of the HSS 8x8x1/4 under predicted the experimental M_{max} by only 0.03% at zero imperfection. The finite element models for the HSS 8x4x3/8, HSS 8x6x3/8, and HSS 10x4x1/4 underpredicted the experimental result by 7.0%, 4.7%, and 4.9% respectively, with zero imperfection applied. Overall, increases in the magnitude of the imperfection led to decreases in the M_{max} value obtained from the finite element analyses. The larger imperfections increased the likelihood of earlier local buckling and hindered stable plastic hinge formations. At the larger imperfection levels, the finite element models for all eleven sections under predicted the maximum moment obtained from experimental testing.

In order to define a rule for the application of imperfections in finite element models for a larger selection of HSS sizes that ensures accurate capture of local buckling behavior, a magnitude of the imperfection was chosen that minimized the average percent error. At 0.05 in. maximum imperfection, the average percent error of all sections was 1.5%. For HSS made of ASTM A500 (2010) material the out of plane tolerance for any side greater than or equal to 5.5 in. is 1% of the side length. A majority of the sides of HSS are larger than 5.5 in., where an imperfection level of 0.05 in. is below the maximum allowable imperfection level. The imperfection level is only greater than specified if the sidewalls are smaller than 5.5 in. Based on these findings, a maximum imperfection of 0.05 in. was applied to all subsequent FEM of HSS.

5.3.3 HSS Beam Model Comparison and Validation

The finite element model was validated by creating models for the eleven experimentally tested sections using the 0.05 in. imperfection level. These models were then placed under the exact same loading protocol that each experimental specimen underwent (Figure 4.7). The resulting moment-rotation hysteresis curves were compared to each of the experimental results to ensure that both the global and local behavior was accurately captured. The finite element analysis results showed the HSS 8x4x1/4 had the smallest overall maximum moment (M_{max}), 896 k-in., and the HSS 8x8x3/8 had the largest overall maximum moment, 1980 k-in. These sections were the same sections in which the minimum (770 k-in.) and maximum (1990 k-in.) M_{max} was observed for the experimental study. The rotation at which the maximum moment was reached and local buckling initiated in the finite element analysis was between 0.018 rad. for the HSS 12x6x1/4 and 0.048 rad. for the HSS 8x4x3/8. These values were similar to those observed during experimental testing, expect for the HSS 8x4x3/8 specimen that reached a higher rotation before reaching its maximum moment than what was observed experimentally. This higher rotation value for the HSS 8x4x3/8 specimen could be attributed to its low width-thickness and depth-thickness values that led to very little degradation in the maximum moment in both the finite element analysis and experimental testing. The HSS 8x4x3/8 member when tested experimentally had a decrease of less than 5% of its overall maximum moment at the largest cycles (0.06 rad) suggesting the difference between the finite element analysis and experimental results was actually minimal. In general, the findings showed that the finite element model accurately captured the general behavior of the HSS under cyclic bending and the appropriate rotation level at which local buckling initiated, which was after reaching the theoretical plastic moment capacity for all of the eleven sections.

Figure 5.5 provides a further comparison of the hysteresis curves from the experimental findings and corresponding finite element analyses for three of the eleven specimens, the HSS 10x8x1/4, HSS 8x6x3/8, and HSS 10x4x1/4. The finite element analysis results for the HSS 10x8x1/4 and HSS 8x6x3/8 (Figure 5.5) closely matched the experimental data. The HSS 10x8x1/4 reached a M_{max} of 1710 k-in., which was only 4.6% greater than the experimental M_{max}. However, the model did tend to show a slight over prediction of the degradation of the maximum moment capacity during intermediate rotation cycles up to 0.050 rad. For cycles greater than 0.055 rad., the experimental results and model again showed very good correlation. Of the three hysteresis curves shown in Figure 5.5, the HSS 10x4x1/4 model showed the largest difference from the experimental results. The M_{max} measured during experimental testing, 1400 k-in., was higher than the maximum moment obtained from the finite element analysis, 1280 k-in. During later cycles to large rotations, the moment capacity was also higher than the experimental results, 552 k-in., compared to 715 k-in. for the finite element results at 0.070 rad. Overall, these results suggested that the finite element models provided a good match to the experimental data for the eleven sections in terms of moment capacity and hysteretic behavior.

The effect of the *b/t* and *h/t* ratios could be quantified by considering the degradation of moment capacity from the overall maximum moment to the moment measured at the first 0.04 rad. cycle. The 0.04 rad. rotation level was chosen because it represented a plastic rotation in the beam member that is greater than that expected at an interstory drift of 0.04 rad. For current seismic design of special moment resisting frames, the connection must be able to achieve 80% of its maximum overall moment at an interstory drift of 0.04 rad. (AISC 2010b). Figure 5.6 (a) shows contour plots of the degradation of the maximum moment capacity based on a multiple linear regression analysis of the experimental data and finite element analysis results for the eleven experimental specimens. The contour lines represent the percent degradation (in decimal form) of M_{max} at the 0.04 rad. rotation cycle with respect to the *b/t* and *h/t* ratio. The HSS 8x4x3/8 was included in the analysis, but omitted from the plots because its degradation was below 5%. Comparing the experimental and finite element analysis results, the models adequately captured the general shape of the contours produced from the experimental results. The finite element results slightly over predicted the amount of degradation at 0.04 rad. This is especially true at low *b/t* and *h/t* ratios. For example at a *b/t* of 14.2 and *h/t* of 31.3, the finite element analysis conservatively predicted a moment degradation of approximately 9.0% of M_{max}, while the experimental results only showed a moment degradation of approximately 4% of M_{max} at 0.04 rad. This difference was likely due to an increase in local buckling seen in the webs of many of the modeled sections compared to experimental observations at intermediate rotation levels.

Another means of quantifying the effect of the *b/t* and *h/t* ratios on the hysteretic behavior was to consider the rotation at which a percentage of M_{max} was preserved such that the stability of the plastic hinge and section ductility was maintained with limited local buckling. The rotation level at which 80% of M_{max} was reached was used for comparison since 80% of M_{max} is typically required at a specified rotation level for seismic design to ensure that proper ductility is maintained (AISC 2010b). This limit can be extended from beam rotation to interstory drift capacity if needed. Figure 5.6 (b) compares the rotational capacity at 80% of M_{max} with respect to the *b/t* and *h/t* ratios for the experimental and finite element analysis results. Three sections, the HSS 8x4x3/8, HSS 8x6x3/8, and HSS 8x8x3/8, experienced stable behavior and did not degrade below $0.8M_{max}$ throughout the loading protocol. For this reason, these sections were excluded from the regression analysis. This stable behavior with limited local buckling could be attributed to low *b/t* and *h/t* ratios. The rotation at which 80% of M_{max} was reached tended to be reasonably conservative, deviating by no more 0.005 rad. The contours plots produced from the finite element analysis results provide a good prediction of the experimental results. Overall, the comparison between the experimental and finite element analysis results suggested that the developed FEM was suitable for extrapolation to other sections.

5.4 Finite Element Model Parametric Study

5.4.1 Parametric Study Specimens

A parametric study was undertaken to consider 133 different HSS beam members under the cyclic loading shown in Figure 4.7. The study utilized the validated finite element model to account for both global and local behavior through the use of geometric imperfections. The additional members allowed for significant expansion of the experimental findings (Chapter 4) to almost all applicable HSS members for seismic bending applications (Table 5.1). The sections ranged in depth, *d*, from 5 in. to 20 in.; in width, *w*, from 2 in. to 14 in.; and in thickness, *t*, from 3/16 in. to 5/8 in. This allowed for consideration of section sizes that ranged between HSS 6x2x3/16 and HSS 20x12x5/8. The geometric properties for these sections fell near the range of *b/t* and *h/t* ratios studied in Chapter 4, with the width-thickness ratios ranging from 7.0 to 31.5 and the depth-thickness ratios ranging from 16.4 to 52.0. The consideration of such a wide range of specimens leads to a better understanding of the limiting parameters for stable plastic hinge formation and degradation of the moment capacity of HSS under cyclic bending. Figure 5.7 provides an overview of the b/t and h/t ratios of the parametric study specimens.

5.4.2 Hysteretic Behavior

The moment-rotation behavior was considered for all 133 sections. The HSS 20x12x5/8 had the largest M_{max} of 15900 k-in., while the HSS 6x2x3/16 showed the smallest M_{max} of 315 k-in. Nearly all sections, except for the HSS 6x3x5/16, showed some degradation of the maximum moment with increasing rotational demands. Between M_{max} and the maximum moment measured during the first 0.08 rad. cycle, the HSS 16x8x5/16 (*b/t*=24.5 and *h/t*=52.0) had the largest decrease in moment capacity from 4130 k-in. at 0.010 rad. to 1640 k-in. at 0.08 rad., a 66.0% reduction. The HSS 6x3x5/16 (*b/t*=7.33 and *h/t*=17.6) had no decrease in moment capacity at a rotation of 0.08 rad. The difference in the amount of degradation clearly could be attributed to the *b/t* and *h/t* ratios.

Normalized moment-rotation hysteresis plots are shown in Figure 5.8 for the HSS 14x10x5/16 (*b/t*=31.4 and *h/t*=45.1), HSS 16x8x1/2 (*b/t*=14.2 and *h/t*=31.4), and HSS 14x6x5/8 (*b/t*=7.33 and *h/t*=21.1). The theoretical value of the plastic moment was determined using $M_p=F_yZ$, where F_y (59.6 k-in.) was obtained from the coupon stress-strain curves for the flats used to model the material behavior of the section. The results from the finite element analyses showed that the HSS produced symmetric hysteretic behavior over a range of sizes and that the degradation of the maximum moment was highly dependent on the local buckling behavior and geometric properties. Of the three sections, the HSS 14x6x5/8 reached the highest overall normalized moment of 1.31, while the HSS 14x10x5/16 had the lowest normalized maximum moment of 1.01. For all of the 133 considered sections, the normalized moment capacities ranged between 0.96 and 1.31. This finding suggested that nearly all of the analyzed sections underwent yielding prior to the occurrence of local buckling. Comparing the three plotted sections, the HSS 16x8x1/2 had the highest M_{max} of 7450 k-in. and the HSS 14x10x5/16 had the lowest M_{max} of 3900 k-in. The values are above their theoretical plastic moment capacities, 6310 k-in. and 3850 k-in., respectively. As a result of these finding, it was clear that a wide range of sections are available for use in seismic design.

The three plotted sections also allowed for comparison of the effect that the *b/t* and *h/t* ratios had on the hysteretic behavior. A section with a moderate *b/t* and *h/t* ratio, such as the HSS 16x8x1/2 with a *b/t* of 14.2 and *h/t* of 31.4, showed consistent and stable degradation of the cyclic moment capacity throughout cycling. Meanwhile the HSS 14x10x5/16 with a higher *b/t* ratio of 31.4 and *h/t* ratio of 45.1 showed an increased amount of degradation of the moment capacity with continued cycling. Additionally, the rate of degradation of the moment capacity was faster. For example, the HSS 16x8x1/2 degraded 20% between the overall maximum moment and the maximum moment measured during the 0.04 rad. cycle, while the HSS 14x10x5/16 degraded 43%. The HSS 14x6x5/8 had a lower *b/t* ratio, 7.3, and *h/t* ratio, 21.1, and experienced very little degradation of the moment capacity. The moment capacity of the section did not decrease between the overall maximum moment and the maximum moment during the 0.04 rad.

cycle. Based on the comparison of these three sections, it was clear that HSS beam sections can develop large stable hysteresis loops if the *b/t* and *h/t* ratios are limited.

5.4.3 Cycling Effects

The hysteretic behavior observed experimentally (Chapter 4, Wilkinson and Hancock 1998) and in previous finite element analyses (Wilkinson and Hancock 2002) suggested that the degree of local buckling was highly dependent on the *b/t* and *h/t* ratios. The importance of the *b/t* and *h/t* ratios also was clear as current non-seismic design specifications limit these values for HSS under axial load to 35.2 for F_y of 46.0 ksi and under flexural load to 28.1 and 60.8 for F_y of 46.0 ksi, respectively (AISC 2011). Further limitations for consideration of HSS as highly ductile members in seismic applications require the *b/t* and *h/t* ratios to be less than 13.8 for F_y of 46.0 ksi (AISC 2010b). This limiting value for the *b/t* and *h/t* ratios in seismic applications was mainly established based on the importance of preventing local buckling in cyclically and axially loaded HSS bracing members (Liu and Goel 1988, Sherman 1995). By considering 133 different HSS undergoing cyclic bending, a needed better understanding of the limiting *b/t* and *h/t* ratios for the use of HSS in seismic bending application could be established.

5.4.3.1 Moment Degradation

The percent degradation of M_{max} at the 0.04 rad. rotation cycle with respect to the *b/t* (Figure 5.9(a)) and *h/t* (Figure 5.9 (b)) ratios was plotted for the 133 modeled sections and the previous experimental results. The results again suggested that the moment degradation was affected by both the *b/t* and *h/t* ratio. For all sections, the average percent degradation of the M_{max} at 0.04 rad. is 14.1% with a standard deviation of 13.9%. This finding implied that some amount of buckling and degradation occurred for most sections during cycling to 0.04 rad. Of all the modeled sections, the HSS 14x10x5/16 had the largest degradation of M_{max} of 44.9% at 0.04 rad. Thirty-four sections with a maximum *b/t* ratio of 17.6 and *h/t* ratio of 31.5 showed no degradation of M_{max} at a rotation of 0.04 rad. On average, these sections had *b/t* and *h/t* ratios of 10.1 and 22.6, respectively.

A linear regression analysis was conducted to relate the *b/t* and *h/t* ratios to the percent degradation of M_{max} at 0.04 rad. (Equation 5.3 and Equation 5.4). The linear regression results showed that the amount of moment degradation increased with increasing *b/t* and *h/t* ratios due to an increased susceptibility to local buckling prior to establishing a good plastic hinge. Based on the similar slopes obtained from the linear regression analyses, 0.012 for *b/t* and 0.012 for *h/t*, an increase in *b/t* or *h/t* caused about the same increase in the percent degradation of moment capacity.

$$Deg_{0.04}\left(\frac{b}{t}\right) = 0.012\left(\frac{b}{t}\right) - 0.064 \qquad \text{for } 7.0 \le \frac{b}{t} \le 31.5 \qquad \text{Equation 5.3}$$

$$Deg_{0.04}\left(\frac{h}{t}\right) = 0.012\left(\frac{h}{t}\right) - 0.228 \qquad \text{for } 16.4 \le \frac{h}{t} \le 52.0 \qquad \text{Equation 5.4}$$

The linear regression analysis results also suggested that a larger value of *h/t* causes less degradation of M_{max} at 0.04 rad. than the same value of *b/t*. This implied that degradation of moment capacity was more dependent on the *b/t* ratio.

Additionally, the percent degradation of M_{max} at 0.04 rad. for the experimental testing is plotted in Figure 5.9. The 133 modeled sections matched closely with the experimental results. Linear regression results for the experimental data (Equation 5.5 and Equation 5.6) showed that only at lower *h/t* ratios did the model predict higher amounts of buckling. Likewise considering the *b/t* ratio, the finite element results show higher amounts of buckling for all values. However on average, a change in the *b/t* ratio will cause the same change in the degradation of the M_{max} at 0.04 rad. in the model compared to what was observed experimentally.

$$Deg_{0.04}\left(\frac{b}{t}\right) = 0.012\left(\frac{b}{t}\right) - 0.077 \qquad \text{for } 14.0 \le \frac{b}{t} \le 22.0 \qquad \text{Equation 5.5}$$

$$Deg_{0.04}\left(\frac{h}{t}\right) = 0.010\left(\frac{h}{t}\right) - 0.170 \qquad \text{for } 22.0 \le \frac{h}{t} \le 26.0 \qquad \text{Equation 5.6}$$

5.4.3.2 Rotational Capacity

The rotational capacity plots shown in Figure 5.10 represent the rotation of the last cycle in which 80% of the maximum overall moment was retained. For the 133 modeled sections thirteen sections did not degrade to 80% of their overall maximum moment capacity throughout the loading protocol. These sections had an average *b/t* and *h/t* ratio of 10.7 and 18.9, respectively. Considering all 133 section sizes, the average rotational capacity was found to be 0.046 rad. with a standard deviation of 0.015 rad. The HSS 16x8x5/16 showed the fastest reduction in moment capacity, reaching 80% of M_{max} at the 0.018 rad. cycle. Since the average rotational capacity was above 0.04 rad., which is the interstory drift requirement for special moment frame systems specified by AISC, the findings suggested that many HSS member sizes achieved suitable behavior for use in large cyclic bending applications.

Linear regression equations for the rotational capacity at 80% of M_{max} with respect to the *b/t* and *h/t* ratios are shown as Equation 5.7 and Equation 5.8 respectively. The equations for the rotational capacity at 80% of M_{max} suggested a higher dependence on changes in the *h/t* than the *b/t* ratios since the slope for was larger for *h/t*. However, the *b/t* ratio tended to affect the rotational capacity more than the *h/t* ratio because larger *h/t* ratios were needed to cause the same reduction in rotational capacity.

$$\theta_{0.8M_{max}}\left(\frac{b}{t}\right) = -12.4 \cdot 10^4 \left(\frac{b}{t}\right) + 0.068 \qquad \text{for } 7.0 \leq \frac{b}{t} \leq 31.5 \qquad \text{Equation 5.7}$$

$$\theta_{0.8M_{max}}\left(\frac{h}{t}\right) = -13.6 \cdot 10^4 \left(\frac{h}{t}\right) + 0.090 \qquad \text{for } 16.4 \leq \frac{h}{t} \leq 52.0 \qquad \text{Equation 5.8}$$

The experimental rotational capacity also is plotted in Figure 5.10 for comparison. The model captured the same general trend as the experimental findings. Comparing the experimental results provided in Equation 5.9 and Equation 5.10 to the results of the parametric study, the parametric findings suggested that HSS are 1.6 times more sensitive to the *b/t* ratio and 1.7 times more sensitive to the *h/t* ratio than the experimental findings of a much smaller subset. This finding was in part a result of the parametric study evaluating the behavior of sections with a larger distribution of *b/t* and *h/t* ratios.

$$\theta_{0.8M_{max}}\left(\frac{b}{t}\right) = -8.0 \cdot 10^{4}\left(\frac{b}{t}\right) + 0.058 \quad \text{for } 14.0 \le \frac{b}{t} \le 22.0 \qquad \text{Equation 5.9}$$

$$\theta_{0.8M_{max}}\left(\frac{h}{t}\right) = -8.0 \cdot 10^{4}\left(\frac{h}{t}\right) + 0.072 \quad \text{for } 22.0 \le \frac{h}{t} \le 26.0 \qquad \text{Equation 5.10}$$

5.4.3.3 Prediction of Cyclic Behavior

Equation 5.3 and Equation 5.4 allow for prediction of the percent degradation of M_{max} at 0.04 rad. ($Deg_{0.04}$) and Equation 5.7 and Equation 5.8 allow for prediction of the rotational capacity at 0.8M_{max} ($\theta_{0.8Mmax}$). In predicting the degradation or rotational capacity both *b/t* and *h/t* should be evaluated because of the interrelated nature of these values. When considering the percent degradation of M_{max} at 0.04 rad., the controlling value will be the maximum of Equation 5.3 and Equation 5.4. In contrast, when predicting the rotational capacity, the minimum value of Equation 5.7 and Equation 5.8 provides the maximum rotational capacity at which 0.8M_{max} is maintained. Figure 5.11 (a) plots the percent degradation of M_{max} at 0.04 rad. as well as the line representing these values plus one standard deviation. Figure 5.11 (b) provides similar plots for the rotational capacity at 0.8M_{max} except a plot is provided for these values minus one standard deviation. Overall, Figure 5.11 provides a useful connection between the geometric properties and cyclic behavior that can be utilized as a preliminary design tool to predict the expected behavior of a section with continued cycling provided its size falls within the range of parameters considered in the parametric study.

Additionally, limiting *b/t* and *h/t* ratios suitable for seismic design can be derived from the linear regression results. Seismic moment connections must maintain 80% of M_{max} at a 0.04 rad. interstory drift (AISC 2010b). Thus, the beam slenderness limit could be conservatively selected such that the member maintains 80% of M_{max} at 0.04 rad. rotation since in reality some of the drift will actually result from deformation of other components. Using Equation 5.3 and Equation 5.4 plus one standard deviation, the limits for the *b/t* and *h/t* ratios were found to be 10.1 and 23.8 respectively. These limits were then normalized by the experimental value of $\sqrt{E/F_y}$. The normalized limits for *b/t* and *h/t* are shown in Equation 5.11 and Equation 5.12.

$$\frac{b}{t} = 0.48\sqrt{\frac{E}{F_y}} \qquad \text{Equation 5.11}$$

$$\frac{h}{t} = 1.13\sqrt{\frac{E}{F_y}} \qquad \text{Equation 5.12}$$

As expected, these limits were more conservative than the AISC specified limits for compact HSS members in flexure where the coefficients are 1.12 for *b/t* and 2.42 for *h/t* (AISC 2010a). Utilizing the minimum yield strength for ASTM A500 Gr. B steel and Equation 5.11 and Equation 5.12, the limit for *b/t* is 12.1 and *h/t* is 28.4 compared to those required of a compact section for non-seismic applications in flexure where the *b/t* and *h/t* limits are 28.1 and 60.8, respectively. The values obtained from Equation 5.11 and Equation 5.12 are closer to those specified for highly ductile members in seismic applications where the coefficients is 0.55 for *b/t* (AISC 2010b). The findings suggest that lower limits for the width-thickness and depth-thickness ratios are needed for use of HSS in seismic bending applications.

5.4.3.4 Secant Stiffness

The change in secant stiffness with cycling of HSS beam members was influenced by both the *b/t* and *h/t* ratios. The secant stiffness was calculated at each cycle as the load at maximum displacement divided by the maximum displacement. The HSS 20x12x5/8 had the highest secant stiffness of 558 k/in. at 0.00375 rad., while the theoretical elastic stiffness was 669 k/in. The HSS 6x2x3/16 had the lowest maximum secant stiffness of 3.54 k/in. at 0.015 rad., while the theoretical elastic stiffness was 3.83 k/in. Because every section underwent some yielding, all HSS members showed degradation of the secant stiffness with increasing displacment thoughout the loading protocol.

Figure 5.12 plots the percent decrease in secant stiffness from its overall maximum value to the secant stiffness recorded for the first 0.08 rad. cycle. The HSS 6x3x5/16 experienced the smallest degradation in secant stiffness losing 67.5% of the maximum secant stiffness of 6.75 k/in. and decreasing to 2.20 k/in. The HSS 16x8x5/16 had the largest degradation of secant stiffness losing 96.0% of the maximum secant stiffness of 143 k/in. while decreasing to 5.72 k/in. On average, the 133 modeled HSS beam members experienced an 88.4% degradation of maximum secant stiffness at the first 0.08 rad. cycle. Figure 5.12 shows that as *b/t* and *h/t* increased the degradation of the secant stiffness of the HSS beam member increased. This correlation was more dependent on the *h/t* ratio than the *b/t* ratio. An increase in the *h/t* ratio caused a larger increase in the reduction of the secant stiffness as compared to the same change in the *b/t* ratio. Typically, increasing the section thickness increased the amount of degradation of the secant stiffness. On average, the 3/16 in. thick sections had an average degradation of 87.0%, while the 5/8 in. thick sections had an average degradation of 90.4%. In general, it was observed that HSS with higher *h/t* ratios tended to show larger secant stiffness degradation with continued cycling. This indicated that secant stiffness might be more dependent on web buckling than flange local buckling.

5.5 Conclusions

The calibration and validation of a finite element model to a set of experimental results was conducted leading to a large parametric study of HSS beam members under cyclic bending. The parametric study considered 133 different sections with *b/t* and *h/t* ratios varying from 7.0 to 31.5 and 16.4 to 52.0, respectively. The calibration of the finite element model included geometric imperfections of the section geometry and experimentally measured material properties. All HSS members were cycled under the same loading protocol simulating the effects of a far-field type ground motion. The effect of the *b/t* and *h/t* ratios on the hysteretic behavior was considered with a focus on the degradation of M_{max} at 0.04 rad., the rotational capacity at $0.8M_{max}$, and degradation of the maximum secant stiffness with continued cycling to large rotation levels. The key conclusions associated with this work are summarized as follows:

1. Finite element models utilizing three dimensional shell elements, experimentally measured material properties, and geometric perturbations were sufficient to accurately model the bending behavior of HSS beam members under large cyclic load reversals. With a 0.05 in. maximum perturbation of the section geometry, the error in estimating the M_{max} was minimized for most HSS members. Comparison of the degradation of M_{max} at 0.04 rad. and the rotational capacity at $0.8M_{max}$ showed good correlation with the experimental results.
2. For all but two of the 133 sections, the moment capacities were greater than the plastic moment capacity. Increasing the b/t and h/t ratios led to a decrease in the moment capacity with increased rotation levels. Additionally, the effect of these ratios was shown to be interrelated.
3. For all modeled sections, the average percent degradation of the M_{max} at 0.04 rad was 14.1% with a standard deviation of 13.9%. The average rotational capacity was 0.046 rad. with a standard deviation of 0.015 rad. Most sections showed some degradation of the maximum overall moment at 0.04 rad. with the exception of 34 members that had an average b/t of 10.1 and h/t of 22.6. Thirteen sections did not degrade past $0.8M_{max}$ throughout the loading protocol with average b/t and h/t of 10.7 and 18.9, respectively.
4. Based on a regression analysis, limiting b/t and h/t ratios were developed that maintain on average 80% of M_{max} at 0.04 rad. The b/t and h/t limits were 12.1 and 28.4, respectively, utilizing specified ASTM A500 Gr. B material properties.
5. The 133 modeled HSS beam members experienced an average of 88.4% degradation in the maximum secant stiffness by the first 0.08 rad. cycle. The secant stiffness was found to be more dependent on web buckling than flange buckling. Also, thickness of the member played an important role as thicker sections showed higher amounts of degradation of the secant stiffness with continued cycling.

Table 5.1 Parametric study parameters

Parametric Study Parameter		Range
Beam depth	*d*	5 in. to 20 in.
Beam width	*w*	2 in. to 14 in.
Thickness	*t*	3/16 in. to 5/8 in.
Width-thickness ratio	*b/t*	7.0 to 31.5
Depth-thickness ratio	*h/t*	16.4 to 52.0

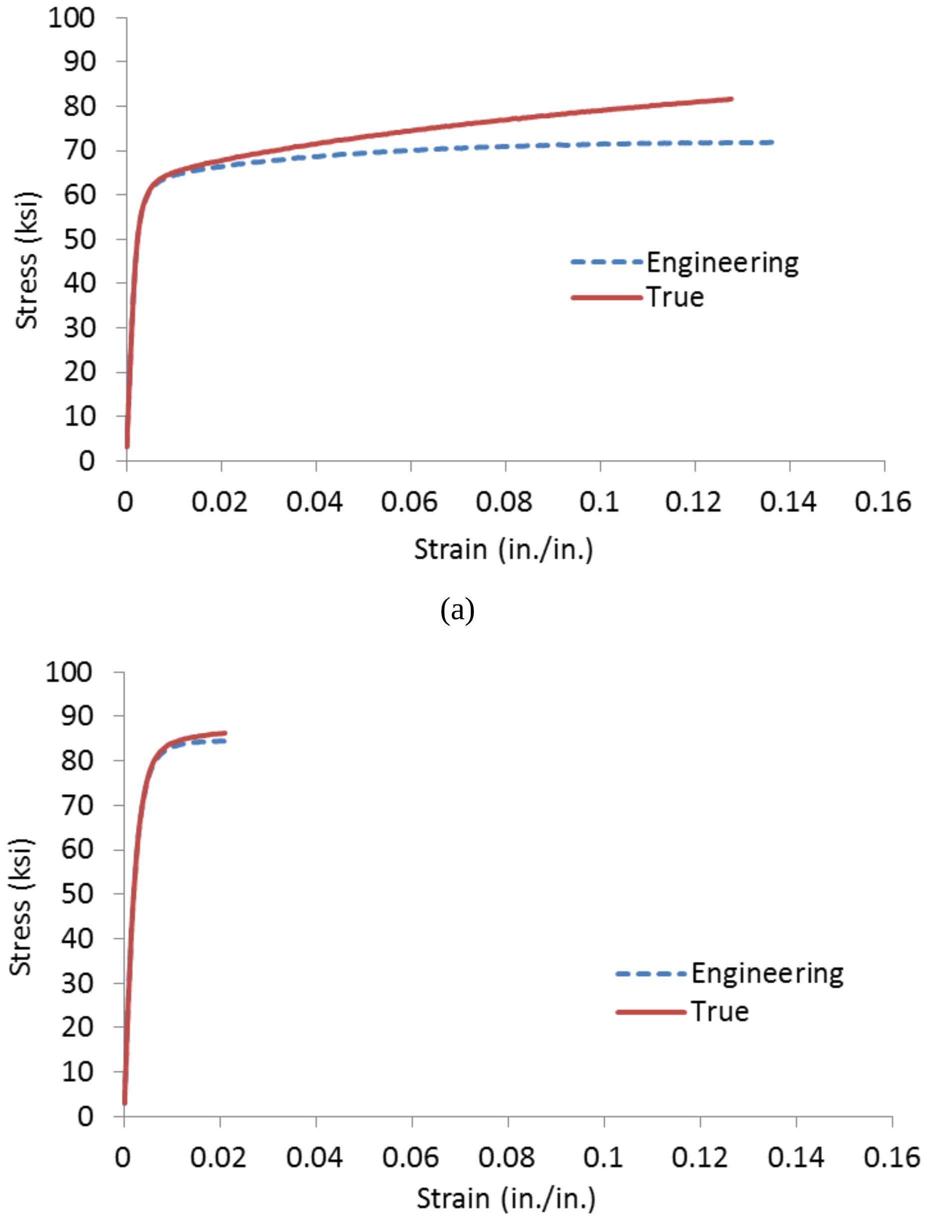

(a)

(b)

Figure 5.1 Engineering and true stress-strain curves for coupon specimen from the HSS 8x6x3/8 (a) c3 and (b) f5 utilized in the FEM

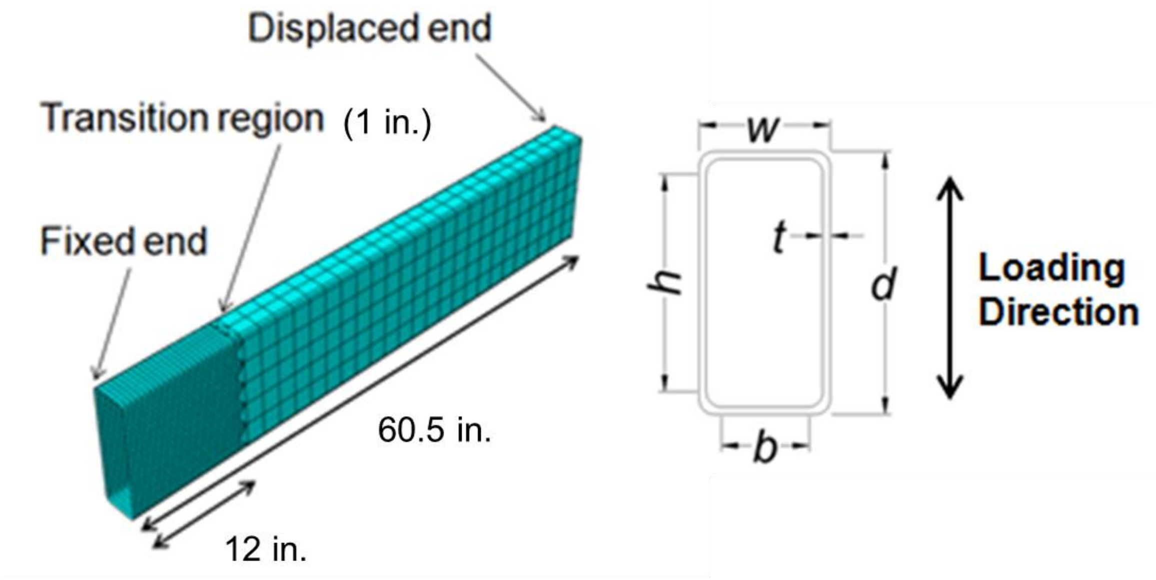

Figure 5.2 Mesh regions and section geometry of a typical HSS finite element model

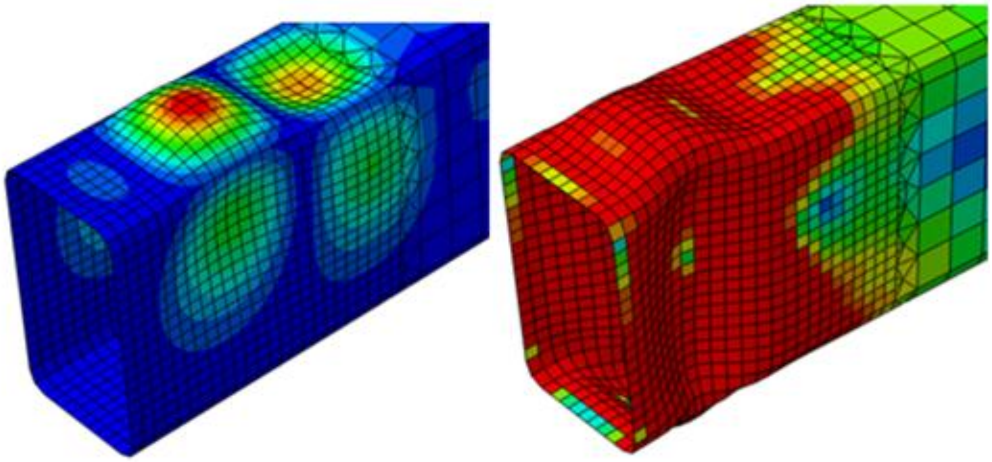

(a) (b)

Figure 5.3 Typical (a) eigenvalue buckling analysis mode shape and (b) resulting buckled shape during cyclic bending loads

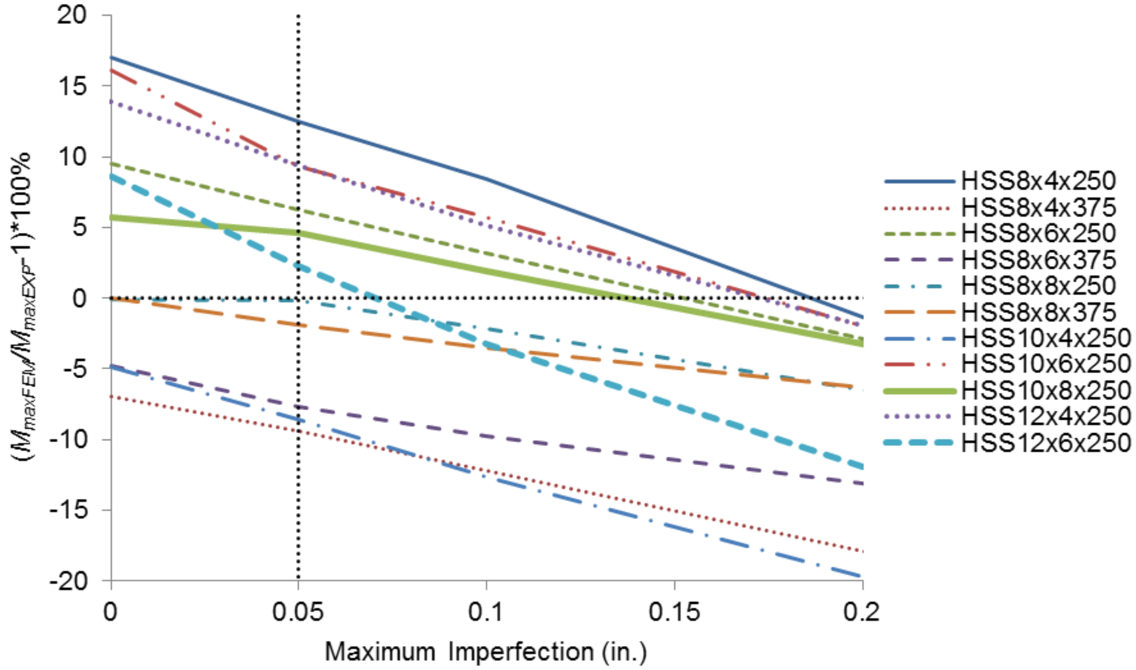

Figure 5.4 Percent error of the maximum moment for the calibrated FEM with respect to the experimental maximum moment

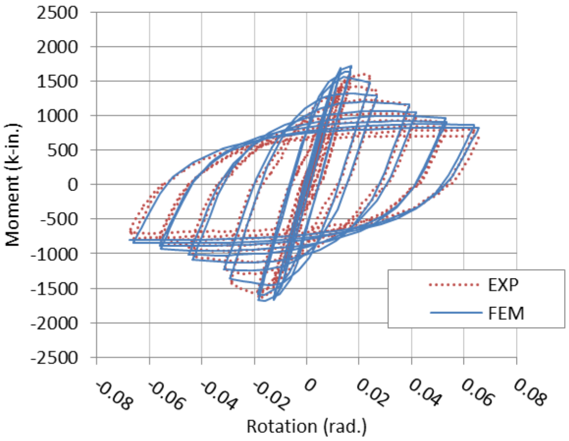

(a) HSS 10x8x1/4

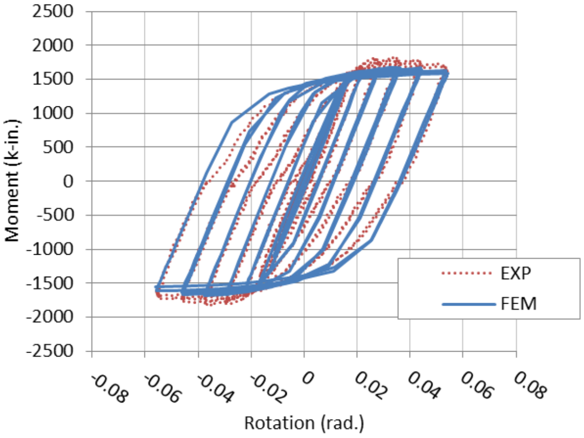

(b) HSS 8x6x3/8

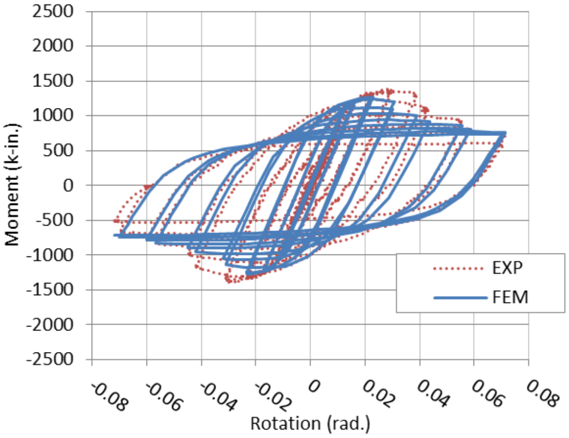

(c) HSS 10x4x1/4

Figure 5.5 Experimental (EXP) and finite element model analysis (FEM) hysteresis curves for the (a) HSS 10x6x1/4, (b) HSS 8x6x3/8, (c) HSS 10x4x1/4

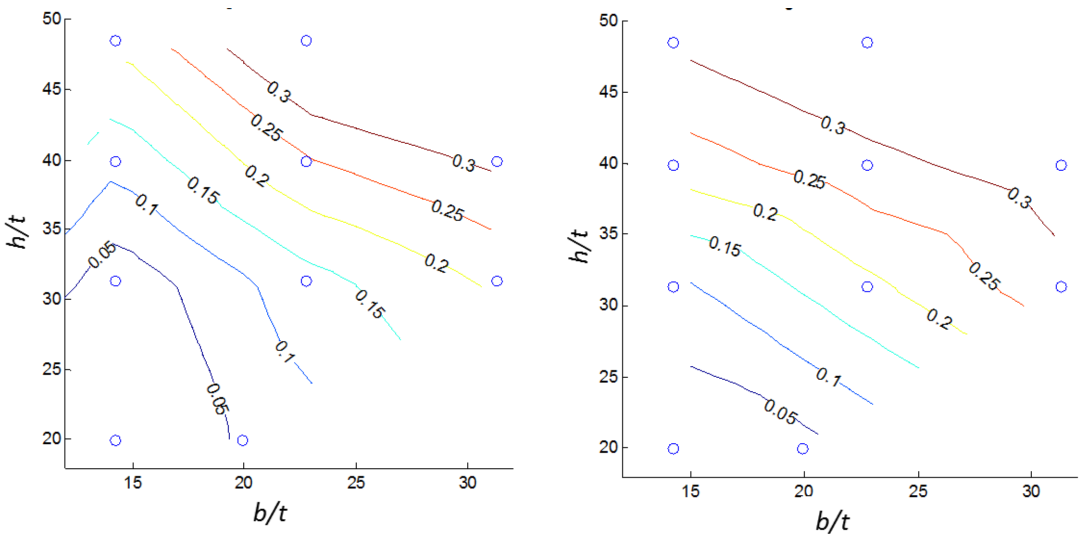

(i) Experimental (ii) Finite element analysis

(a) Degradation of M_{max} at 0.04 rad.

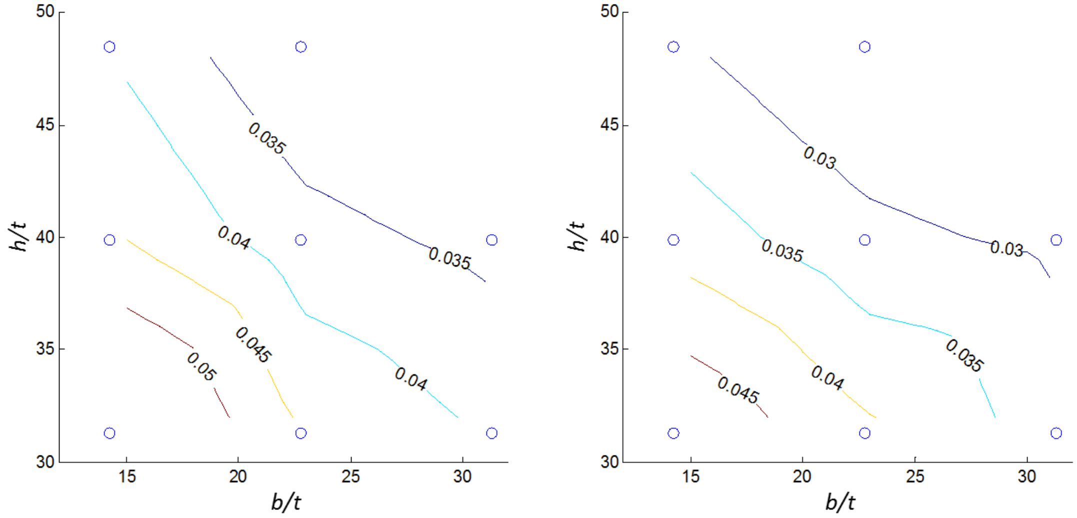

(i) Experimental (ii) Finite element analysis

(b) Rotation at $0.8M_{max}$

Figure 5.6 Effect of the *b/t* and *h/t* ratio for the (a) degradation of M_{max} at 0.04 rad. and the (b) rotational capacity at $0.8M_{max}$

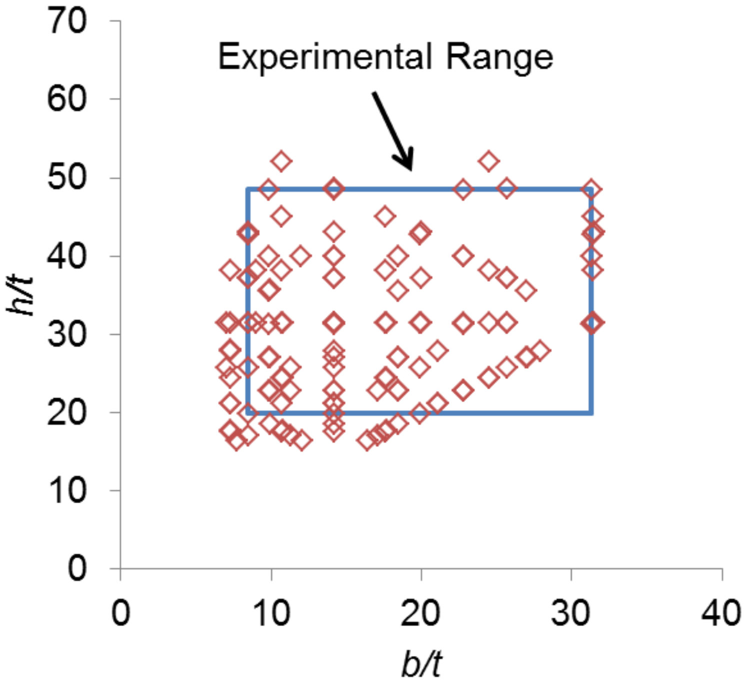

Figure 5.7 133 parametric study specimens with respect to *b/t* and *h/t* ratios

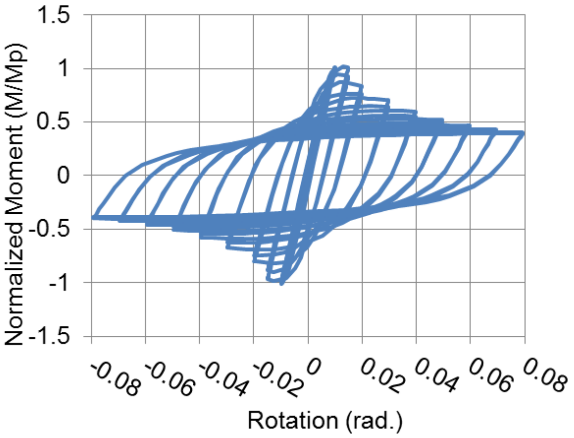

(a) HSS 14x10x5/16

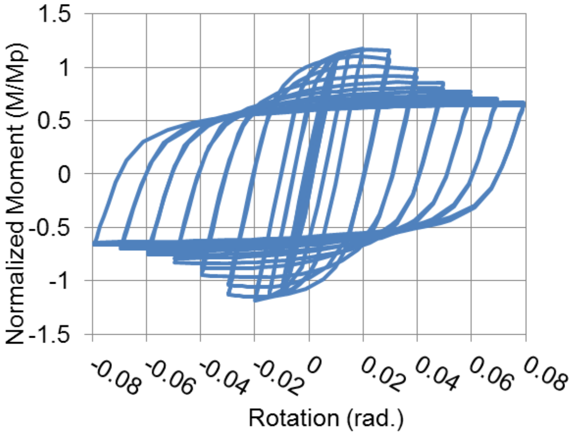

(b) HSS 16x8x1/2

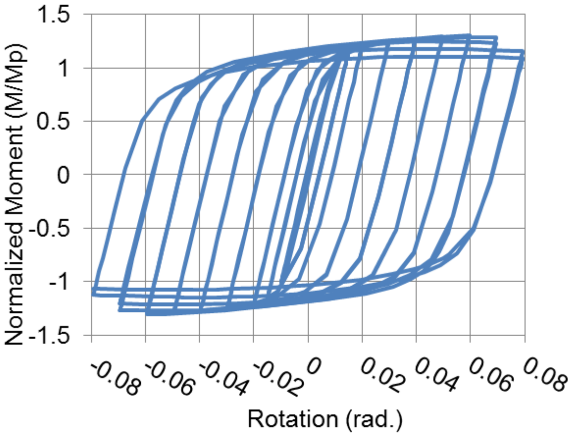

(c) HSS 14x6x5/8

Figure 5.8 Moment-rotation hysteresis from the calibrated FEM for the (a) HSS 14x10x5/16, (b) HSS 16x8x1/2, and (c) HSS 14x6x5/8

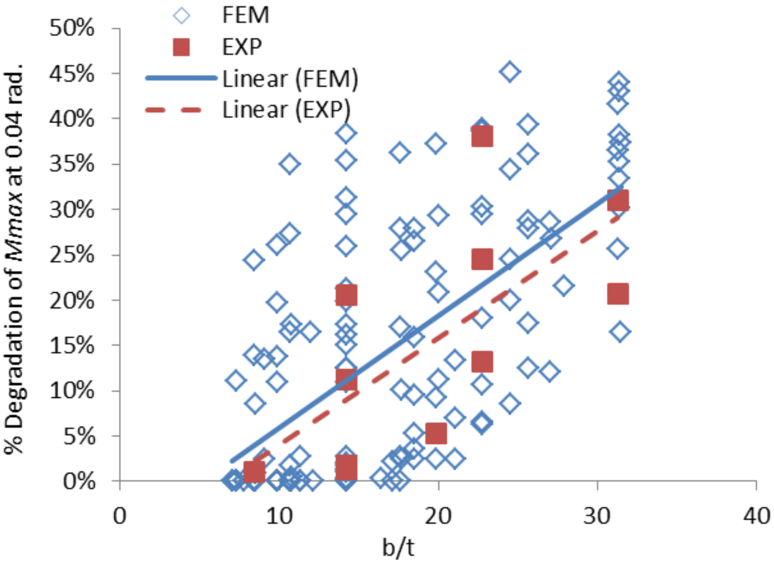

(a)

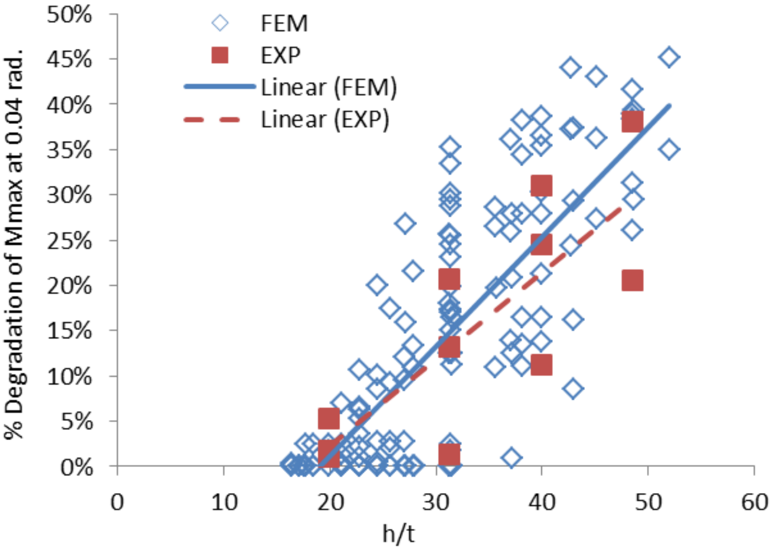

(b)

Figure 5.9 Effect of the (a) *b/t* and (b) *h/t* ratios on the percent degradation of M_{max} at 0.04 rad. for the finite element model and experimental results

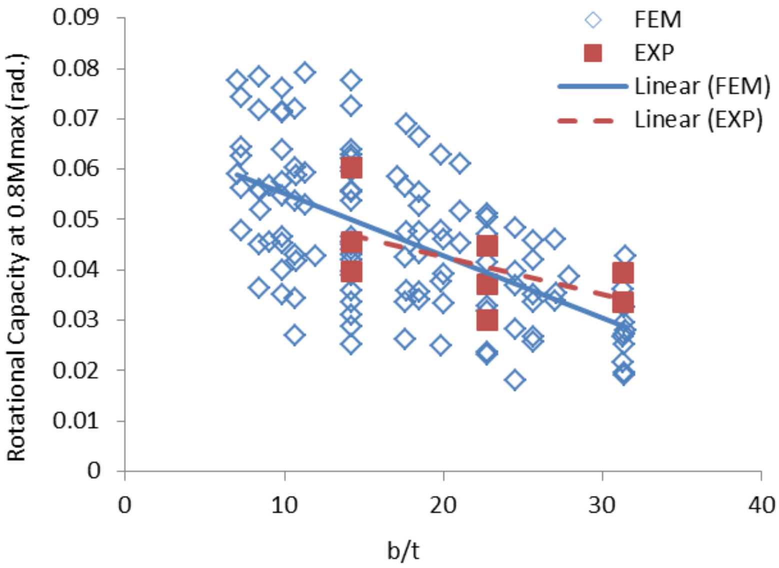

(a)

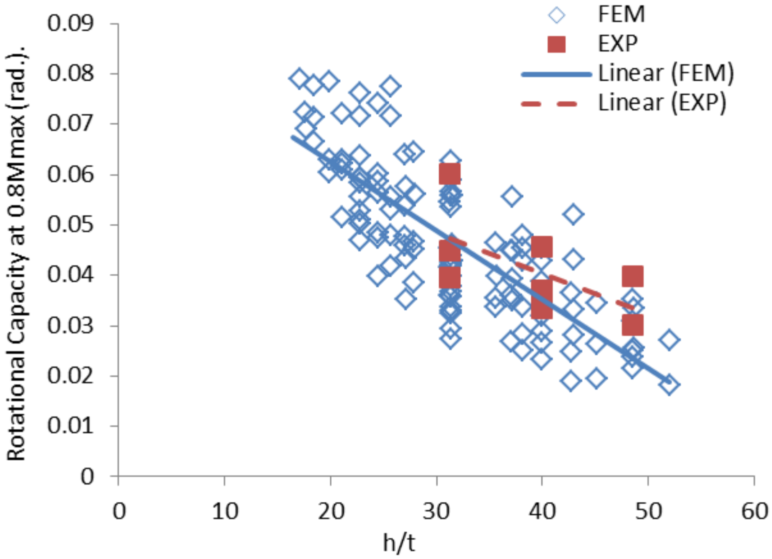

(b)

Figure 5.10 Effect of the (a) *b/t* and (b) *h/t* ratios on the rotational capacity at $0.8M_{max}$ for the finite element model and experimental results

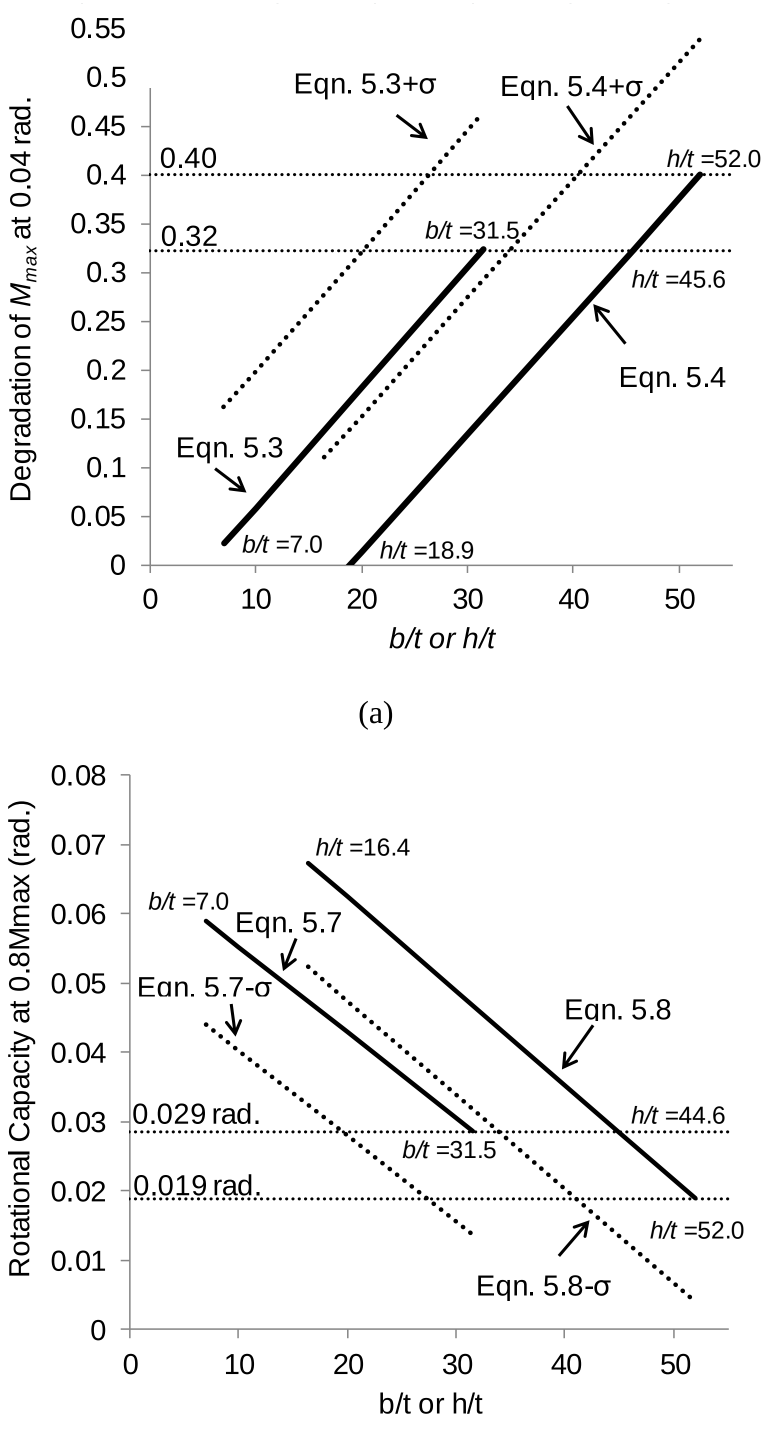

(a)

(b)

Figure 5.11 Prediction of the degradation of the M_{max} at 0.04 rad. and (b) rotational capacity at $0.8M_{max}$

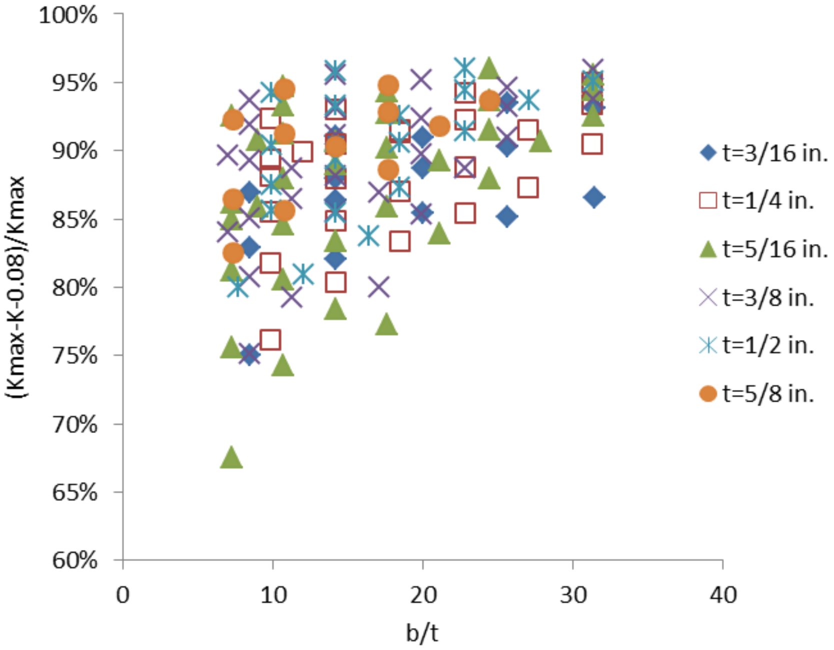

(a)

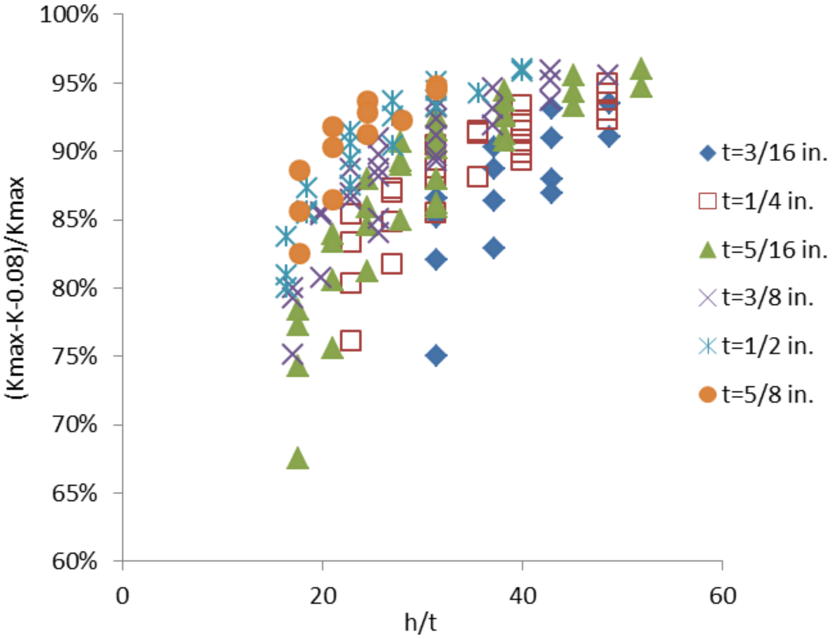

(b)

Figure 5.12 Effect of (a) *b/t* and (b) *h/t* ratios on the percent degradation of the maximum secant stiffnesss at the first 0.08 rad. rotation cycles

CHAPTER 6: DESIGN AND MODELING OF HSS-to-HSS MOMENT CONNECTIONS

6.1 Introduction

Steel moment resisting frames (MRF) have been used in seismic regions because of their ability to resist lateral forces through rigid frame action. In particular, steel MRFs are popular because of their ability to undergo large deformations in a ductile manner. These intermediate and special moment frames are able to withstand large plastic deformations without significant loss of moment capacity or instability that can lead to collapse. The majority of past research has focused on the utilization of moment frame systems composed of wide-flange members. However, hollow structural sections (HSS) have many desirable properties that make them a consideration for use in MRFs in seismic regions including favorable bending, compression, and torsional resistance. These benefits have the potential to further improve the performance of steel MRFs and open up new opportunities for robust and resilient moment frame systems. HSS-to-HSS moment resisting frames have the potential to reduce the seismic weight of a structure, limit lateral bracing requirements, and open new applications for HSS. To fully utilize HSS-to-HSS MRFs in seismic regions, HSS bending behavior and connection detailing requirements suitable for large inelastic cyclic loads must be understood.

HSS have been used extensively in planar and multi-planar truss connections and HSS column-to-wide flange beam connections. Research on HSS truss systems has shown that the ratio of the width of the brace-to-the width of the chord governs the connection load carrying capacity (Davies et al. 1984, Koskimaki and Niemi 1990). As this ratio approaches 1.0, the failure mode changes abruptly because the webs of the chord stiffen the connection. Since moment frame connections must behave in a rigid manner, unstiffened HSS columns typically have not been considered in the past (Packer and Henderson 1997). In Japan, a number of studies addressed this inadequacy by including internal and external connection diaphragms (Kamba and Tabuchi 1994) or by increasing the wall thickness in the connection region (Kamba et al. 1994, Tanaka et al. 1996). Currently, design guides are available with recommendations for the design of HSS-to-HSS moment connections under static loads (CIDECT 2010, Packer et al. 2010) and seismic HSS-to-wide flange moment connections (CIDECT 2005, AISC 2006).

HSS-to-HSS moment connection studies are limited. Many early studies of the behavior of HSS-to-HSS moment connections were performed on Vierendeel truss connections. Unequal width connections are incapable of full moment transfer without reinforcement and are generally too flexible to be considered rigid (Korol et al. 1977). Experimental testing has shown that doubler plates, stiffeners, and haunches can improve performance in monotonically loaded connections.

After the 1994 Northridge earthquake in the U.S., research focused on modeling the behavior of beam-to-column sub-assemblages (El-Tawil et al. 1998). These finite element models more closely examined the state of stress in connections that experienced large inelastic rotations and made recommendations for improving detailing requirements. Only a few models have been developed to consider HSS-to-HSS moment connection behavior. Korol and Mizra (1982) performed a study of 73 combinations of Vierendeel truss branch-to-chord connections considering their ability to transfer moment. The findings showed that increasing the width of the brace from 40% to 80% of the chord width increased the moment capacity by 60%. More recent studies considered the behavior of HSS connections, validating yield line theory approaches (Kosteski et al. 2003). However, again the majority of these approaches focused on behavior under monotonic loading.

Based on the understanding gained for the limiting parameters of HSS in cyclic bending (Chapter 4 and 5) and design philosophies utilized in CIDECT (2005, 2010) and AISC (2010a, 2010b), design procedures for unreinforced and reinforced HSS-to-HSS moment connections are developed. Finite element models of HSS-to-HSS moment connections are used to consider the effect of the beam width-column width ratio (β), beam thickness-column thickness ratio (t_b/t_c), and beam depth on the connection behavior. The use of internal and external diaphragms is also examined to better understand the connections ability to develop the full moment capacity of the HSS beam member. The diaphragm plate thickness (t_{pl}) and length (L_{pl}) are varied to understand their improvement on the performance of the connection under cyclic loads. This study provides insight into connection configurations that are likely suitable for HSS-to-HSS moment connections in seismic applications.

6.2 HSS-to-HSS Moment Connection Design

Design of HSS-to-HSS moment connections is briefly covered in the AISC Specification Chapter K (2010a). The design equations are similar to those implemented in CIDECT Design Guide 3 for Rectangular Hollow Section Joints under Predominately Static Loading (2010). In addition, recommendations are made in the American Welding Society (AWS) D1.1 Specification for prequalified welds connecting HSS members (AWS 2010). The following design procedure utilizes recommendations from these design guides as well as CIDECT Design Guide 9 (2005) regarding seismic design with HSS members, the findings of the beam bending study, and current requirements for wide flange seismic moment connections. All connections are designed to achieve a ductile failure mode. Welds are designed such that brittle weld failure will theoretically not occur in the unreinforced and reinforced HSS-to-HSS connections under large cyclic loads. In all cases, the objective of the design is to allow the connection capacity to reach the plastic moment capacity of the beam. As such, the plastic moment capacity is used as the required minimum load for the connection leading to a capacity based procedure.

6.2.1 Unreinforced HSS-to-HSS Moment Connections

The design of unreinforced moment connections is largely affected by the ability of welds between the beam and column to sustain the required load to achieve plastic hinging in the beam member. The calculation of the effective length of the weld for static loads is detailed in AISC Specification Table K4.1 (AISC 2010a). Some beam members are not able to develop the proper effective weld length to allow the moment capacity of the beam member to be reached. In order to provide the largest capacity weld, all unreinforced HSS-to-HSS moment connections in this study are specified to use complete joint penetration (CJP) welds to connect the HSS beam to the HSS column face.

CJP welds have the advantage of having a strength equivalent to at least the base metal of the joint as specified in AISC Specification Table J2.5 (AISC 2010a).

To determine if base metal yield or rupture will occur, a required weld thickness can be calculated based on Equation 6.1. If the required weld thickness is greater than the thickness of the thinner HSS member being connected, which controls the thickness of the CJP weld, then there is a potential for base metal failure and the full capacity of the beam member may not be met.

$$t_w \geq \frac{\phi_{BM} F_{BM} t}{\phi_w F_w} \qquad \text{Equation 6.1}$$

where,

$F_{BM} = 0.6F_y$ for shear yielding

$F_{BM} = 0.6F_u$ for shear rupture

where, ϕ_{BM} and ϕ_w are resistance factors equal to 0.75, t_w is the weld thickness, F_w is the weld metal tensile strength, and t is the base metal thickness of the thinner connecting member.

A shop drawing for a typical unreinforced connection based on this design is shown in Figure 6.1. Additionally, prequalified weld detailing requirements for HSS-to-HSS joints are shown in Figure 6.2 taken from AWS D1.1 (AWS 2010). Although the design of this connection is straightforward with a CJP weld around the connection, the performance of this connection is not clear under large cyclic loads. The design is meant to minimize weld failure, but has potential for other limitations due to excessive column face plastification, column sidewall crippling, and punching shear failure.

6.2.2 Reinforced HSS-to-HSS Moment Connections

The reinforced moment connection design is determined such that the welds do not fail prior to the formation of the plastic hinge in the HSS beam. This approach will allow for a desired failure mechanism of plastic hinging of the beam member or yielding of the diaphragm plates rather than failure of the weld. A flowchart outlines the design procedure in Figure 6.3. Figure 6.4 and Figure 6.5 show typical details for welded internal and external diaphragm plate HSS-to-HSS moment connections designed based on this procedure. The design procedure is partially based on recommendations from CIDECT Design Guide 9 for connections between HSS columns and wide-flange beam members (CIDECT 2005), particularly in regards to sizing of the diaphragm plate.

The design procedure for external and internal diaphragm plate connections is essentially the same since CJP welds are required to connect both the internal and external diaphragm plates to the HSS column member. However there is a distinct difference in the fabrication of the two connections, the internal diaphragm connection utilizes plates that are continuous through the column. This connection requires cutting the column in two locations and reconnecting the column through CJP welds to the diaphragm plates. The external diaphragm plate connection utilizes plates that are cut to fit around the column face and sidewalls and is CJP welded to the sidewalls of the column. For both connection types, flare bevel groove welds between the beam and diaphragm plates are required and fillet welds are used between the beam and column and between the end of the diaphragm plate and beam.

The determination of the required diaphragm plate thickness and weld sizes differs for the internal and external plate connection because of their different plate widths. A diagram of the forces in the proposed connection is shown in Figure 6.6. All moment developed at the column face is assumed to transfer through the flange plates as a tension and compression force (F_f) as a result of the formation of a plastic hinge in the beam where the diaphragm plates terminate (Equation 6.2, Equation 6.3, and Equation 6.4), while the shear force (V_{cf}) is assumed to transfer through the beam webs (Equation 6.5). Design forces can be calculated considering the requirements of the AISC Seismic Provisions (2010b):

$$M_p = 1.1 R_y F_y Z \qquad \text{Equation 6.2}$$

$$M_{cf} = M_p \frac{\frac{L_b}{2}}{\frac{L_b}{2} - L_{pl}} \qquad \text{Equation 6.3}$$

$$F_f = \frac{M_{cf}}{d_b}$$ Equation 6.4

$$V_{cf} = \frac{M_{cf}}{\frac{L_b}{2}} + V_g$$ Equation 6.5

where M_p is the beam moment capacity, R_y is the material overstrength factor equal to 1.4 for ASTM A500 steel, M_{cf} is the beam moment at the column face, L_b is the beam length, L_{pl} is the plate length extending from the column face, d_b is the beam depth, and V_g is additional shear due to gravity loads.

In order to determine the plate length (L_{pl}) and thickness (t_{pl}), the required weld lengths are selected such that the required thickness due to base metal failure of the diaphragm plate is greater than the required thickness of the plate based on weld requirements needed for connecting the HSS beam to the diaphragm plate. This ensures that the weld connection is not critical. The design is an iterative process such that a plate length extending from the column face is first assumed, then checked to meet the previously stated requirement. Based on the selected length of the plate extending from the column face, the capacity of the two flare-bevel groove welds is calculated (Equation 6.6 and Equation 6.7). The remaining load that could not be carried by the flare bevel groove welds (Equation 6.8) must be transferred through a transverse fillet weld at the end of the diaphragm plate along the beam flange (Equation 6.9). Fillet welds are required to be 0.0625 in. smaller than the connecting element loading to the required diaphragm plate thickness (Equation 6.10).

$$\phi_w R_{n,fb} = 2\phi_w (0.6F_{EXX}) L_{pl} t_{w,fb}$$ Equation 6.6

$$t_{w,fb} = 5/16(R)$$ Equation 6.7

$$\phi_w R_{n,fillet} = \phi_w R_{n,fb} - F_f$$ Equation 6.8

$$t_{w,fillet} = \frac{\phi_w R_{n,fillet}}{\phi_w (0.707)(0.6F_{EXX})(1.5)(b_b - 3t_b)}$$ Equation 6.9

$$t_{pl,weld} = t_{w,fillet} + 0.0625\ in.$$ Equation 6.10

where $\phi_w R_{n,fb}$ is the flare bevel groove weld design strength, $t_{w,fb}$ is the effective thickness of the flare bevel groove weld, R is the flare-bevel groove weld throat, $\phi_w R_{n,fillet}$ is the design strength required in the fillet weld, $t_{w,fillet}$ is the required thickness of fillet weld between the beam flange and the diaphragm plate, F_{EXX} is the weld metal strength, b_b is the width of the flat portion of the beam flange, and $t_{pl,weld}$ is the required plate thickness based on the weld capacity.

Next, a required thickness for the diaphragm plate is determined based on the maximum required thickness of the following limit states modified from AISC for this design procedure: tension yielding (Equation 6.11) (AISC Spec. Eq. J4-1), tension rupture (Equation 6.12) (AISC Spec. Eq. J4-2), and block shear failure (Equation 6.13) (AISC Spec. Eq. J4-5). The maximum plate thickness required based on plate yielding, rupture, and block shear is chosen (Equation 6.14).

$$t_{pl,yield} = \frac{F_f}{\phi_{yield} R_y F_y w_{pl}}$$ Equation 6.11

$$t_{pl,rupture} = \frac{F_f}{\phi_{rupture} R_t F_u w_{pl}}$$ Equation 6.12

$$t_{pl,block\ shear} = \frac{F_f}{\phi_{rupture}\left(0.6R_t F_u \left(2L_{pl}\right) + R_t F_u w_b\right)} \leq \frac{F_f}{\phi_{rupture}\left(0.6R_y F_y \left(2L_{pl}\right) + R_t F_u w_b\right)}$$ Equation 6.13

$$t_{pl,plate} = \max\left[t_{pl,yield}, t_{pl,rupture}, t_{pl,block\ shear}\right]$$ Equation 6.14

where R_y is the material yield overstrength factor equal to 1.3 for ASTM A36 steel, ϕ_{yield} is 0.9, w_{pl} is the plate width at the column face, R_t is the material ultimate tensile overstrength factor equal to 1.2 for ASTM A36 steel, $\phi_{rupture}$ is 0.75, w_b is the beam width, and $t_{pl,plate}$ is the required plate thickness based on plate failure.

The required diaphragm plate thicknesses based on the weld design and plate design are then compared. If the required thickness of diaphragm plate due to weld requirements is greater than the required thickness based on plate requirements, then the plate length is increased and the design procedure is repeated. Increasing the plate length increases the capacity of the flare bevel groove welds and decreases the demand on the fillet weld between the diaphragm plate and the beam flange. This criterion ensures a more ductile failure mechanism (Equation 6.15).

$$t_{pl} = t_{pl,plate} \text{ if } t_{pl,plate} \geq t_{pl,weld} \qquad \text{Equation 6.15}$$

where t_{pl} is the design plate thickness.

Additionally, the panel zone should be checked for its ability to carry the shear forces imparted by the flange plates. The CJP welds between the diaphragm plates and the column allow for complete continuity between the two components. Due to the connection continuity, all the force in the connection is assumed to transfer from the flange plates into the column. AISC Spec. Eq. J10-9 is utilized (Equation 6.16) to calculate the design strength and does not incorporate capacity increases allowed when frame analysis considers panel-zone deformation or frame stability.

$$\phi R_{n,pz} = \phi_{pz} 2\left(0.6 R_y F_y d_c t_c\right) \qquad \text{Equation 6.16}$$

where $\phi_{pz}R_{n,pz}$ is the panel zone design strength, ϕ_{pz} is 0.9, R_y is the material overstrength factor equal to 1.4 for ASTM A500 Gr. B steel, d_c is the column depth, and t_c is the column wall thickness.

Finally, the fillet welds that carry the shear force from the beam to the column face are sized (Equation 6.17).

$$t_{w,shear} = \frac{V_{cf}}{\phi_{weld}(0.707)(2)(0.6F_{EXX})(h_b - 3t_b)} \geq \frac{3}{16} in. \qquad \text{Equation 6.17}$$

where F_{EXX} is the weld metal strength, h_b is the length of the flat portion of the beam web, and t_b is the beam wall thickness

This design procedure is intended to permit the beam member to develop a plastic hinge outside the reinforced diaphragm plate region. Additionally, the reinforced connection intends to limit the likelihood of a brittle weld failure by ensuring that the connection limit state is the ductile failure of the diaphragm plate.

6.3 FEM of HSS-to-HSS Moment Connection

HSS-to-HSS connection designs were developed based on the described procedures considering no shear force due to gravity loads. All of the connection designs had a HSS 10x10x5/8 column and varied in the beam size and reinforcement configuration. The finite element model configuration and boundary conditions are shown in Figure 6.7. Figure 6.8 shows examples of the finite element model for the unreinforced and two (internal and external diaphragm) reinforced connections. The column was 156 in. long and pinned at each end, while the beam member was 115 in. long. This represents a 20 ft. wide bay with a 13 ft. story height. The loading protocol that was applied through displacement of the beam end is shown in Figure 6.9 producing equivalent inter-story drifts up to 0.06 rad.

The finite element mesh was optimized through a convergence study utilizing S4R shell elements in the beam and column members, but did not include initial imperfections as the beam bending study did. For the unreinforced connections, the dense mesh region extended out 24 in. from the column face to better capture the stress fields in the beam plastic hinge region with an element size of 0.5 in. square. The beam was centered and fixed to the column member along all of the beam edges with a tie constraint to represent a fully welded connection. For the unreinforced connection, these constraints represented the CJP weld around the base of the beam member.

The reinforced connections utilized C3D8H hexahedral elements for the diaphragm plates. The dense mesh extended 48 in. away from the column face to approximately 24 in. beyond the end of the diaphragm plate where plastic hinging was expected to occur. Tie constraints were used between all adjoining edges and surfaces in the model to connect the diaphragms and members. For the reinforced connections, the tie constraints represented the CJP welds between the diaphragm plates and column, flare bevel groove welds, and fillet welds along the walls of the HSS beam member.

The material properties for the beam and columns were the same as those used for the beam bending study $F_y = 59.6$ ksi and $F_u = 71.9$ ksi. The diaphragm plates were assumed to behave in an elastic perfectly plastic manner with a yield strength of 36 ksi. Neither the reinforced, nor the unreinforced connection models were able to capture weld failures or material failures. This will have an impact on the accuracy of the results at large rotations. However, this study was intended to give a preliminary understanding of the behavior of HSS-to-HSS moment connection and not necessarily capture their failure mechanism under large deformations.

6.4 HSS-to-HSS Parametric Study Specimens

6.4.1 Unreinforced Connections

Previous studies considered the behavior of monotonically loaded unstiffened HSS-to-HSS exterior and interior connections (Korol et al. 1977). These connections were limited by several failure modes including column face plastification, chord punching shear, fracture of the beam, chord sidewall yielding, and column shear. For connections with small beam width-column width ratios ($\beta \leq 0.85$), the moment capacity could be determined by a yield line analysis. Connections with large beam width-column width ratios ($\beta > 0.85$) were limited by chord side wall failure. To better understand the effect of the beam width-column width ratio (β), beam thickness-column thickness ratio (t_b/t_c), and depth of the beam member on the cyclic hysteretic behavior, finite element models were created considering 39 different beam members. The beam members had depths of 8 in. to 14 in. and ranged in width from 6 in. to 10 in. The beam member wall thickness ranged from 1/4 in. to 5/8 in. These parameters allowed for a wide range of β values to be considered from 0.6 to 1.0. The analysis also allowed for careful consideration of the t_b/t_c ratio that ranged from 0.4 to 1.0. The relevant properties of the column and beam members are provided in Table 6.1 and Table 6.2, respectively.

6.4.2 Reinforced Connections

Based on the design procedure both internal diaphragm and external diaphragm connections were considered. The connections utilized internal and external diaphragms to attempt to decrease the amount of force transferred through the column face while transferring more of the force through the rigid column sidewalls.

This study considered varying beam width-column width ratios (β) from 0.6 to 1.0, beam thickness-column thickness ratios (t_b/t_c) from 0.40 to 1.0, and beam member depths of 8 in., 10 in., 12 in., and 16 in. Additionally for each different beam section, the diaphragm length (L_{pl}) and thickness (t_{pl}) was varied to better understand how these parameters affect the hysteric behavior. The diaphragm plate length and thickness was determined based on the design procedure (Figure 6.3). The minimum length of the diaphragm for each connection was taken as the minimum length needed to ensure that diaphragm plate yielding controlled, avoiding undesirable weld failure that could not be captured in the model. Three diaphragm plate lengths were considered: L_{pl}, L_{pl}+3 in., and L_{pl}+6 in., where L_{pl} is the minimum plate length. The effect of plate thickness (t_{pl}) on the connection behavior was also studied. However, the plate thickness was a function of the plate length. The relevant connections and their properties are shown in Table 6.3. In addition, the diaphragm plate properties are listed in Table 6.4 for the internal diaphragm connections and Table 6.5 for the external diaphragm connection.

6.5 Parametric Study Results

6.5.1 Unreinforced Connections

6.5.1.1 Hysteretic Behavior

All 39 unreinforced connections showed symmetric hysteretic behavior with increasing moment capacity throughout the loading protocol. The connection with the

HSS 12x10x3/8 beam member reached the highest maximum moment capacity of 3420 k-in at 0.06 rad. rotation, while the connection with the HSS 8x6x5/8 beam had the lowest maximum moment of 870 k-in. at 0.06 rad. rotation. The normalized moment capacity was also considered where the connection moment capacity was normalized by the beam moment capacity ($M_{p,beam}=F_{y,exp}Z$ where $F_{y,exp}$=59.6 ksi).. The connection with an HSS 9x9x5/16 beam reached a normalized moment capacity of 0.96 at 0.06 rad. rotation, while the connection with an HSS 12x6x5/8 beam member only achieved a normalized moment capacity of 0.38 at 0.06 rad. These connections correspond to the connections with the largest and smallest normalized moment capacities of all the unreinforced connections, respectively.

As previously noted, the beam width-column width ratio, β, had an important effect on the behavior of the connection. Figure 6.10 shows the normalized moment versus rotation plots for the connections with HSS 12x6x3/8 (β =0.6), HSS 12x8x3/8 (β =0.8), and HSS 12x10x3/8 (β =1.0) beams, while Figure 6.11 shows the displaced shape and von Mises yield contours at 0.06 rad. As β increased from 0.6 to 1.0, the normalized maximum moment increased from 0.60 to 0.94 with larger and fuller hysteresis loops for the connections with larger β values. This behavior was typical of all 39 tested specimens (Figure 6.12). However, none of the connections reached a normalized moment capacity greater than unity. This indicated that the plastic moment capacity of the beam member was not achieved. On average at a β of 0.6, the normalized moment capacity was 0.60, while for connections with β of 1.0, the normalized moment capacity was 0.84. This was a direct result of the beam member more effectively transferring forces to the column sidewalls rather than the flexible column face when β equaled 1.0.

The majority of the inelastic behavior in the connection was concentrated at the column face for all three plotted connections, which was an undesirable mechanism leading to column face plastification and an eventual loss of stiffness in the actual connection (Figure 6.11). The contour plots showed that as the beam width-column width ratio increased, so did the amount of yielding occurring in the beam member. Additionally with an increase in β from 0.6 to 1.0, the distribution of inelastic behavior in regions other than the column face was greatly increased. However even at large beam width-column width ratios, there was still significant yielding at the column face.

The effect the beam thickness-column thickness ratio had on the normalized moment capacity was also explored. The average normalized moment capacity for t_b/t_c of 0.4 was 0.89 and at a t_b/t_c of 1.0 the average normalized moment capacity was 0.48. This finding indicated that a beam member with a large wall thickness relative to the column wall thickness was unable to fully utilize the moment capacity of the HSS beam member leading to prying of the column face. A stiffer beam member tended to pry more against a less stiff column face reducing the connection moment capacity.

6.5.1.2 Energy Dissipation

The ability of a connection to dissipate energy under seismic loads is important given the expected beam hinging mechanisms during a seismic event. The relationship between cumulative energy dissipation at 0.04 rad. rotation and the beam width-column width ratio is plotted in Figure 6.13. The 0.04 rad. drift level was chosen because of current requirements of special moment resisting frames to be able to remain ductile out to this drift level (AISC 2010b). Considering all of the modeled unreinforced HSS-to-HSS moment connections, the connection with the HSS 8x4x1/4 beam member provided the lowest cumulative energy dissipation, 24.8 k-in., up to the 0.04 rad. rotation cycle. The connection with the HSS 10x10x5/8 beam had the highest cumulative energy dissipation up to the 0.04 rad. rotation cycle of 329 k-in. On average, connections with β of 0.6 had a maximum cumulative energy dissipation of 93.5 k-in. at 0.04 rad., while connections with β of 1.0 had an average energy dissipation of 254 k-in. This result indicated that the connections with larger beam width-column width ratios underwent greater inelasticity in the connection.

Additionally, the cumulative energy dissipation increased for deeper beam members. Connections that had β of 0.8 and an 8 in. beam depth had an average cumulative energy dissipation of 80.8 k-in. at 0.04 rad. rotation., while connections with a 12 in. beam depth and a β of 0.8 had an average cumulative energy dissipation of 236 k-in. Analysis of these results reiterated the fact that the amount of energy dissipation is largely a function of the member size. Based on the results, connections most suitable to dissipate energy over their loading protocol would be connections with deep and wide beam members.

6.5.1.3 Secant Stiffness

Secant stiffness of the connection was also calculated for each cycle. The maximum secant stiffness of all modeled connections was 28.8 k/in., which was observed for the connection with the HSS 12x6x5/8 beam member. The minimum secant stiffness of any connection came from the connection with the HSS 8x8x3/8 beam member and was 7.23 k/in. Unlike the normalized moment capacity, there was no strong correlation between maximum secant stiffness and the beam width-column width ratio.

In Figure 6.14 the relationship between the maximum secant stiffness and the beam depth and beam thickness-column thickness ratio is plotted. Connections with a smaller beam depth tended to have lower secant stiffness values. Connections with a beam depth of 8 in. had an average secant stiffness of 9.28 k/in., while connections with a 12 in. beam depth had an average secant stiffness of 17.8 k/in. The secant stiffness was also a function of the beam thickness-column thickness ratio. The average secant stiffness for the unreinforced connection with t_b/t_c=0.4 was 9.24 k/in. and for a connection with t_b/t_c=1.0 the average secant stiffness was 19.8 k/in. The relationship between secant stiffness and the beam depth and beam thickness-column thickness ratio is a function of the properties of both the beam and the column. Deeper and thicker beam sections have inherently higher stiffness and are better able to minimize the lateral displacement in frame systems. However, these beams also have the ability to pry on a relatively less stiff column face, possibly causing an undesirable failure mechanism.

6.5.2 Reinforced Connections

6.5.2.1 Hysteretic Behavior

All internal diaphragm plate reinforced HSS-to-HSS moment connections showed symmetric hysteretic behavior. Unlike the unreinforced connections, nearly all internal diaphragm connections showed some amount of degradation by the 0.04 rad. rotation cycle. This was a result of the beam members to reaching their capacity and subsequently locally buckling. The internal diaphragm connection with an HSS 16x8x3/8 beam and 24 in. long diaphragm plates had the highest maximum moment capacity of 6450 k-in, while the connection with an HSS 8x8x3/8 beam and 12 in. long diaphragm plates had the lowest moment capacity of 2140 k-in. All moment capacities were greater than unity when normalized by the plastic moment capacity of the beam member. The range of normalized plastic moment capacities was 1.13 for the connection with a HSS 12x8x1/4 beam 15 in. long diaphragm plates to 1.35 for the connection with an HSS 12x6x3/8 beam and 21 in. long diaphragm plates. This finding suggested that the connection design procedure was suitable for developing the beam moment capacity.

The beam width-column width ratio, beam thickness-column thickness ratios, beam depth, diaphragm plate length, and diaphragm plate thickness, were varied to consider their effect on connection properties. Figure 6.15 provides the normalized moment rotation hysteresis for the internal diaphragm plate connections with an HSS 10x8x3/8 (L_{pl}=15 in. and t_{pl}=0.75 in.), HSS 12x10x3/8 (L_{pl}=15 in. and t_{pl}=1.0 in.), and HSS 12x8x1/4 (L_{pl}=15 in. and t_{pl}=0.625 in.) beam member, these three connections utilized the shortest allowable diaphragm plate lengths for a given beam size. Additionally, Figure 6.16 provides distributions of the von Mises stresses for the corresponding connections at the maximum moment cycle and at the completion of the loading protocol (0.06 rad.). Of the three sections, the connection with the HSS 10x8x3/8 beam reached the highest normalized maximum moment of 1.26. This connection showed more stable behavior, while the connections with the HSS 12x8x1/4 beam and HSS 12x10x3/8 beam showed degradation after the maximum moment capacity was reached due to local buckling of the beam member. For the connection with the HSS 12x8x1/4 beam, it was evident that local buckling in the beam had begun during the 0.03 rad. rotation cycle (Figure 6.16 (c)).

Similar behavior was observed when analyzing the external diaphragm plate connections. Again, all connections showed symmetric hysteretic behavior with nearly all connections showing some level of degradation by the 0.04 rad. rotation cycle. The connection with the HSS 16x8x3/8 beam and 27 in. long diaphragm plate reached a maximum moment capacity of 6650 k-in, while the connection with the HSS 8x8x3/8 beam and a 15 in. long diaphragm plate had the lowest moment capacity of 2180 k-in. All moment capacities were greater than unity when normalized by the plastic moment capacity of the beam member. The range of normalized plastic moment capacities was 1.15 for the connection with an HSS 12x8x5/8 beam and a 21 in. long plate to 1.37 for the connection with an HSS 12x8x3/8 beam with a 24 in. long plate. These results differed only slightly from the internal diaphragm plate connection and were a function of the connection design.

Figure 6.17 and Figure 6.18 provide the normalized hysteresis and contour plots of the von Mises stresses for the connections with HSS 10x8x3/8 (L_{pl}=18 in. and t_{pl}=0.625 in.), HSS 12x10x3/8 (L_{pl}=18 in. and t_{pl}=0.75 in.), and HSS 12x8x1/4 (L_{pl}=18 in. and t_{pl}=0.5 in.) beams and the smallest allowable diaphragm plate length. Of the three external diaphragm plate connections, the connection with the HSS 10x8x3/8 beam reached the highest normalized maximum moment of 1.28. The connection with the HSS 10x8x3/8 had more stable behavior with continued cycling, while the connections with the HSS 12x10x3/8 and HSS 12x8x1/4 beams showed degradation after the maximum moment capacity was reached as a result of local buckling of the beam member. For the connection with an HSS 12x8x1/4 beam it is evident that a buckle was forming during the 0.03 rad. cycle at which the maximum moment capacity was reached (Figure 6.18 (c)).

For both reinforced connection configurations, the connection detail moved yielding away from the column face and into the beam member. A visual comparison between the von Mises stress in the unreinforced connections (Figure 6.11) and in the reinforced connections (Figure 6.16 and Figure 6.18) made this point evident. Figure 6.19 and Figure 6.20 show the normalized maximum moment capacity with respect to the beam width-column width ratio for the internal and external diaphragm plate connections, respectively. Both connections showed a slight decrease in the normalized moment capacity with an increase in the beam width-column width ratio. Additionally, the beam width-column thickness ratio played an important role in the normalized moment capacity. At a β equal to 0.8 the connections with t_b/t_c of 0.4 and 1.0 tended to have lower maximum moment capacities compared to connections with t_b/t_c of 0.6. Internal diaphragm plate connections with t_b/t_c of 0.4 had an average normalized maximum moment of 1.17 and connections with t_b/t_c of 1.0 had an average normalized maximum moment of 1.20, while connections with t_b/t_c of 0.6 had an average normalized maximum moment of 1.28. Similar results were observed in the external diaphragm plate connection. For the connections, t_b/t_c of 0.6 was found to be more optimal in terms of increasing the normalized maximum moment capacity. This is a result of connections with t_b/t_c of 0.6 representing a balance between being compact enough to develop the beam moment capacity without first buckling and not being so stiff as to buckle the diaphragm plates or the column face.

The plate length had only a small effect on the connection behavior (Figure 6.21 and Figure 6.22). For example, an internal diaphragm plate connection utilizing an HSS 12x8x3/8 beam showed increases in moment capacity from 3910 k-in., to 4000 k-in., to 4160 k-in. for plate lengths of 15 in., 18 in, and 21 in. respectively. This result did not represent a large increase in connection moment capacity. However, in practice the utilization of longer plate lengths is likely advantageous since it reduces stress in the welds.

Overall, reinforced connections performed better in many respects to the unreinforced connections. In terms of moment capacity, the connection with the HSS 12x8x3/8 beam reached a normalized moment capacity 0.77. However, both the internal and external diaphragm connections reached a moment capacity greater than unity. The internal diaphragm connection with the HSS 12x8x3/8 beam (L_{pl}=15 in.) reached a normalized moment capacity of 1.24. The external diaphragm connection with the HSS 12x8x3/8 beam (L_{pl}=18 in.) reached a normalized moment capacity of 1.28. The reinforcing diaphragm plates allowed the connections to form plastic hinges in the beam member increasing their suitability for seismic applications.

6.5.2.2 Energy Dissipation

Reinforced connections were able to develop larger cumulative energy dissipation levels at 0.04 rad. than their corresponding unreinforced connections. The unreinforced connection with the HSS 12x8x3/8 beam member had cumulative energy dissipation at 0.04 rad. of 229 k-in., while the internally reinforced connection with an HSS 12x8x3/8 beam member and a 15 in. long plate had a cumulative energy dissipation of 362 k-in. at 0.04 rad. and the corresponding externally reinforced connection with a 18 in. long plate had a cumulative energy dissipation of 353 k-in. at 0.04 rad. It is clear that both internal and external diaphragms greatly improved the connection’s energy dissipation capacity throughout cycling in addition to developing a more desirable yielding mechanism.

Figure 6.23 and Figure 6.24 provide the cumulative energy dissipation at the 0.04 rad. rotation level with respect to β for the internal and external diaphragm plate connections. Analysis of the data showed that increasing the beam width-column width ratio led to increased cumulative energy dissipation capacity for both reinforced connections. For the internal diaphragm connection with β of 0.6 the average cumulative energy dissipation was 332 k-in. at 0.04 rad. and with a β of 1.0 the average cumulative energy dissipation was 417 k-in. at 0.04 rad. A similar result is found for the external diaphragm connection with β of 0.6, the average cumulative energy dissipation was 336 k-in. at 0.04 rad. and with a β of 1.0, the average cumulative energy dissipation was 406 k-in. at 0.04 rad. Connections with higher beam width-column width ratios are better able to move load into the column sidewalls further improving on the reinforced connection performance. Additionally, when comparing the connections with β of 0.8, increasing the beam depth from 8 in. to 16 in. improved the cumulative energy dissipation at 0.04 rad. from an average of 100 k-in. to an average of 655 k-in. for the internal diaphragm connection and from an average 105 k-in. to an average of 660 k-in. for the external diaphragm connection. Deeper beam members allowed for increased cumulative energy dissipation as a result of the ability of the reinforced connection to develop the beam moment capacity.

6.5.2.3 Secant Stiffness

The maximum secant stiffness observed for the reinforced connections was greater than the maximum secant stiffness observed for the unreinforced connections. The unreinforced connection with the HSS 12x8x3/8 beam member had a maximum secant stiffness of 19.4 k/in, while the internally reinforced connection with an HSS 12x8x3/8 beam member and a 15 in. long plate (t_{pl}=0.875 in.) had a maximum secant stiffness of 32.3 k/in. and the corresponding externally reinforced connection with a 18 in. long plate (t_{pl}=0.75 in.) had a maximum secant stiffness 33.1 k/in. The overall maximum secant stiffness, 53.6 k/in., was seen in the internal diaphragm connection with an HSS 16x8x3/8 beam and a 24 in. long plate (t_{pl}=1.0 in.). The external diaphragm connection with an HSS 16x8x3/8 beam and a 27 in. long plate (t_{pl}=0.875 in.) had the largest secant stiffness of 55.2 k/in. for the external diaphragm plate connections. Because increasing the thickness of the diaphragm plates increased the moment of inertia, it was not surprising that the maximum secant stiffness correlated with the plate thickness (Figure 6.25 and Figure 6.26). Secant stiffness is important in limiting the story drift, so to minimize drift levels the maximum plate thickness that allows for ductile yielding of the plate rather than weld failure should be used.

6.6 Conclusions

A design procedure for detailing unreinforced and reinforced HSS-to-HSS moment connections was developed. The welded reinforced HSS-to-HSS moment connections were detailed to develop plastic hinging in the HSS beam member while minimizing the likelihood of a non-ductile weld failure. This behavior was accomplished in the design by ensuring a failure mechanism of diaphragm plate yielding or plastic hinging of the beam member. Finite element models of 39 unreinforced, 24 internal diaphragm plate, and 24 external diaphragm plate HSS-to-HSS moment connections were analyzed. Several important geometric parameters, such as the beam width-column width and beam thickness-column thickness ratio, were considered to understand their effect on the connection moment capacity, energy dissipation, and secant stiffness.

1. A design procedure for the design of fully-welded reinforced HSS-to-HSS moment connections utilizing external and internal diaphragm plate connections was developed. The procedure used the beam moment capacity to design the connection and required yielding in the beam diaphragm plates or plastic hinging in the beam member to avoid non-ductile failure of the connection welds.
2. Finite element models of 39 different unreinforced HSS-to-HSS moment connections showed the unreinforced connections lacked the ability to develop the beam moment capacity with a maximum normalized moment capacity of 96% of the expected beam plastic moment capacity.
3. Analyses showed that the behavior of unreinforced HSS-to-HSS moment connections was highly dependent on the beam width-column width ratio (β). Increasing β from 0.6 to 1.0 caused an average increase of 23% of the normalized moment capacity.

4. Twenty-four internal and twenty-four external diaphragm plate connection models showed that both internal and external reinforced HSS-to-HSS diaphragm plate connections had improved hysteretic behavior with all connections having a normalized moment capacity greater than unity.
5. When utilizing reinforced HSS-to-HSS moment connections, *b/t* and *h/t* ratios should be selected to minimize local buckling of the beam member based on recommendations in Chapter 5.
6. A comparison of the unreinforced, external diaphragm (L_{pl}=18 in.), and internal diaphragm (L_{pl}=15 in.) HSS-to-HSS moment connections utilizing a HSS 12x8x3/8 beam and HSS 10x10x5/8 column showed that diaphragm plates significantly improved the connection performance in terms of normalized moment capacity, energy dissipation, and secant stiffness.

Table 6.1 HSS-to-HSS moment connection column section properties

HSS Column Member (in. x in. x in.)	Depth d_c (in.)	Width w_c (in.)	Thickness t_c (in.)	h/t	b/t	Column Plastic Section Modulus Z (in.^{3})	Column Plastic Moment Capacity $M_{p,c}$ (k-in.)
HSS 10x10x5/8	10	10	0.581	15.7	15.7	73.2	4360

Table 6.2 Unreinforced HSS-to-HSS moment connection sections

HSS Beam Member (in. x in. x in.)	Depth d_b (in.)	Width w_b (in.)	Thickness t_b (in.)	h/t	b/t	Beam Plastic Section Modulus Z (in.^{3})	Beam Plastic Moment Capacity $M_{p,b}$ (k-in.)	Beam Width-Column Width Ratio β	t_b/t_c
HSS 8x6x1/4	8	6	0.233	32.8	24.3	16.9	1007	0.6	0.40
HSS 8x6x5/16	8	6	0.291	26.0	19.1	20.6	1227	0.6	0.50
HSS 8x6x3/8	8	6	0.349	21.4	15.7	24.1	1435	0.6	0.60
HSS 8x6x1/2	8	6	0.465	15.7	11.4	30.5	1817	0.6	0.80
HSS 8x6x5/8	8	6	0.581	12.3	8.83	36.1	2150	0.6	1.00
HSS 10x6x1/4	10	6	0.233	41.4	24.3	23.6	1406	0.6	0.40
HSS 10x6x5/16	10	6	0.291	32.9	19.1	28.8	1715	0.6	0.50
HSS 10x6x3/8	10	6	0.349	27.2	15.7	33.8	2013	0.6	0.60
HSS 10x6x1/2	10	6	0.465	20.0	11.4	43	2561	0.6	0.80
HSS 10x6x5/8	10	6	0.581	15.7	8.83	51.3	3055	0.6	1.00
HSS 12x6x5/16	12	6	0.291	39.7	19.1	38.1	2269	0.6	0.50
HSS 12x6x3/8	12	6	0.349	32.9	15.7	44.8	2668	0.6	0.60
HSS 12x6x1/2	12	6	0.465	24.3	11.4	57.4	3419	0.6	0.80
HSS 12x6x5/8	12	6	0.581	19.2	8.83	68.8	4098	0.6	1.00
HSS 14x6x3/8	14	6	0.349	38.6	15.7	57.3	3413	0.6	0.60
HSS 9x7x1/4	9	7	0.233	37.1	28.5	22.2	1322	0.7	0.40
HSS 9x7x5/16	9	7	0.291	29.4	22.6	27.1	1614	0.7	0.50
HSS 9x7x3/8	9	7	0.349	24.3	18.6	31.8	1894	0.7	0.60
HSS 9x7x1/2	9	7	0.465	17.9	13.6	40.5	2412	0.7	0.80
HSS 9x7x5/8	9	7	0.581	14.0	10.5	48.3	2877	0.7	1.00

Table 6.2 (cont.) Unreinforced HSS-to-HSS moment connection sections

HSS Beam Member (in. x in. x in.)	Depth d_b (in.)	Width w_b (in.)	Thickness t_b (in.)	h/t	b/t	Beam Plastic Section Modulus Z (in.^{3})	Beam Plastic Moment Capacity $M_{p,b}$ (k-in.)	Beam Width-Column Width Ratio β	t_b/t_c
HSS 8x8x5/16	8	8	0.291	26.0	26.0	25.1	1495	0.8	0.50
HSS 8x8x3/8	8	8	0.349	21.4	21.4	29.4	1751	0.8	0.60
HSS 8x8x1/2	8	8	0.465	15.7	15.7	37.5	2234	0.8	0.80
HSS 8x8x5/8	8	8	0.581	12.3	12.3	44.7	2662	0.8	1.00
HSS 10x8x5/16	10	8	0.291	32.9	26.0	34.4	2049	0.8	0.50
HSS 10x8x3/8	10	8	0.349	27.2	21.4	40.5	2412	0.8	0.60
HSS 10x8x1/2	10	8	0.465	20.0	15.7	51.9	3091	0.8	0.80
HSS 10x8x5/8	10	8	0.581	15.7	12.3	62.2	3705	0.8	1.00
HSS 12x8x5/16	12	8	0.291	39.7	26.0	44.9	2674	0.8	0.50
HSS 12x8x3/8	12	8	0.349	32.9	21.4	53	3157	0.8	0.60
HSS 12x8x1/2	12	8	0.465	24.3	15.7	68.1	4056	0.8	0.80
HSS 9x9x5/16	9	9	0.291	29.4	29.4	32.1	1912	0.9	0.50
HSS 9x9x3/8	9	9	0.349	24.3	24.3	37.8	2251	0.9	0.60
HSS 9x9x1/2	9	9	0.465	17.9	17.9	48.4	2883	0.9	0.80
HSS 9x9x5/8	9	9	0.581	14.0	14.0	58.1	3460	0.9	1.00
HSS 10x10x3/8	10	10	0.349	27.2	27.2	47.2	2811	1.0	0.60
HSS 10x10x1/2	10	10	0.465	20.0	20.0	60.7	3615	1.0	0.80
HSS 10x10x5/8	10	10	0.581	15.7	15.7	73.2	4360	1.0	1.00
HSS 12x10x3/8	12	10	0.349	32.9	27.2	61.1	3639	1.0	0.60

Table 6.3 Reinforced HSS-to-HSS moment connection sections

HSS Beam Member (in. x in. x in.)	Depth d_b (in.)	Width w_b (in.)	Thickness t_b (in.)	h/t	b/t	Beam Plastic Section Modulus Z (in.^{3})	Beam Plastic Moment Capacity $M_{p,b}$ (k-in.)	Beam Width-Column Width Ratio β	t_b/t_c
HSS 12x6x3/8	12	6	0.349	32.9	15.7	44.8	2668	0.6	0.60
HSS 8x8x3/8	8	8	0.349	21.4	21.4	29.4	1751	0.8	0.60
HSS 10x8x3/8	10	8	0.349	27.2	21.4	40.5	2412	0.8	0.60
HSS 12x8x1/4	12	8	0.233	50.0	32.8	36.6	2180	0.8	0.40
HSS 12x8x3/8	12	8	0.349	32.9	21.4	53	3157	0.8	0.60
HSS 12x8x5/8	12	8	0.581	19.2	12.3	82.1	4890	0.8	1
HSS 16x8x3/8	16	8	0.349	44.3	21.4	82.1	4890	0.8	0.60
HSS 12x10x3/8	12	10	0.349	32.9	27.2	61.1	3639	1	0.60

Table 6.4 Internal reinforced HSS-to-HSS connection diaphragm plate sizes

HSS Beam Member (in. x in. x in.)	Diaphragm Plate Length L_{pl} (in.)	Diaphragm Plate Thickness t_{pl} (in.)
HSS 12x6x3/8	15	0.75
	18	0.75
	21	0.75
HSS 8x8x3/8	12	0.75
	15	0.75
	18	0.75
HSS 10x8x3/8	15	0.75
	18	0.75
	21	0.875
HSS 12x8x1/4	15	0.625
	18	0.625
	21	0.625
HSS 12x8x3/8	15	0.875
	18	0.875
	21	0.875
HSS 12x8x5/8	18	1.25
	21	1.375
	24	1.375
HSS 16x8x3/8	18	1.0
	21	1.0
	24	1.0
HSS 12x10x3/8	15	1.0
	18	1.0
	21	1.0

Table 6.5 External reinforced HSS-to-HSS connection diaphragm plate sizes

HSS Beam Member (in. x in. x in.)	Diaphragm Plate Length L_{pl} (in.)	Diaphragm Plate Thickness t_{pl} (in.)
HSS 12x6x3/8	18	0.625
	21	0.625
	24	0.625
HSS 8x8x3/8	15	0.625
	18	0.625
	21	0.625
HSS 10x8x3/8	18	0.625
	21	0.625
	24	0.625
HSS 12x8x1/4	18	0.5
	21	0.5
	24	0.5
HSS 12x8x3/8	18	0.75
	21	0.75
	24	0.75
HSS 12x8x5/8	21	1.125
	24	1.125
	27	1.125
HSS 16x8x3/8	21	0.875
	24	0.875
	27	0.875
HSS 12x10x3/8	18	0.75
	21	0.75
	24	0.875

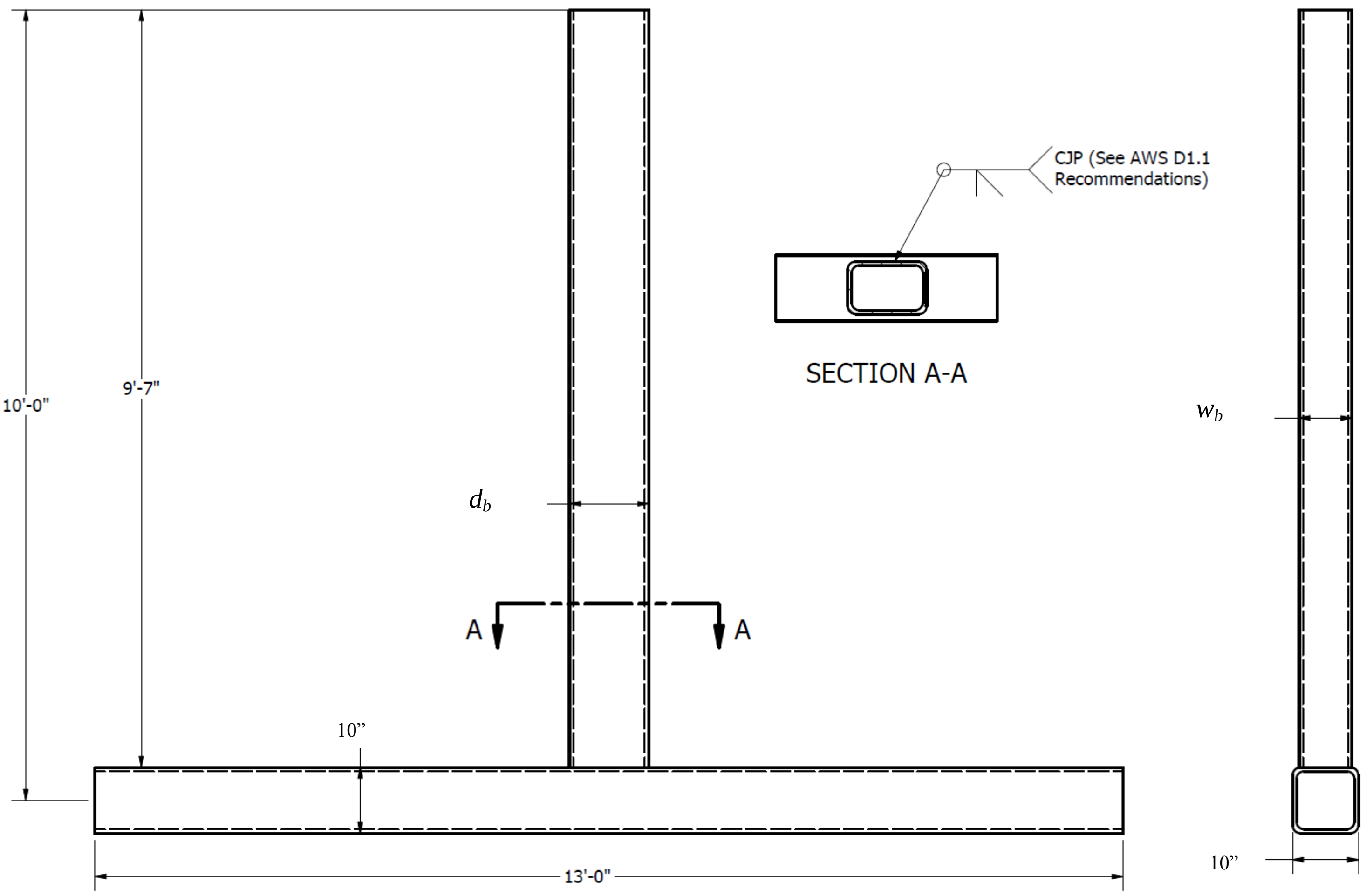

Figure 6.1 Typical unreinforced HSS-to-HSS moment connection

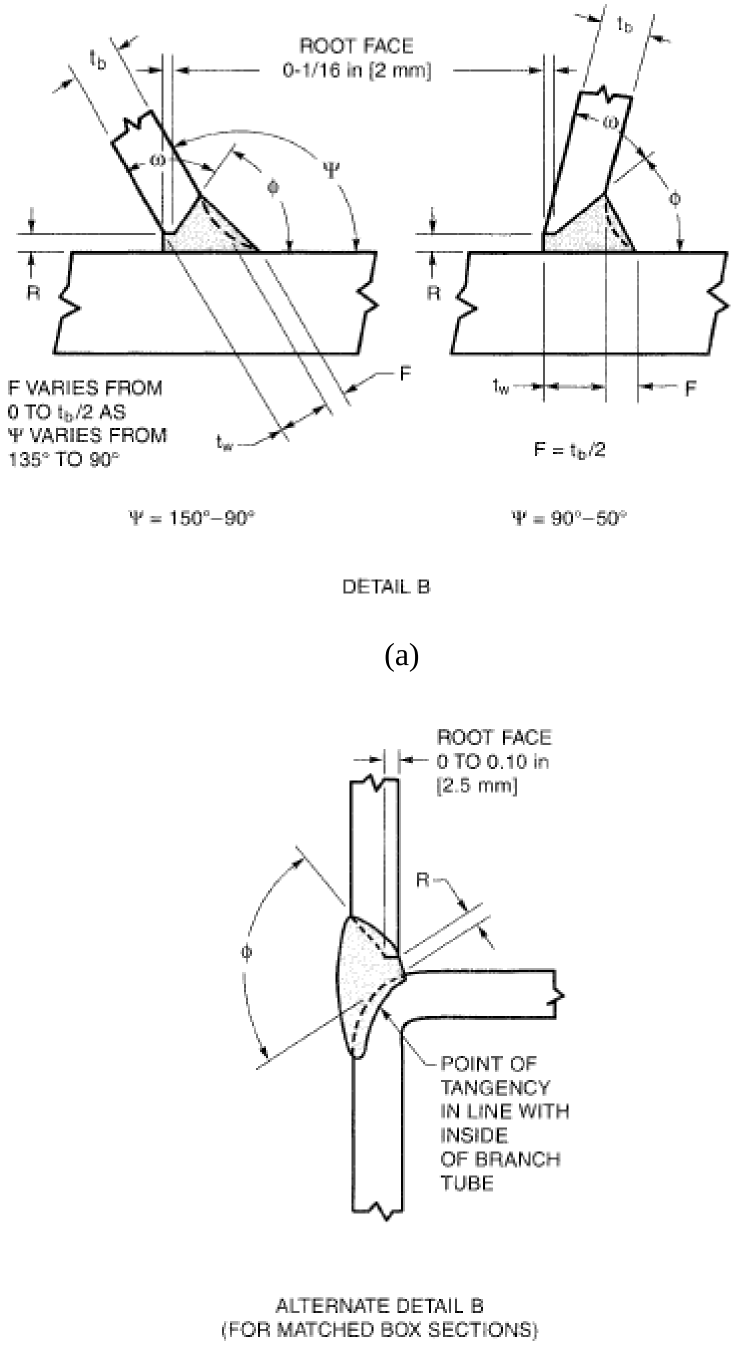

(a)

(b)

Figure 6.2 Prequalified CJP welds for HSS-to-HSS connections (a) matched and unmatched connections and (b) webs of matched connections (AWS 2010)

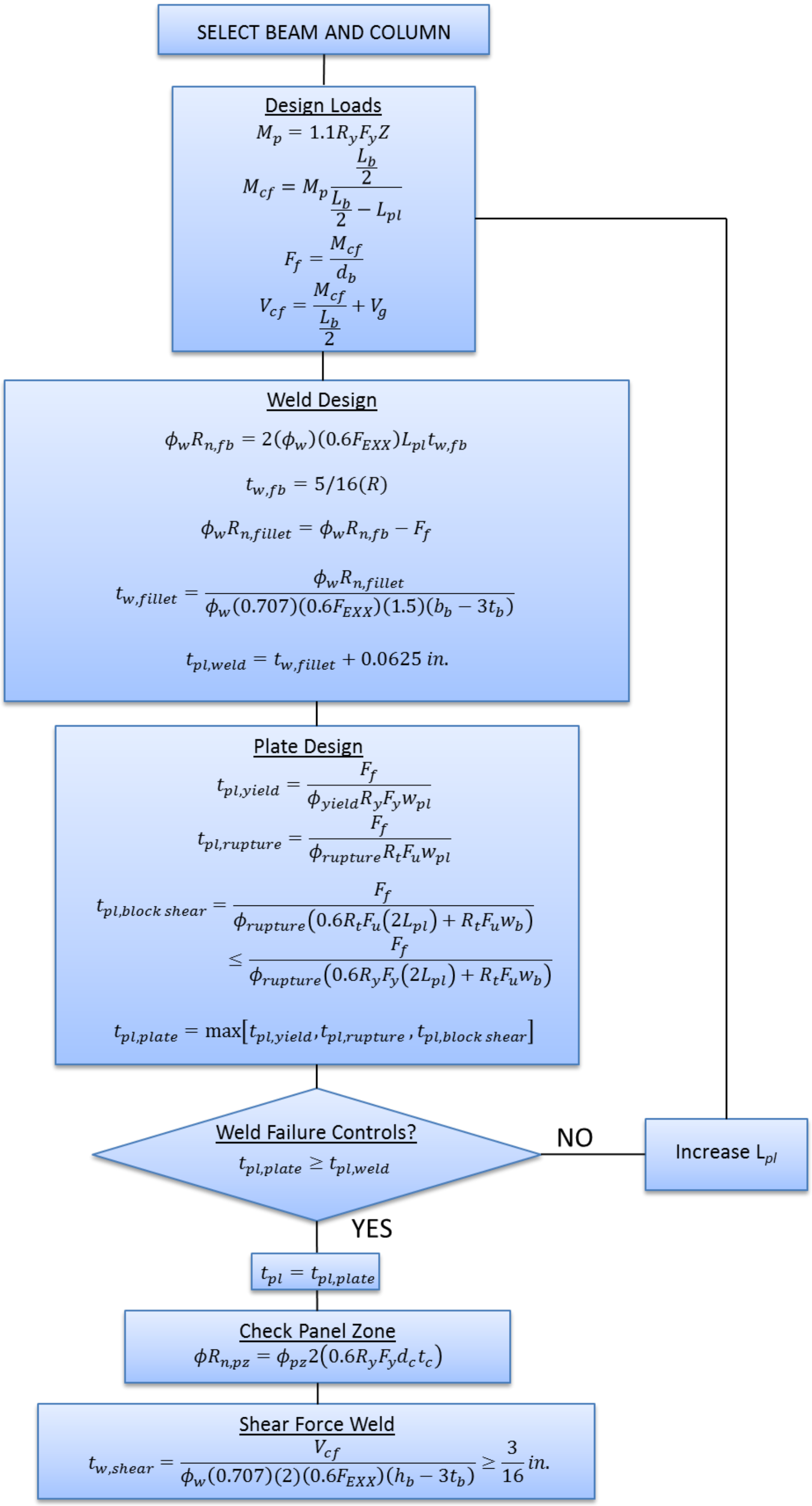

Figure 6.3 Flowchart for the design of internal and external reinforced diaphragm plate connections

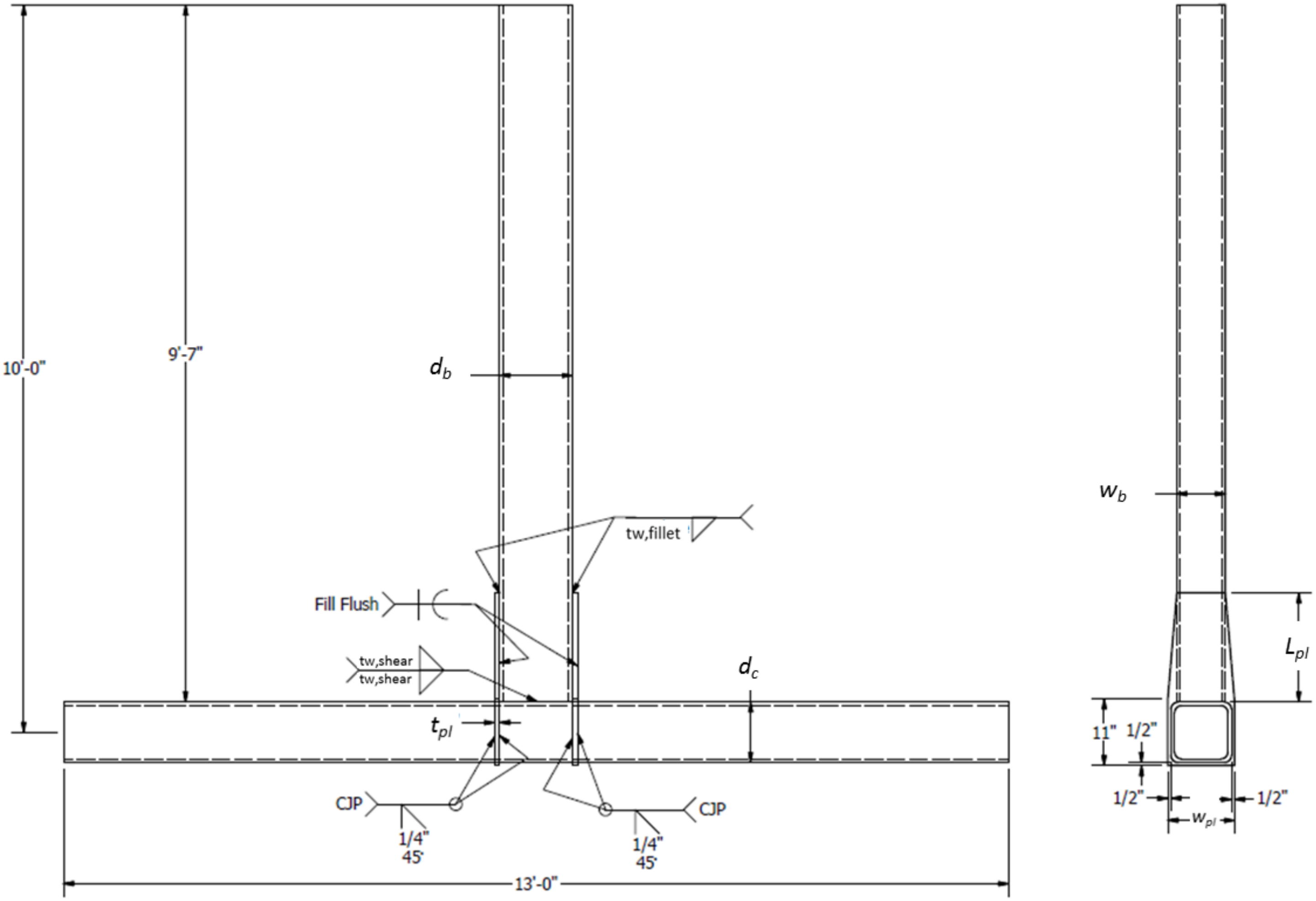

Figure 6.4 Typical internal diaphragm plate HSS-to-HSS moment connection

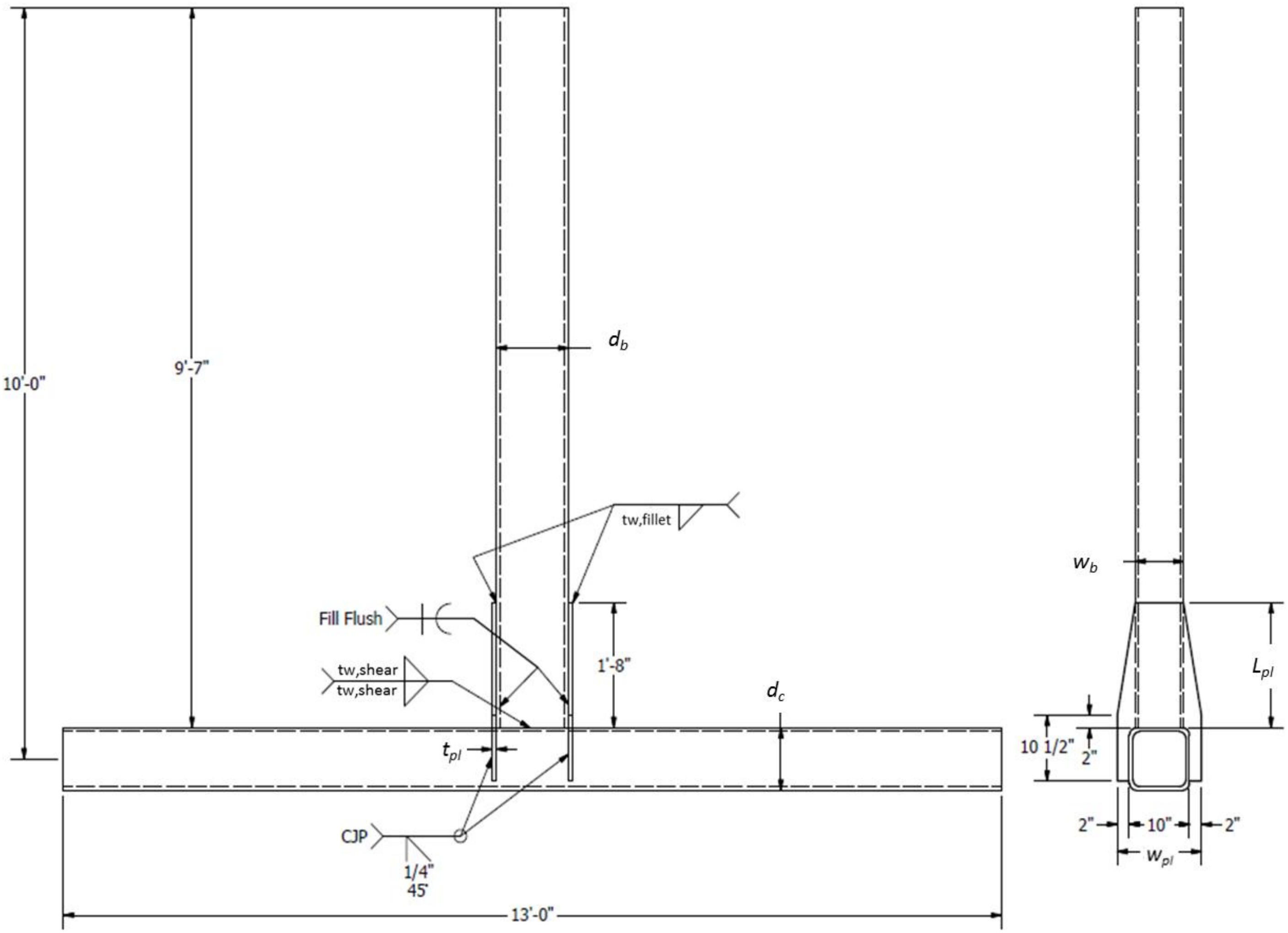

Figure 6.5 Typical external diaphragm plate HSS-to-HSS moment connection

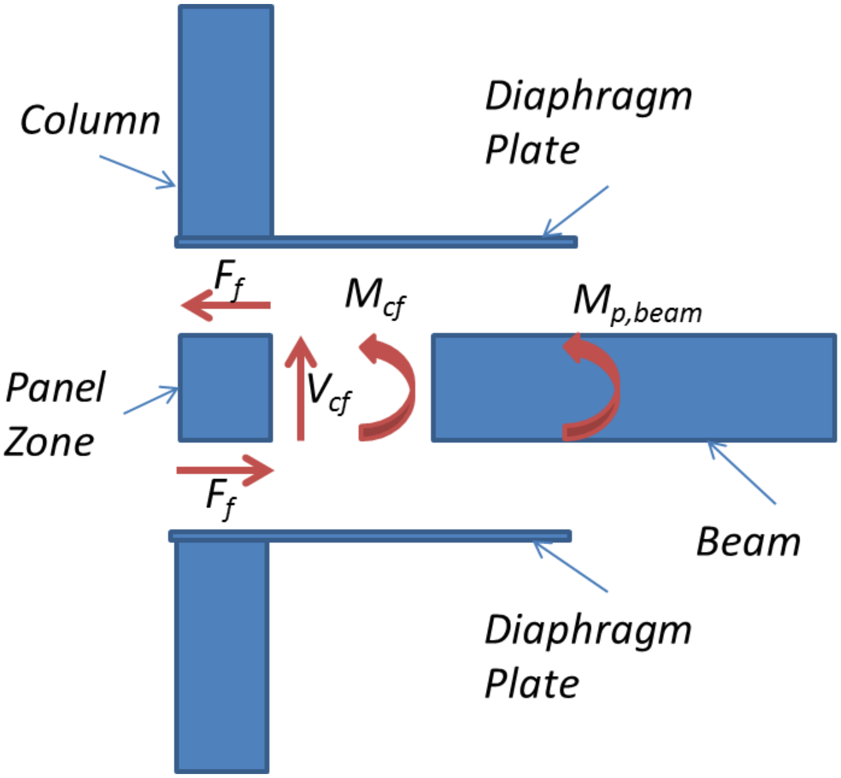

Figure 6.6 Reinforced HSS-to-HSS moment connection forces

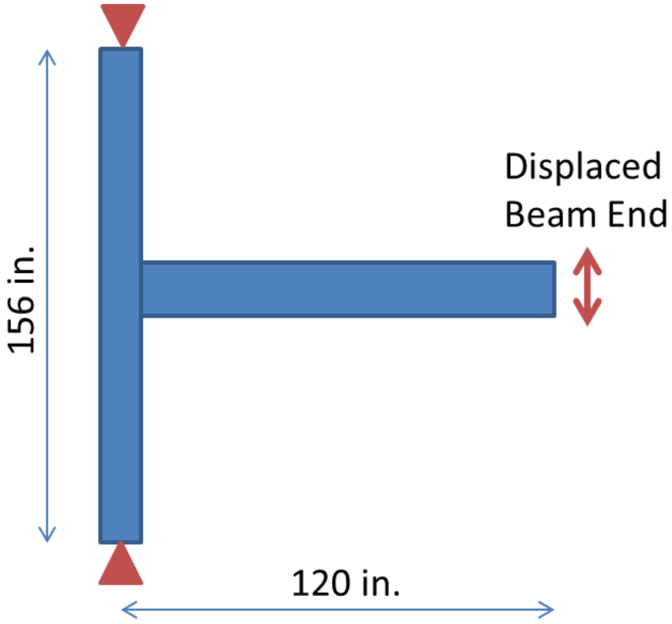

Figure 6.7 Finite element model configuration and boundary conditions

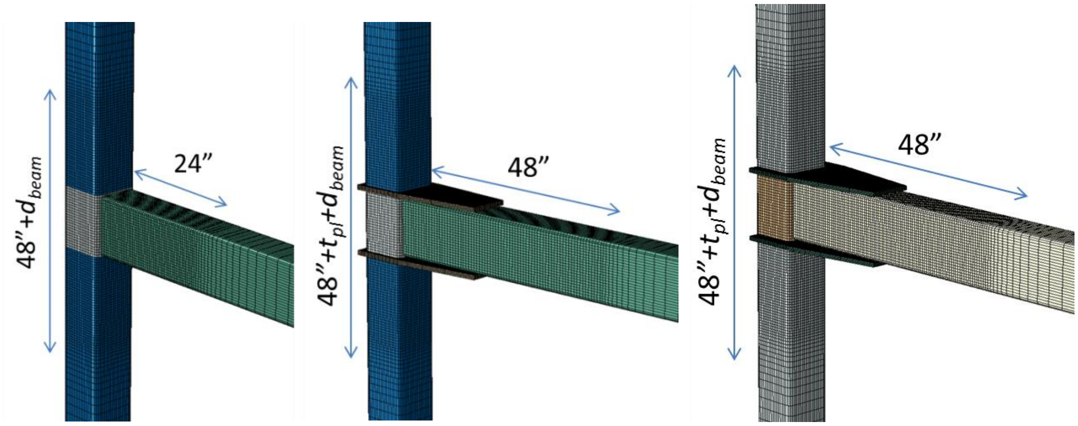

(a) (b) (c)

Figure 6.8 Finite element model of the (a) unreinforced, (b) internal diaphragm plate, and (c) external diaphragm plate connections

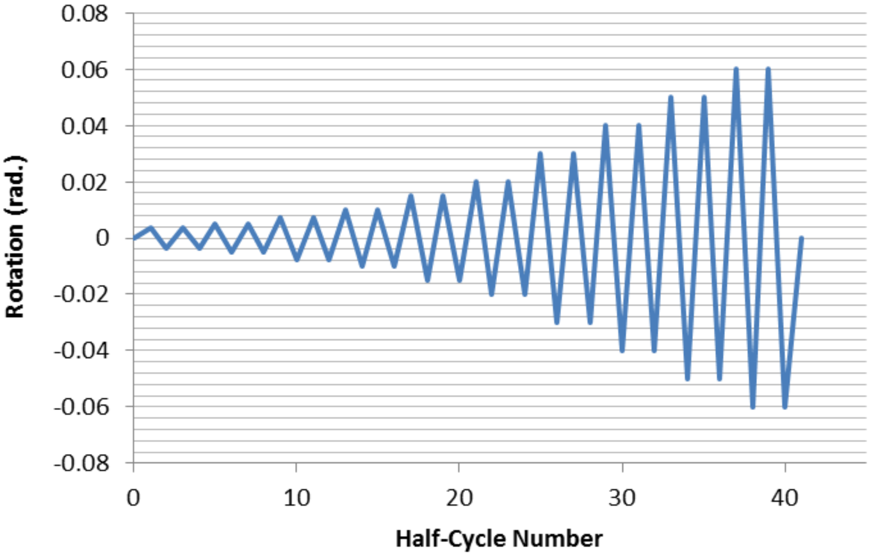

Figure 6.9 Loading protocol for the finite element HSS-to-HSS connection study

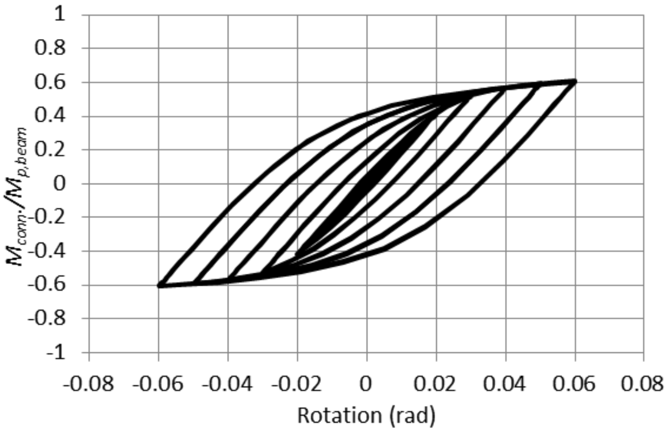

(a) HSS 12x6x3/8 beam (β=0.6)

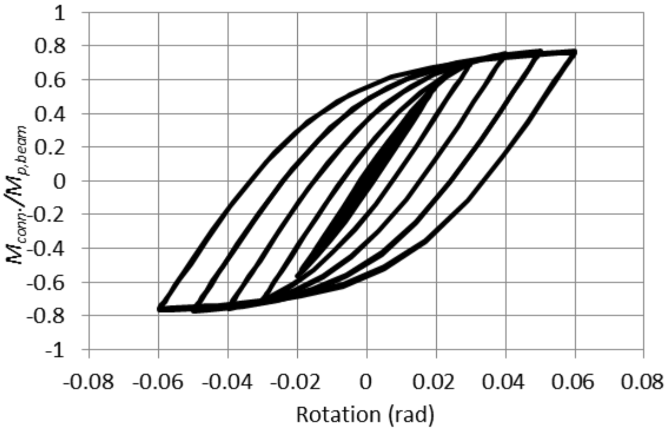

(b) HSS 12x8x3/8 beam (β=0.8)

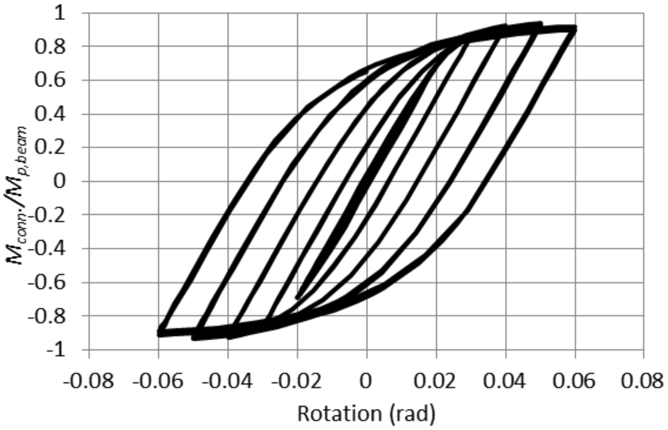

(c) HSS 12x10x3/8 beam (β=1.0)

Figure 6.10 Normalized moment-rotation hysteretic behavior for the unreinforced connection with (a) HSS 12x6x3/8, (b) HSS 12x8x3/8, and (c) HSS 12x10x3/8 beams

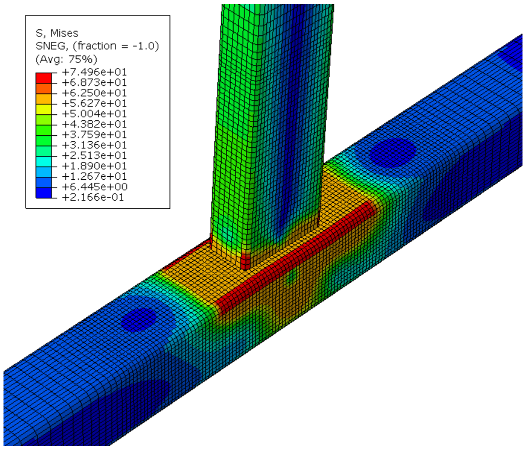

(a) HSS 12x6x3/8 beam (β=0.6)

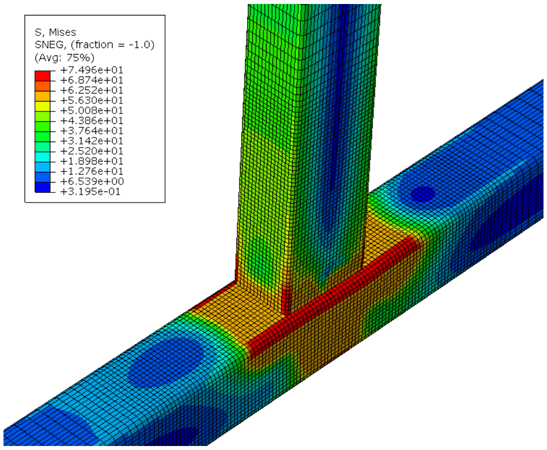

(b) HSS 12x8x3/8 beam (β=0.8)

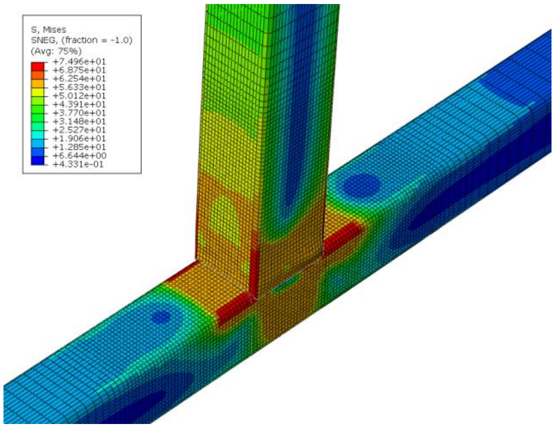

(c) HSS 12x10x3/8 beam (β=1.0)

Figure 6.11 von Mises stress distribution for the unreinforced connections with (a) HSS 12x6x3/8, (b) HSS 12x8x3/8, and (c) HSS 12x10x3/8 beams

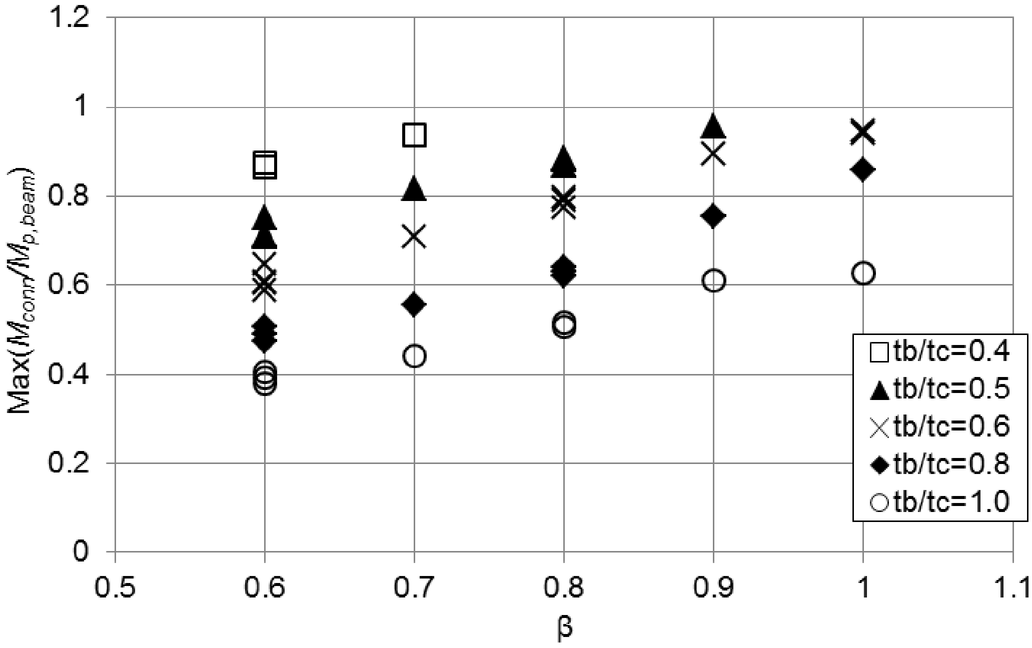

Figure 6.12 Effect of beam width-column width ratio (*β*) and the beam thickness-column thickness ratio (t_b/t_c) on the maximum normalized moment capacity for unreinforced connections

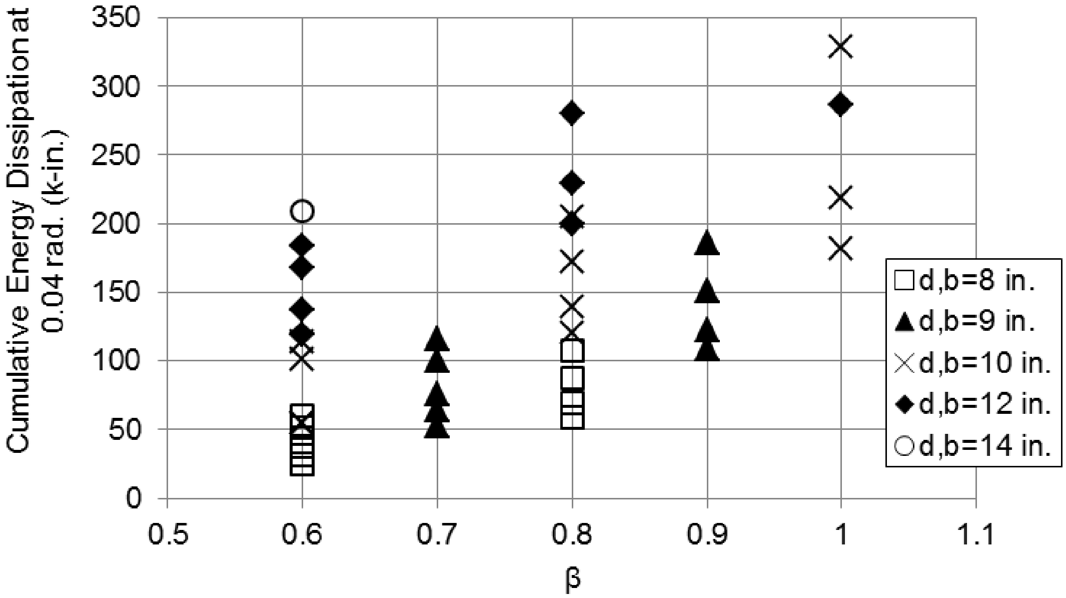

Figure 6.13 Effect of the beam width-column width ratio (*β*) and beam depth (d_b) on the cumulative energy dissipation capacity at 0.04 rad. for the unreinforced connections

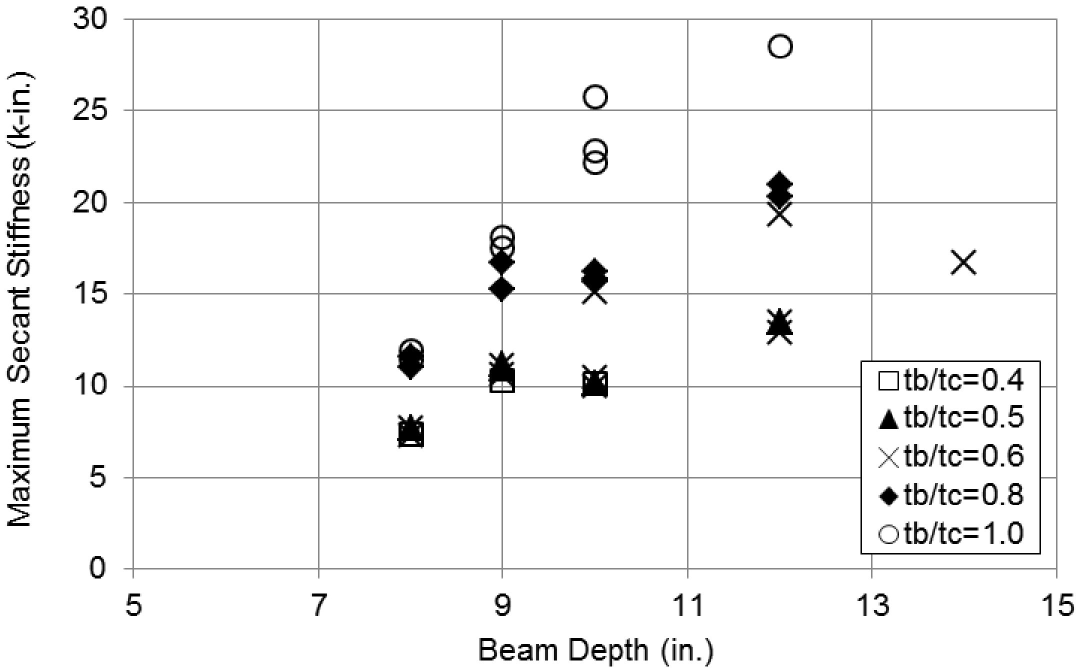

Figure 6.14 Effect of beam width-column width ratio (β) and the beam thickness-column thickness ratio (t_b/t_c) on the maximum secant stiffness for the unreinforced connections

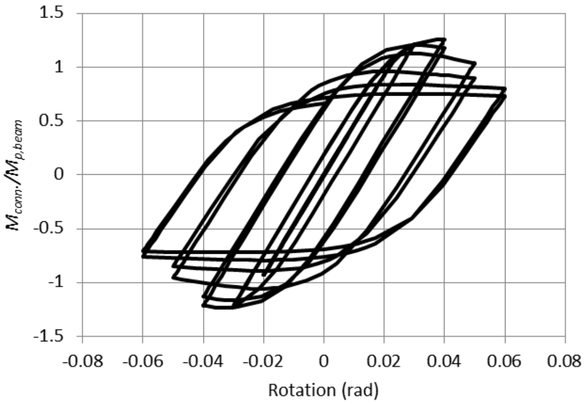

(a) HSS 10x8x3/8 beam (L_{pl}=15 in. and t_{pl}=0.75 in.)

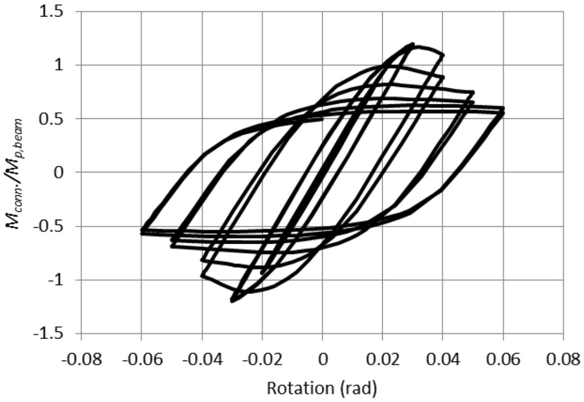

(b) HSS 12x10x3/8 beam (L_{pl}=15 in. and t_{pl}=1.0 in.)

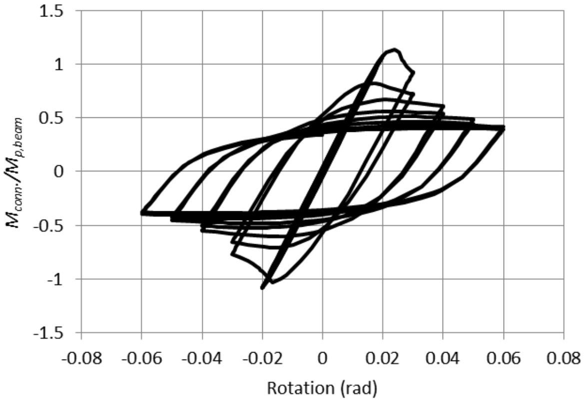

(c) HSS 12x8x1//4 beam (L_{pl}=15 in. and t_{pl}=0.625 in.)

Figure 6.15 Normalized moment-rotation hysteretic behavior for the internal diaphragm plate connection with (a) HSS 10x8x3/8 (b) HSS 12x10x3/8, and (c) HSS 12x8x1/4 beams

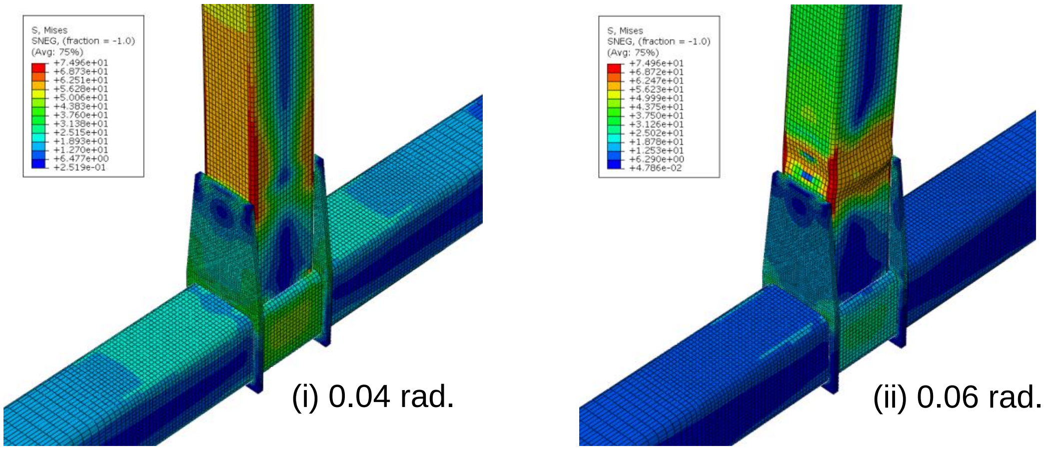

(a) HSS 10x8x3/8 beam (L_{pl}=15 in. and t_{pl}=0.75 in.)

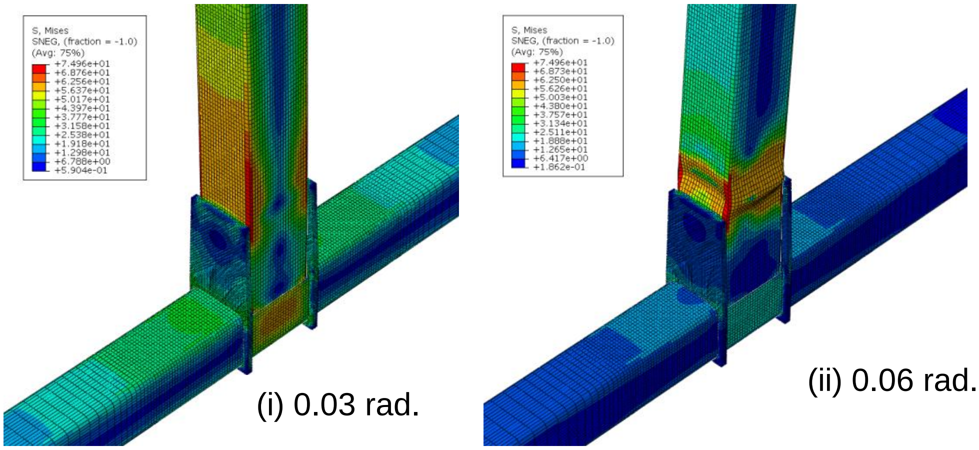

(b) HSS 12x10x3/8 beam (L_{pl}=15 in. and t_{pl}=1.0 in.)

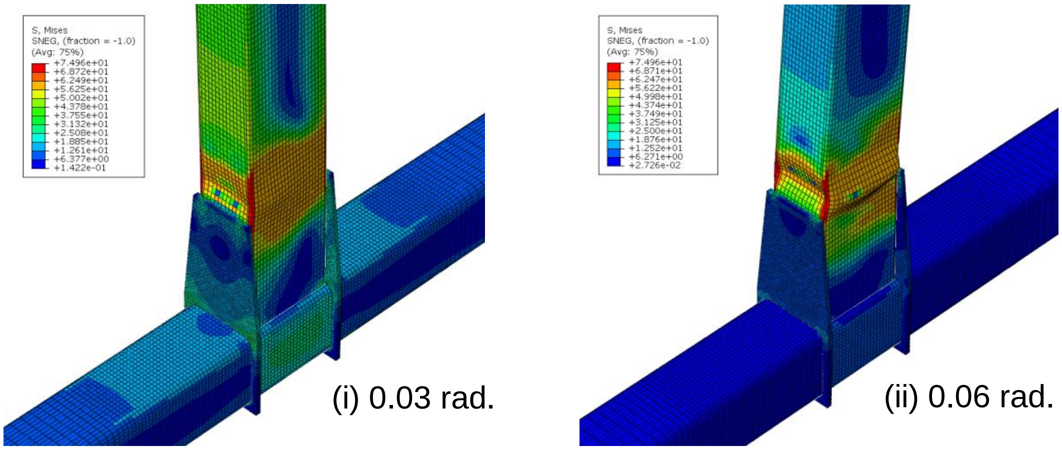

(c) HSS 12x8x1/4 beam (L_{pl}=15 in. and t_{pl}=0.625 in.)

Figure 6.16 von Mises stress distribution for the internal diaphragm plate connections with (a) HSS 10x8x3/8 (b) HSS 12x10x3/8, and (c) HSS 12x8x1/4 beams

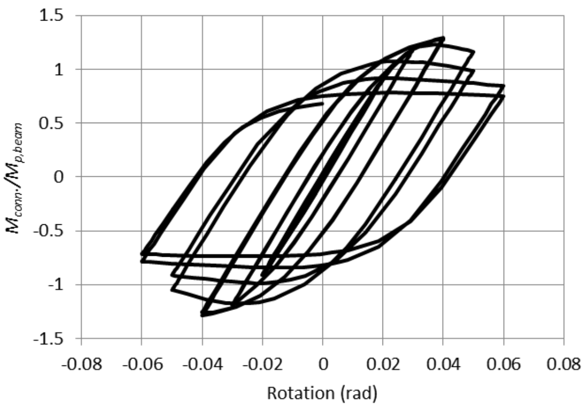

(a) HSS 10x8x3/8 beam (L_{pl}=18 in. and t_{pl}=0.625 in.)

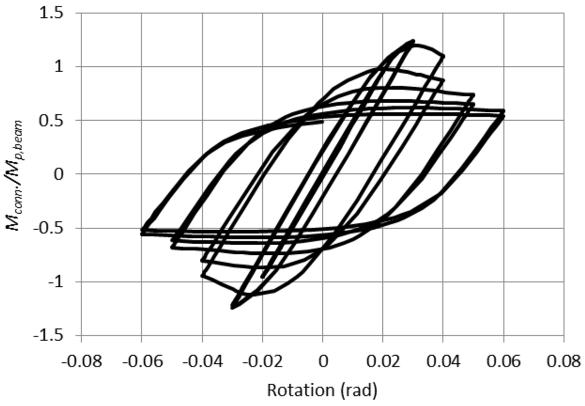

(b) HSS 12x10x3/8 beam (L_{pl}=18 in. and t_{pl}=0.75 in.)

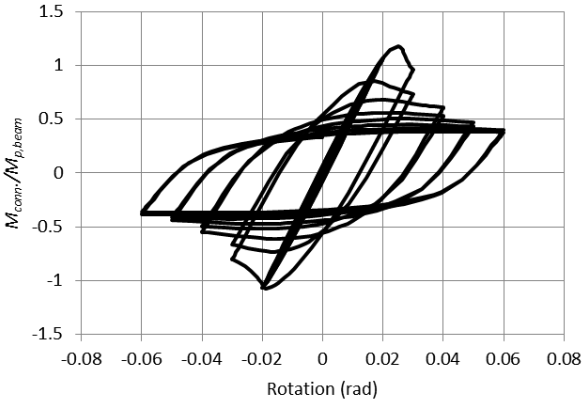

(c) HSS 12x8x1/4 beam (L_{pl}=18 in. and t_{pl}=0.5 in.)

Figure 6.17 Normalized moment-rotation hysteretic behavior for the external diaphragm plate connection with (a) HSS 10x8x3/8 (b) HSS 12x10x3/8, and (c) HSS 12x8x1/4 beams

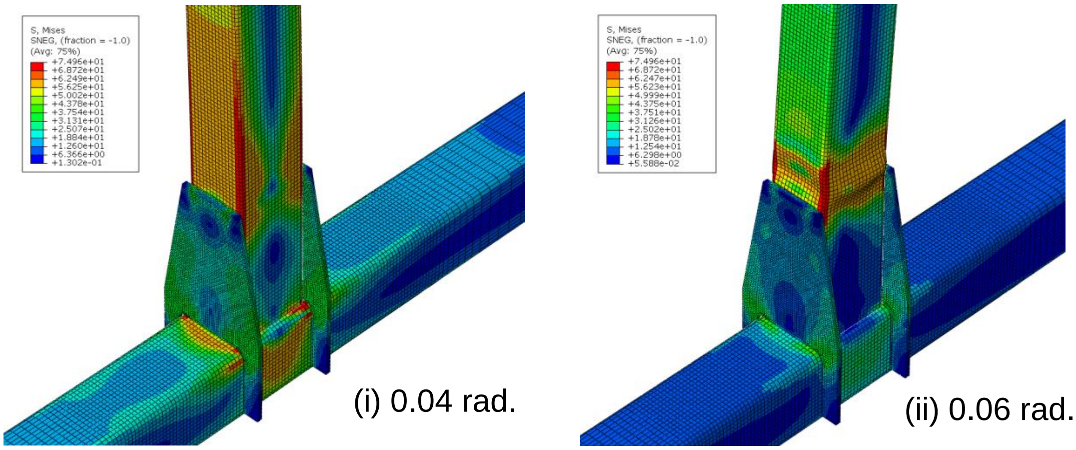

(a) HSS 10x8x3/8 beam (L_{pl}=18 in. and t_{pl}=0.625 in.)

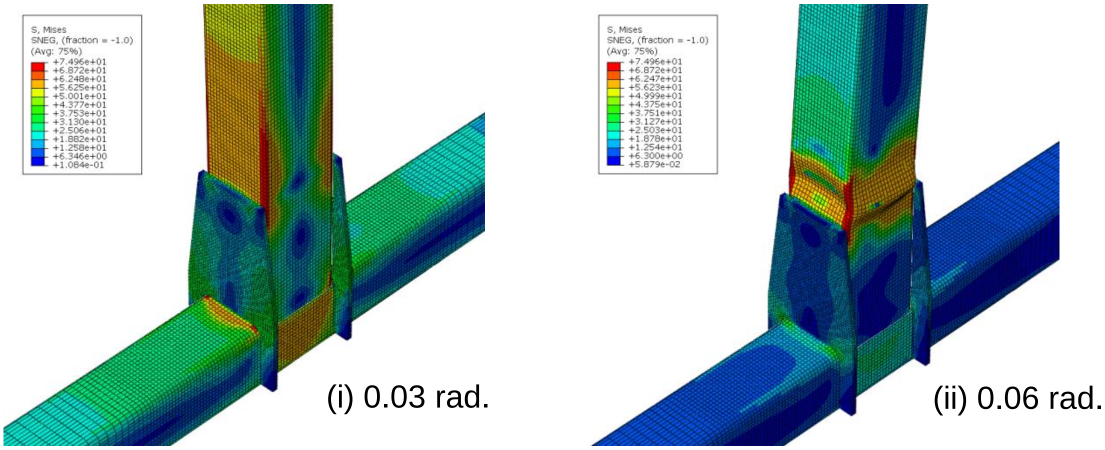

(b) HSS 12x10x3/8 beam (L_{pl}=18 in. and t_{pl}=0.75 in.)

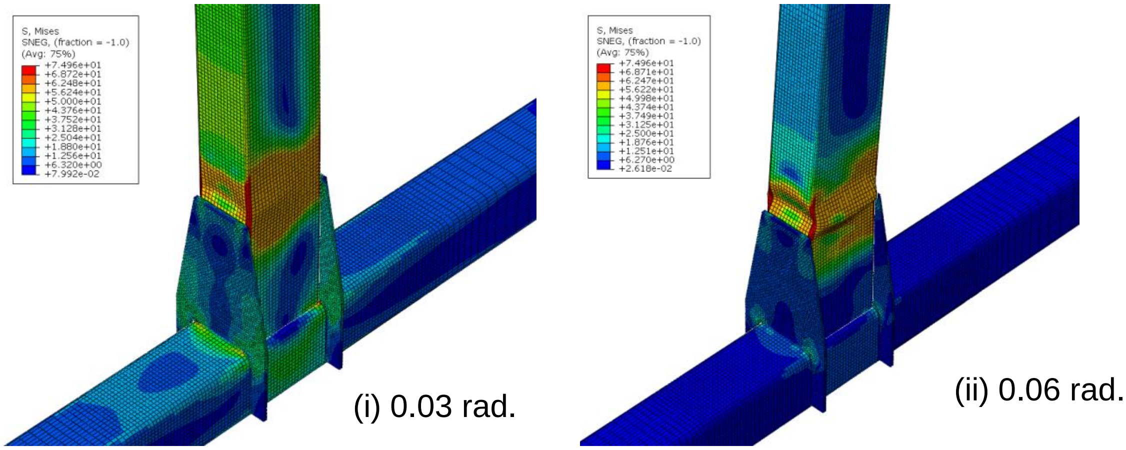

(c) HSS 12x8x1/4 beam (L_{pl}=18 in. and t_{pl}=0.5 in.)

Figure 6.18 von Mises stress distribution for the external diaphragm plate connections with (a) HSS 10x8x3/8 (b) HSS 12x10x3/8, and (c) HSS 12x8x1/4 beams

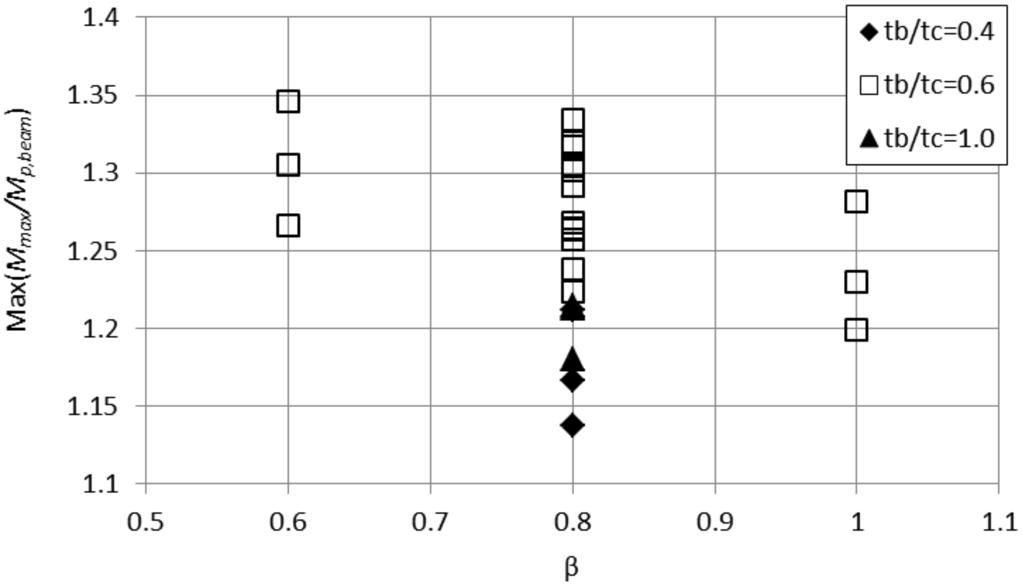

Figure 6.19 Effect of beam width-column width ratio (*β*) and the beam thickness-column thickness ratio (t_b/t_c) on the normalized maximum moment for the internal diaphragm plate connections

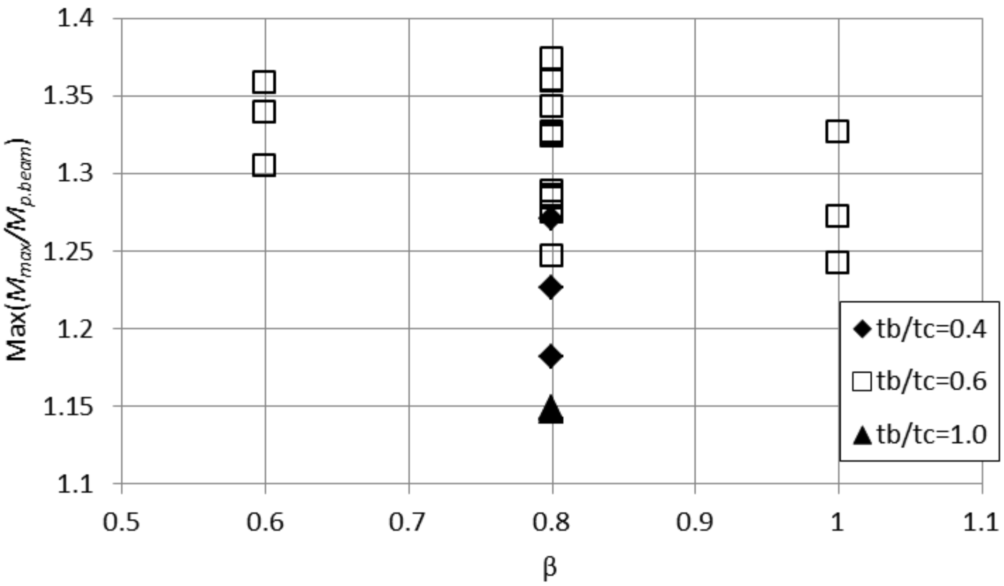

Figure 6.20 Effect of beam width-column width ratio (*β*) and the beam thickness-column thickness ratio (t_b/t_c) on the normalized maximum moment for the external diaphragm plate connections

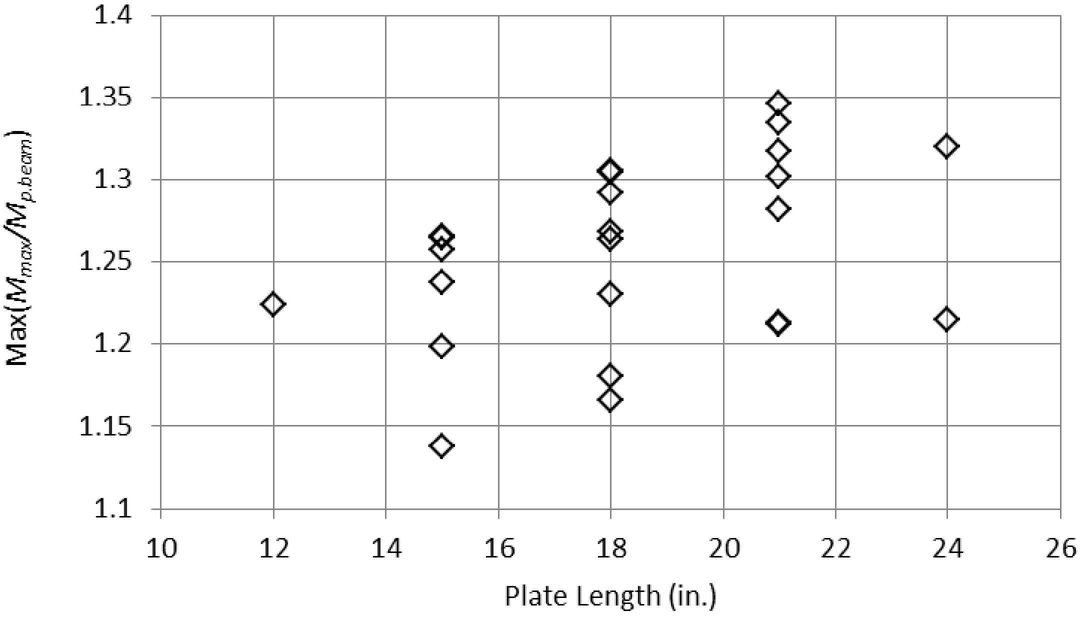

Figure 6.21 Effect of plate length (L_{pl}) on the normalized maximum moment for the internal diaphragm plate connections

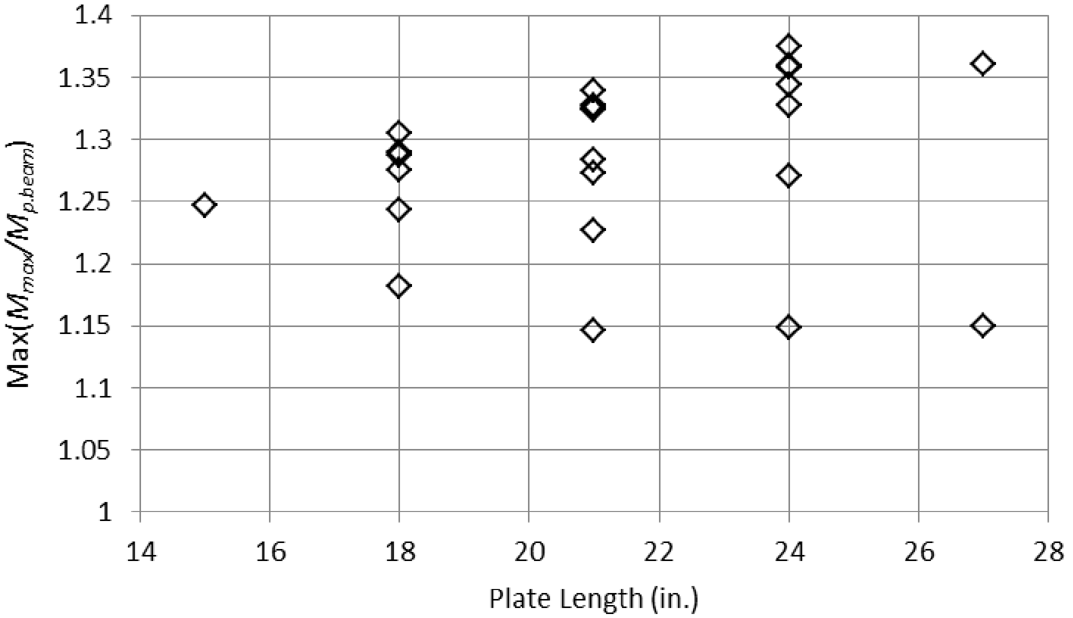

Figure 6.22 Effect of plate length (L_{pl}) on the normalized maximum moment for the external diaphragm plate connections

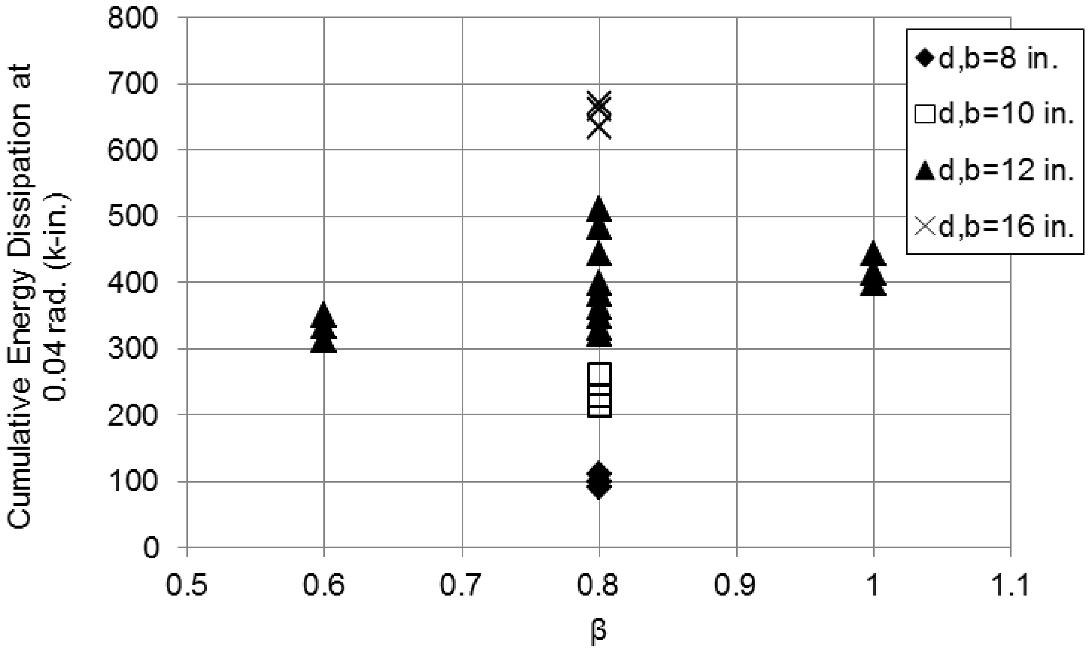

Figure 6.23 Effect of beam width-column width ratio (β) and beam depth (d_b) on the cumulative energy dissipation at 0.04 rad. for the internal diaphragm plate connections

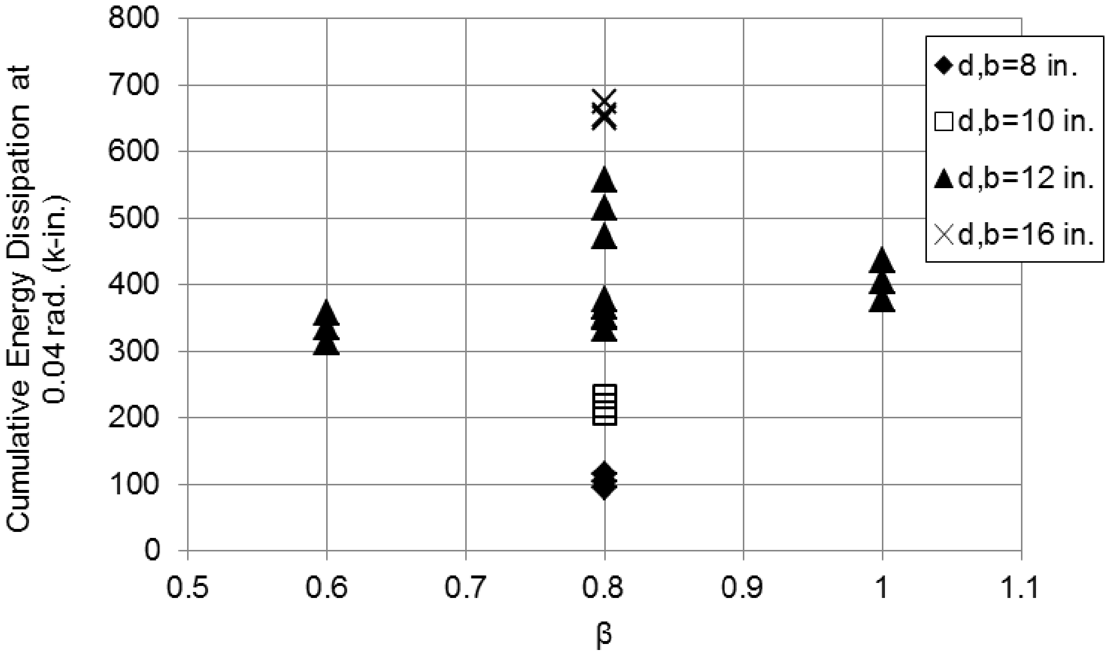

Figure 6.24 Effect of beam width-column width ratio (β) and beam depth (d_b) on the cumulative energy dissipation at 0.04 rad. for the external diaphragm plate connections

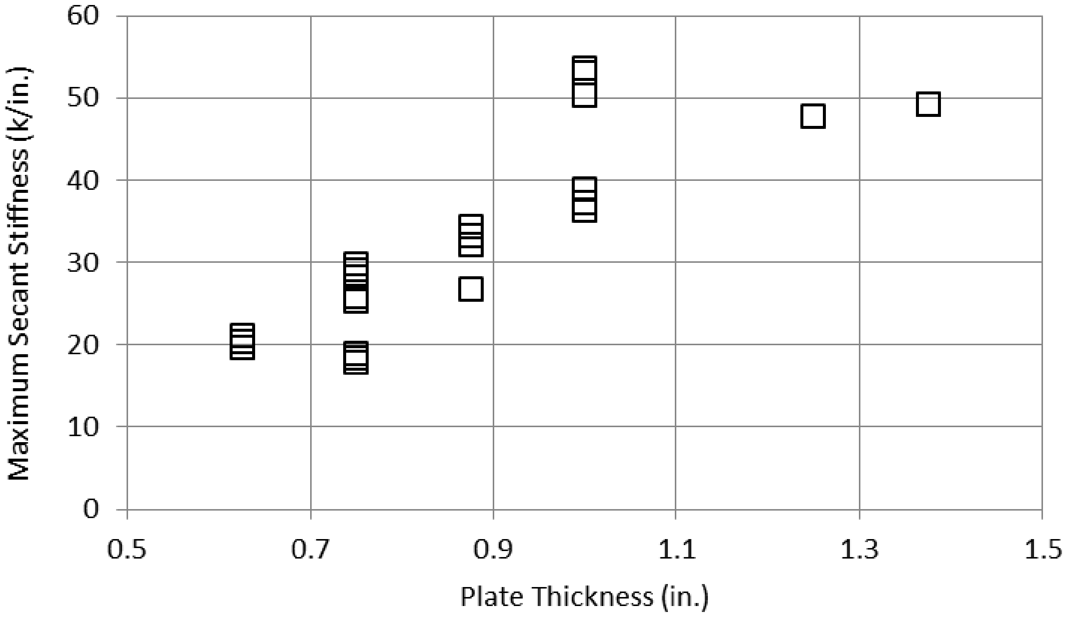

Figure 6.25 Maximum secant stiffness versus diaphragm plate thickness for the internal diaphragm plate connections

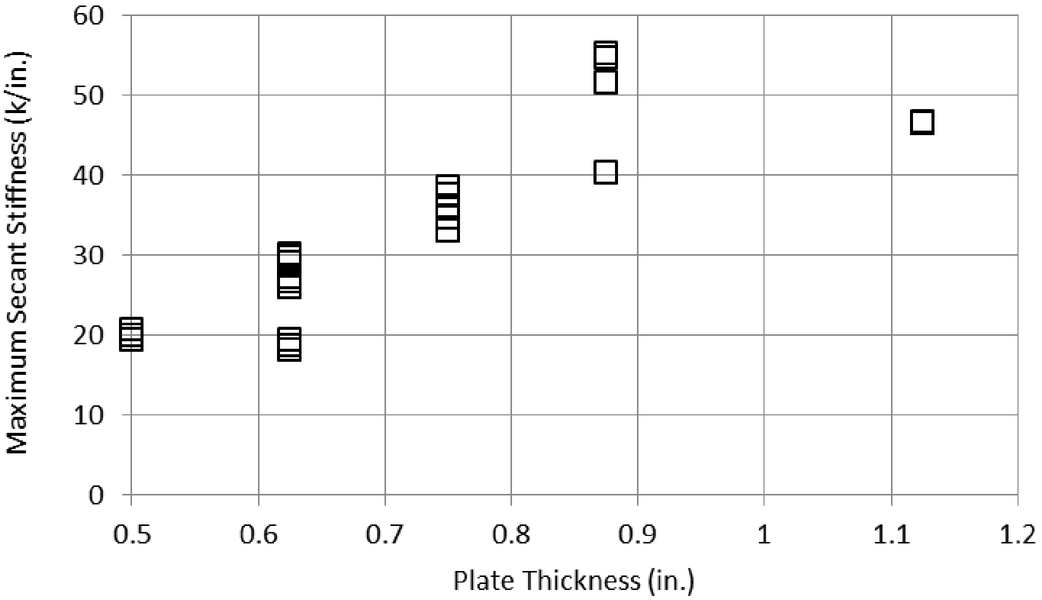

Figure 6.26 Maximum secant stiffness versus diaphragm plate thickness for the external diaphragm plate connections

CHAPTER 7: UNREINFORCED HSS-to-HSS MOMENT CONNECTIONS

7.1 Introduction

Use of steel moment resisting frames (MRF) became popular in the 1960's because of an ability to withstanding large plastic deformations without significant degradation or development of local or global instabilities that could lead to collapse (SAC 2000). The ductile nature of steel moment frames resulted in the use of higher ductility factors for these systems, allowing a reduction in the force for which they are designed (Bruneau et al. 1998). The reduced seismic loads led to increased use of steel moment frame systems in the high seismic regions of the western United States (SAC 2000).

For ductile steel MRFs the inelastic rotational demands are accommodated through plastic deformation of the beams and panel zones and to a lesser extent the columns. Early studies suggest the maximum rotations that must be sustained by the beam member are between 0.02 to 0.025 rad. (Popov and Tsai 1989, Roeder et al. 1989). More recent studies suggest larger required beam rotational capacities of 0.03 to 0.04 rad. for new construction depending on the frame type (AISC 2010b). In addition, column buckling must be avoided because of the potential for a non-ductile failure mode.

Although many studies have considered the performance of various steel moment frame systems under seismic loads, few studies have considered the suitability of HSS-to-HSS moment frame systems for seismic design. The experimental study described in this chapter considered the performance of two unreinforced HSS-to-HSS moment connections under large cyclic deformations, while also providing information on potential failure modes of the connections not captured in the previous finite element study (Chapter 6). The study, which utilized full scale specimens, allowed for the determination of the effects of cyclic loading on unmatched (β=0.8) and matched (β=1.0) HSS-to-HSS moment connections. The hysteretic behavior was carefully evaluated through the use of extensive instrumentation to extract the sources of inelastic rotation.

The effects of continued cycling were assessed in terms of energy dissipation, equivalent viscous damping, and secant stiffness. Additionally, strain levels in the connection region were evaluated to better understand the load transfer mechanism in the connection. These findings provided insight into the suitability of unreinforced HSS-to-HSS moment connections for seismic applications and baseline values to compare further connection configurations against in the future.

7.2 Experimental Program

7.2.1 Test Setup and Loading Protocol

The experimental test setup is shown in Figure 7.1 and Figure 7.2. The subassembly was rotated 90 degrees from horizontal due to laboratory constraints resulting in the beam being vertical and column being horizontal. The subassembly represented a connection in a 12 ft. high by 21 ft. wide bay of a low-rise steel moment frame where the column and beam members of the subassembly were pinned at their inflection points. The distance between the column pins was 144 in., while the distance between the column centerline and beam tip was 126 in. The column is supported by two pins fixtures that are connected to the strong floor through a stiff spreader beam. Using an end plate connection, the pins are connected to the HSS column. The HSS beam member was bolted to a loading fixture that attached to the hydraulic actuator also utilizing a bolted endplate. A 150 kip hydraulic actuator with a 30 in. stroke (+/-15 in.) applied the required beam end displacements representing possible interstory drifts in excess of 0.1 rad.

To simulate deformation imposed on a structure during a major earthquake, the AISC loading protocol for prequalification of seismic moment connections was utilized (AISC 2010b). The loading protocol is provided in Figure 7.3 and consists of 34 cycles increasing from 0.00375 rad. to 0.06 rad or failure depending on which occurs first. The test was run at a quasi-static rate of 0.05 in./min, since steel systems do not often show significant strain rate effects. The large rotations prescribed in this loading protocol allowed for the inelastic behavior and failure mechanisms of the connections to be observed.

7.2.2 Test Specimens

The experimental test program consisted of two full size HSS-to-HSS moment connections. For both specimens the HSS column member was an HSS 10x10x5/8. This section was chosen because it was the largest section that meets the moderately ductile seismic compactness criteria specified by AISC (2010b). The limit for moderately ductile members was 16.1 assuming an elastic modulus of 29,000 ksi and yield strength of 46 ksi. The *b/t* and *h/t* ratio for the HSS 10x10x5/8 column were 15.7 (Table 7.1). The limit for highly ductile systems was somewhat smaller with a required *b/t* and *h/t* ratio of 13.8. However, this limit was not a necessary criterion due to the fact that members that meet this requirement are often too small to be utilized in low-rise moment frame systems. Two different HSS beam members were chosen, HSS 12x8x3/8 (*b/t*=21.4 and *h/t*=32.9) and HSS 12x10x3/8 (*b/t*=27.2 and *h/t*=32.9), such that both matched (β=1.0) and unmatched (β=0.8) beam-column connections could be assessed (Table 7.2). The sections were chosen because they represent *b/t* and *h/t* ratios that are expected to have a degradation of 20% at 0.04 rad. based on the findings in Chapter 5. By considering both matched and unmatched connections, the effect of different beam width-column width ratios on the load transfer mechanism could be readily explored and addressed to determine the suitability and behavior of unreinforced connections.

Both test specimens were designed based on the procedure discussed in Chapter 6. Schematics of the specimens are provided in Figure 7.4 for the unmatched connection (HSS 12x8x3/8 beam) and in Figure 7.5 for the matched connection (HSS 12x10x3/8). Each specimen had 1 in. thick endplates fillet welded to the beam and column ends to allow the subassembly to be bolted into the test setup. The connections between the beam and column sections utilized prequalified CJP groove welds as specified in AWS D1.1 (2010) and shown in Figure 6.2. The CJP grove welds utilized a backer bar on the inside of the HSS beam member to provide a joint filling surface. Because CJP welds were used there was no capacity check for the weld itself. However, the thickness of the weld was checked against the base metal thickness to try to aviod shear yielding or rupture of the base metal.

7.2.3 Instrumentation

Instrumentation was utilized to capture the behavior of the connection subassemblies during testing. Each specimen was outfitted with Optotrak infrared optical tracking markers, potentiometers, and strain gages. The Optotrak layout and marker numbers can be seen in Figure 7.6 and Figure 7.7. The layout of the markers allowed for monitoring of rotations in the beam, column, and panel zone region.

Additionally, potentiometers (Figure 7.8) were mainly utilized as a secondary system to measure beam, column, and panel zone rotations. Potentiometers also provided a measure of any undesired slip that occurred during testing. Specifically, a potentiometer was placed at the column end to measure the horizontal connection setup slip (WPS) and another potentiometer was placed between the actuator fixture and beam end plate to measure the relative slip between the components (TPS). A clinometer was also placed on the actuator to measure the angle of load applied to the beam. However, the change in angle of the actuator was very small and axial loads applied to the beam were found to be negligible. For the unmatched (HSS 12x8x3/8) connection, no slip of the test setup was observed, while for the matched (HSS 12x10x3/8) connection a small amount of slip was observed at WSP. This slip initiated at a rotation level of 0.015 rad. when the maximum load was reached. The reached a maximum value of 0.25 in. This slip was subtracted from the displacement measured by the actuator for all calculations. Other potentiometers utilized were SP to measure the beam tip displacement, BEP and BWP to measure the beam plastic hinge rotation, PZ0 and PZ1 to measure the panel zone rotation, and CEP and CWP to measure column rotations. Whenever possible, the Optotrak makers were used to measure rotations rather than the potentiometers.

Strain gages were utilized on the column and beam. Location selection for the strain gages was based on recommendations made during the SAC Study after the Northridge and Hyogo-ken Nanbu events (Clark et al. 1997). However, modifications were made to the strain gage layout to make it more suitable for HSS-to-HSS connections. Four gages were placed on each beam flange (*be0-be3* and *bw0-bw3*) to better understand the load transfer mechanism and monitor the formation and growth of the plastic hinge region (Figure 7.9). The column strain gages were placed on the column face near the beam member, on the face opposite to the connection, and within the panel zone region. For the HSS 12x8x3/8 specimen three strain gages (*cf0-cf2*) were used on the column face. The HSS 12x10x3/8 specimen utilized six strain (*cf0-cf5*) gages on the column face to better identify locations of localized strain and potential for weld failure (Figure 7.10). The face opposite the beam connection used four strain gages (*cb0-cb3*) to understand the ability of the connection to transfer force to the opposite side of the connection (Figure 7.11). The panel zone of each specimen was instrumented with four strain gage rosettes (*pz0-pz3*) to capture the strain within the panel zone region (Figure 7.12).

7.3 Experimental Results

7.3.1 Hysteretic Behavior

The hysteretic behavior of each subassembly was evaluated for its ability to withstand increased interstory drift. Both the unmatched (HSS 12x8x3/8 beam) and matched (HSS 12x10x3/8 beam) connections were cycled according to the prescribed loading protocol. The moment in the connection was calculated based on the applied load divided by the length of the beam in the subassembly plus half the column depth. The interstory drift or connection rotation was calculated based on Equation 7.1. The inclination of the actuator did not result in a change to the connection rotation and was ignored for all subsequent calculations.

$$\theta_{conn} = \frac{\delta_{actuator}}{\left(l_b + \frac{d_c}{2}\right)}$$

Equation 7.1

where $\delta_{actuator}$ is the actuator displacement, $l_b$is the beam length (subassembly), and d_c is the column depth.

The unmatched connection reached a maximum rotation of 0.05 rad. and underwent 31 full-cycles (Figure 7.13). The maximum moment the connection reached was 2750 k-in. at a rotation of 0.040 rad. The connection was flexible with an elastic stiffness of 7.6 k/in. compared to the theoretical elastic stiffness of the beam of 12.9 k/in. After reaching the maximum moment at 0.04 rad., a visible fracture was observed at the toe of the CJP weld in the column near the corner of the connection. The point of fracture is represented on the hysteresis plots by a small circle. During subsequent cycles, the fracture propagated away from the corner toward the center of the webs and flanges. As a result of the fracture, the capacity of the connection decreased rapidly with continued cycling. At a story drift of 0.05 rad., the capacity dropped to 775 k-in., which corresponded to a 71.8% decrease in the moment capacity from maximum. As a result of the decrease in capacity and the propagation of the fracture along the whole length of the beam web, the test was stopped. The extent of the fracture at the end of the test is shown in Figure 7.14. The fracture was longer along the beam web than along the flange where a portion of the beam flange and column face was still connected. The fracture did not occur in the weld metal, but rather in the column base metal at the toe of the weld (Figure 7.15).

The matched connection reached a higher maximum story drift than the unmatched connection of 0.06 radians (Figure 7.16). As a result, the matched connection underwent 34 full-cycles. A small amount of slip was observed at the higher drift levels that was accounted for in the story drift calculation. The maximum moment capacity of the matched connection was 4220 k-in. which was reached at a story drift of 0.049 rad. The matched connection was stiffer than the unmatched connection with an elastic stiffness of 9.7 k/in. Compared to the theoretical elastic stiffness of the beam of 15.2 k/in., the connection was very flexible. After reaching the maximum moment, a similar fracture to that seen in the unmatched connection was observed near the corner of the HSS 12x10x3/8 beam member at the toe of the weld. Again, the point of fracture is represented in the hysteresis by a small circle. During subsequent cycles the moment capacity decreased rapidly as the connection rotations grew. At the final cycle to 0.06 rad., the moment capacity decreased to 874 k-in. leading to a 79.3% decrease in the maximum moment capacity and prompting stoppage of the test. Like the unmatched connection, the fracture initiated at the corner of the connection region and propagated the whole length of the beam web and partially along the flange of the beam (Figure 7.17). During the first 0.06 rad. rotation cycle in the negative direction, the fracture quickly propagated along over half of the beam web. Complete fracture along the web of the beam led to the sharp drop in the moment capacity observed at -0.054 rad. As with the unmatched connection, the failure occurred in the column base metal at the toe of the CJP weld, not in the weld metal (Figure 7.18).

The results of this study showed that the connection behavior is largely dependent on the base metal capacity near the toe of the weld. The matched connection performed better, fracturing later into the loading protocol. However, both connections lost much of their moment capacity in the immediate cycles after fracture. The rapid degradation of capacity and large flexibility indicated that these unreinforced connection configurations are likely not suitable for seismic moment frame systems.

7.3.2 Plastic Rotation

The extent of the plastic deformations was also considered to better understand the amount of inelasticity concentrated in each connection component. The moment capacity versus overall plastic story drift is shown for the unmatched (Figure 7.19) and matched (Figure 7.20) connection. The connection plastic rotation is calculated by summing the plastic rotations from all inelastic rotations sources: beam, column, panel zone and column face (Equation 7.2). The inelastic rotations for each component are calculated in the following sections.

$$\theta_{conn,pl} = \theta_{beam,pl}^{CL} + \theta_{pz,pl} + \theta_{col,pl} + \theta_{cf,pl}^{CL} \qquad \text{Equation 7.2}$$

where $\theta_{beam,pl}^{CL}$ is the beam plastic rotation about the column centerline, $\theta_{pz,pl}$ is the panel zone plastic rotation, $\theta_{col,pl}$ is the column plastic rotation, and $\theta_{cf,pl}^{CL}$ is the column face plastic rotation about the column centerline.

For the connection plastic rotations, plastic rotation measurements were only valid up to fracture due to the formulation of the column face plastic rotation measurement. The column face rotation measurement began to capture rotations due to facture after the maximum moment was reached. For the matched connection the plastic rotation at maximum moment was 0.016 rad. when fracture first initiated during the first 0.04 rad. cycle, which meant that 40% of the rotation at this point was a result of inelastic deformations. The matched connection underwent a larger amount of plastic rotation prior to failure. At the maximum moment the plastic rotation was 0.025 rad. resulting in

51% of the 0.049 rad. overall connection rotation. This analysis indicated that the elastic rotations were significant for both connections.

7.3.2.1 Beam Plastic Rotation

Based on current seismic design requirements requirments, it was desirable to have a majority of the inelastic rotations stemming from the formation of a plastic hinge in the beam member. Both connections had yield ($M_y=R_yF_yS$) and plastic ($M_p=R_yF_yZ$) moment capacities (based on a specified tensile strength of 46 ksi) greater than the measured maximum moment capacity of the connection. The beam moment demand at the column face, M_{cf}, is calculated based on Equation 7.3.

$$M_{cf} = l_b P \qquad \text{Equation 7.3}$$

where P is the applied load at the beam tip.

The unmatched connection had a maximum connection moment demand of 2650 k-in., while the beam yield moment capacity was calculated to be 2810 k-in. and the beam plastic moment capacity was calculated to be 3410 k-in. This resulted in a maximum moment normalized to the yield moment of 0.94 and maximum moment normalized to the plastic moment of 0.77. The matched connection had a maximum connection moment demand of 4050 k-in. The beam yield moment was calculated to be 3320 k-in. and the beam plastic moment was calculated to be 3930 k-in. This resulted in a maximum moment normalized to the yield moment of 1.22 and a maximum moment normalized to the plastic moment of 1.03. This indicated that the matched connection was able to develop the capacity of the beam member.

However in both test specimens, the beam rotations were not necessarily the main source of plastic rotation for the connection. The beam rotations were calculated based on the output of four different Optotrak markers. Markers 47 and 51 (Figure 7.7) at the base of beam member were used to determine rigid rotation ($\theta_{beam,rigid}$) (Equation 7.4).

$$\theta_{beam,rigid} = \frac{m51_y - m47_y}{m51_x - m47_x} \qquad \text{Equation 7.4}$$

where $m47_x$, $m47_y$, $m51_x$, and $m51_y$ correspond to the markers horizontal and vertical displacements.

Markers 49 and 96 were then used to determine the beam rotation ($\theta_{beam,overall}$) (Equation 7.5).

$$\theta_{beam,overall} = \frac{m96_x - m49_x}{m96_y - m49_y} \qquad \text{Equation 7.5}$$

where $m49_x$, $m49_y$, $m96_x$, and $m96_y$ correspond to the markers horizontal and vertical displacements.

The rigid rotation was subtracted from the overall rotation to find the actual rotation the beam due to deformation (Equation 7.6).

$$\theta_{beam} = \theta_{beam,overall} - \theta_{beam,rigid} \qquad \text{Equation 7.6}$$

Assuming all plasticity occurred within the instrumented region, the beam plastic rotation was calculated using Equation 7.7.

$$\theta_{beam,pl} = \theta_{beam} - \frac{M_{conn}}{K_{beam}} \qquad \text{Equation 7.7}$$

where $M_{conn}$is the connection moment, and K_{beam} is the stiffness of the beam measured from the beam moment-rotation hysteresis during the first 0.01 rad. cycle.

The beam rotation is then converted to an equivalent rotation about the connection center point along the centerline of the column using Equation 7.8.

$$\theta_{beam,pl}^{CL} = \theta_{beam,pl}\left(\frac{l_b}{l_b + \frac{d_c}{2}}\right) \qquad \text{Equation 7.8}$$

The unmatched connection reached a maximum plastic beam rotation of 0.0049 rad. during the cycle in which fracture was first observed (Figure 7.21). This was approximately 30% of the total plastic rotation the connection underwent during that cycle. Since typical seismic connections require a majority of the plastic rotation to occur in the beam member, this connection would not meet these requirements. In subsequent cycles, the plastic rotation in the beam reduced as the fracture propagated and more of the rotation was due to deformations of the column face. Overall, the beam plastic rotation was relatively small compared to the overall plastic rotation of the connections.

The matched connection showed a similar trend to the unmatched connection in terms of the beam plastic rotation (Figure 7.22). The matched connection reached a plastic rotation of 0.0049 rad. during the same cycle that fracture was first observed. The beam plastic rotation accounted for only 20% of the overall plastic rotation measured during this cycle. The low percentage of plastic rotation coming from the beam member indicated that the connections are unlikely suitable for seismic moment frames regardless of whether the connection was matched or unmatched.

7.3.2.2 Panel Zone Plastic Rotation

Rotations as a result of panel zone deformation are another important parameter in describing the behavior of moment connections. Excessive rotations in the connection due to shear deformation of the panel zone can lead to large lateral deflections in a moment frame system. In current seismic design of steel moment connections, a balanced connection where the panel zone is allowed to undergo inelastic deformation and contribute to the overall plastic rotation of the connection is suggested provided that it is not the main deformation mechanism. During an earthquake the panel zone can see large shear forces as a result of tension and compression transferred from the beam to the column. Additionally, the panel zone can play an important role in the behavior of the connection with regards to energy dissipation and load carrying capacity.

In terms of panel zone capacity, both connections had capacities greater than the demand. The panel zone shear demand for the unmatched connection was 213 kip and for the matched connection was 326 kip at maximum load. The panel zone shear demand was calculated as follows using Equation 7.3, Equation 7.9, and Equation 7.10.

$$V_{u,pz} = \frac{M_{cf}}{0.95d_b} - V_c$$

Equation 7.9

$$V_c = P\left(\frac{l_b + \frac{d_c}{2}}{l_c}\right)$$ Equation 7.10

where $V_{u,pz}$ is the panel zone shear demand, M_{cf} is the moment at the column face, and V_c is the story shear.

The panel zone shear capacity was calculated using Equation 7.11 following the methodology discussed in Chapter 6.

$$V_{n,pz} = 2\left(0.6R_yF_yd_ct_c\right)$$ Equation 7.11

where $V_{n,pz}$ is the panel zone shear capacity, $R_y$is the material overstrength factor, and t_c is the column thickness.

The panel zone capacity for both connections was 539 kip, much greater than the demand for either connection. For the unmatched connection the capacity was 2.54 times greater than the demand, while the capacity of the matched connection was 1.65 times greater than the demand. This indicated that both matched and unmatched connections had sufficient capacity to prevent failure in the panel zone, and limited yielding is likely.

The rotations due to panel zone shear were calculated using the Optotrak markers. Four markers 3, 7, 30, and 34 that make up the corners of the panel zone region were used to calculate the deformation within the panel zone. The distance between these points (and change in distance), L1 through L6, were calculated as shown in Figure 7.23. The change in geometry was then utilized to calculate the panel zone rotation using the law of cosines (Equation 7.12 and Equation 7.13).

$$\gamma_1 \ = \frac{\pi}{2} - acos\left(\frac{L_1^2 + L_4^2 - L_5^2}{2L_1\,L_4}\right)$$ Equation 7.12

$$\gamma_2 \ = -\frac{\pi}{2} + acos\left(\frac{L_2^2 + L_4^2 - L_6^2}{2L_2\,L_4}\right)$$ Equation 7.13

These rotation angles correspond to the panel zone rotation at the back of the connection, $\gamma_{1,}$ and the front of the connection near the beam, γ_2. The rotation in the panel zone was taken as the average deformation in this region (Equation 7.14) and the plastic panel zone rotation was calculated to find $\theta_{pz,pl}$ (Equation 7.15).

$$\theta_{pz} = \frac{\gamma_1 + \gamma_2}{2} \quad \text{Equation 7.14}$$

$$\theta_{pz,pl} = \theta_{pz} - \frac{M_{conn}}{K_{pz}} \quad \text{Equation 7.15}$$

where K_{pz} is the stiffness of the moment-panel zone rotation hysteresis during the first 0.01 rad. cycle.

The plastic rotation associated with the panel zone for the unmatched connection only reached 0.0018 rad. (Figure 7.24). For nearly the entirety of the loading protocol, the panel zone region remained elastic. Since β was equal to 0.8, the ability of the HSS beam member to transfer loads to the panel zone region was greatly diminished. The unmatched connection was not able to effectively move loads into the column sidewalls and much of the deformation occurred at the unstiffened column face.

The matched connection had a β of 1.0 that meant the webs of the beam member were aligned with the webs of the column allowing more force to be directly transferred to the panel zone and avoiding the column face. As a result, larger deformations were observed in the panel zone of the matched connection (Figure 7.25). A plastic panel zone rotation of 0.0077 rad. was measured during the cycle where fracture occurred. The matched connection reached a maximum panel zone rotation of 0.0145 rad. which occurred during the 0.06 rad. story drift cycle. For both the matched and unmatched connection, there was no indication of buckling or non-ductile failure in the panel zone region. These results indicated that sections with β of 1.0 perform better in terms of utilizing the panel zone as a source of connection plastic rotation capacity.

7.3.2.3 Column Rotation

Since a soft story collapse mechanism is undesirable in a seismic moment frame system, column rotations should be kept small. However for the experimentally tested unmatched and matched HSS-to-HSS moment connections, much of connection rotation occurred as a result of deformation outside the beam member and panel zone. It was important to determine the magnitude of the column plastic rotation to ensure that column plastic hinging was avoided.

To calculate the column rotations, the Optotrak markers were again utilized. Four markers were used to calculate the rotations, markers 11, 17, 20, and 26. The rotations were calculated twice (Equation 7.16 and Equation 7.17) and then averaged (Equation 7.18). This was done to average the rotations about the column centerline. The formulation is shown below assuming small rotations.

$$\theta_{col,1} = \frac{m17_y - m11_y}{m17_x - m11_x} \qquad \text{Equation 7.16}$$

$$\theta_{col,2} = \frac{m26_y - m20_y}{m26_x - m20_x} \qquad \text{Equation 7.17}$$

$$\theta_{col} = \frac{\theta_{col,1} + \theta_{col,2}}{2} \qquad \text{Equation 7.18}$$

where, $m11_x$, $m11_y$, $m17_x$, $m17_y$, $m20_x$, $m20_y$, $m26_x$, and $m26_y$ correspond to the markers horizontal and vertical displacements.

The plastic rotation was then calculated using Equation 7.19.

$$\theta_{col,pl} = \theta_{col} - \frac{M_{conn}}{K_{col}} \qquad \text{Equation 7.19}$$

where K_{col} is the elastic stiffness of the column based on the column moment-rotation hysteresis during the first 0.01 rad. cycle.

For the unmatched connection, plastic column rotations were very small (Figure 7.26). The column had a plastic rotation of only 0.0011 rad. during the cycle corresponding to maximum moment prior to the initiation of fracture. The plastic rotation increased to 0.0017 rad. during the 0.05 rad. story drift cycle after fracture. Overall, the column plastic rotations for the unmatched connection were negligible.

Column rotations for the matched connection were larger than for the unmatched connection (Figure 7.27). At 0.05 rad. story drift prior to fracture, the column plastic rotation was 0.0047 rad. This value increased with increasing rotation levels. The matched connection reached a maximum plastic rotation of 0.0086 rad. during the 0.06 rad. story drift cycle. Overall, the column plastic rotations for both connections remained within reasonable limits for a seismic moment connection.

7.3.2.4 Column Face Rotations

The main contribution to the connection rotations was prying of the column face. Figure 7.14 and Figure 7.17 show the extent of the prying action on the column face for the unmatched and matched connection. The column face only supported at its edges and as a result had a much smaller stiffness compared to the column sidewalls. Deformation of the column face was not desirable due to its lower load carrying capacity and susceptibility to large deformations.

To calculate the amount of rotation attributed to the column face, the rotations at the base of the beam were compared to those at the edge of the column:

$$\theta_{cf} = \frac{m51_y - m47_y}{m51_x - m47_x} - \frac{m34_y - m30_y}{m34_x - m30_x} \qquad \text{Equation 7.20}$$

$$\theta_{cf,pl} = \theta_{cf} - \frac{M_{conn}}{K_{cf}} \qquad \text{Equation 7.21}$$

$$\theta_{cf,pl}^{CL} = \theta_{cf,pl}\left(\frac{l_b}{l_b + \frac{d_c}{2}}\right) \qquad \text{Equation 7.22}$$

where $m30_x$, $m30_y$, $m34_x$, $m34_y$, $m47_x$, $m47_y$, $m51_x$, and $m51_y$ correspond to the markers horizontal and vertical displacements and K_{cf} is the elastic stiffness of the column face based on the moment-column face hysteresis during the first 0.01 rad. cycle.

At maximum moment just prior to fracture the column face plastic rotations of the unmatched connection were 0.009 rad. (Figure 7.28) contributing 58% of the overall plastic rotation measured for this cycle. As a result of a loss of continuity between the beam and column face due to fracture, the column face plastic rotation measurement was no longer valid after the maximum moment was reached.

For the matched connection, the plastic rotations were more concentrated in the beam, panel zone, and column up to the cycle where fracture initiated (Figure 7.29). During this cycle the maximum plastic rotations attributed to the column face were only 0.008 rad. and accounted for only 32% of the overall plastic rotations at the 0.05 rad. story drift cycle.

By increasing β from 0.8 to 1.0, smaller plastic rotations were observed in the column face. However, the ability to limit plastic rotations to the beam, panel zone, and column for both unmatched and matched connections was not observed. The non-ductile failure mode of the connection and the low stiffness of the column face were both undesirable. Future connection details should ensure that column face plastic rotations are limited by attempting to move the load to the column sidewalls avoiding excessive undesirable deformation.

7.3.3 Sources of Inelastic Rotation

It is beneficial to consider the sources of inelastic rotation up to fracture to better understand the ultimate behavior of the connection. Figure 7.30 plots the plastic rotation for each component of the plastic rotation based on beam, column, panel zone, and column face plastic rotations between 0.01 rad. and 0.04 rad. at the first positive cycle at each drift level up to fracture of the unmatched connection. For all drift levels considered the plastic rotation in the column face dominated the behavior contributing a minimum of 55% of the plastic rotation at every drift level. During the 0.03 and 0.04 rad. cycles, the beam contributed 34% and 30% of the overall plastic rotation, respectively. The panel zone and column contributed less than 8.9% each to the overall plastic rotation of the connection throughout the entire loading protocol. These data showed that the connection deformation mechanism for unmatched connections was dominated by column face plastification.

The matched connection showed considerably different behavior compared to the unmatched connection with respect to the distribution of the plastic rotations. A similar bar chart provides the sources of plastic rotation from the first 0.01 rad. to 0.05 rad. drift level (Figure 7.31). With increasing connection displacements, the amount of observed plastic rotation also increased. Compared to the unmatched connection, the matched connection did a better job at utilizing the beam and panel zone regions throughout loading. The column face contributed a maximum of 32% of the plastic rotation at the 0.03 rad. cycle. This contribution remained fairly consistent as the story drift increased to 0.05 rad. The distribution of inelastic rotations was more desirable with β of 1.0. During the 0.03 rad. cycle the beam contributed its highest percentage of plastic rotation, 30%. At a story drift of 0.05 rad. immediately prior to fracture, the panel zone contributed 30% of the plastic rotation, the column contributed 19% of the plastic rotation, and the beam contributed 20% of the plastic rotation. This analysis showed that matched connections perform considerably better than unmatched connections at distributing deformations away from the column face. However, the behavior was undesirable in terms of the unreinforced connections seismic performance where the beam and panel zone should undergo the majority of the plastic rotations.

7.4 Secant Stiffness Behavior

The degradation of the secant stiffness of the connection was studied by analyzing the load at peak displacement for each cycle and dividing by the peak displacement. The decrease in lateral stiffness for both the matched and unmatched connections was attributed to increased yielding and eventual fracture of the connection. Figure 7.32 shows the degradation of secant stiffness for both connections at the first cycle of each drift level. For small drift levels, where the deformations were mostly elastic, both connections showed very small degradations in the secant stiffness. Once rotations became large, the secant stiffness decreased. The secant stiffness was dependent on member size and the connection configuration. The matched connection showed higher maximum secant stiffness, 9.7 k/in., than the unmatched connection, 7.6 k/in. Prior to fracture of each connection, the degradation of the secant stiffness was gradual. Near the story drift levels where facture was first observed, 0.04 rad. for the unmatched connection and 0.05 rad. for the matched connection, the degradation rate increased. The matched connection showed a larger decrease in the secant stiffness of 6.4 k/in. versus 5.4 k/in. for the unmatched connection in the cycle after fracture occurred. However, the unmatched connection had a larger percent degradation of the secant stiffness capacity throughout the loading protocol, 72% compared to 66% for the matched connection. The matched beam and column sections were better able to conserve their secant stiffness at increased rotation levels. In designing moment frame structures ensuring the connections will be sufficiently stiff is important in reducing story drifts during earthquakes. The discussion showed that matched connections are better suited for maintaining their stiffness with increased cycling to large drift levels.

7.5 Energy Dissipation Capacity

One of the main means of dissipating seismic input energy is through inelastic deformation of specific elements. Typically frames dissipate energy through inelastic deformation of the beams, panel zones, and column bases. Therefore, it is important to consider the energy dissipation capacity of the connection to gain a sense of the connections ability to dissipate earthquake input energy. The energy dissipation capacity is calculated for each drift level as the total area enclosed by the load versus displacement hysteresis.

Figure 7.33 plots the energy dissipation for each connection at the first cycle of each story drift level. Up to a rotation of 0.015 rad., the energy dissipated remained very small for both unmatched and matched connections, since the connections essentially behaved elastically. At the 0.03 rad. rotation cycle the energy dissipated increased significantly for the unmatched and matched connection. For the unmatched connection at 0.04 rad. the energy dissipation was 130 k-in. increasing 75.2 k-in. from the 0.03 rad. cycle. However at 0.05 rad., fracture was observed and the increase in energy dissipation was much smaller reaching a maximum value of 142 k-in. Similar behavior was observed for the matched connection. Between the 0.04 rad. and 0.05 rad. story drift cycles, the energy dissipated increased from 133 k-in. to 263 k-in, a 130 k-in. increase. Again after fracture was observed at the 0.06 rad. rotation level, the energy dissipated increased only 28.5 k-in. to 291 k-in. at the final cycle. This change in slope of the energy dissipation curve was indicative of the behavior of a connection that had fractured. Further cycling would lead to decreased levels of energy dissipation and reduced ability of the connection to dissipate seismic input energy.

The cumulative energy dissipation is plotted for both connections in Figure 7.34. For both connections the cumulative energy dissipation before fracture was similar. At the 0.04 rad. rotation level, prior to fracture of either connection, the cumulative energy dissipated was 286 k-in. for the unmatched connection and 264 k-in. for the matched connection. However, once fracture initiated the connections began to perform very differently. The matched connection reached a cumulative energy dissipation of 670 k-in. at 0.05 rad., while the unmatched connection reached a maximum cumulative energy dissipation of 560 rad. in the same cycle. This result indicated that the unmatched connection had lost the ability to dissipate energy in comparison with the matched connection after fracture.

7.6 Equivalent Viscous Damping Ratio

The energy dissipation was also evaluated in terms of the equivalent viscous damping ratio. The equivalent viscous damping ratio is the energy dissipated per cycle normalized by the strain energy (E_{S0}) and 4π. In Equation 7.23, E_D is the energy dissipated in one cycle. The equivalent viscous damping ratio is important in comparing the response of different moment connections and their hysteretic behavior providing a normalized comparison of the energy dissipation capacity.

$$\xi_{eq} = \frac{1}{4\pi}\frac{E_D}{E_{S0}} \qquad \text{Equation 7.23}$$

Figure 7.35 compares the equivalent viscous damping ratio versus the maximum positive rotation for the first cycle at each drift level. The equivalent viscous damping was very small during the elastic cycles and increased during inelastic cycles. Both connections showed increasing damping ratios throughout the loading. At the 0.05 rad. drift level the unmatched connections achieved 26.6% equivalent viscous damping. This was larger than the 24.3% damping ratio observed in the matched connection The unmatched connection had higher equivalent viscous damping indicating that this connection had slightly more efficient energy dissipation properties than the matched connection.

7.7 Distribution of Strain in the Connection

7.7.1 Strain in the Beam

Strain gages were placed on the beam flanges to better infer the force transfer mechanism from the beam to the column for both the unmatched and matched connections. The locations of strain gages *be0-be3* are shown in Figure 7.9. The gages *bw0-bw3* were mirrored on the opposite beam flange and symmetry of the connection was assumed. For both connections the hysteretic strain behavior was analyzed.

Figure 7.36 and Figure 7.37 provide the strain in the east and west beam flange at maximum rotation for the first cycle of each drift level to 0.01 rad. through 0.05 rad. Overall the maximum strain observed in the east side was at *be2* reaching -0.0036 at 0.04 rad. On the west side, the maximum strain observed is in *bw2*, reaching a strain of -0.0040 at 0.04 rad. These strain gages were the closest gages to the corner of each beam specimen. Strain gages *be0*, *be1*, *bw0*, and *bw1* showed small maximum strain at all rotational levels until fracture with a maximum strain of -0.0018 at *be1* during the 0.03 rad. rotation cycle. After fracture the strain in the corners (*be2* and *bw2*) reduced by up to 101% of the maximum strain in *be2* and 99% in *bw2*, while more load was transferred through the beam flanges. As a result, *be2* and *bw2* carry nearly zero strain in the final 0.05 rad. rotation cycle. Strain gages *be3* and *bw3* had nearly the same strain levels throughout the loading protocol as *be2* and *bw2*. The strain gages for the unmatched connection indicated that the load moved from the beam flanges into the beam corners at the connection interface. Only when fracture occurred resulting in no continuity between the corner and the column face did a larger portion of the load transfer to the column through the beam flanges.

Similar behavior was observed for the matched connection (Figure 7.38 and Figure 7.39). In the matched connection, higher maximum strains were observed in gages *be2* and *bw2* than the unmatched connection, 0.0069 for *be2* and 0.0064 for *bw2*. These maximum strains were observed at the 0.05 rad. story drift, when fracture started to be observed and the maximum moment was reached. There was a better distribution of strain across the beam flanges than in the unmatched connection. Gages *be1* and *bw1* reached a maximum strain of 0.0044 and 0.0041, respectively. This was higher than what was observed in the unmatched connection. Again, after fracture the ability of corners to transfer load was greatly reduced because of a lack of continuity between the beam and column. The strain in *be0, be1, bw0,* and *bw1* reduced to zero in at least one direction at 0.06 rad. indicating that continuity between the beam and column was nearly lost. This behavior showed that for the matched connection the column sidewalls stiffened the connection causing high levels of strain at the corners of the beam. This eventually led to fracture and a rapid decrease in the connection capacity.

7.7.2 Strain in the Column Face

Strain in the column face could become large as a result of the beam prying on the column face. Figure 7.40 shows the strain in the three gages along the column face for the unmatched connection. Strain was highest at the center of the column face until facture. In compression, the center gage *cf0* reached a maximum strain of -0.0031 at 0.05 rad. drift level. Very little strain was seen in gage *cf2* throughout the loading protocol prior to fracture reaching a strain of -0.0006 before the 0.05 rad. drift cycle. After fracture the magnitude of the strain in *cf2* was 0.0101 as a result of the large prying on the column face.

The matched connection utilized three additional strain gages (Figure 7.10). This allowed for a more careful study of the strain levels near the welded connection (Figure 7.41). The strain in the column face was smaller for the matched connection than the unmatched connection. Before fracture at 0.05 rad. story drift the strains in *cf0, cf2,* and *cf4* were small. This indicated that much of the force was being transferred into the column sidewalls rather than the column face and yielding was limited. However, after fracture very high strain levels were observed in the column face localized near the beam. During the 0.05 rad. story drift cycle gage *cf2* reached a maximum strain of -0.0145. These results show that a matched beam width to column width was effective in moving the load into the column sidewalls and reducing strain at on the column face.

7.7.3 Strain at the Back of the Column

For both connections the strain on the column back was also monitored to understand the continuity of the connection (Figure 7.11). For both connections the strain on the column back was relatively small. In the unmatched connection, strain in the column back achieved a maximum value of 0.0004 in *cb2* (Figure 7.42). Strain in the beam and on the column face reached nearly 0.0150 for the matched connection, while the column back strain barely exceeded 0.0010 (Figure 7.43). Of all the strain gages, gage *cb2* of the matched connection achieved the maximum strain at the 0.05 rad. rotation level of 0.0013. For both connections after fracture the strains in the column back drop to nearly zero due to the large amount of force being transferred through the column face.

7.7.4 Strain in Panel Zone

Four strain gage rosettes were utilized to monitor the state of stress in the panel zone region (Figure 7.12). Shear strain versus story drift is plotted in Figure 7.44 for the unmatched connection and in Figure 7.45 for the matched connection. Shear strain from each rosette was calculated as follows:

$$\gamma_{xy} = 2\varepsilon_{45} - \varepsilon_x - \varepsilon_y \qquad \text{Equation 7.24}$$

where ε_x is the strain in the gage that lies parallel to the beam, $\varepsilon_y$is the strain in the gage that lies perpendicular to the beam member, and ε_{45} is the strain in the gage making a 45 degree angle with the beam member.

For the unmatched connection, shear strain remained small at all rotations. During the 0.04 rad. story drift cycle the largest shear strain, 0.0049, was at the center of the panel zone, *pz1*. Formation of compression and tension struts in the panel zone caused shear strain in *pz0* and *pz2* to increase up to 0.0029 and 0.0012 during the 0.04 rad. rotation cycle. After fracture the shear strain at the center of the panel zone (*pz1*) decreased to a maximum of 0.0024 at 0.05 rad. rotation. This behavior indicated that the panel zone was experiencing smaller deformations and was not being utilized to transfer connection forces. Shear strains in *pz3* remained small until after fracture where the maximum shear strain increased to 0.0023 at 0.05 rad. rotation. This was a result of redistribution of load inside the panel zone. Overall, the shear strain remained low as a result of the panel zone deformations being small.

In the matched connection the maximum shear strain was an order of magnitude greater than that for the unmatched connection. The matched connection reached a maximum shear strain at the center of the panel zone (*pz1*) equal to 0.0194 at 0.05 rad. rotation. The shear strain at the corner of the panel zone near the connection was also large at 0.05 rad. rotation reaching 0.0165 for *pz0* and 0.0091 for *pz2*. After fracture during the 0.06 rad. story drift cycle the shear strain at *pz1* decreased substantially to 0.0048. The shear strains at the corners near the connection increased after fracture to 0.0180 for *pz0* and to 0.0158 for *pz2*. Throughout the loading protocol strain near the backside of the connection where *pz3* was located remained small. The maximum shear strain in *pz3* was 0.0029 during the 0.05 rad. story drift cycle. Based on this analysis the matched connection performed better in terms of transferring loads to the column sidewalls, developing tension and compression struts in the panel zone, and reducing the reliance on the column face to carry load.

7.8 Applications to Design

Based on the experimental test of the unreinforced unmatched and matched connections, both connections were unable to behave in a manner appropriate for steel seismic moment frames. The plastic rotations typically occurred outside the beam and panel zone regions. Neither connection fully formed a stable plastic hinge or balanced connection behavior.

These tests still provided useful data for the utilization of HSS-to-HSS moment connections. Designers now have a better understanding of the limitations of HSS-to-HSS moment connections experiencing low-cycle fatigue. The performance of unmatched and matched connections in terms of plastic rotations, failure rotation, and normalized moment capacity under cyclic loads is better understood. Unreinforced HSS-to-HSS moment connections can experience large drifts without failure, but the sources of inelasticity are not suitable for seismic moment frame design. The stiffness of unreinforced connections was shown to be low and degraded quickly with increased rotations. Due to the low stiffness, care should be used in limiting drifts in these connections. Strain in the connection region was high, especially at the weld toe where fracture occurred. Procedures that minimize the effects of stress concentration in this region should be utilized such as ductile weld metals and shot peening.

7.9 Conclusions

The experimental connection study described in this chapter addressed the ability of two unreinforced HSS-to-HSS moment connections to form stable plastic hinges in the beam member under large cyclic rotations. The hysteretic behavior was carefully evaluated and the sources of inelastic rotation were considered. The effects of continued cycling were assessed in terms of energy dissipation, equivalent viscous damping, and secant stiffness. Additionally, the distribution of strain in the connection region was evaluated to better understand the load transfer mechanism and failure mode. Several conclusions were derived from these experiments.

1. The HSS-to-HSS moment connections showed stable hysteretic behavior at rotations equal up to 0.04 rad. story drift for the unmatched connection (β=0.8) and 0.05 rad. story drift for the matched connection (β=1.0). At these rotation levels, fracture was observed in the connection and the moment capacity decreased by over 75% of the maximum moment capacity.
2. The plastic rotation of the connection was analyzed. At maximum moment, the beam rotation was only 30% of the inelastic rotation for the unmatched connection and only 20% of the inelastic rotation for the matched connection.
3. Matched connections were better suited to moving deformations to the column sidewalls. Rotation in the column face exceeded 55% of the inelastic rotation for all drift levels in the unmatched connection, while rotation in the column face contributed up to 32% of all inelastic rotation for the matched connection.
4. The degradation of the secant stiffness increased with increasing loss of moment capacity. The matched connection was better able to reduce loss of stiffness at increased rotation levels since there was less reliance on the column face as a source of connection capacity.
5. The cumulative energy dissipation at 0.04 rad. was lower for the unmatched connection, 142 k-in., than the matched connection, 291 k-in. However, the unmatched connection had a higher percentage of equivalent viscous damping

(26.6%) compared to the matched connection (24.3%), indicating that it was slightly more efficient at dissipating energy.

6. Analysis of the strain gage data showed that load transfers from the beam corners into the column face and sidewalls. The matched connection was more effective at spreading strain across the beam flange before fracture, leading to reduced strain in the column face at maximum moment capacity.
7. Shear strain in the panel zone was small for the unmatched connection reaching only 0.0049 in the middle of the panel zone (*pz1*) at maximum moment. For the matched connections shear strain in the center of the panel zone (*pz1*) was much larger with a maximum value of 0.0194 at maximum moment. As a result of the matched connections ability to transfer loads to the column sidewalls, the panel zone was utilized more effectively.

Table 7.1 Unreinforced HSS-to-HSS moment connection column section properties

HSS Column Member (in. x in. x in.)	Depth d_c (in.)	Width w_c (in.)	Thickness t_c (in.)	h/t	b/t	Column Plastic Section Modulus Z (in.^{3})	Column Plastic Moment Capacity $M_{p,c}$ (k-in.)
HSS 10x10x5/8	10	10	0.581	15.7	15.7	73.2	4360

Table 7.2 Unreinforced HSS-to-HSS moment connection experimental beam section properties

HSS Beam Member (in. x in. x in.)	Depth d_b (in.)	Width w_b (in.)	Thickness t_b (in.)	h/t	b/t	Beam Plastic Section Modulus Z (in.^{3})	Beam Plastic Moment Capacity $M_{p,b}$ (k-in.)	Beam Width-Column Width Ratio β	$M_{p,b}/M_{p,c}$	t_b/t_c
HSS 12x8x3/8	12	8	0.349	32.9	21.4	53	2438	0.8	0.72	0.60
HSS 12x10x3/8	12	10	0.349	32.9	27.2	61.1	2811	1.0	0.83	0.60

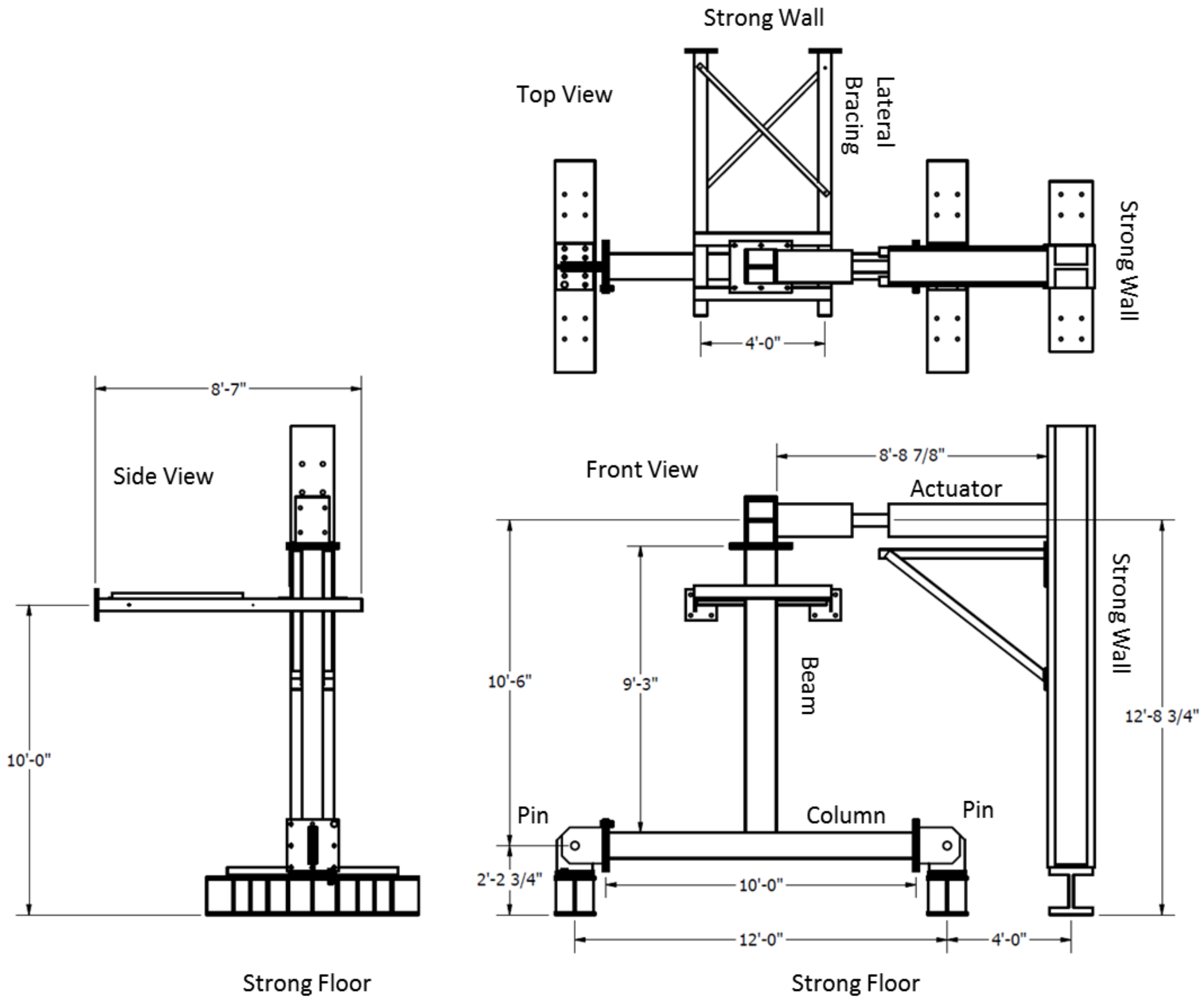

Figure 7.1 HSS-to-HSS moment connection test setup

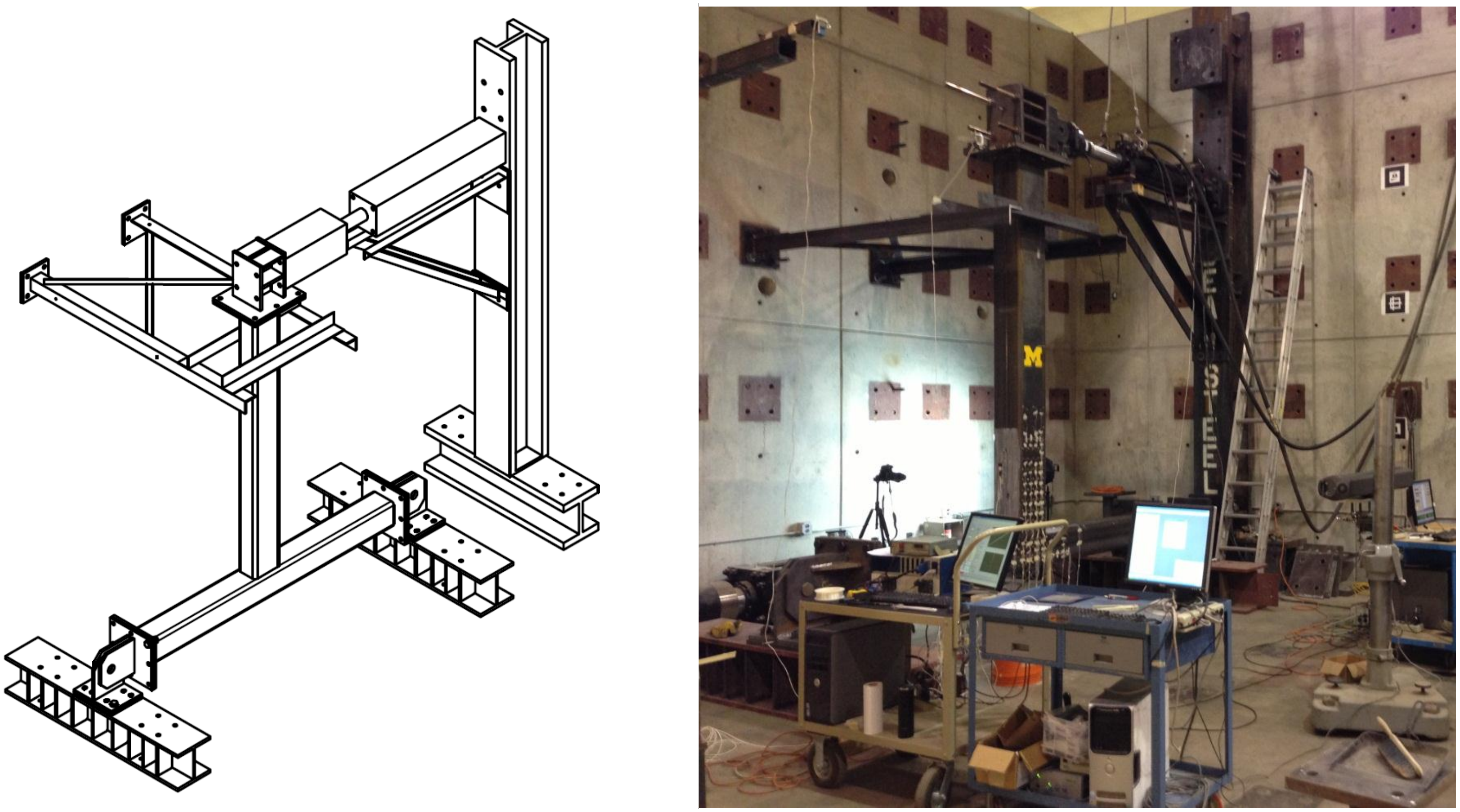

(a)

(b)

Figure 7.2 HSS-to-HSS moment connection test setup (a) isometric view and (b) photograph

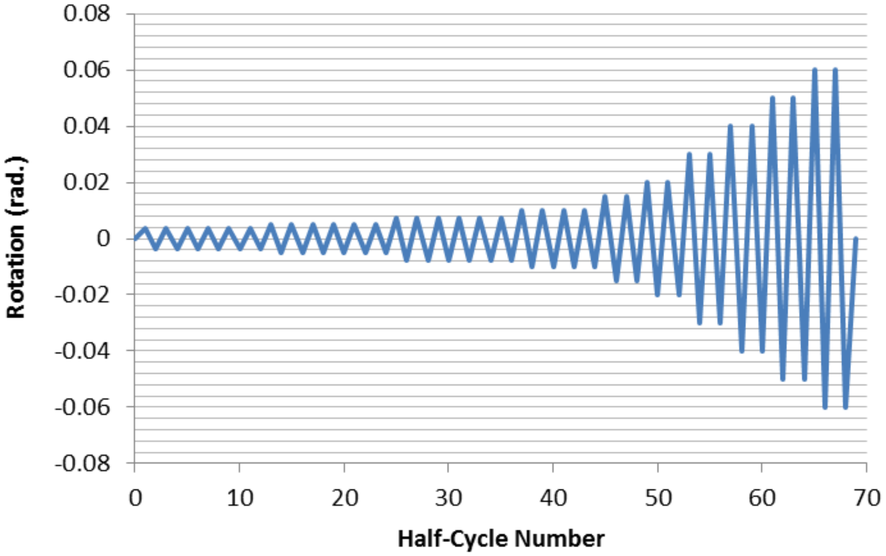

Figure 7.3 Experimental loading protocol for the HSS-to-HSS connection tests

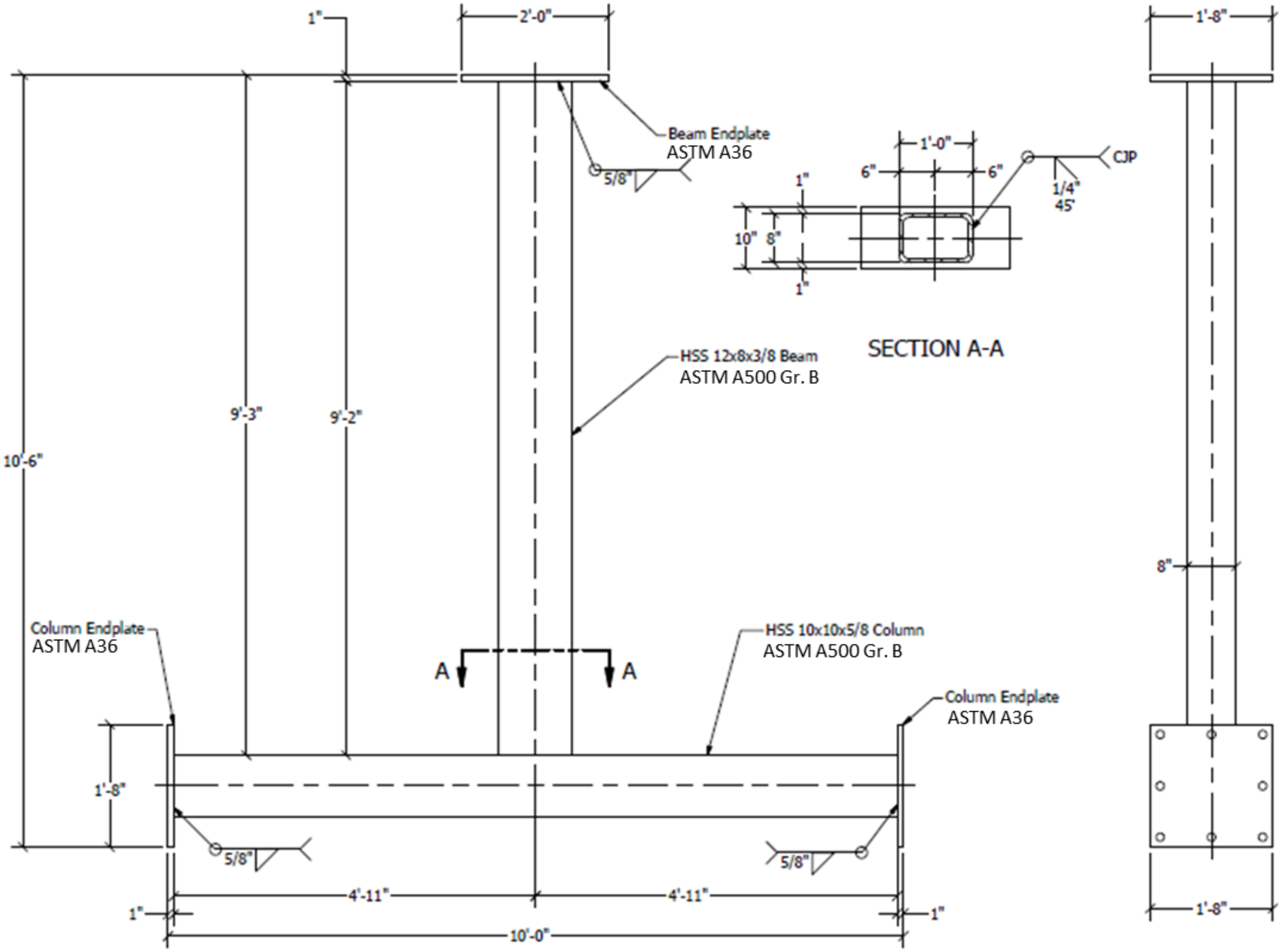

Figure 7.4 Unmatched (HSS 12x8x3/8 beam) HSS-to-HSS moment connection

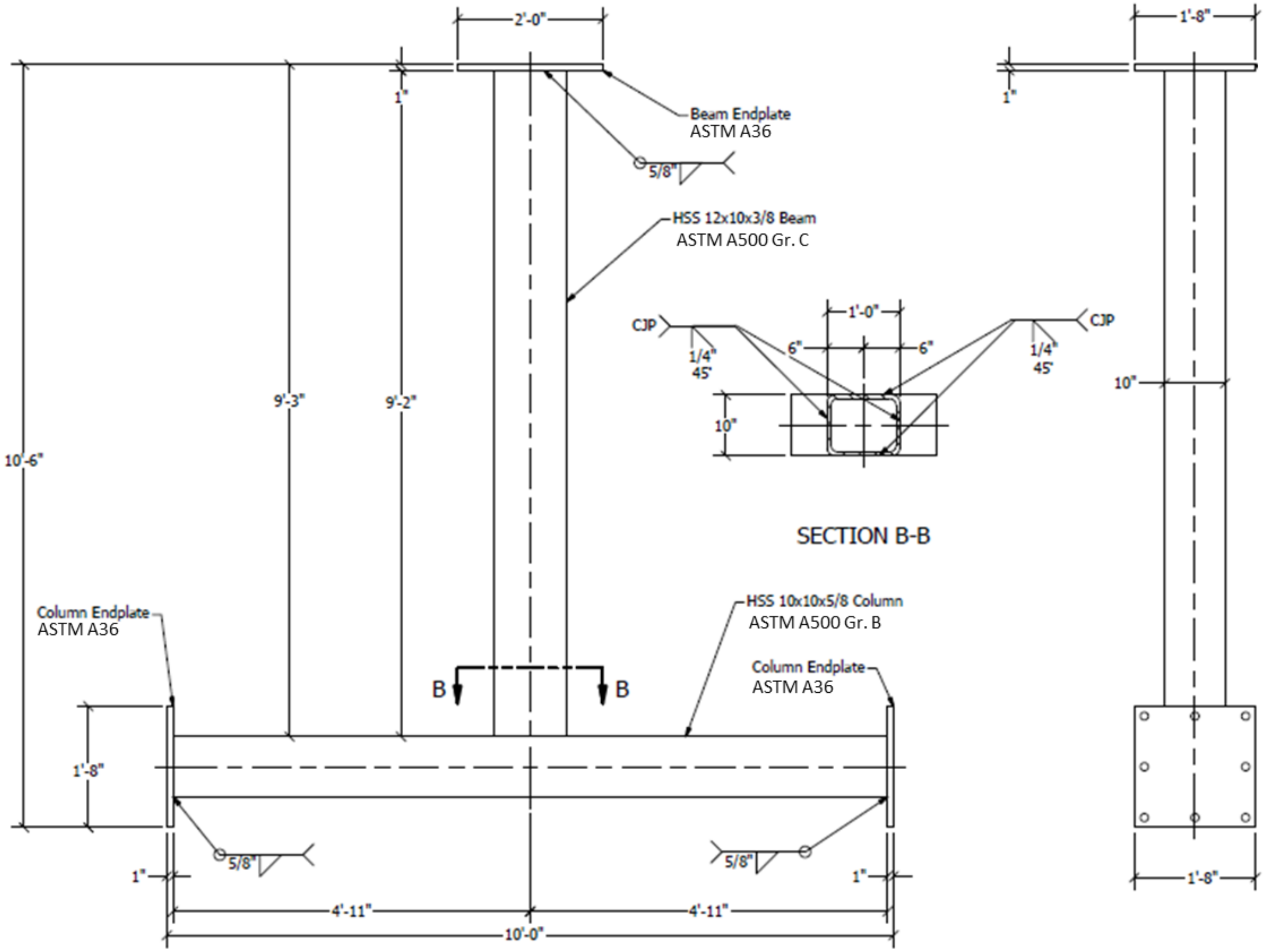

Figure 7.5 Matched (HSS 12x10x3/8 beam) HSS-to-HSS moment connection

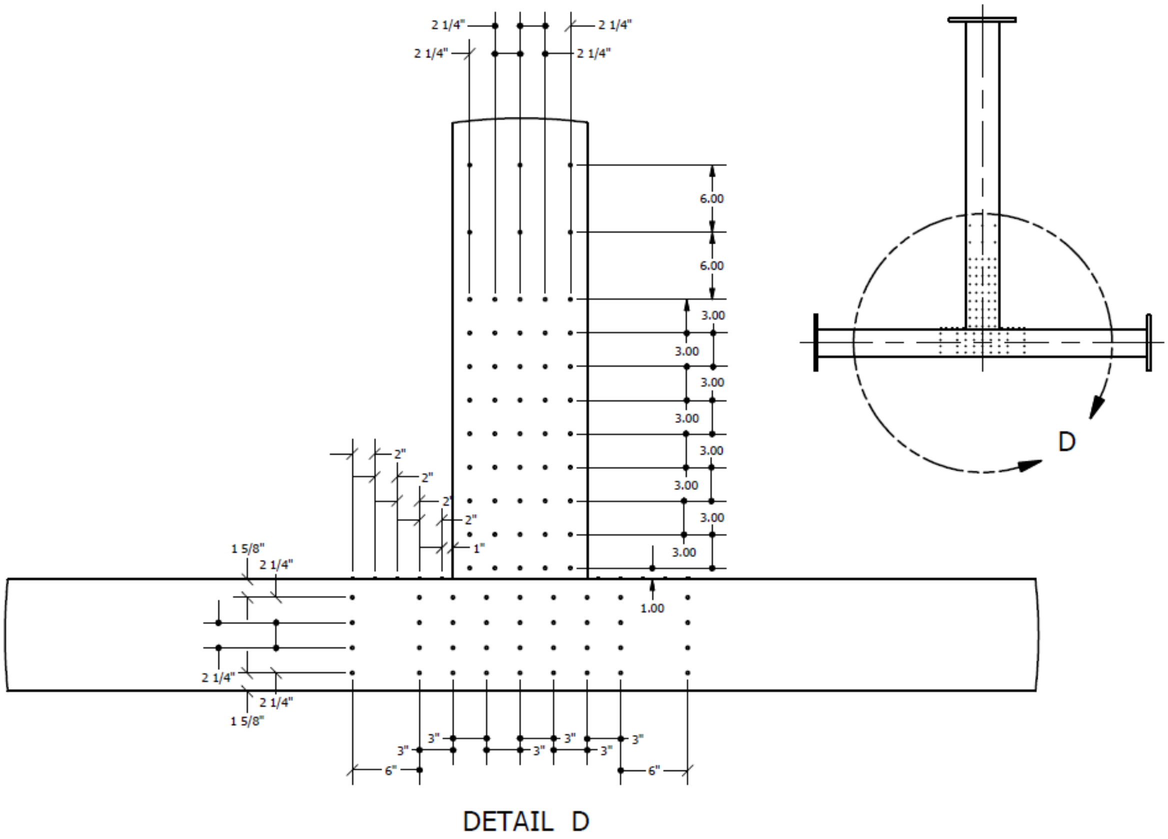

Figure 7.6 Optotrak maker layout (where each black dot represents one marker)

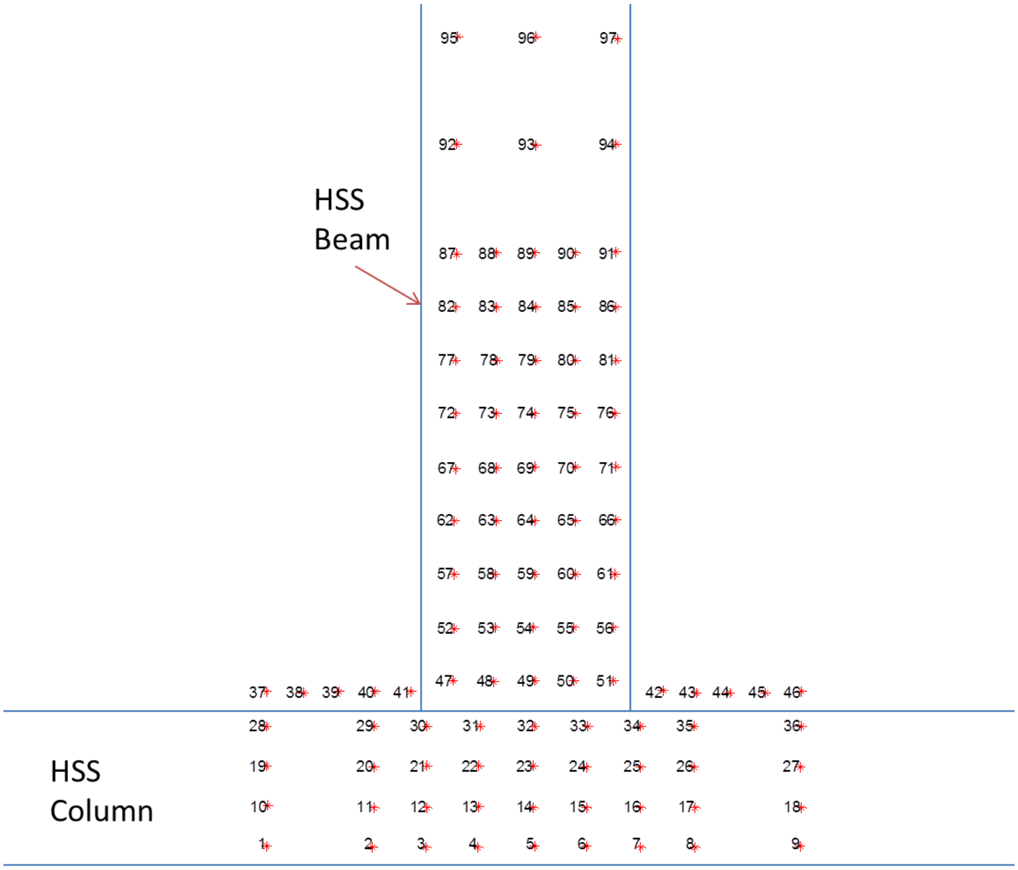

Figure 7.7 Optotrak marker numbering scheme

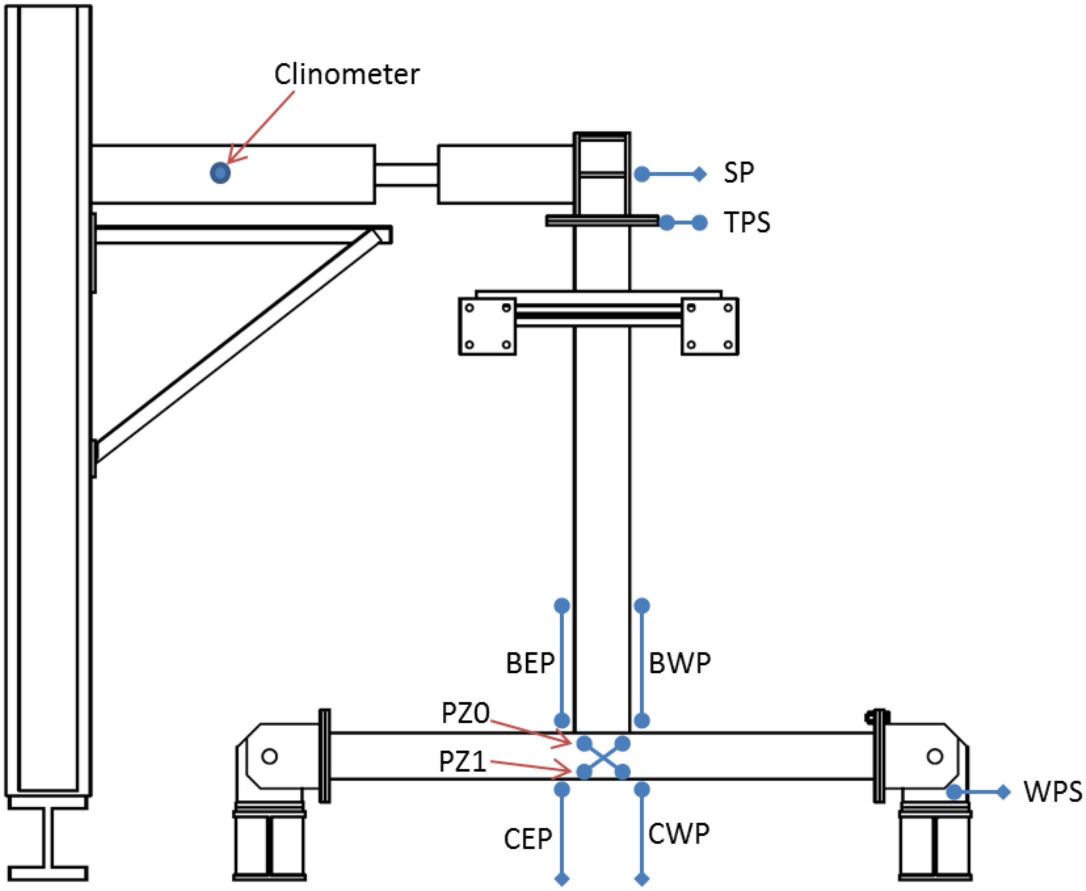

Figure 7.8 Layout of non-optical marker instrumentation primarily used for secondary measurements

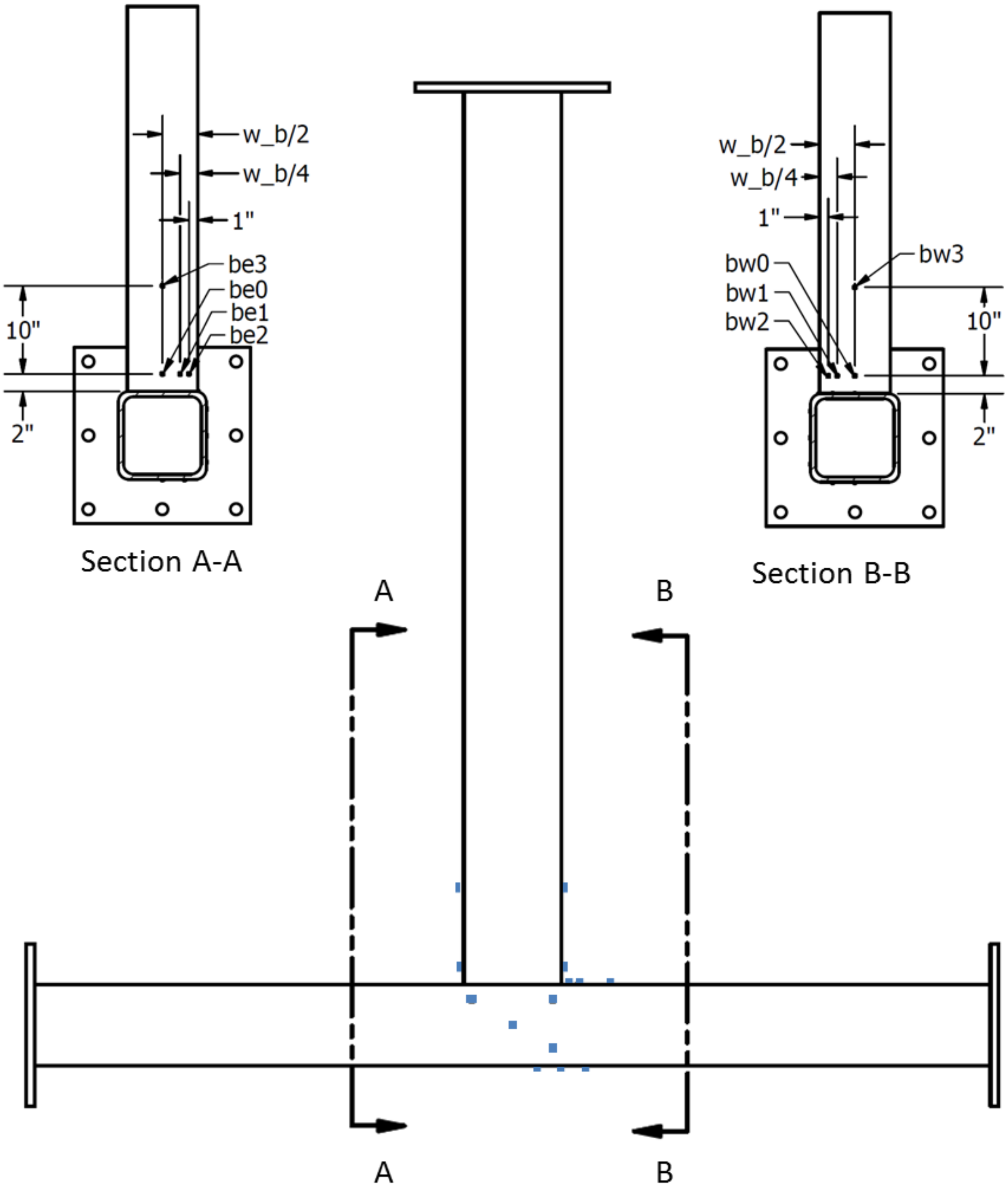

Figure 7.9 Beam strain gage locations

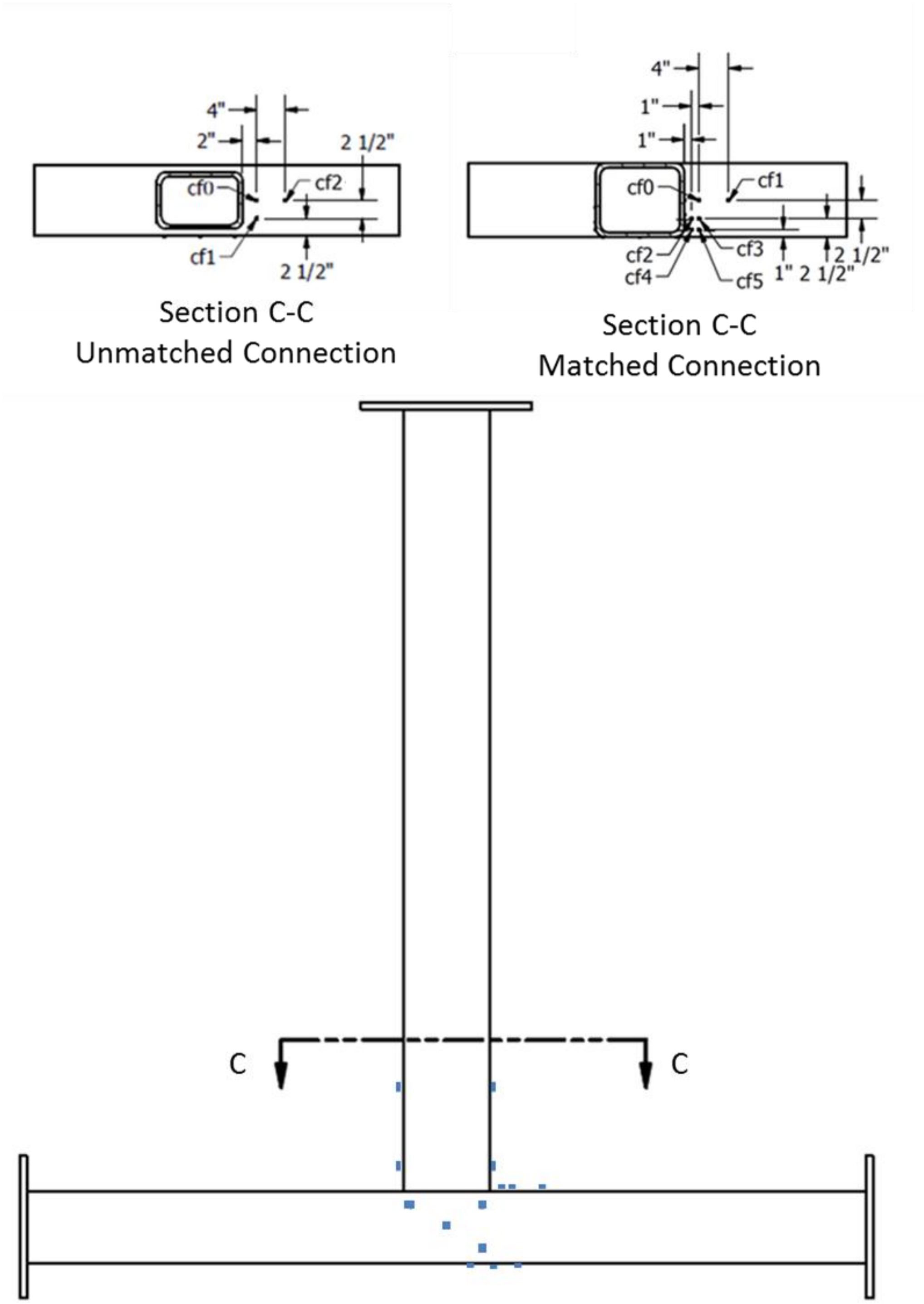

Figure 7.10 Column face strain gage locations

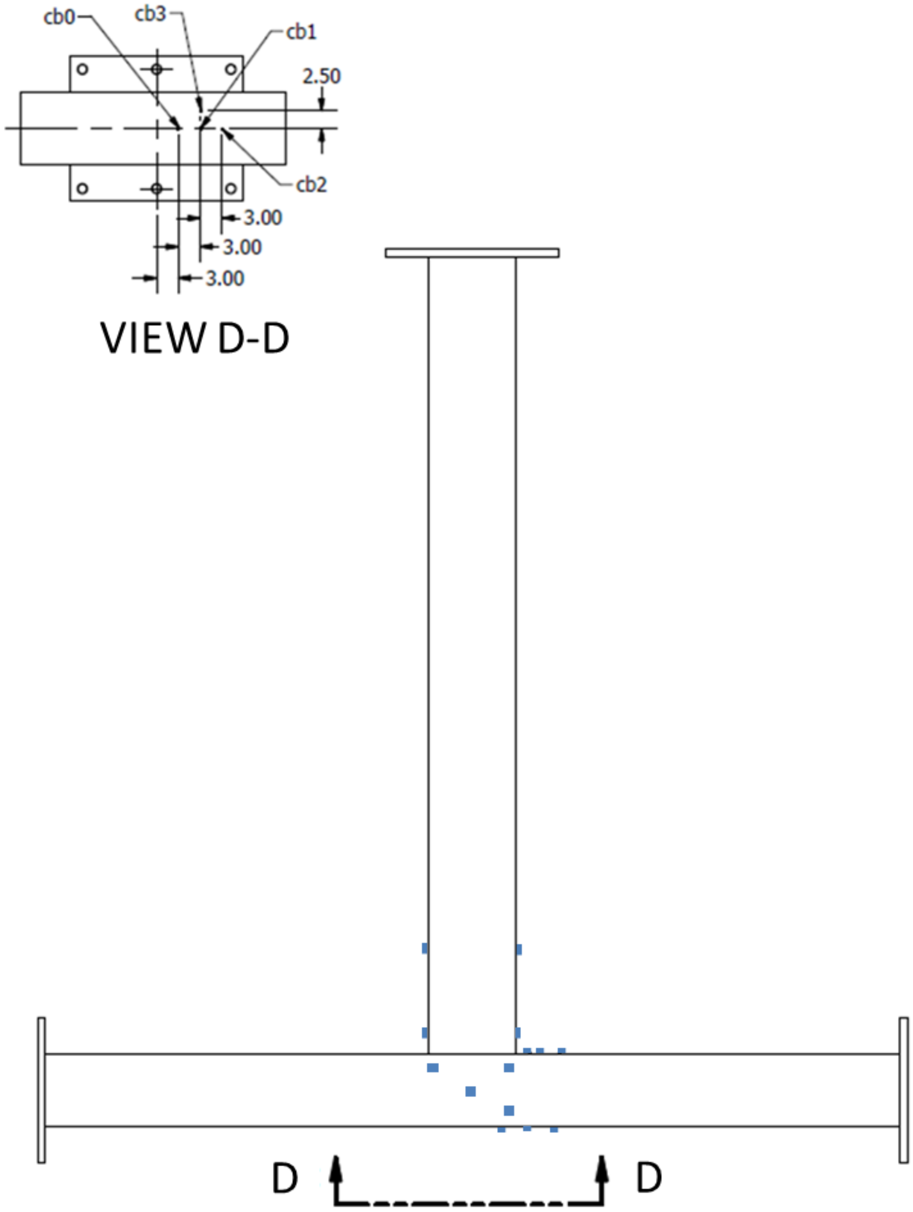

Figure 7.11 Column back strain gage locations

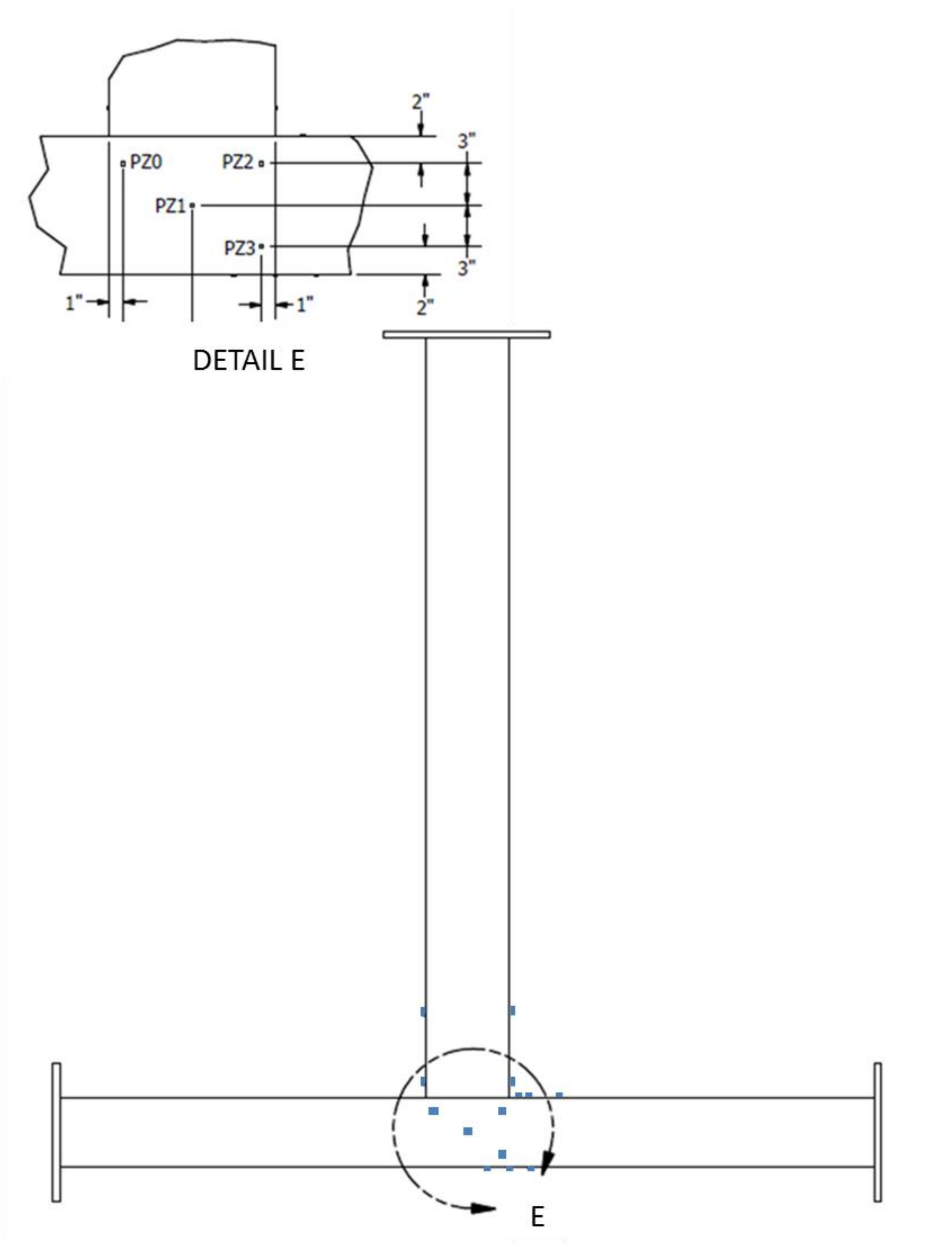

Figure 7.12 Panel zone strain gage locations

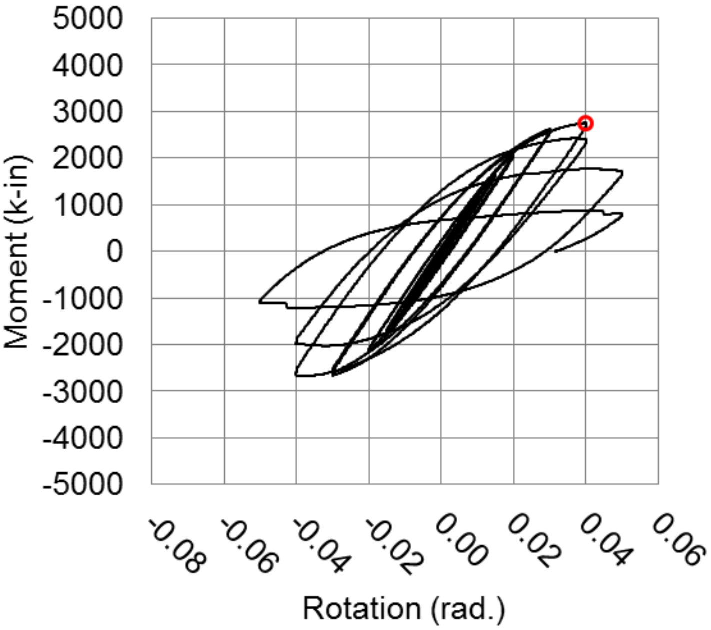

Figure 7.13 Unmatched connection (HSS 12x8x3/8 beam) moment versus connection rotation

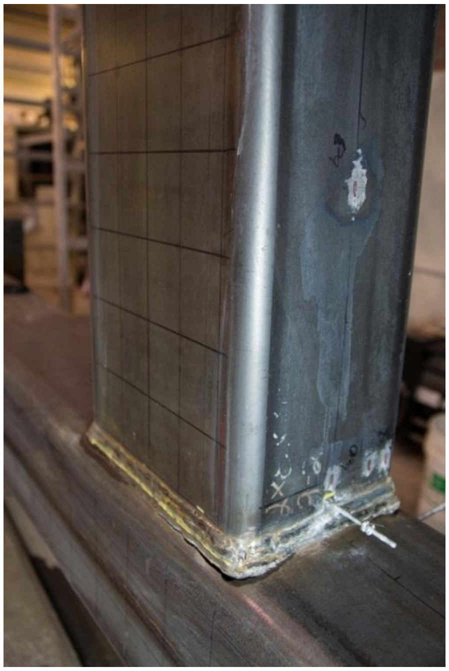

Figure 7.14 Extent of the observed fracture in the unmatched connection at the completion of the test

Figure 7.15 Close up of the fracture in the base metal of the column at the toe of the weld in the unmatched connection at the completion of the test

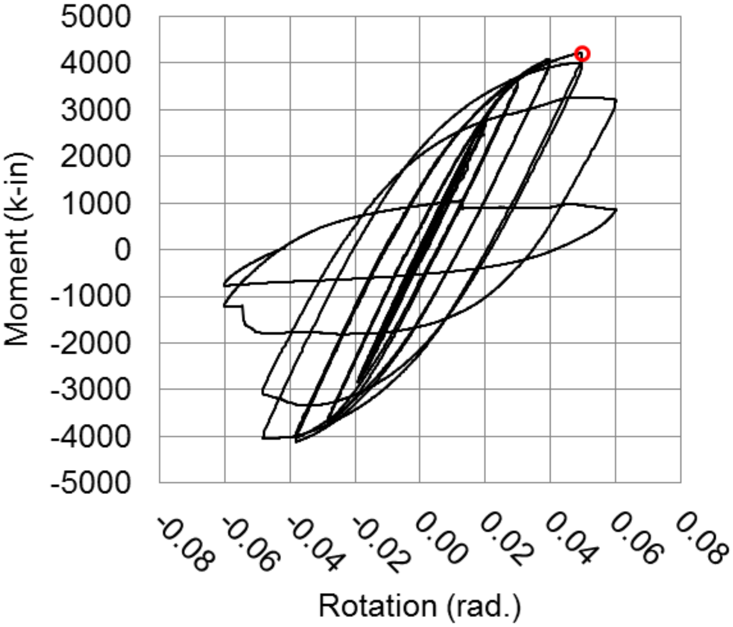

Figure 7.16 Matched connection (HSS 12x10x3/8 beam) moment versus connection rotation

Figure 7.17 Extent of the observed fracture in the matched connection at the completion of the test.

Figure 7.18 Close up of the fracture in the base metal of the column at the toe of the weld in the matched connection at the completion of the test

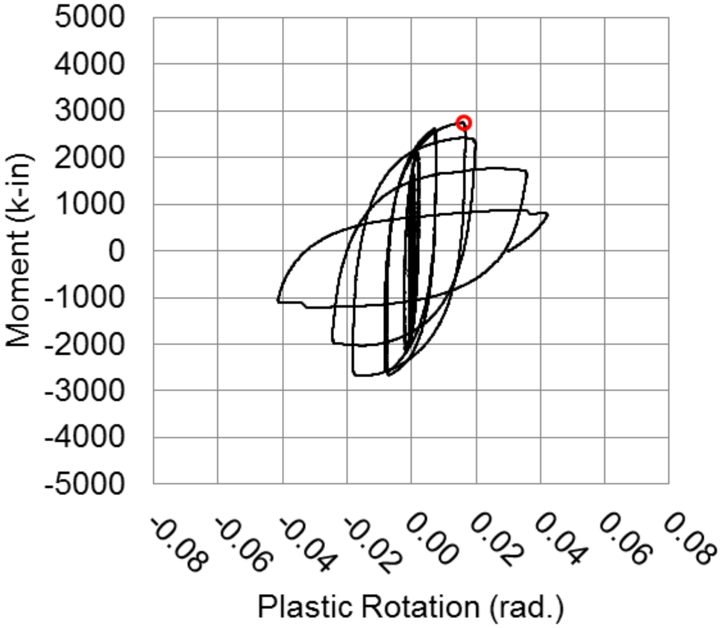

Figure 7.19 Experimental moment-plastic rotation hysteresis for the unmatched connection (HSS 12x8x3/8 beam)

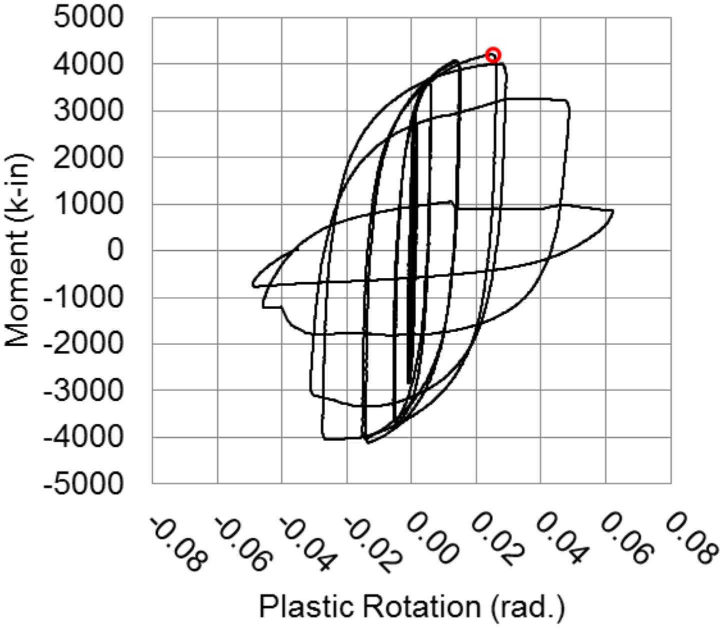

Figure 7.20 Experimental moment-plastic rotation hysteresis for the matched connection (HSS 12x10x3/8 beam)

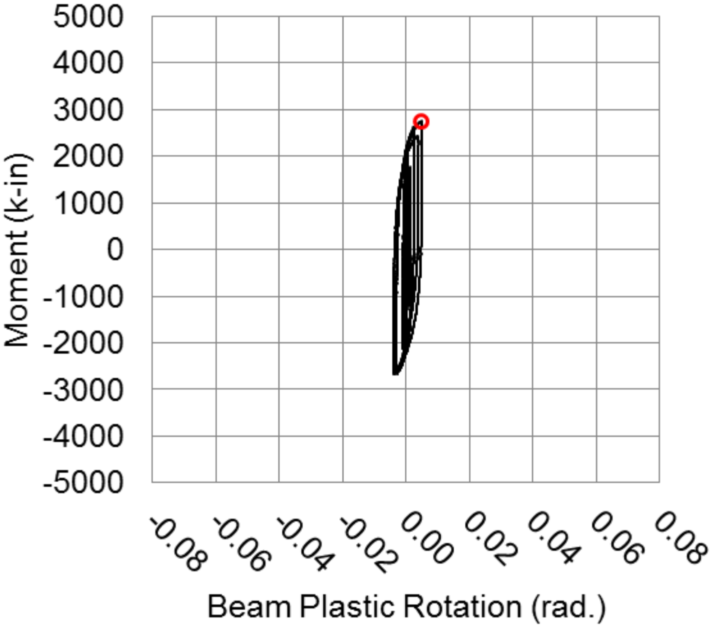

Figure 7.21 Experimental moment-beam plastic rotation hysteresis for the unmatched connection (HSS 12x8x3/8 beam)

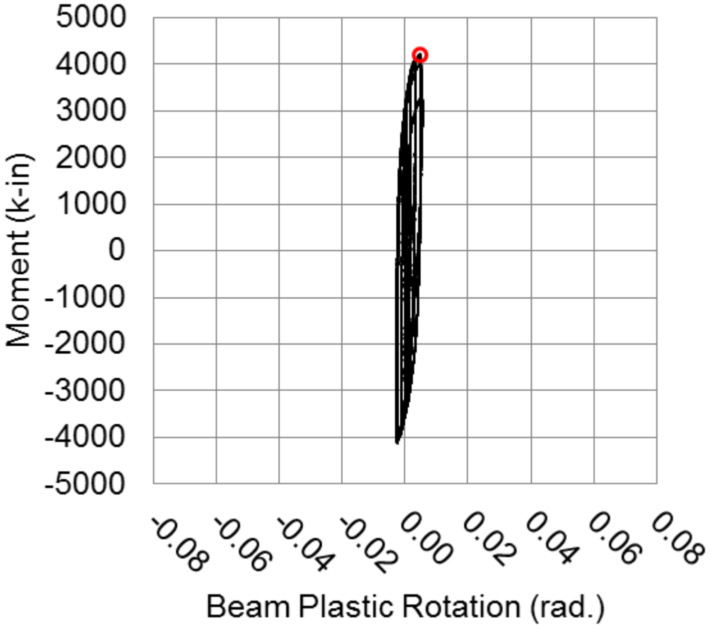

Figure 7.22 Experimental moment-plastic beam rotation hysteresis for the matched connection (HSS 12x10x3/8 beam)

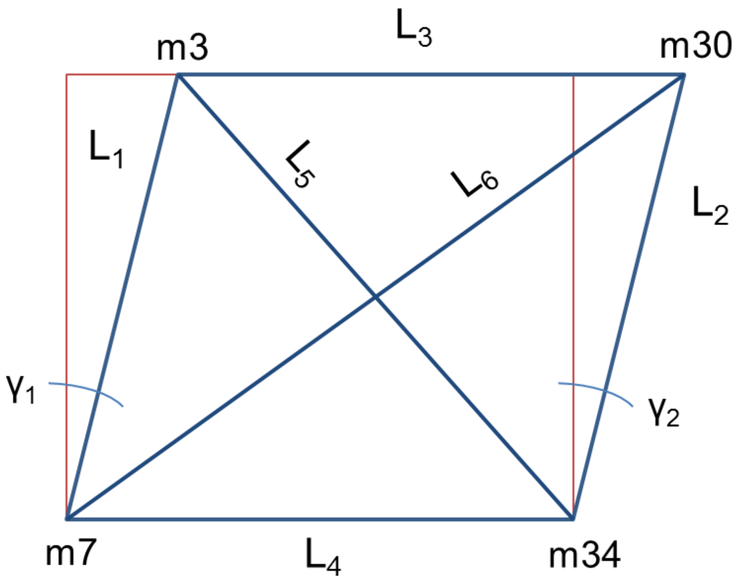

Figure 7.23 Panel zone distortion and parameters

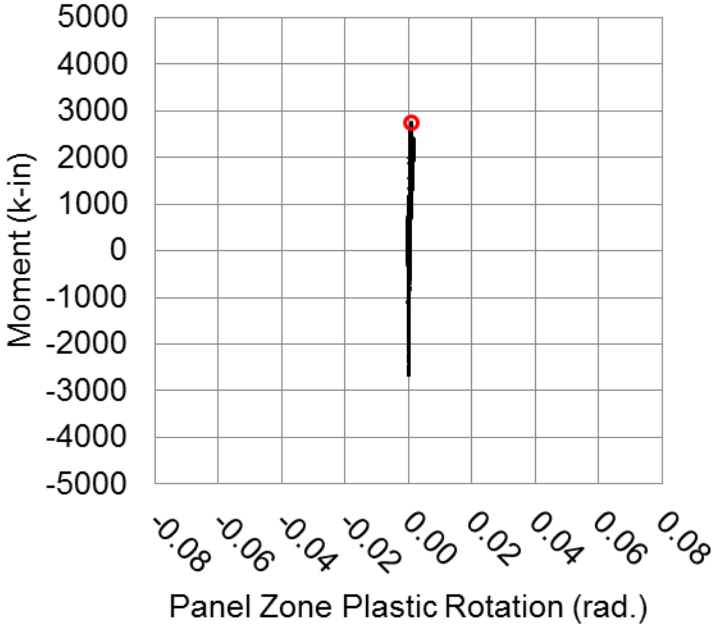

Figure 7.24 Experimental moment-plastic panel zone rotation hysteresis for the unmatched connection (HSS 12x8x3/8 beam)

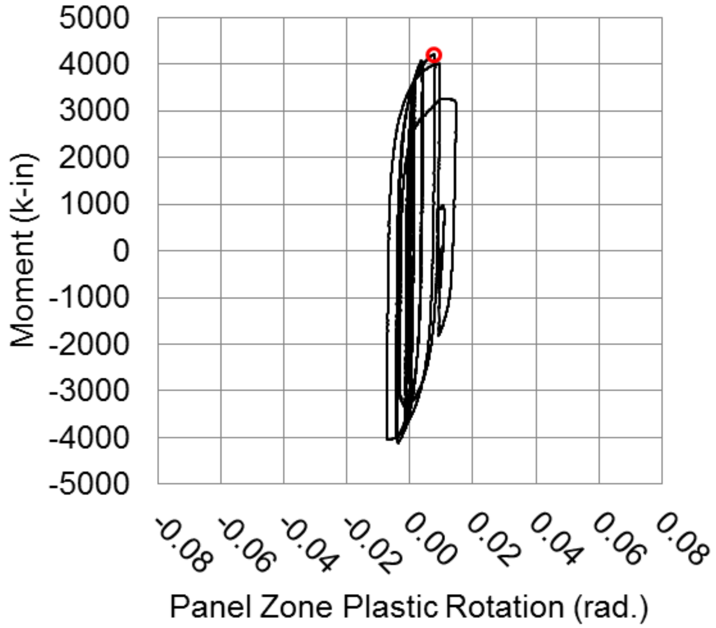

Figure 7.25 Experimental moment-plastic panel zone rotation hysteresis for the matched connection (HSS 12x10x3/8 beam)

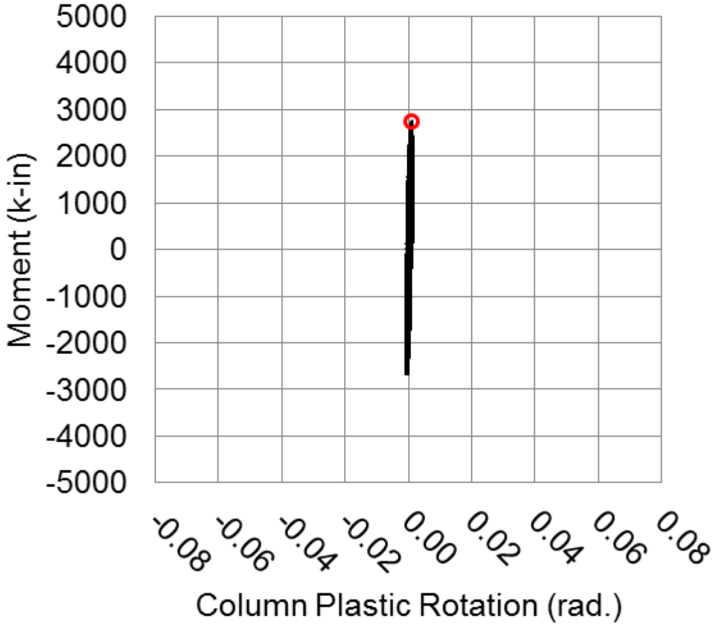

Figure 7.26 Experimental moment-plastic column rotation hysteresis for the unmatched connection (HSS 12x8x3/8 beam)

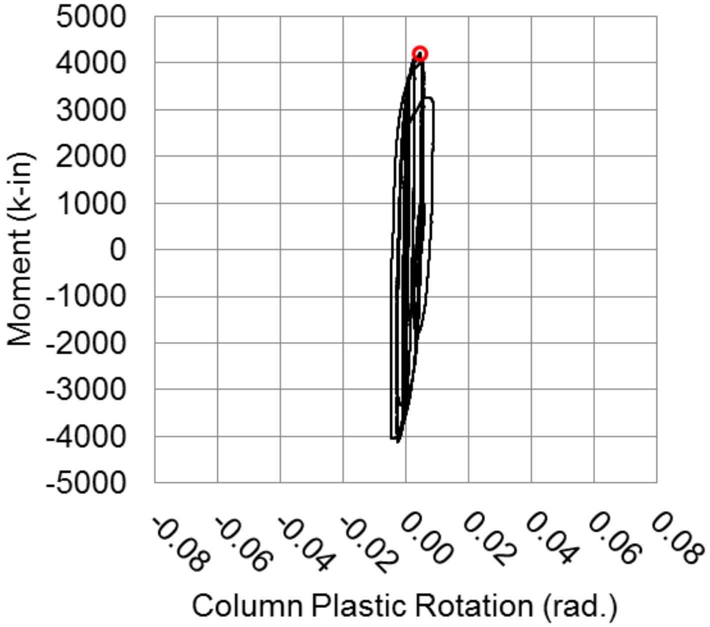

Figure 7.27 Experimental moment-plastic column rotation hysteresis for the matched connection (HSS 12x10x3/8 beam)

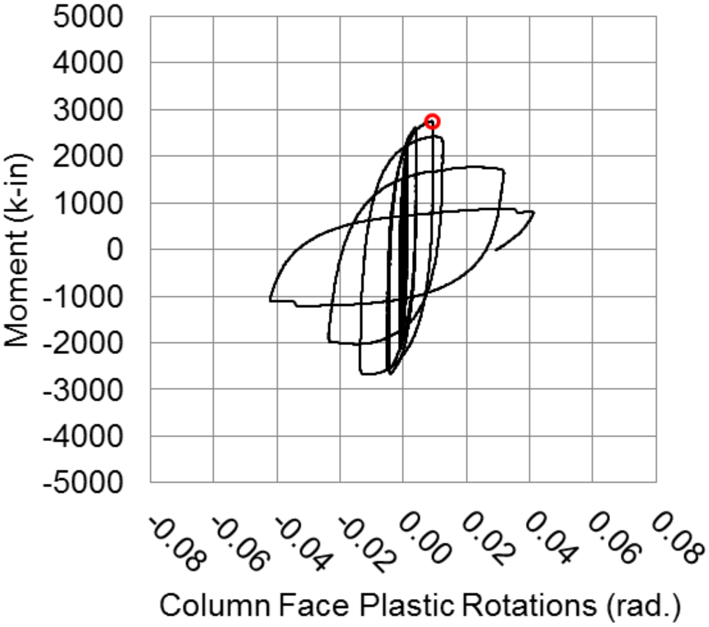

Figure 7.28 Experimental moment-column face rotations hysteresis for the unmatched connection (HSS 12x8x3/8 beam)

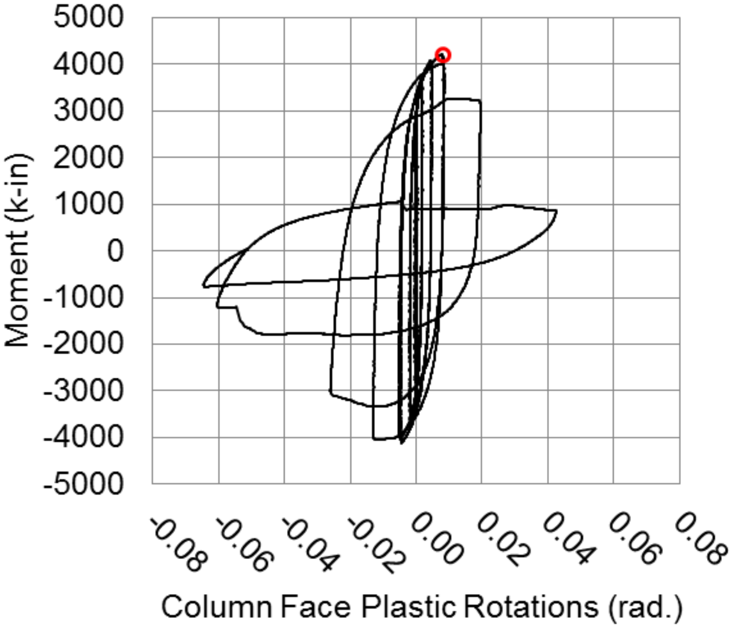

Figure 7.29 Experimental moment-column face rotations hysteresis for the matched connection (HSS 12x8x3/8 beam)

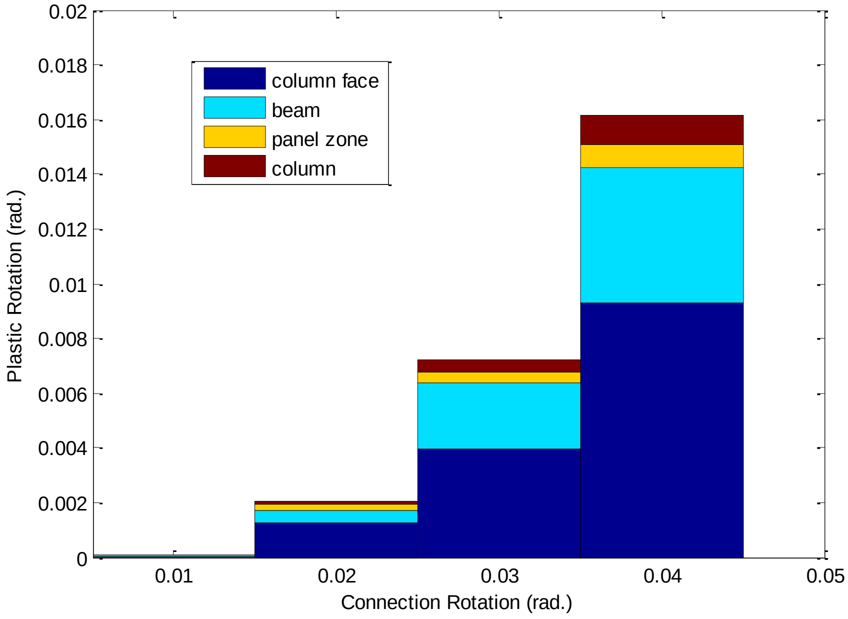

Figure 7.30 Contribution of plastic rotation components for the unmatched connection (HSS 12x8x3/8 beam)

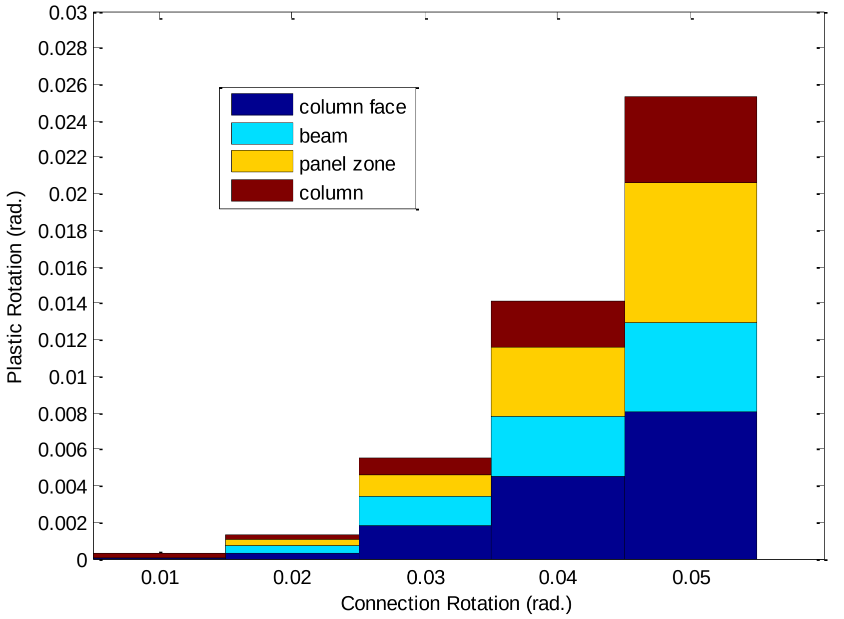

Figure 7.31 Contribution of plastic rotation components for the matched connection (HSS 12x10x3/8 beam)

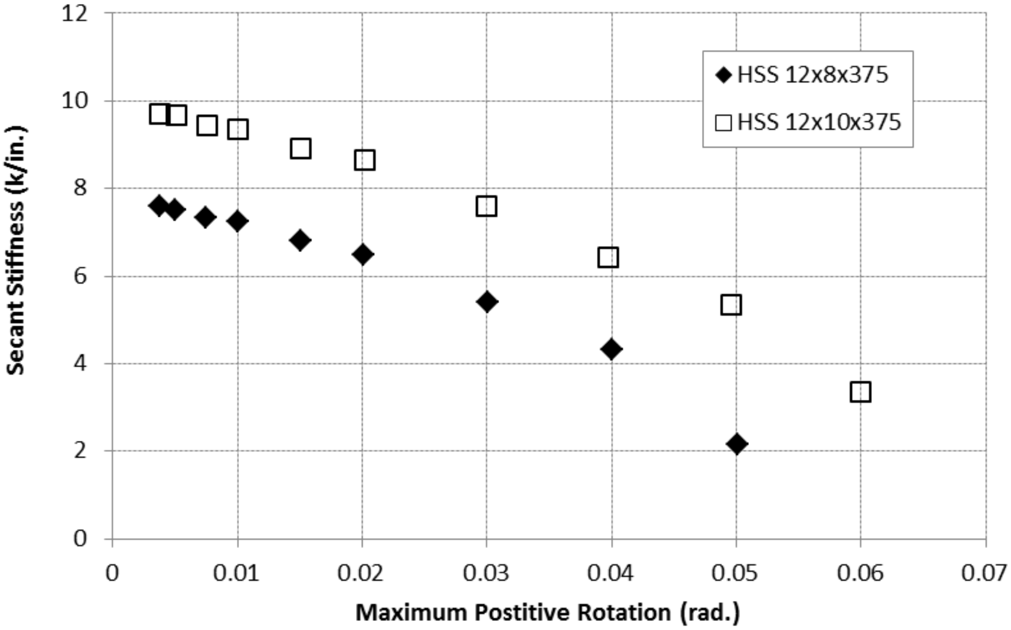

Figure 7.32 Secant stiffness versus maximum positive rotation

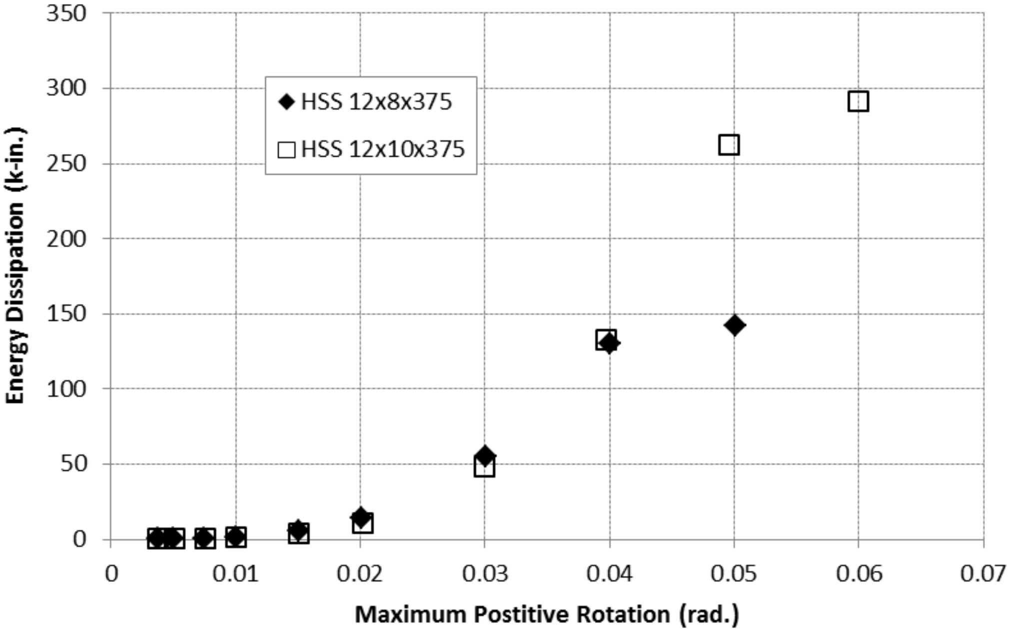

Figure 7.33 Energy dissipation versus maximum positive rotation

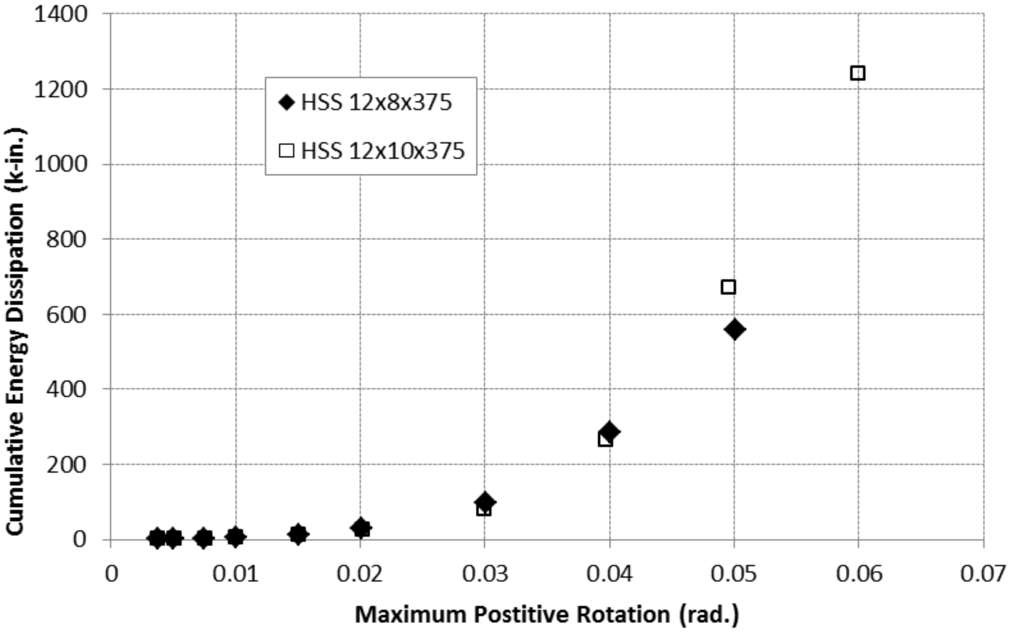

Figure 7.34 Cumulative energy dissipation versus maximum positive rotation

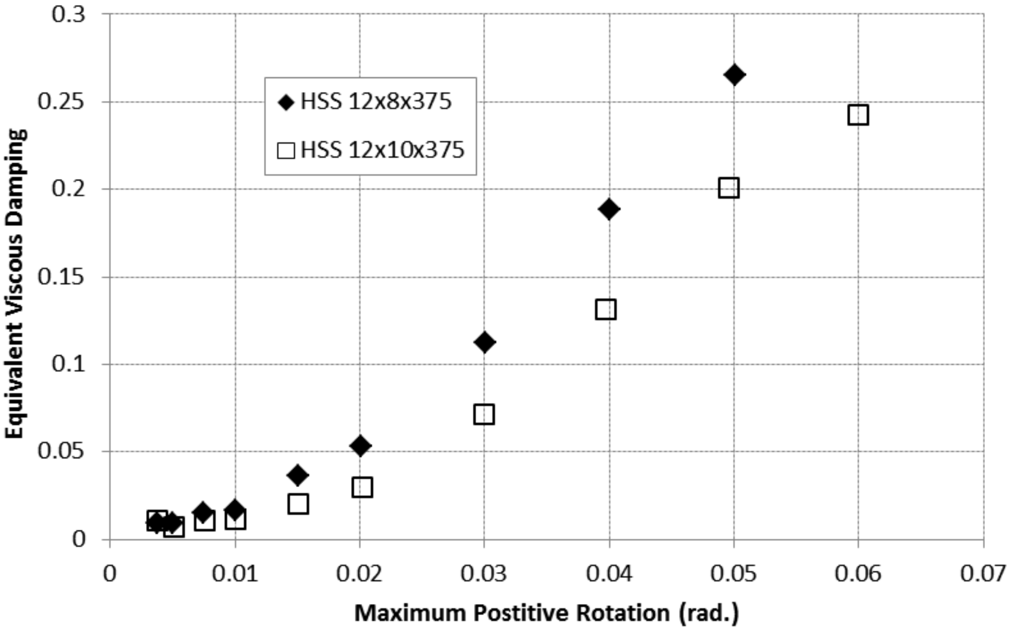

Figure 7.35 Equivalent viscous damping versus maximum positive rotation

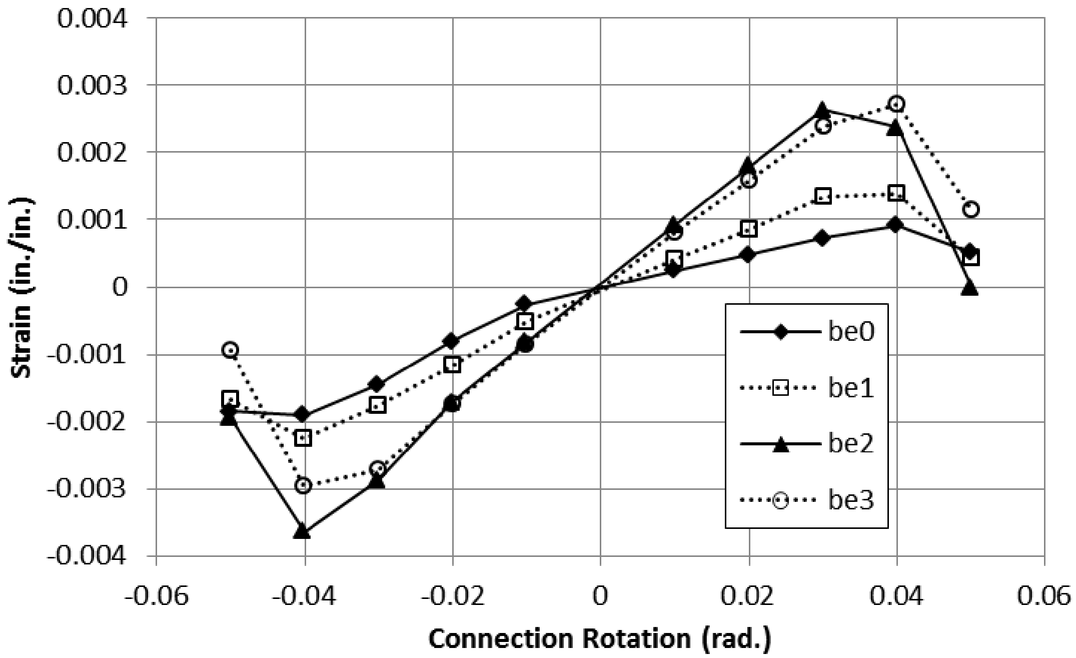

Figure 7.36 Strain in the beam versus connection rotation (*be1-be3*) for the unmatched connection

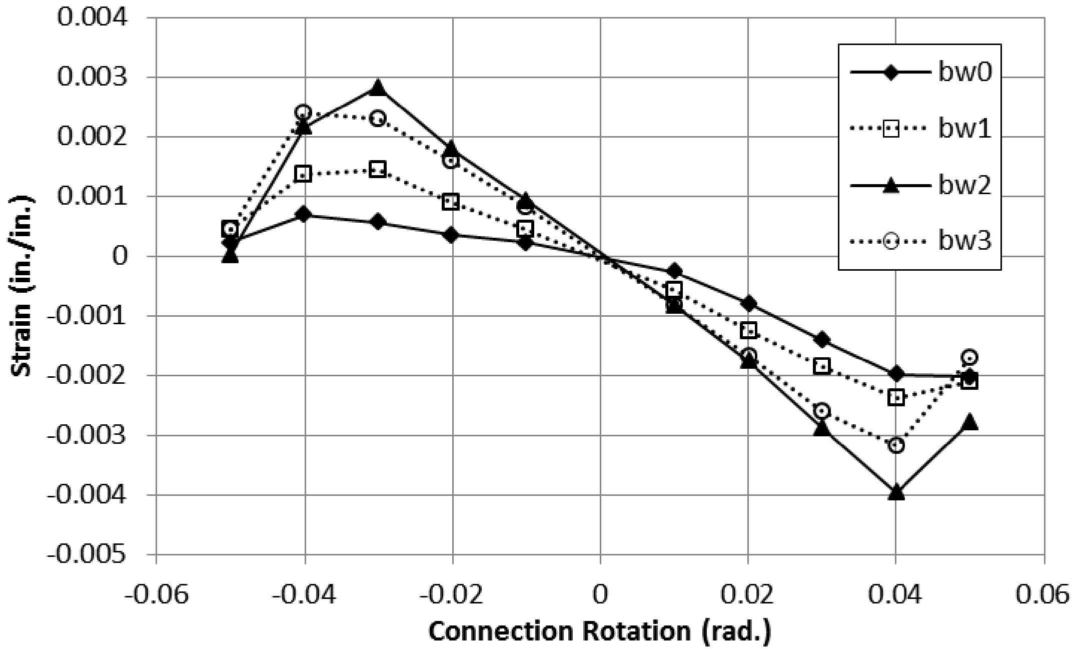

Figure 7.37 Strain in the beam versus connection rotation (*bw1-bw3*) for the unmatched connection

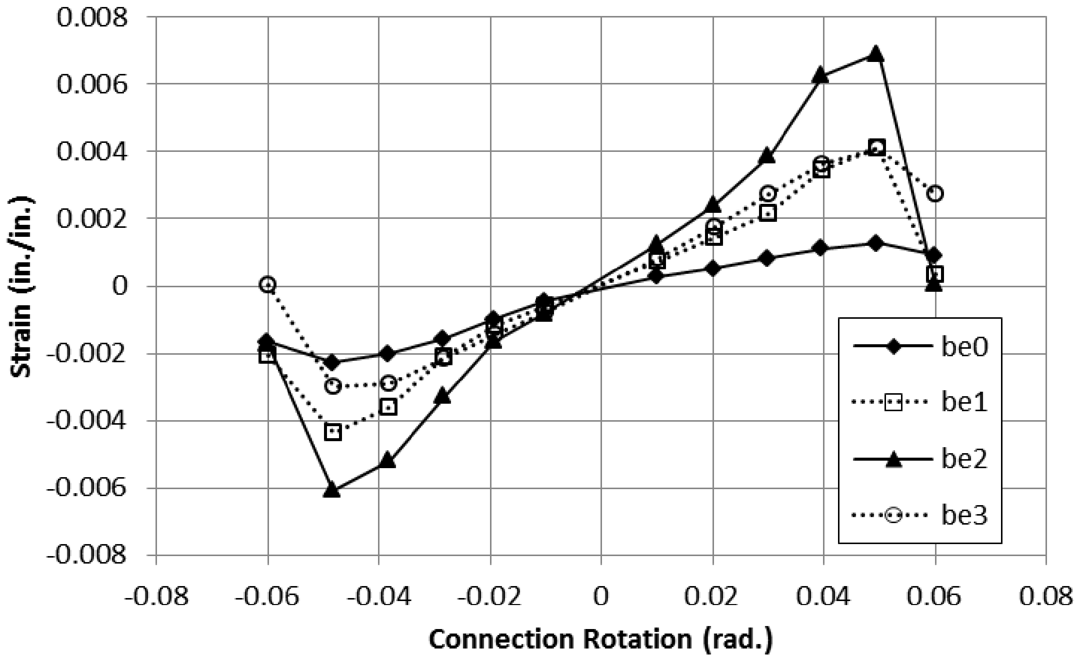

Figure 7.38 Strain in the beam versus connection rotation (*be1-be3*) for the matched connection

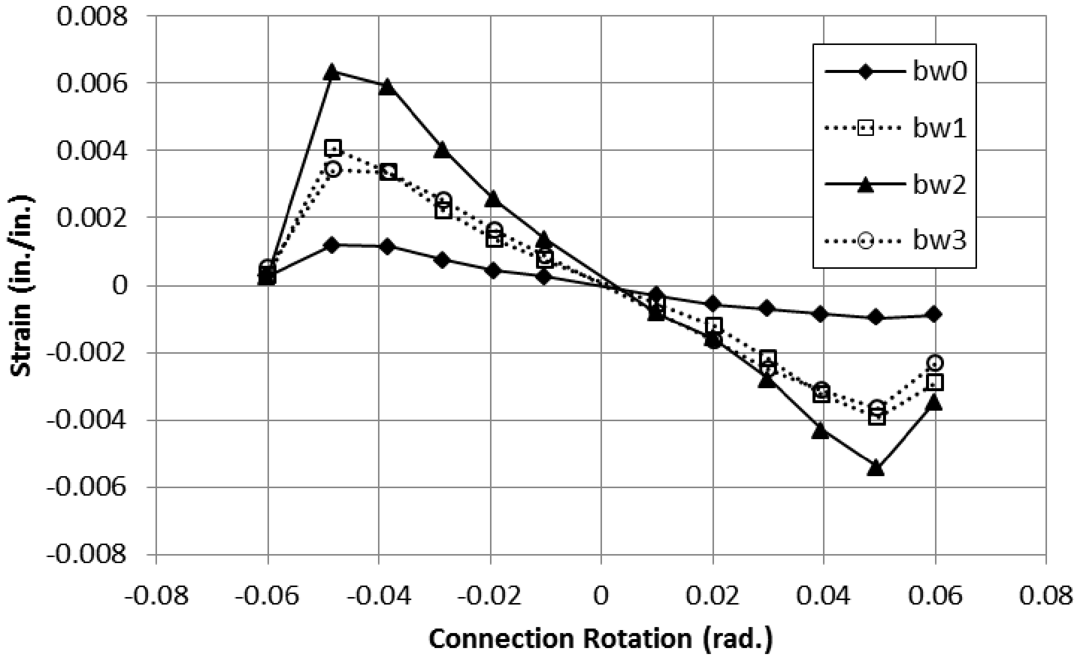

Figure 7.39 Strain in the beam versus connection rotation (*bw1-bw3*) for the matched connection

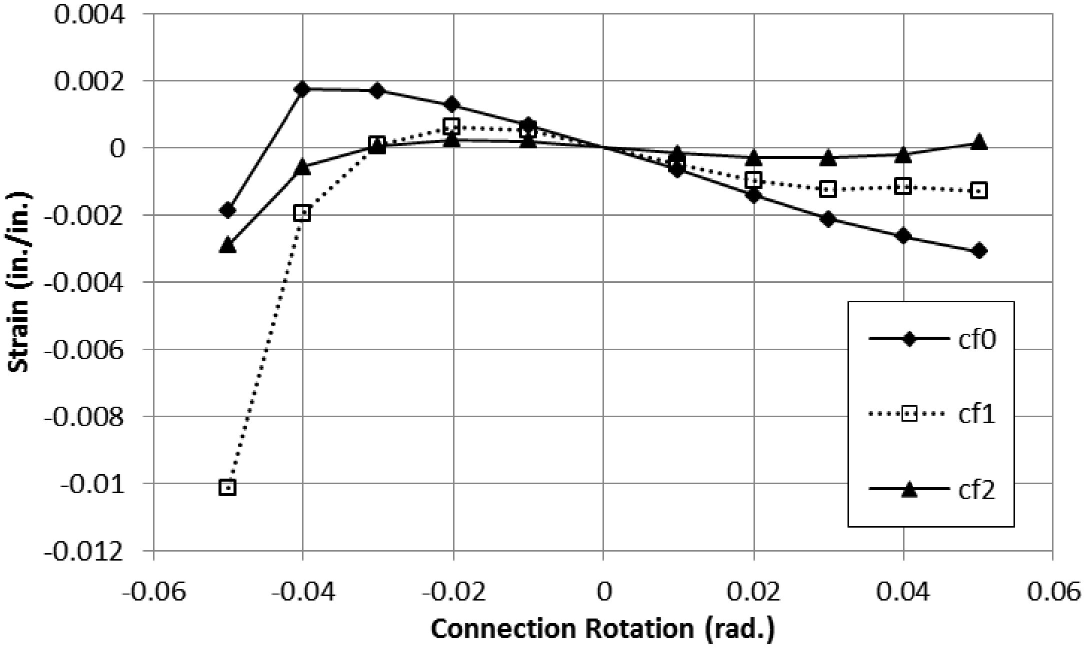

Figure 7.40 Strain in the column face versus connection rotation for the unmatched connection

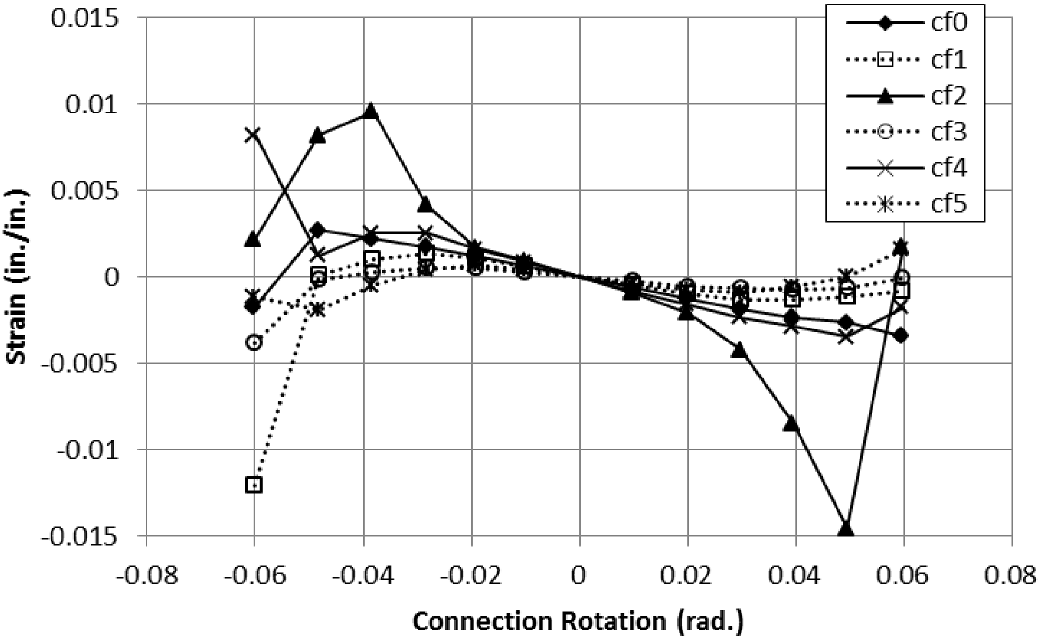

Figure 7.41 Strain in the column face versus connection for the matched connection

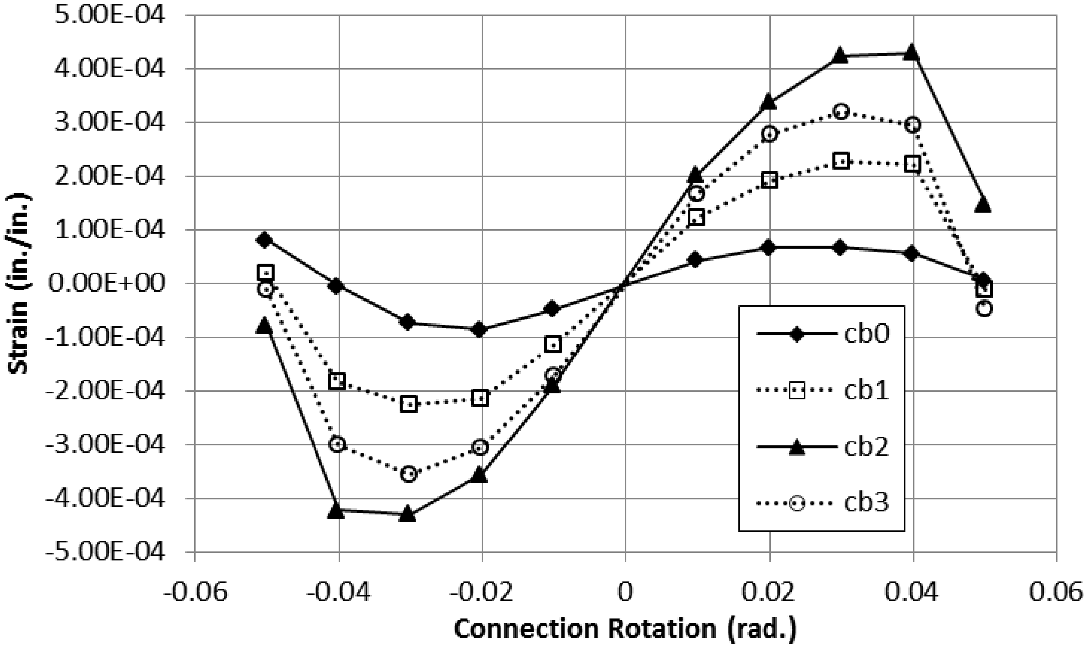

Figure 7.42 Strain in the column back versus connection rotation for the unmatched connection

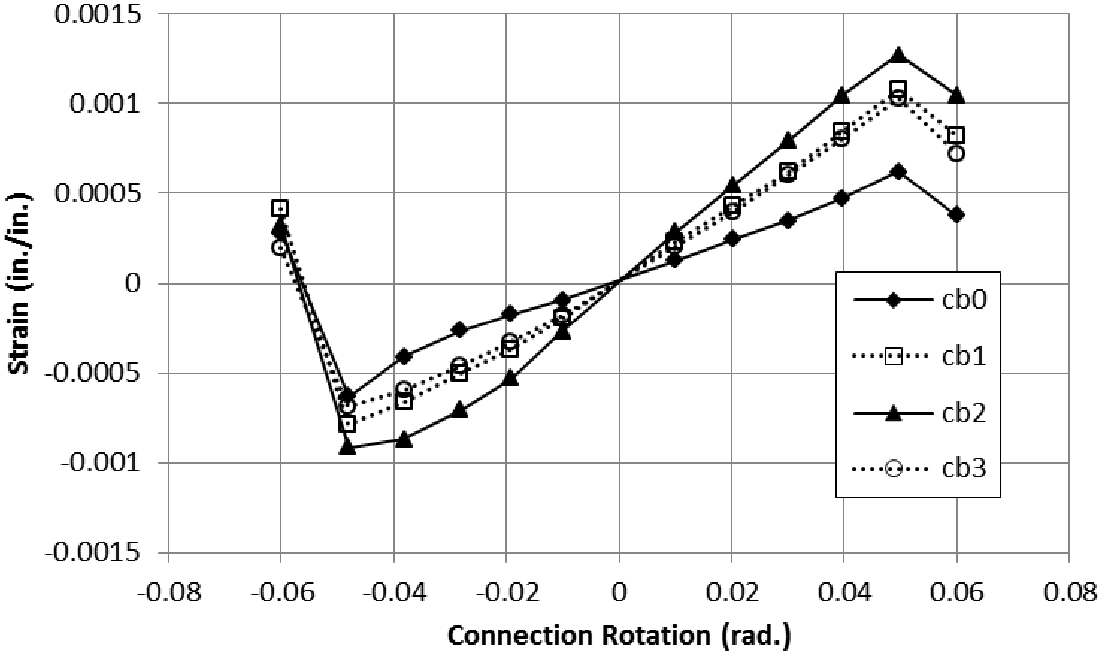

Figure 7.43 Strain in the column back versus connection rotation for the matched connection

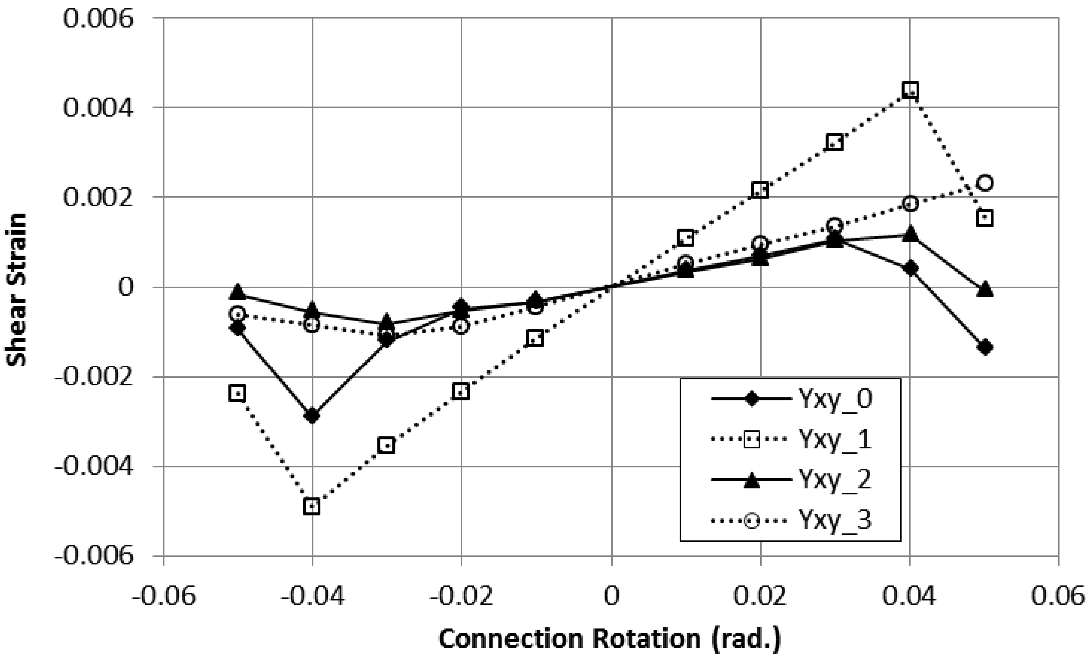

Figure 7.44 Shear strain versus connection rotation for the unmatched connection

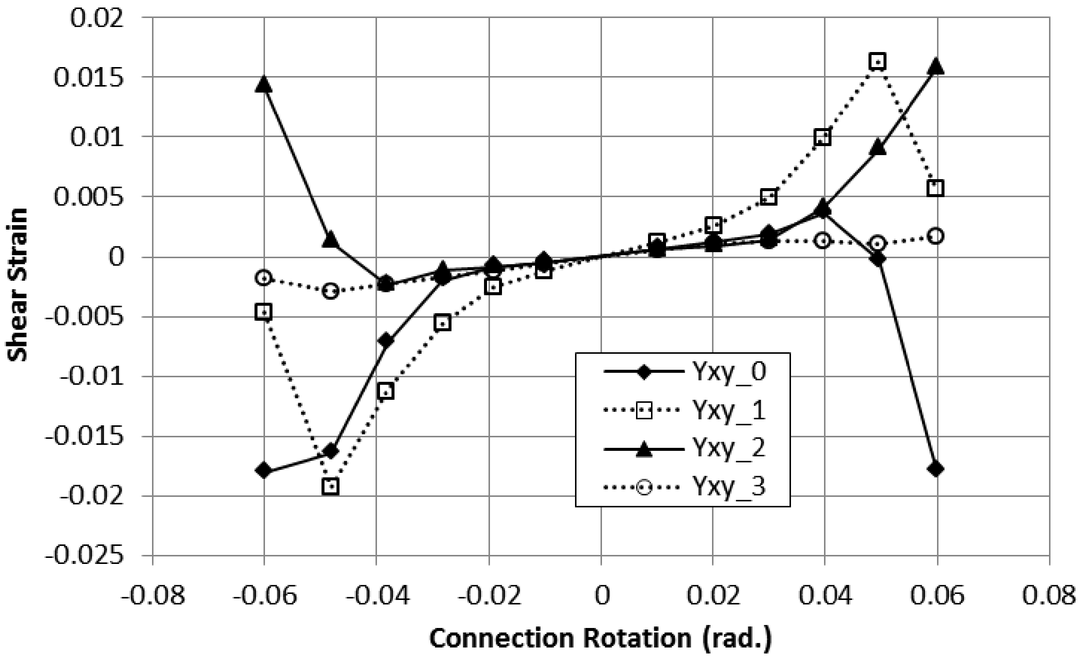

Figure 7.45 Shear strain versus connection rotation for the matched connection

CHAPTER 8: SUMMARY AND CONCLUSIONS

8.1 Summary

Hollow structural sections (HSS) are steel tubes formed from steel plates into square, rectangular, and circular cross-sections. They have been used in a variety of structural applications including as column members, truss elements, bracing members, and cladding supports because of their excellent compression, bending and torsional properties. Studies of HSS members dating back to the 1960's have considered the behavior of HSS beams, columns, axially loaded braced frame and truss members, and their connections. However, most of this work has focused on static or monotonic loading conditions leading to a reduced number of applications in seismic systems. In particular, the lack of understanding of the cyclic bending behavior of HSS members has limited their use in tube-based seismic moment frame systems as both beam and column members. Such a system has potential benefits with respect to reduction of seismic weight, potential reduced lateral bracing requirements, applications to modular construction, use in steel-concrete composite systems, and implementation in architecturally exposed structural steel frames. The beneficial properties of HSS can lead to more resilient and robust steel frame systems under seismic hazards. As a result, *the goal of this project was to characterize the behavior of HSS beams and welded HSS-to-HSS moment connections both experimentally and analytically under large cyclic deformations to provide a basis for the design and utilization of HSS-to-HSS moment frame systems for low to mid-rise structures in regions of high seismicity.*

The approach that has been taken to achieve this goal includes both experimental and analytical components in three phases. The first phase has experimentally explored the behavior of eleven full size HSS beam members under large cyclic rotations. The second phase has focused on expanding the experimental finding through advanced finite element methods to capture the local buckling and global hysteretic behavior of HSS members in cyclic bending. The final phase has focused on the development of a design procedure for HSS-to-HSS moment connections. A finite element model of unreinforced and reinforced HSS-to-HSS moment connections has been used to analyze these connections leading to an experimental study of two full-scale unreinforced welded HSS-to-HSS moment connections. These connection tests have provided an understanding of the behavior, potential limitations, and design requirements for seismic HSS-to-HSS moment connections.

8.1.1 Summary of HSS Beam Study

An HSS beam study was completed to characterize the cyclic bending behavior of HSS and better define limits for their use in seismic building applications outside of braced frame systems. Current limiting parameters for the use of HSS in seismic applications were based on tests conducted under monotonic bending, cyclic bending under large axial loads, or under cyclic axial loads. The HSS beam bending study was divided into three main phases: (1) experimental testing of HSS member material properties, (2) cyclic testing of eleven full scale HSS beam members up to large rotation levels, and (3) finite element modeling of 133 HSS beam members.

The first phase of the HSS beam study considered the variability of the material properties of cold formed HSS members across their cross-sections. An extensive study of the material properties of 11 different HSS members was carried out utilizing 114 coupon specimens. The subsize coupon specimens were taken from the flanges, webs, corners, and weld of each HSS member. Stress and strain were measured for each specimen to characterize the behavior in terms of yield and ultimate tensile strength along with yield and ultimate tensile strain. Additionally, the effects of cold working and electrical resistance welding were considered.

The second phase of the HSS beam study considered the behavior of eleven standard U.S. HSS members of the same length with width-thickness and depth-thickness ratios varying from 8.46 to 31.3 and 19.9 to 48.5, respectively. These members were tested experimentally under large inelastic bending cycles to analyze the resulting hysteretic behavior. The test setup was configured so the beams were cantilevered and subjected to cyclic displacement causing rotations up to 0.08 rad. Cycling effects associated with the degradation of the moment capacity, rotation capacity, secant stiffness, and energy dissipation were observed out to large rotation levels. Strain measurements in the flange also provided insight into the formation of the plastic hinge with increasing rotation.

The final phase of the HSS beam study addressed the limited amount of experimental data on the behavior of HSS beam members under cyclic loads. The calibration and validation of a finite element model to the experimental results was conducted leading to a large parametric study of HSS beam members under cyclic bending. The parametric study considered 133 different sections with *b/t* and *h/t* ratios varying from 7.0 to 31.5 and 16.4 to 52.0, respectively. The calibration of the finite element model included geometric imperfections of the section geometry and experimentally measured material properties. All HSS members were cycled under the same loading protocol simulating the effects of a far-field type ground motion up to 0.08 rad. of beam rotation. The effect of the *b/t* and *h/t* ratios on the hysteretic behavior was considered with a focus on the degradation of the maximum overall moment capacity at 0.04 rad., the rotational capacity at 80% of the maximum overall moment capacity, and degradation of the maximum secant stiffness with continued cycling to large rotation levels. Finally, equations for predicting the behavior of HSS based on the *b/t* and *h/t* ratios and design recommendations for the utilization of HSS beam members in cyclic bending applications were derived.

8.1.2 Summary of HSS-to-HSS Moment Connection Study

The HSS-to-HSS moment connection study was performed to understand the behavior of unreinforced and reinforced HSS-to-HSS connections under cyclic loading. The overlying goal of this work was to determine detailing requirements and limiting parameters that ensure proper ductility and capacity for use of HSS-to-HSS connections in seismic moment frame systems. This work was completed in two phases: (1) development of the unreinforced and reinforced HSS-to-HSS moment connection design procedure and a parametric finite element study of these connections and (2) experimental testing of two full-scale unreinforced HSS-to-HSS moment connections.

The first phase of the welded HSS-to-HSS moment connection study determined a design a procedure for detailing unreinforced and reinforced HSS-to-HSS moment connections with potential for seismic applications. The welded reinforced HSS-to-HSS moment connections were designed and detailed to develop plastic hinging in the HSS beam member while minimizing the likelihood of a non-ductile weld failure. This performance was accomplished in the design by ensuring a yield failure in the diaphragm plate prior to weld failure. Finite element models of 39 different unreinforced, 24 different internal diaphragm plate, and 24 different external diaphragm plate HSS-to-HSS moment connections were analyzed. Several important parameters, such as the beam width-column width ratio and beam thickness-column thickness ratio were considered in terms of their effect on connection moment capacity, ductility, energy dissipation, and stiffness.

During the second phase of the HSS-to-HSS moment connection study, two full-scale unreinforced HSS-to-HSS moment connections were experimentally tested to identify potential limit states not captured in the finite element modeling and to assess their ability to meet seismic design requirements. The hysteretic behavior was evaluated along with utilizing the instrumentation to extract the sources of inelastic rotation. The effects of continued cycling were assessed in terms of energy dissipation, equivalent viscous damping, and secant stiffness. Additionally, the effects of strain in the connection region were evaluated to better understand the load transfer mechanism in the connection and regions of high stress concentration.

8.2 Conclusions

1. For the HSS material properties, it was found that the heat affected zone near the weld seam and cold working in the corners led to localized changes in the material properties. The effects did not spread into a significant portion of the flats of the HSS member. Additionally, the degree of cold working did not affect the material strength as much as it affected the ductility of the corner material. Finally, the yield and ultimate strengths obtained from these tests suggest slightly lower material overstrength ratios, R_y and R_t, than specified in the seismic provisions (AISC 2010b).

2. Experimental testing of HSS beam members confirmed that *b/t* and *h/t* ratios affected the cyclic hysteretic behavior. All tested HSS specimens produced stable hysteretic behavior during early cycling with moment capacities at least 1.23 times greater than the predicted theoretical plastic moment capacity and 0.90 times the predicted experimental plastic moment capacity. However, large *b/t* and *h/t* ratios led to a decrease in hysteretic area and loss of moment capacity with continued cycling to rotation levels above 0.02 rad. This continued deformation after buckling also led to fatigue induced fracture at the corner of the HSS members that propagated across the face of the flange with increased cycling.
3. Experimental testing of HSS beam members showed that the effects on the behavior from the *b/t* and *h/t* ratios were interrelated. Contour plots for predicting the degradation of the moment capacity between maximum moment and the moment measured at the peak of the 0.04 rad. rotation cycle provided a good estimate of limiting width-thickness and depth-thickness ratios by taking into account the observed interaction between these two parameters. HSS beams with larger *b/t* ratios led to a more significant decrease in the moment capacity and rotation capacity due to the importance of the flange in resisting cyclic bending.
4. Finite element models utilizing three dimensional shell elements, experimentally measured material properties, and geometric perturbations were sufficient to accurately model the bending behavior of HSS beam members under large cyclic load reversals. With a 0.05 in. maximum perturbation of the section geometry, the error in estimating the maximum overall moment was minimized for most HSS members. Comparison of the degradation of the maximum overall moment at 0.04 rad. and the rotation at 80% of the maximum overall moment showed good correlation with the experimental results.
5. For all but two of the 133 analyzed sections the moment capacities were greater than the plastic moment capacity. Increasing the *b/t* and *h/t* ratios led to a decrease in the moment capacity with increased rotations levels. Based on a regression analysis, limiting *b/t* and *h/t* ratios were obtained that ensure moments of at least 80% of the maximum overall moment at 0.04 rad. The *b/t* and *h/t* limits were 12.1 and 28.4, respectively, utilizing specified ASTM A500 Gr. B material properties.

6. The full-scale cyclic bending tests and HSS beam member finite element models demonstrated that HSS are viable for use in cyclic bending applications. Stable plastic hinging behavior could be obtained provided that the width-thickness and depth-thickness ratios are adequately chosen to limit local buckling at small rotation levels. Fracture and tearing in the corners indicated that low cycle fatigue effects also need to be considered.
7. A design procedure for fully-welded reinforced HSS-to-HSS moment connections utilizing external and internal diaphragm plates was developed. The procedure used the beam moment capacity to develop the connection capacity and required a yield failure in the beam diaphragm plates prior to a non-ductile failure of the connection welds.
8. Based on the finite element analysis, increase in of the beam width-column width ratio, from 0.6 to 1.0 and a decrease in the beam thickness-column thickness ratio from 1.0 and 0.4, for unreinforced HSS-to-HSS moment connections would increase the connection moment capacity. When the reinforced connections were considered, beam width-column width and beam thickness-column thickness ratios had less effect on the connection moment capacity due to the fact that the connection allowed for formation of a plastic hinge in the beam member outside the connection. The reinforcing diaphragm plate lengths and thicknesses were shown to cause small changes in the connection performance in terms of moment capacity and secant stiffness.
9. Utilizing the connection finite element models, no unreinforced connections showed normalized moment capacities greater than unity, while all reinforced connections showed normalized moment capacities greater than unity. A comparison of the unreinforced and reinforced HSS-to-HSS moment connections showed that both internal and external diaphragm plate connections greatly improved the connection performance. Additionally, the results showed there was no distinct advantage to using one reinforcing configuration over the other.
10. Both tested unreinforced HSS-to-HSS moment connections showed stable hysteretic behavior at rotations up to 0.04 rad. for the unmatched connection (β=0.8) and 0.05 rad. for the matched connection (β=1.0). However, at these

rotations, fracture occurred in the column member at the toe of the weld in the base metal and the hysteretic moment capacity decreased suddenly to less than 75% of the maximum moment capacity.

11. For both the unmatched and matched connections, formation of a stable plastic hinge was not possible. At the cycle associated with the maximum moment, the beam rotation accounted for only 30% of the inelastic rotation for the unmatched connection and only 20% of the inelastic rotation for the matched connection. However, matched connections were able to move the inelastic deformation into the column sidewalls. Rotation in the column face exceeded 58% of the inelastic rotation in the unmatched connections, while rotation in the column face contributed up to 32% of the inelastic rotation for the matched connection.
12. Analysis of the strain gage data showed that the load transferred through the beam corners and into the column member. The matched connection was more effective at spreading the load across the beam flange, leading to reduced strain in the column face at maximum moment capacity.

8.3 Research Impact

1. Experimental testing of HSS material properties showed that the effect of cold working at the corners and the heat affected zone at the weld was limited to the immediate vicinity of these areas. As a result, changes in material strength provided only limited concern when modeling HSS behavior. However, cold working was shown to seriously affect the ductility in these regions suggesting low cycle fatigue is a concern.
2. The HSS beam member study provided an important understanding of the behavior of HSS beam members under cyclic loading conditions. As a result, HSS beam members were shown to be capable of sustaining seismic loads provided limiting parameters are met.
3. A finite element model that is capable of capturing the local buckling behavior of many HSS beam members under cyclic loads was calibrated and validated allowing for more detailed studies of HSS members under seismic loads.

4. Geometric limits to decrease undesirable behavior are disseminated. The *b/t* and *h/t* limits for HSS members in flexure to mitigate local buckling and degradation of the moment capacity were found to be 12.1 and 28.4, respectively, utilizing specified ASTM A500 Gr. B material properties.
5. The study of HSS-to-HSS moment connections showed that the utilization of welded reinforced and unreinforced HSS-to-HSS moment systems was feasible from a design standpoint. Specific design procedures were provided that allow for detailing of exterior fully-welded internal and external diaphragm plate reinforced moment connections.
6. Analysis of finite element models of reinforced HSS-to-HSS moment connections showed that the utilization of internal and external diaphragm plates in HSS-to-HSS moment connections was suitable for developing the moment capacity of the HSS beam member.
7. Experimental testing of matched and unmatched unreinforced HSS-to-HSS moment connections showed that these connections had a shortcoming in terms of brittle failure in the weld region necessitating reinforcing details to mitigate such failure modes.
8. The results from this study allowed for a more effective utilization of HSS members under cyclic loading conditions and expanded potential applications for HSS members and tube-based systems.

8.4 Recommendations for Future Research

This research addressed several topics regarding the utilization of HSS beam members under large cyclic displacements. Additionally, a design procedure for the development of welded reinforced HSS moment connections was derived. However, to demonstrate the suitability of HSS members and connections, further work is needed prior to using HSS members in a tube-based seismic moment frame system. The following recommendations for continued research are:

1. Weld requirements for unreinforced HSS-to-HSS connections undergoing cyclic loads are not well understood. The AISC Specification requirements are based on monotonic axially loaded HSS truss members. Details and design procedures

suitable for cyclic bending loads are needed to fully utilize unreinforced HSS-to-HSS moment connections in regions where cyclic loading may occur.

2. Experimental cyclic testing of internal and external diaphragm reinforced HSS-to-HSS moment connections is recommended. The results from the finite element modeling study indicated that reinforced HSS-to-HSS moment connections are likely suitable for developing a ductile and stable mechanisms. However, this study did not consider the effects of weld failure on the connection performance
3. Further research should consider different HSS-to-HSS moment connection configurations that are likely suitable for use in seismic moment frame systems. These systems should employ extremely efficient fabrication and construction practices that would allow for rapid or modular construction. Possible connections include a welded steel collar or blind bolted seismic moment connections.
4. Currently, AISC does not include any recommendations to limit lateral torsional buckling of HSS beam members. Some research has considered this behavior, but more work is required to develop lateral bracing requirements for HSS beam members in seismic frame systems.

REFERENCES

AIJ. (1990). Standard for limit state design of steel structures. Tokyo, Japan: Architectural Institute of Japan. (In Japanese)

AIJ. (1998). Recommendation for Enhancement of Disaster Mitigation in Buildings and Urban Areas – Based on Damage Observed in 1995 Hyogoken-Nanbu Earthquake. Building Science, 113(1418), 9-24. (In Japanese)

AISC. (1993). Load and resistance factor design specification for structural steel buildings. Chicago, IL: American Institute of Steel Construction.

AISC. (1997). Hollow structural sections connections manual. Chicago, IL: American Institute of Steel Construction.

AISC. (2000). Load and resistance factor design specification for steel hollow structural sections. Chicago, IL: American Institute of Steel Construction.

AISC. (2001). Manual of steel construction load and resistance factor design (3rd. ed.). Chicago, IL: American Institute of Steel Construction.

AISC. (2005). Specification for Structural Steel Buildings,. Chicago, IL: American Institute of Steel Construction. Chicago, IL: American Institute of Steel Construction.

AISC. (2006). Seismic Design Manual, Chicago, IL: American Institute of Steel Construction.

AISC. (2010a). Specification for Structural Steel Buildings. Chicago, IL: American Institute of Steel Construction.

AISC. (2010b). Seismic Provisions for Structural Steel Buildings. Chicago, IL: American Institute of Steel Construction.

AISC. (2011). Steel Construction Manual. (14th ed.). Chicago, IL: American Institute of Steel Construction.

ASTM (2010). ASTM A500/A500M-10a Standard Specification for Cold-Formed Welded and Seamless Carbon Steel Structural Tubing in Rounds and Shapes. West Conshohocken, PA. ASTM International.

ASTM (2012). ASTM A370-12a Standard Test Methods and Definitions for Mechanical Testing of Steel Products. West Conshohocken, PA. ASTM International.

AWS (2010). Structural welding code - ANSI/AWS D1.1:2010. Miami, FL: American Welding Society.

Bergmann, R. (1994). Load introduction in composite columns filled with high strength concrete. Tubular Structures VI, Rotterdam, The Netherlands.

Bertero, V. V., Uang, C. M., Llopiz, C. R., & Igarashi, K. (1989). Earthquake simulator testing of concentric braced dual system. Journal of Structural Engineering, 115(8), 1877.

Brescia, M., Landolfo, R., Mammana, O., Iannone, F., Piluso, V., & Rizzano, G. (2009). Preliminary results of an experimental program on the cyclic response and rotation capacity of steel members. STESSA 2009.

Bruneau, M., Uang, C.-M., Whittaker, A. (1998). “Ductile design of steel structures.” McGraw Hill, Boston, MA.

BSI. (2000). Structural use of steelwork in building, BS 5950, part 1. London, UK: British Standards Institute.

Chen, C. H., Huang, Y., & and Mahin, S. A. (2009). Comparison of seismic demands for a three-story SCBF system considering fiber and finite element models. SEAOC 2009 Convention, San Diego, CA, United States.

CIDECT (2005) Design Guide 9 - Design guide for structural hollow section column connections, (1st ed.). Comite International pour le Developpement et l’Etude de la Construction Tubulaire (CIDECT), Ontario, Canada.

CIDECT. (2010). CIDECT Design Guide 3, 2nd Edition - Design guide for rectangular hollow section (RHS) joints under predominantly static loading, Comite International pour le Developpement et l’Etude de la Construction Tubulaire (CIDECT), Ontario, Canada.

Clark, P., Frank, K., Krawinkler, H., & and Shaw, R. (1997). Protocol for fabrication, inspection, testing, and documentation of beam-column connection tests and other experimental specimens. SAC Steel Project Background Document. October, Report no. SAC/BD-97/02.

Corona, E., & Vaze, S. P. (1996). Buckling of elastic-plastic square tubes under bending. International Journal of Mechanical Science, 38(7), 753.

CSA. (2001). Steel structures for buildings (limit state design), CSA-S16-01. Toronto, ON: Canadian Standards Association.

Davies, G., Packer, J. A., & Coutie, M. G. (1984). The behaviour of full width RHS cross joints., 411.

Davies, G., Owen, J. S., & Kelly, R. B. (2001). The effect of purlin loads on the capacity of overlapped bird beak K joints. ISTS, 229.

Dawe, J. L., & Grondin, G. Y. (1990). Shear connections using stub tees between W beams and HSS columns. Canadian Journal of Civil Engineering, 17(5), 788.

Dawe, J. L., & Guravich, S. J. (1993). Branch plate to reinforced HSS connections in tension and compression. Canadian Journal of Civil Engineering, 20(4), 631.

Dawe, J. L., & Mehendale, S. V. (1995). Shear connections using stub tees between W beams and HSS columns. Canadian Journal of Civil Engineering, 22(4), 683.

Dean, M., Wilkinson, T., & Hancock, G. J. (2001). Bending and compression tests of cold formed rectangular hollow sections. Tubular Structures IX, Düsseldorf, Germany.

Denavit, M. D., Hajjar, J. F., Perea, T., and Leon, R. T. (2010). Cyclic evolution of damage and beam-column interaction strength of concrete-filled steel tube beam-columns. In Proc. 9th US National and 10th Canadian Conference on Earthquake Engineering, Toronto, 25-59 July, 2010. EERI.

DSS (2008). Abaqus FEA Version 6.8-1 Documentation Collection. Dassault Systemes Simulia Corp. Providence, RI.Dutta, D. (2002). Structures with hollow sections. Darmstadt, Germany: Ernst & Eohn.

Dwyer, T. J., & Galambos, T. (1965). Plastic behavior of tubular beam columns. American Society of Civil Engineers Proceedings, Journal of the Structural Division, 91(4), 153.

Earls CJ. (2000). Geometric factors influencing structural ductility in compact I-shaped beams. , ASCE Journal of Structural Engineering, 126(8): 860–866. EC3. (2003).

Eurocode 3: Design of steel structures - part 1.1: General rules and rules for buildings. Brussels, Belgium: European Committee for Standardization.

Eekhout, M. (1996). Tubular structures in architecture. Delft, The Netherlands: Delft University Press.

Elchalakani, M. (2003). Tests of cold-formed circular tubular braces under cyclic axial loading. Journal of Structural Engineering, 129, 507.

El-Tawil, S. and Kunnath, S. K. (1998). Strength and Ductility of FR Welded-Bolted Connections,"Update No. 4, SAC Steel Project.

Febres, R., Inglessis, P., & Florez-Lopez, J. (2003). Modeling of local buckling in tubular steel frames subjected to cyclic loading. Computers and Structures, 81, 2237.

FEMA. (2000). Recommended seismic design criteria for new Steel Moment-frame buildings (FEMA 350). Washington, DC.: Federal Emergency Management Agency.

Foutch, D. A., Goel, S., & Roeder, C. (1987). Seismic testing of full-scale steel building: Part I. Journal of Structural Engineering, ASCE, 113(11), 2111.

Frater and Packer (1992a). Weldment Design for RHS Truss Connections. I: Applications. Journal of Structural Engineering, ASCE, 118(10), 2784–2803.

Frater and Packer (1992b). Weldment Design for RHS Truss Connections. II: Experimentation, Journal of Structural Engineering, ASCE, 118(10), 2804-2820.

Fukuta, T., Nishiyama, I., Yamanouchi, H., & Kato, B. (1989). Seismic performance of steel frames with inverted V braces. Journal of Structural Engineering, 115, 2016.

Furlong, R. W. (1967). Strength of steel encased concrete beam-columns. Journal of the Structural Division, 93(ST5), 113.

Giroux, Y. M., & Picard, A. (1977). Rigid framing connections for tubular columns. Canadian Journal of Civil Engineering, 4(2), 134.

Goggins, J. M., Broderick, B. M., Elghazouli, A. Y., & Lucas, A. S. (2005). Experimental cyclic response of cold-formed hollow steel bracing members. Engineering Structures, 27(7), 977.

Goto, ., Wang, Q., and Obata, M. (1998). FEM Analysis for Hysteretic Behavior of Thin-Walled Columns. J. Struct. Eng., 124(11), 1290–1301.

Grube, R., & Landskroner, S. (2001). SIGMA - a new joint for rigid connections in tubular structures. ISTS, 511.

Guerrero, N. (2007). Model of local buckling in steel hollow structural elements subjected to biaxial bending. Journal of Constructional Steel Research, 63(6), 779.

Gugerli, H. (1982). Inelastic cyclic behavior of steel members. (Ph.D. Thesis, Department of Civil Engineering, University of Michigan).

Hajjar, J. F., & Gourley, B. C. (1996). Representation of concrete-filled steel tube cross-section strength. Journal of Structural Engineering, 122(11), 1327.

Hajjar, J. F., Molodan, A., & Schiller, P. H. (1998). A distributed plasticity model for cyclic analysis of concrete-filled steel tube beam-columns and composite frames. Engineering Structures, 20(4-6), 398.

Hajjar, J. F. (2000). Concrete-filled steel tube columns under earthquake loads. Progress in Structural Engineering and Materials, 2(1), 72-81.

Hancock, G. J., Davids, A. J., Key, P. W., Lau, S. C. W., & Rasmussen, K. J. R. (1990). Recent developments in the buckling and nonlinear analysis of thin-walled structural members. Thin-Walled Structures, 9, 309.

Hancock, G. J., & Zhao, X. L. (1992). Research into the strength of cold-formed tubular sections. Journal of Constructional Steel Research, 23(1), 55.

Hancock, G. J. (1998). Design of cold-formed steel structures, 3rd edition. Sydney, Australia: Australian Institute of Steel Construction.

Hancock, G. J., & Rasmussen, K. J. R. (1998). Recent research on thin-walled beam-columns. Thin-Walled Structures, 32(1-3), 3.

Hancock, G. J., Zhao, X. L., & Wilkinson, T. (2000). Future directions in cold-formed tubular structures. The Paul Grundy Symposium, Dept. of Civil Engineering, Monash University. 17.

Hancock, G. J., Murray, T., & Ellifritt, D. (2001). Cold formed steel structures to the AISI specification. New York, USA: Marcel Dekker, Inc.

Hasan, S. W., & Hancock, G.J. (1988). Plastic bending tests of cold-formed rectangular hollow sections. research report, no R586. Sydney, Australia: School of Civil and Mining Engineering, The University of Sydney.

Hassan, O. F., & Goel, S. C. (1991). Modeling of bracing members and seismic behavior of concentrically braced steel structures No. Research Report UMCE 91-1). Ann Arbor, MI: Department of Civil Engineering, University of Michigan.

Heinila, S., Bjork, T., Marquis, G., Backstrom, M., and Ilvonen, R. (2008) Fatigue crack paths and residual stresses in cold formed rectangular structural tubes. European Structural Integrity Society. ECF15.

Huang, Y. (2009). Simulating the inelastic seismic behavior of steel braced frames including the effects of low-cycle fatigue. (PhD, University of California).

Ikeda, K., & Mahin, S. (1986). Cyclic response of steel braces. Journal of Structural Engineering, 112(2), 342.

Jin, J., & El-Tawil, S. (2003). Inelastic cyclic model for steel braces. Journal of Engineering Mechanics, 129(5), 548.

Jubb, J. E. M., & Redwood, R. G. (1966). Design of joints to box sections. The Institution of Structural Engineers, Conference on Industrialised Building and the Structural Engineer.

Kamba, T., Kanatani, H., & Wakida, T. (1994). CHS column-to-beam connections without diaphragms. ISTS, 249.

Kamba, T., & Tabuchi, M. (1994). Database for tubular column to beam connections in moment-resisting frames. International Institute of Welding Document, no.IIW-XV-E-94-208.

Kawaguchi, J., Morino, S., & Surimoto, T. (1998). Elasto-plastic behavior of concrete-filled tubular frames. In C. D. Buckner, & B. M. Shahrooz (Eds.), Composite construction in steel and concrete III (pp. 272). New York, NY: ASCE.

Kawano, A., & Matsui, C. (1997). New connections using vertical stiffeners between h-shaped beams and hollow or concrete-filled square tubular columns. In C. D. Buckner, & B. M. Shahrooz (Eds.), Composite construction in steel and concrete III (pp. 272). New York, NY: ASCE.

Key, P. W., Hasan, S. W., & Hancock, G. J. (1988). Column behavior of cold-formed hollow sections. Journal of Structural Engineering, 114(2), 390.

Key, P. W., & Hancock, G. J. (1993). A theoretical investigation of the column behaviour of cold-formed square hollow sections. Thin-Walled Structures, 16(1-4), 31.

Kishi, N., & Chen, W. F. (1990). Moment-rotation relation of semirigid connections with angles. Journal of the Structural Division, 116(7), 1813.

Korol, R. M., & Hudoba, J. (1972). Plastic behavior of hollow structural sections, Journal of the Structural Division, 98(ST5), 1007-1023.

Korol, R. M., El-Zanaty, M., & Brady, F. J. (1977). Unequal width connections of square hollow sections in Vierendeel trusses. Canadian Journal of Civil Engineering, 4(2), 190.

Korol, R. M., & Mizra, F. A. (1982). Finite element analysis of RHS T-joints. Journal of the Structural Division, 108(ST9), 2081.

Koskimaki, M., & Niemi, E. (1990). Finite element studies on the behavior of rectangular hollow section K-joints. ISTS, 28.

Kosteski, N., Packer, J.A., and Puthli, R.S. (2003). A finite element method based yield load determination procedure for hollow structural section connections. Journal of Constructional Steel Research, 59(4), 453-471.

Kumar, S. R. S., & Rao, D. V. P. (2006). RHS beam-to-column connection with web opening-experimental study and finite element modeling. Journal of Constructional Steel Research, 62(8), 739-46.

Kurata, M., Nakashima, M., & Suita, K. (2005). Effect of column base behavior on the seismic response of steel moment frames. Journal of Earthquake Engineering, 9(2), 415-438.

Kurobane, Y., & Ogawa, K. (1993). New criteria for ductility design of joints based on complete CHS truss tests. ISTS, 570.

Kurobane, Y., Makino, Y., Miura, K., Tokutome, K., & Tanaka, M. (2001). Testing of new RHS column-to-beam connections with U-shaped welded joints. ISTS, 493.

Kurobane, Y. (2002). Connections in tubular structures. Progress in Structural Engineering and Materials, 4(1), 35.

Lee, G., Jishan, X., An, G., & Zhang, K. C. (1991). Experimental studies on concrete-filled tubular short columns subjected under compression and torsion. Proceedings 3rd International Conference on Steel-Concrete Composite Structures, Fukuoka, Japan. 143.

Lee, S., & Goel, S. (1987). Seismic behavior of hollow and concrete-filled square tubular bracing members No. Research Report UMCE 87-11). Ann Arbor, MI: Department of Civil Engineering, University of Michigan.

Linder, J. (1993). Bolted connections to hollow sections with through bolts. ISTS, 133.

Liu, D. K., & Wardenier, J. (1998). Effect of boundary conditions and chord preload on the strength of RHS multiplanar gap KK-joints. ISTS, 231.

Liu, D. K., Yu, Y., & Wardenier, J. (1998). Effect of boundary conditions and chord preload on the strength of RHS uniplanar gap K-joints. ISTS, 223.

Liu, D. K., & Wardenier, J. (2001). Multiplanar influence on the strength of RHS multiplanar gap KK-joints. ISTS, 203.

Liu, Z. (1987). Investigation of concrete-filled steel tubes under cyclic bending and buckling. (Ph.D Thesis, Department of Civil Engineering, University of Michigan).

Liu, Z., & Goel, S. C. (1988). Cyclic load behavior of concrete-filled tubular braces. Journal of Structural Engineering, 114(7), 1488.

Lu, J., Flavenot, J.F., and Turbat, A. (1988). Prediction of residual stress relaxation during fatigure, Mechanical Relaxation of Residual Stresses, ASTM STP 993, L Mordfin, Ed. ASTM International, West Conshohocken, PA.

Lu, L.H. (1997). “The static strength of I-beam to rectangular hollow section column connections.” PhD Thesis, Delft University of Technology, Delft, The Netherlands.

Lu, Y. Q., & Kennedy, D. J. L. (1994). The flexural behavior of concrete-filled hollow structural sections. Canadian Journal of Civil Engineering, 21(1), 111.

Morino, S., Kawaguchi, J., Yasuzaki, C., & et al. (1993). Behavior of concrete-filled steel tubular three-dimensional subassemblages. In W. S. Easterling, & W. M. K. Roddis (Eds.), Composite construction in steel and concrete II (, pp. 726)

Marshall, P. W. (1992). Design of welded tubular connections - basis and use of AWS code provisions. Amsterdam, The Netherlands: Elsevier Science Publishers.

Miller (2006). Design Guide 21: Welded Connections – A Primer for Engineers, Chicago, IL: American Institute of Steel Construction.

Mourad, S., Ghobarah, A., & Korol, R. M. (1995). Dynamic response of hollow section frames with bolted moment connections. Engineering Structures, 17(10), 737.

Nakashima, M., & Liu, D. (2005). Instability and complete failure of steel columns subjected to cyclic loading. Journal of Engineering Mechanics, 131(6), 559.

Nishiyama, I., & Marino, S. (2004). US-Japan cooperative earthquake research program on CFT structures: Achievements on the Japanese side. Progress in Structural Engineering and Materials, 6, 39.

NZS. (1997). Steel structures standard, NZS 3404, part 1. Wellington, New Zealand: Standards New Zealand.

Ono, T., Iwata, M., & Ishida, K. (1991). An experimental study on joints of new truss system using rectangular hollow sections. ISTS, 344.

Ono, T., Iwata, M., & Ishida, K. (1993). Local failure of joints of new truss system using rectangular hollow sections subjected to in-plane bending moments. ISTS, 503.

Ono, T., Ishida, K., & Iwata, M. (1994). Local failure of joints of new truss system using rectangular hollow sections subjected to out-of-plane bending moments. ISTS, 441.

Owen, J. S., Davies, G., & Kelly, R. B. (1996). A comparison of the behavior of RHS bird beak T-joints with normal RHS and CHS systems. ISTS, 173.

Packer J. A., Wardenier J., Kurobane Y., Dutta D, and Yeomans N., (1992), Design Guide for Rectangular Hollow Section (RHS) Joints under Predominantly Static Loading, CIDECT Design Guide No. 3, Verlag TÜV Rhineland GmbH, Köln, Germany.

Packer, J. A. (1995). Concrete-filled HSS connections. Journal of Structural Engineering, 121(3), 458.

Packer, J. A., & Henderson, J. E. (1997). Hollow structural section connections and trusses. Ontario, Canada: Canadian Institute of Steel Construction.

Packer, J. A. (2000). Tubular construction. Progress in Structural Engineering and Materials, 2(1), 41-49.

Packer, J., Sherman, D., and Lecce, M. (2010). Steel design guide 24: Hollow structural section connections, Chicago, IL: American Institute of Steel Construction.

Packer, J. and Sun, M. (2011). Fillet weld design for rectangular HSS connections. Engineering Journal, AISC, 48(1), 31-48.

Perea, T., Leon, R. T., Denavit, M. D., & Hajjar, J. F. (2010). Experimental tests on cyclic beam-column interaction strength of concrete-filled steel tubes. Proceedings of the 9th U.S. National and 10th Canadian Conference on Earthquake Engineering, Toronto, ON.

Picard, A., & Giroux, Y. M. (1976). Moment connections between wide flange beams and square tubular columns. Canadian Journal of Civil Engineering, 3(2), 174.

Popov, E.P. and Tsai, K.C. (1989). “Performance of large seismic steel moment connections under cyclic loads.” Engineering Journal. AISC. Vol. 26, No. 2:51-60.

Prion, H. G. L., & Boehme, J. (1994). Beam-column behavior of steel tubes filled with high strength concrete. Canadian Journal of Civil Engineering, 21(2), 207.

Rao, D. V. P., & Kumar, S. R. S. (2006). RHS beam-to-column connection with web opening-parametric study and design guidelines. Journal of Constructional Steel Research, 62(8), 747-756.

Roeder, C.W., Carpenter, J.E., and Taniguchi, H. (1989). “Predicted ductility demand for steel moment-resisting frames.” Earthquake Spectra. Vol 5, No. 2: 409-427.

Roeder, C. W. (1998). Development of hybrid and composite systems for seismic design in the United States. Engineering Structures, 20(4-6), 355-363.

Sabol, T. A. (2006). Program recommendations to qualify HSS connections for seismic applications. Submitted to the American Institute of Steel Construction.

SAC (2000). FEMA-355D State of the art report on connection performance. Federal Emergency Management Agency, Washington, DC.

Sakino, K., & Tomii, M. (1981). Hysteretic behavior of concrete filled square steel tubular beam-columns failed in flexure. Transactions of the Japan Concrete Institute, 3, 439. (In Japanese)

Sakino, K., & Ishibashi, H. (1985). Experimental studies on concrete filled square steel tubular short columns subjected to cyclic shearing force and constant axial force. Journal of Structural and Construction Engineering, Transactions of the Architectural Institute of Japan, 353, 81. (In Japanese)

Shanmugam, N. E., Ting, L. C., & Lee, S. L. (1991). Behaviour of I-beam to box-column connections stiffened externally and subjected to fluctuating loads. Journal of Constructional Steel Research, 20(2), 129.

Sherman, D. R. (1995). Simple framing connections to HSS columns. National Steel Construction Conference, San Antonio, TX. 30.1.

Sohal, I. S., & Chen, W. F. (1988). Local buckling and inelastic cyclic behavior of tubular sections. Thin-Walled Structures, 6, 63.

Standards Australia. (1998). Structural steel hollow sections, Australian Standard AS 4100. Sydney, Australia: Standards Australia.

Sully, R. M., & Hancock, G. J. (1996). Behavior of cold-formed SHS beam-columns. Journal of Structural Engineering, 122(3), 326.

Sully, R. M., & Hancock, G. J. (1998). The behaviour of cold-formed slender square hollow section beam-columns. Tubular Structures VIII, Singapore.

Tanaka, T., Tabuchi, M., Furumi, K., Morita, T., Usami, K., Murayama, M., & Matsubara, Y. (1996). Experimental study on end plate to SHS column connections reinforced by increasing wall thickness with one side bolted. ISTS, 253.

Tang, X., & Goel, S. C. (1987). Seismic analysis and design considerations of braced steel structures, research report UMCE 87-4.

Ting, L. C., Shanmugam, N. E., & Lee, S. L. (1990). Box-column to I-beam connections with external stiffeners. Journal of Constructional Steel Research, 18(3), 209.

Tizani, W., & Ridley-Ellis, D. J. (2003). The performance of a new blind-bolt for moment-resisting connections. ISTS, 395.

Tomii, M., & Sakino, K. (1979). Experimental studies on the ultimate moment of concrete filled square steel tubular beam-columns. Transactions of the Architectural Institute of Japan, 275, 55. (In Japanese)

Tremblay, R. (2002). Inelastic seismic response of steel bracing members. Journal of Constructional Steel Research, 58(5-8), 665.

Tremblay, R., Archambault, M. H., & Filiatrault, A. (2003). Seismic response of concentrically braced steel frames made with rectangular hollow bracing members. Journal of Structural Engineering, 129(12), 1626.

Tremblay, R., Haddad, M., Martinez, G., Richard, J., & Moatt, K. (2008). Inelastic cyclic testing of large size steel bracing members. Proceedings of 14th World Conference on Earthquake Engineering, Beijing, China.

Tsuda, K., Matsui, C., & Mino, E. (1996). Strength and behavior of slender concrete filled steel tubular columns. Proceeding 5th International Colloquium on Structural Stability, 489.

Uriz, P., Filippou, F. C., & Mahin, S. A. (2008). Model for cyclic inelastic buckling of steel braces. Journal of Structural Engineering,134(4), 619-628.

U.S. DOT (1994). Effects of catastrophic events on transportation system management and operations – Northridge Earthquake – January 17, 1994. U.S. Department of Transportation John A. Volpe National Transportation Systems Center. Cambridge, MA.

Varma, A. H., Ricles, J. M., Sause, R., & et al. (1998). Behavior of high strength square CFT columns. Proceedings 6th US National Conference on Earthquake Engineering, Seattle, WA.

Walpole, W. R. (1996). Behaviour of cold-formed steel RHS members under cyclic loading No. Research Report No. 96-4). Christchurch, New Zealand: Univ. of Canterbury.

Wang, T., McCormick, J. P., Yoshitake, N., Pan, P., Murata, Y., & Nakashima, M. (2008). Collapse simulation of a four-story steel moment frame by a distributed online hybrid test. Earthquake Engineering Structural Dynamics, 37(6), 955.

Wardenier, J. (1982). Hollow section joints. Delft, The Netherlands: Delft University Press.

Wardenier, J., Kurobane, Y., Packer, J. A., Dutta, D., & Yeomans, N. (1991). Design guide for circular hollow section (CHS) joints under predominantly static loading. Koln, Germany: TUV-Verlag.

Wardenier, J. (2001). Hollow sections in structural applications. The Netherlands: CIDECT.

Weng, C.C. and Pekoz, T. (1988). Residual stresses in cold-formed steel members. 9th International Conference on Cold-Formed Steel Structures. 167-189.

Wheeler, A. T., Clarke, M. J., & Hancock, G. J. (1998). Finite element modeling of bolted moment end plate connections in tubular members. ISTS, 549.

Wheeler, A. T., Clarke, M. J., & Hancock, G. J. (2000). FE modeling of four-bolt, tubular moment end-plate connections. Journal of Structural Engineering, 126(7), 816-822.

White, R. N., & Fang, P. J. (1966). Framing connections for square structural tubing. Journal of the Structural Division, 92(ST2), 4782.

Wilkinson, T., & Hancock, G. J. (1998). Tests to examine compact web slenderness of cold-formed RHS. Journal of Structural Engineering, 124(10), 1166.

Wilkinson, T., & Hancock, G. J. (2002). Predicting the rotation capacity of cold-formed RHS beams using finite element analysis. Journal of Constructional Steel Research, 58, 1455.

Yang, F., & Mahin, S. (2005). Limiting net section fracture in slotted tube braces Structural Steel Education Council.

Yeomans, N. (1998). Rectangular hollow section column connections using the Lindapter Hollobolt. ISTS, 559.

Zhao, X. L., & Hancock, G. J. (1991). T-joints in rectangular hollow sections subject to combined actions. Journal of Structural Engineering, 117(8), 2258.

Zhao, X. L., & Hancock, G. J. (1992). Square and rectangular hollow sections subject to combined actions. Journal of Structural Engineering, 118(3), 648.

Zhao, X. L., Hancock, G. J., & Trahair, N. (1995). Lateral-buckling tests of cold-formed RHS beams. Journal of Structural Engineering, 121(11), 1565.

Zhao, X. L., Wilkinson, T., & Hancock, G. J. (2005). Cold-formed tubular members and connections: Structural behaviour and design. Oxford: Elsiever.